KANNUR UNIVERSITY

Theoretical Studies on Ternary Fission

Project report submitted to
University Grants Commission
Government of India

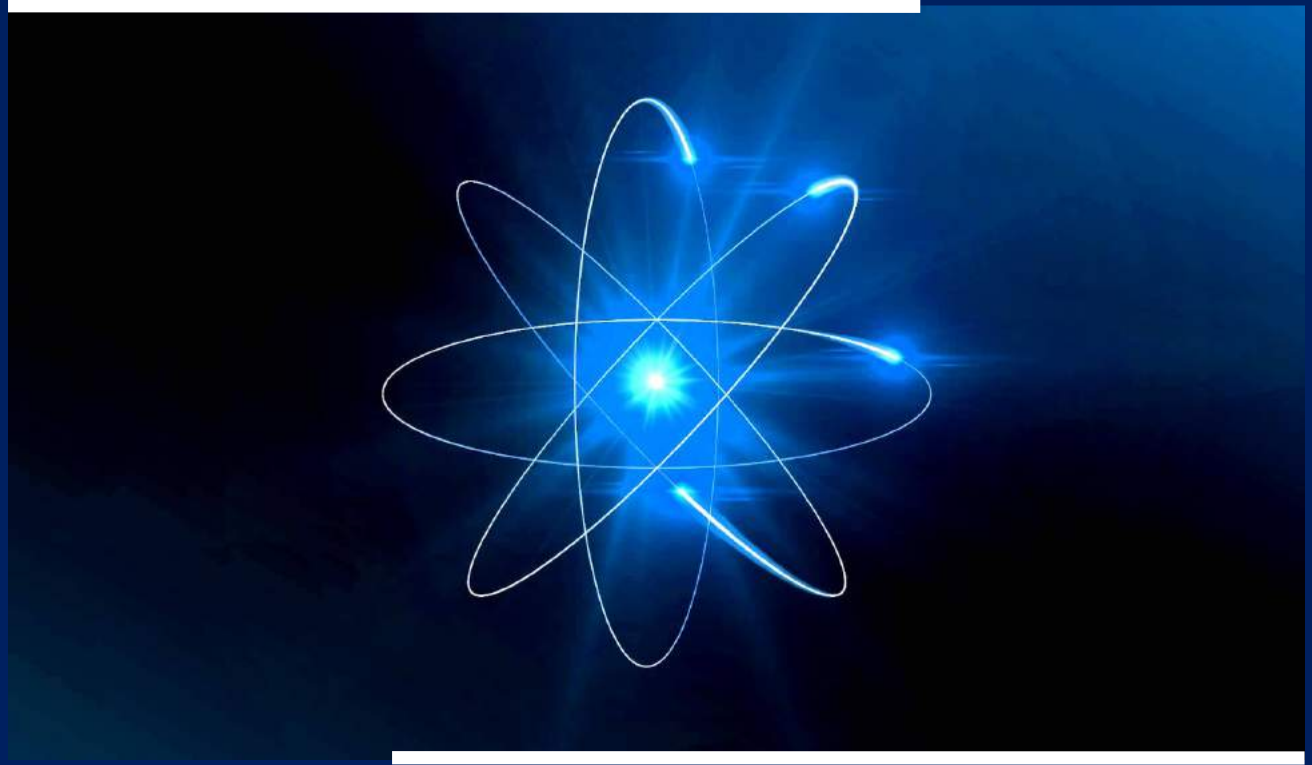

Dr. K. P. Santhosh

Associate Professor & Head
Department of Physics
Kannur University, Kerala

THEORETICAL STUDIES ON TERNARY FISSION

PROJECT REPORT

Major Research Project
University Grants Commission
Government of India, New Delhi
No.42-760/2013 (SR) dated 22-03-2013

By

Dr. K. P. SANTHOSH

DEPARTMENT OF PHYSICS
SWAMI ANANDATHEERTHA CAMPUS
KANNUR UNIVERSITY
KERALA

DECLARATION

I hereby declare that the project work entitled "Theoretical Studies on Ternary Fission" has been carried out by me at Department of Physics, Kannur University, Swami Anandatheertha Campus, Payyanur, Kerala under the Major Research Project of University Grants Commission, Government of India.

Place: Payyanur

Date: **Dr. K. P. Santhosh**

ACKNOWLEDGEMENT

First of all, I may express my heartfelt thanks to the Authorities of the Kannur University as I have been allowed to carry out the UGC Major Research Project (MRP) in the Department of Physics, Swami Anandatheertha Campus, Payyanur, Kerala.

I have always been grateful to University Grants Commission, Government of India, New Delhi, as I have been sanctioned the project and provided the financial support and timely instructions under the Major Research Project.

I should make special attention about the very cooperative and kind colleagues of my institution; Dr. N. K. Deepak and Dr. K. M. Nissamudeen, Department of Physics; Dr. K. R. Haridas, Dr. S. Sudheesh and Dr. K. V. Baiju, Department of Chemistry; Dr. P. K. Vijayan and Dr. G. Jayapal, Department of Geography; Dr. S. Mini and Dr. K. L. Saraladevi, Department of Music; for their valuable suggestions and care extended towards the progress of the project.

I would like to extend my heartfelt thanks to Mr. Sreejith Krishnan, the project fellow, whom I whole heartedly trust, is a very sincere, very cooperative and with a very high sense of responsibility in performing his work punctually and deserves high appreciation of all in the department throughout his course of the project work.

I have great pleasure to extend my thanks to my research scholars Dr. Priyanka B and Annu Cyriac who rendered valuable helps in performing the duties regarding the project work and other matters concerned with it. I am thankful to my research scholars Indu Sukumaran, Safoora V, Nithya C, Jayesh George Joseph, Preethi Rajan M K, Subha P V and M. G. V. Sankaracharyulu for their kind support.

I am also very much thankful to the non teaching staff in the Department of Physics, Swami Anandatheertha Campus, Payyanur.

Finally, I would like to thank Planning and Development Wing and pre-audit section of Finance Branch of Kannur University.

Dr. K. P. Santhosh

List of Publications

Details of the Papers Published in International Journals

[1] K. P. Santhosh, Sreejith Krishnan and B. Priyanka, European Physical Journal A **50**, 66 (2014).

[2] K. P. Santhosh and B. Priyanka, Nuclear Physics A **929**, 20 (2014).

[3] K. P. Santhosh and B. Priyanka, Physical Review C **89**, 064604 (2014).

[4] K. P. Santhosh, Sreejith Krishnan and B. Priyanka, Journal of Physics G: Nuclear and Particle Physics **41**, 105108 (2014).

[5] K. P. Santhosh and B. Priyanka, International Journal of Modern Physics E **23**, 1450059 (2014).

[6] K. P. Santhosh, Sreejith Krishnan and B. Priyanka, International Journal of Modern Physics E **23**, 1450071 (2014).

[7] K. P. Santhosh, Sreejith Krishnan and B. Priyanka, International Journal of Modern Physics E **24**, 1550001 (2015).

[8] K. P. Santhosh, Sreejith Krishnan and B. Priyanka, Physical Review C **91**, 044603 (2015).

[9] K. P. Santhosh, Annu Cyriac and Sreejith Krishnan, Nuclear Physics A **949**, 8 (2016).

[10] K. P. Santhosh and Sreejith Krishnan, European Physical Journal A **52**, 108 (2016).

[11] K. P. Santhosh and Sreejith Krishnan, Canadian Journal of Physics **95**, 573 (2017).

[12] K. P. Santhosh and Sreejith Krishnan, International Organization of Scientific Research-Journal of Applied Physics **2**, 13 (2017).

[13] K. P. Santhosh, Sreejith Krishnan and Jayesh George Joseph, Pramana Journal of Physics **91**, 5 (2018).

Details of Papers Presented in various Symposia on Nuclear Physics

[1] K. P. Santhosh, Sreejith Krishnan and B. Priyanka, Proceedings of the DAE-BRNS Symposium on Nuclear Physics (Mumbai, India) **58**, 398 (2013).

[2] Sreejith Krishnan, B. Priyanka and K. P. Santhosh, Proceedings of the DAE-BRNS Symposium on Nuclear Physics (Varanasi, India) **59**, 78 (2014).

[3] K. P. Santhosh, Sreejith Krishnan and B. Priyanka, Proceedings of the DAE-BRNS Symposium on Nuclear Physics (Varanasi, India) **59**, 446 (2014).

[4] Sreejith Krishnan, B. Priyanka and K. P. Santhosh, Proceedings of the DAE-BRNS Symposium on Nuclear Physics (Puttaparthi, India) **60**, 438 (2015).

[5] Sreejith Krishnan and K. P. Santhosh, 28th Kerala Science Congress (Calicut, India), 2124 (2016).

[6] Sreejith Krishnan and K. P. Santhosh, National Conference on Current Advancements in Physics (Palayamkottai, Tamilnadu, India), (2017).

CONTENTS

CHAPTER 1

CHAPTER 2

CHAPTER 3

Binary Fission

CHAPTER 4

Ternary Fission

CHAPTER 5

CHAPTER 1

Introduction

Nuclear fission is a complex reaction process in which a radioactive nucleus breaks up into two or more fragments. In 1939, it was Meitner and Frisch provided a theoretical explanation for the nuclear fission process based on the nuclear liquid drop model. The stability of nuclei was treated in terms of cohesive nuclear forces of short range, analogous to a surface tension and an electrostatic energy of repulsion. Usually a fission process takes place with the splitting of a radioactive nucleus into two fragments and such process are commonly referred to as binary fission. Instead of two fragments, three particles have been observed with very low probability from a fission process which makes the experimentalist and theoreticians more interesting and such process is referred to as ternary fission. Usually, one of the ternary fission fragments is very light compared to the main fission fragments and hence the ternary fission is often referred to as light charged particle (LCP) accompanied fission. In most cases of ternary fission, the light charged particle is an alpha particle emitted in a direction perpendicular to the other two fission fragments. The light charged particle can be emitted in two different configurations named as equatorial and collinear configurations. In equatorial configurations the light charged particle is emitted in a direction perpendicular to the main fission fragments, whereas in collinear configuration the light charged particle is emitted along the direction of main fission fragments.

The main objectives of the project work are to find the most probable ternary fragmentation from the study of potential energy surface treating three fragments as spherical, to study the sensitivity of potential energy surface to ground state deformation and orientation effects of fragments, to study the role of closed shell effects and ground state deformation of fragments in true ternary fission and in light charged particle accompanied fission, to compute Q value, driving potential, half life and yield for different modes of ternary splitting and their comparison with experimental data.

In **chapter 2**, the theoretical studies based on the alpha decay and heavy particle radioactivity from the various superheavy nuclei has been mentioned. The past few decades have witnessed tremendous strides in the production and spectroscopic studies of heavy elements due to the prodigious advancements in the heavy-ion beam technologies and accelerator facilities. As the superheavy isotopes synthesised in various fusion reactions decay primarily through consecutive alpha emissions and gets terminated by spontaneous fission, decay mechanisms like alpha decay and spontaneous fission may be considered as the major experimental signatures for the production of superheavy nuclei. A well established model named as Coulomb and proximity potential model (CPPM) and its modified version Coulomb and proximity potential model for deformed nuclei (CPPMDN) is used to study the barrier penetrability and the alpha decay half lives of various isotopes is also elaborated in the **chapter 2**.

In **chapter 3**, the cold binary fission studies on the various isotopes of californium, plutonium and uranium has been studied. The most probable fragmentation is obtained by calculating the barrier penetrability and the relative yield of all possible fragmentations. Even though the studies based on binary fission process has found to be a common aspect, the inclusion of pre-formation probability of fragments formed in the binary fission makes the study much more interesting and erudite. The model which describes how to calculate the barrier penetrability and the relative yield of various fission fragments is described in the **chapter 3**.

In **chapter 4**, the theoretical studies on the ternary fission of various isotopes have been mentioned. The process of ternary fission has been found to be of extreme interest for both the theoreticians and for the experimentalists, because the third particle is believed to be emitted very near the time of scission. There exists no well detailed theory which matches with the various experimental observations found in the splitting of a nucleus into three or more fragments. As the dynamics of this kind of complex fission process which involves three or more fission fragments is not much clearly known, the experimentalist have been willing to meet the theoreticians on their half way. Using computations, one can justify the physical separation of fragments and also the interactions among the fragments under Coulomb field and nuclear forces. After a thoroughly involved and painstaking research in the field of ternary fission process, a model has been developed by us named as Unified ternary fission model (UTFM), which is also described in the **chapter 4**.

The entire results and discussion related to the alpha decay and heavy particle radioactivity from the various superheavy nuclei, binary fission and ternary fission process of various isotopes has been summarized in **chapter 5**.

CHAPTER 2

Alpha Decay and Heavy Particle Radioactivity from Superheavy Nuclei

Alpha decay, observed by Rutherford [1, 2] a century ago, is one of the prominent decay modes of the superheavy nuclei. As valuable information regarding the mode of decay and low-energy nuclear structure of unstable superheavy nuclei can be obtained from their alpha decay studies, the observation and characterization of the alpha decay properties of the superheavy elements are very important. The production of some new superheavy nuclei has resulted in the identification of some stable alpha emitters in this region. The α emitters usually span an enormous range of lifetimes ranging from 10 ns to 10^{17} years and the quantum mechanical phenomenon of tunneling may be attributed to the origin of this large spread. The theoretical and experimental studies on the superheavy elements may result in many new findings, especially the possible appearance of new magic shell numbers or more precisely the prediction of the doubly magic nucleus next to ^{208}Pb (Z = 82, N = 126). Several theoretical models [3-8] have been employed for the predictions on the alpha decay of superheavy nuclei and a number of theoretical studies have been performed recently [9-14], concentrating on various alpha decay properties of these nuclei.

The synthesis and identification of new isotopes in the superheavy region [15] is one of the most rewarding and challenging investigations for the experimental nuclear physicists and these new discoveries are aimed at expanding simultaneously, the periodic table of elements and the Segre chart of nuclei. Recent experiments and those in progress at various laboratories drive at validating the predictions done within several theoretical approaches and hypothesis which can be aged back to forty years, on the existence of an enhanced stability in the region of the superheavy nuclei (SHN) [16]. The prediction of the existence of a "magic island" or the "Island of Stability", around Z = 120, 124 or 126 and N = 184 [17], in the domain of the superheavy elements may be quoted as one of the fundamental outcomes of the nuclear shell model. The heaviest neutron-rich nuclei with N > 170 in the vicinity of the closed spherical shells, Z = 114 (or possibly 120, 122, or 126) and N = 184, were expected to mark a considerable increase in nuclear stability, similar to the effect of the closed shells on the stability of doubly magic ^{208}Pb (Z = 82 and N = 126) [18]. Hence, several experiments were performed by Oganessian *et al.,* [15, 16, 18-21] with the purpose in view of synthesizing SHN close to the predicted neutron magic number N=184, through the complete fusion reactions of long lived even-Z target nuclei ^{242,244}Pu, ^{249}Cf and ^{248}Cm with ^{48}Ca projectiles, with the maximum accessible neutron-richness.

In reviewing the production of a century of radioactive elements up to *Z*=119 [22-24], historically [25, 26], different periods have to be considered, both theoretically and experimentally. The development of the particle accelerators and particle detectors during the mid 20th century [27] brought about the techniques of fusing light elements with long-lived isotopes of the heaviest actinides (^{233,238}U, ^{237}Np, ^{242,244}Pu, ^{243}Am, ^{245,248}Cm and ^{249}Cf) produced in nuclear reactors, usually termed as the "hot fusion" or "actinide-based fusion" as the compound nuclei formed after fusion, is hot owing to excitation energies between 40MeV and 50MeV. SHN with Z=113-116 [18-20] and Z=118 [15, 16] have been synthesized at JINR-FLNR, Dubna, in collaboration with the LLNL researchers using this method and very recently the authors were also successful in the synthesis of two isotopes of Z=117 [28, 29]. Later the 1970's [30, 31] witnessed the synthesis of heavier elements through the fusion of the closed-shell nuclei, ^{208}Pb and ^{209}Bi, with the medium-mass neutron-rich isotopes such as ^{54}Cr to ^{70}Zn. The SHN with Z=107 to 112 were synthesized at GSI, Darmstadt [22, 32-35] using this method and an isotope of *Z*=113 has been identified at RIKEN, Japan [36, 37] and they have also reconfirmed [38, 39] the existence of the superheavy elements Z=110, 111 and 112 reported earlier by GSI group.

2.1 Coulomb and Proximity Potential Model (CPPM)

The interacting potential barrier for a parent nucleus exhibiting cluster decay is given by,

$$V = \frac{Z_1 Z_2 e^2}{r} + V_p(z) + \frac{\hbar^2 \ell(\ell+1)}{2\mu r^2}, \text{ for z} > 0 \qquad (2.1.1)$$

Here Z_1 and Z_2 are the atomic numbers of the daughter and emitted cluster, 'z' is the distance between the near surfaces of the fragments, 'r' is the distance between fragment centers and is given as $r = z + C_1 + C_2$, where, C_1 and C_2 are the Süsmann central radii of fragments. The term ℓ represents the angular momentum, μ the reduced mass and V_P is the proximity potential. The proximity potential is V_P given by Blocki *et al.,* [40] as,

$$V_p(z) = 4\pi\gamma b\left[\frac{C_1 C_2}{(C_1 + C_2)}\right]\Phi\left(\frac{z}{b}\right), \qquad (2.1.2)$$

with the nuclear surface tension coefficient,

$$\gamma = 0.9517[1 - 1.7826(N-Z)^2 / A^2] \text{ MeV/fm}^2 \qquad (2.1.3)$$

where N, Z and A represent neutron, proton and mass number of parent respectively, Φ represents the universal proximity potential [41] given as,

$$\Phi(\varepsilon) = -4.41 e^{-\varepsilon/0.7176}, \text{ for } \varepsilon > 1.9475 \qquad (2.1.4)$$

$$\Phi(\varepsilon) = -1.7817 + 0.9270\varepsilon + 0.0169\varepsilon^2 - 0.05148\varepsilon^3, \text{ for } 0 \le \varepsilon \le 1.9475 \qquad (2.1.5)$$

with $\varepsilon = z/b$, where the width (diffuseness) of the nuclear surface $b \approx 1$ and Süsmann central radii C_i of fragments related to sharp radii R_i as,

$$C_i = R_i - \left(\frac{b^2}{R_i}\right) \qquad (2.1.6)$$

For R_i we use semi empirical mass formula in terms of mass number A_i as [40],

$$R_i = 1.28 A_i^{1/3} - 0.76 + 0.8 A_i^{-1/3} \qquad (2.1.7)$$

The potential for the internal part (overlap region) of the barrier is given as,

$$V = a_0 (L - L_0)^n, \text{ for } z < 0 \qquad (2.1.8)$$

Here $L = z + 2C_1 + 2C_2$ and $L_0 = 2C$, the diameter of the parent nuclei. The constants a_0 and n are determined by the smooth matching of the two potentials at the touching point.

Using one dimensional WKB approximation, the barrier penetrability P is given as,

$$P = \exp\left\{ -\frac{2}{\hbar}\int_a^b \sqrt{2\mu(V-Q)}\,dz \right\} \tag{2.1.9}$$

Here the mass parameter is replaced by reduced mass $\mu = mA_1A_2/A$, where 'm' is the nucleon mass and A_1, A_2 are the mass numbers of daughter and emitted cluster respectively. The turning points 'a' and 'b' are determined from the equation $V(a) = V(b) = Q$. The above integral can be evaluated numerically or analytically, and the half life time is given by,

$$T_{1/2} = \left(\frac{\ln 2}{\lambda}\right) = \left(\frac{\ln 2}{\nu P}\right) \tag{2.1.10}$$

where, $\nu = \left(\frac{\omega}{2\pi}\right) = \left(\frac{2E_v}{h}\right)$ represents the number of assaults on the barrier per second and λ the decay constant. E_v, the empirical vibration energy is given as [42],

$$E_V = Q\left\{0.056 + 0.039\exp\left[\frac{(4-A_2)}{2.5}\right]\right\}, \text{ for } A_2 \geq 4 \tag{2.1.11}$$

Within the fission model (CPPM), the cluster formation probability S can be calculated as the penetrability of the internal part (overlap region) of the barrier given as,

$$S = \exp(-K) \tag{2.1.12}$$

where $$K = \frac{2}{\hbar}\int_a^0 \sqrt{2\mu(V-Q)}\,dz \tag{2.1.13}$$

here, 'a' is the inner turning point and is defined as $V(a) = Q$ and $z = 0$ represents the touching configuration.

In the present model, we have included the probability of formation of the cluster before its emission. The decay constant λ and the penetrability through the total potential barrier P is related as, $\lambda = \nu P$, where ν is the assault frequency and $P = SP^{ext.}$. The cluster formation probability S can be calculated as the penetrability through the internal part (overlap region) of the barrier and is given in equations (2.1.12) and (2.1.13). $P^{ext.}$ is the penetrability through the external part of the potential barrier and is given as,

$$P = \exp\left\{-\frac{2}{\hbar}\int_0^b \sqrt{2\mu(V-Q)}\,dz\right\} \tag{2.1.14}$$

The first turning point z=0, represents the touching configuration and z=*b* represents the outer turning point which can be determined using the condition $V(b)=Q$.

2.2 Coulomb and Proximity Potential Model for Deformed Nuclei (CPPMDN)

The Coulomb interaction between the two deformed and oriented nuclei with higher multipole deformation included [43, 44] is taken from Ref. [45] and is given as,

$$V_C = \frac{Z_1 Z_2 e^2}{r} + 3Z_1 Z_2 e^2 \sum_{\lambda,i=1,2} \frac{1}{2\lambda+1}\frac{R_{0i}^{\lambda}}{r^{\lambda+1}} Y_{\lambda}^{(0)}(\alpha_i)\left[\beta_{\lambda i} + \frac{4}{7}\beta_{\lambda i}^2 Y_{\lambda}^{(0)}(\alpha_i)\delta_{\lambda,2}\right] \tag{2.2.1}$$

with $R_i(\alpha_i) = R_{0i}\left[1 + \sum_{\lambda}\beta_{\lambda i} Y_{\lambda}^{(0)}(\alpha_i)\right]$ (2.2.2)

where $R_{0i} = 1.28A_i^{1/3} - 0.76 + 0.8A_i^{-1/3}$. Here α_i is the angle between the radius vector and symmetry axis of the i^{th} nuclei (see Fig.1 of Ref [43]) and it is to be noted that the quadrupole interaction term proportional to $\beta_{21}\beta_{22}$, is neglected because of its short range character.

The proximity potential and the double folding potential can be considered as the two variants of the nuclear interaction [46, 47]. In the description of interaction between two fragments, the latter is found to be more effective. The proximity potential which describes the interaction between two pure spherically symmetric fragments has one term based on the first approximation of the folding procedure and the two-term proximity potential of Baltz *et al.*, (equation (11) of [48]) includes the second component as the second approximation of the more accurate folding procedure. The authors have shown that the two-term proximity potential is in excellent agreement with the folding model for heavy ion reaction, not only in shape but also in absolute magnitude (see figure 3 of [48]). The two-term proximity potential for interaction between a deformed and spherical nucleus is given by Baltz *et al*., [48] as,

$$V_{P2}(R,\theta)=2\pi\left[\frac{R_1(\alpha)R_C}{R_1(\alpha)+R_C+S}\right]^{1/2}\left[\frac{R_2(\alpha)R_C}{R_2(\alpha)+R_C+S}\right]^{1/2}$$

$$\text{x}\left[\left[\varepsilon_0(S)+\frac{R_1(\alpha)+R_C}{2R_1(\alpha)R_C}\varepsilon_1(S)\right]\left[\varepsilon_0(S)+\frac{R_2(\alpha)+R_C}{2R_2(\alpha)R_C}\varepsilon_1(S)\right]\right]^{1/2} \quad (2.2.3)$$

where $R_1(\alpha)$ and $R_2(\alpha)$ are the principal radii of curvature of the daughter nuclei at the point where polar angle is α, R_C is the radius of the spherical cluster, S is the distance between the surfaces along the straight line connecting the fragments and $\varepsilon_0(S)$ and $\varepsilon_1(S)$ are the one dimensional slab-on-slab function.

2.3 Alpha decay half lives

The various formalisms like Universal Curve (UNIV), Universal Decay Law (UDL), Scaling Law and various semi-empirical relations to evaluate the alpha decay half lives of isotopes are briefly discussed in the following sections.

2.3.1 Universal Curve (UNIV)

The decay half lives have been explained using several simple and effective relationships, which are obtained by fitting the experimental data. Among them, the universal curve (UNIV) of Poenaru *et al.,* [49-52], derived by extending a fission theory to larger mass asymmetry should be mentioned with great importance. Based on the quantum mechanical tunnelling process [53, 54], the disintegration constant λ, valid in both fission-like and α-like theories, is related to the partial decay half life T of the parent nucleus as, $\lambda=\ln 2/T=\nu SP_S$ (2.3.1.1)

Here ν, S and P_s are three model-dependent quantities: ν is the frequency of assaults on the barrier per second, S is the pre-formation probability of the cluster at the nuclear surface (equal to the penetrability of the internal part of the barrier in a fission theory [49, 50]), and P_s is the quantum penetrability of the external potential barrier. By using the decimal logarithm,

$$\log_{10} T(s) = -\log_{10} P - \log_{10} S + [\log_{10}(\ln 2) - \log_{10} \nu] \quad (2.3.1.2)$$

To derive the universal formula, it was assumed that ν = constant and that S depends only on the mass number of the emitted particle A_e [50, 53] as the microscopic calculation of the preformation probability [55] of many clusters from ^{8}Be to ^{46}Ar had shown that it is dependent only upon the size of the cluster. Using a fit with experimental data for α decay, the corresponding numerical values [50] obtained were, S_α = 0.0143153, ν = $10^{22.01}s^{-1}$. The decimal logarithm of the pre-formation factor is given as,

$$\log_{10} S = -0.598(A_e - 1) \quad (2.3.1.3)$$

and the additive constant for an even-even nucleus is,

$$c_{ee} = [-\log_{10} \nu + \log_{10}(\ln 2)] = -22.16917 \quad (2.3.1.4)$$

The penetrability through an external Coulomb barrier, having separation distance at the touching configuration $R_a = R_t = R_d + R_e$ as the first turning point and the second turning point defined by $e^2 Z_d Z_e / R_b = Q$, may be found analytically as,

$$-\log_{10} P_S = 0.22873(\mu_A Z_d Z_e R_b)^{1/2} \times [\arccos\sqrt{r} - \sqrt{r(1-r)}] \quad (2.3.1.5)$$

where $r = R_t / R_b$, $R_t = 1.2249(A_d^{1/3} + A_e^{1/3})$ and $R_b = 1.43998 Z_d Z_e / Q$.

The released energy Q is evaluated using the mass tables [56, 57] and the liquid-drop-model radius constant r_0 = 1.2249 fm.

2.3.2 Universal Decay Law (UDL)

Starting from the α-like (extension to the heavier cluster of α-decay theory) R-matrix theory and the microscopic mechanism of the charged-particle emission, a new universal decay law (UDL) for α-decay and cluster decay modes was introduced [58, 59] by Qi *et al.*,. The model was presented in an interesting way, which made it possible to represent, on the same plot with a single straight line, the logarithm of the half lives minus some quantity versus one of the two parameters (χ' and ρ') that depend on the atomic and mass numbers of the daughter and emitted particles as well as the Q value. UDL relates the half-life of monopole radioactive decay with the Q

values of the outgoing particles as well as the masses and charges of the nuclei involved in the decay and can be written in the logarithmic form as,

$$\log_{10}(T_{1/2}) = aZ_cZ_d\sqrt{\frac{A}{Q_c}} + b\sqrt{AZ_cZ_d(A_d^{1/3} + A_c^{1/3})} + c = a\chi' + b\rho' + c \quad (2.3.2.1)$$

where the quantity $A = \frac{A_d A_c}{A_d + A_c}$ and the constants a = 0.4314, b = -0.4087 and c = -25.7725 are the coefficient sets of equation (2.3.2.1), determined by fitting to experiments of both α and cluster decays [58]. The effects that induce the clusterization in the parent nucleus are included in the term $b\rho' + c$. As this relation holds for the monopole radioactive decays of all clusters, it is called the Universal Decay Law (UDL) [58].

2.3.3 Scaling law of Horoi *et al.,*

In order to determine the half lives of both the alpha and cluster decays, a new empirical formula for cluster decay was introduced by Horoi *et al.,* [60] and is given by the equation,

$$\log_{10} T_{1/2} = (a_1\mu^x + b_1)[(Z_1Z_2)^y/\sqrt{Q} - 7] + (a_2\mu^x + b_2) \quad (2.3.3.1)$$

where μ is the reduced mass. The six parameters are a_1 = 9.1, b_1 = -10.2, a_2 = 7.39, b_2 = -23.2, x = 0.416 and y = 0.613.

2.3.4 Viola-Seaborg Semi-empirical relationship (VSS)

The Viola-Seaborg semi-empirical relationship (VSS), with constants determined by Sobiczewski, Patyk and Cwiok [63], is given as,

$$\log_{10}(T_{1/2}) = (aZ + b)Q^{-1/2} + cZ + d + h_{\log} \quad (2.3.4.1)$$

Here the half-life is in seconds, Q value is in MeV and Z is the atomic number of the parent nucleus. The quantities a, b, c, and d are adjustable parameters and the quantity $h_{\log}$ represents the hindrances associated with odd proton and odd neutron numbers, as given by Viola-Seaborg [64]. Instead of using the original set of constants given by Viola and Seaborg [64], more recent values determined by Sobiczewski *et al.,* [63] taking account of the new data for even-even nuclei, have been used here. The constants are a = 1.66175, b = -8.5166, c = -0.20228, d = -33.9069 and

$h_{\log} = 0$, for Z, N even

$h_{\log} = 0.772$, for Z = odd, N = even

$h_{\log} = 1.066$, for Z = even, N = odd

$h_{\log} = 1.114$, for Z, N odd

2.3.5 The Analytical Formulae of Royer

Several expressions [61, 63-65] were developed for the α decay half-lives, subsequent to the earliest law formulated by Geiger and Nuttall [66]. By applying a fitting procedure on a set of 373 alpha emitters, Royer [67] formulated the analytical formulae for alpha decay with an RMS deviation of 0.42, given as,

$$\log_{10}[T_{1/2}(s)] = -26.06 - 1.114A^{1/6}\sqrt{Z} + \frac{1.5837Z}{\sqrt{Q_\alpha}} \qquad (2.3.5.1)$$

Here, A and Z are the mass and charge numbers of the parent nuclei and Q_α is the energy released during the reaction. Assuming the same dependence on the mass and charge of the mother nucleus and experimental Q_α, equation (2.3.5.1) was adjusted to a subset of 131 even-even nuclei and a relation was obtained with a rms deviation of only 0.285 and is given as,

$$\log_{10}[T_{1/2}(s)] = -25.31 - 1.169A^{1/6}\sqrt{Z} + \frac{1.5864Z}{\sqrt{Q_\alpha}} \qquad (2.3.5.2)$$

For a subset of 106 even-odd nuclei the rms deviation was found to be 0.39, and the relation is given as,

$$\log_{10}[T_{1/2}(s)] = -26.65 - 1.0859A^{1/6}\sqrt{Z} + \frac{1.5848Z}{\sqrt{Q_\alpha}} \qquad (2.3.5.3)$$

2.4 Spontaneous Fission Half Lives

Spontaneous fission, the limiting factor that determines the stability of newly synthesized super heavy nuclei, may be considered as one of the most prominent decay modes, energetically feasible for both heavy and superheavy nuclei with proton number $Z \geq 90$. The spontaneous fission half lives of the parent isotopes under study have been evaluated using the semi-empirical relation of Santhosh *et al.,* and Xu *et al.,* are discussed below.

2.4.1 Semi-empirical relation of Santhosh *et al.,*

Spontaneous fission, the limiting factor that determines the stability of newly synthesized super heavy nuclei, may be considered as one of the most prominent decay modes, energetically feasible for both heavy and superheavy nuclei with proton number $Z \geq 90$. The spontaneous fission half lives of the parent isotopes under study have been evaluated using the semi-empirical relation of Santhosh *et al.,* [61] discussed below.

A new semi empirical formula for explaining spontaneous fission was developed by Santhosh *et al.,* [61] by making least squares fit to the available experimental data. The formula obtained for logarithmic half-life time for spontaneous fission is given by,

$$\log_{10}(T_{1/2}/yr) = a\frac{Z^2}{A} + b\left(\frac{Z^2}{A}\right)^2 + c\left(\frac{N-Z}{N+Z}\right) + d\left(\frac{N-Z}{N+Z}\right)^2 + e, \qquad (2.4.1.1)$$

where, the constants are a = -43.25203, b = 0.49192, c = 3674.3927, d = -9360.6 and e = 580.75058. Here the quantities $\frac{Z^2}{A}$ and $I = \frac{N-Z}{N+Z}$ are the fissionability parameter and the neutron excess of the decaying parent nuclei respectively. It is to be noted that the semi-empirical formula works well for the nuclei in the mass regions ^{232}Th to ^{286}114 [61].

2.4.2 Semi empirical relation of Xu *et al.,*

The mode of decay of the isotopes under study can be identified through the calculations on the spontaneous fission (SF) half lives of the corresponding nuclei. The semi empirical relation given by Xu *et al*., [62], originally made to fit the even-even nuclei, has been used for evaluating the spontaneous fission half lives, and is given as,

$$T_{1/2} = \exp\left\{2\pi\left[C_0 + C_1 A + C_2 Z^2 + C_3 Z^4 + C_4 (N-Z)^2 - (0.13323\frac{Z^2}{A^{1/3}} - 11.64)\right]\right\} \qquad (2.4.2.1)$$

Here the constants C_0 = -195.09227, C_1 = 3.10156, C_2 = -0.04386, C_3 = 1.4030x10^{-6} and C_4 = -0.03199.

2.5 α decay chains from Z=118 superheavy nuclei in the range 271 ≤ A ≤ 310

The feasibility of alpha decay from the isotopes of the superheavy nuclei with Z=118, which span the range 271 ≤ A ≤ 310, has been studied extensively by taking the external drifting potential barrier as the sum of deformed Coulomb potential, deformed two term proximity potential and centrifugal potential (within CPPMDN). The possibility to the alpha decay process is related to its exothermicity, Q>0. The energy released in the alpha transitions between the ground state energy levels of the parent nuclei and the ground state energy levels of the daughter nuclei is given as,

$$Q_{gs\to gs} = \Delta M_p - (\Delta M_\alpha + \Delta M_d) + k(Z_p^\varepsilon - Z_d^\varepsilon) \qquad (2.5.1)$$

where ΔM_p, ΔM_d, ΔM_α are the mass excess of the parent, daughter and cluster respectively. The Q values for the alpha decays are calculated using the experimental mass excess values of Wang *et al.,* [56] and some of the mass excess were taken from Koura-Tachibana-Uno-Yamada (KTUY) [57]. As the effect of atomic electrons on the energy of the alpha particle has not been included in Ref. [56, 57], for a more accurate calculation of Q value, we have included the electron screening effect [68] in equation (2.5.1). The term $k(Z_p^\varepsilon - Z_d^\varepsilon)$ represents this correction, where the quantity kZ^ε represents the total binding energy of the Z electrons in the atom. Here the values of $\boldsymbol{k}$=8.7eV and ε=2.517 for nuclei with Z ≥ 60; and $\boldsymbol{k}$=13.6eV and ε=2.408 for nuclei with Z<60, have been derived from data reported by Huang *et al.,* [69]. Attempts to synthesize the superheavy element with Z = 118 has been under progress since 1999 and recently Oganessian *et al.*, [15, 16] have been successful in the synthesis of the ^{294}118 isotope and have determined the alpha decay properties of ^{294}118 and its successive decay products. Hence in the present study, the alpha decay properties of ^{294}118 isotope has been studied separately and is given in **Table 2.1**.

The isotope under study and the corresponding decay products in the α decay chain is given in the first column and in column 2, the respective experimental Q values available has been shown. The experimental α decay half-lives taken from the Ref. [15] are given in column 4. The experimental Q values have been used for the evaluation of the alpha half lives and the calculations done within both our formalisms, the Coulomb and proximity potential model (CPPM) and the Coulomb and proximity potential model for deformed nuclei (CPPMDN) (including the ground state quadrupole (β_2) and hexadecapole (β_4) deformation of both the parent and daughter nuclei), are given in the columns 5 and 6 respectively.

Table 2.1. The alpha decay half lives of ^{294}118 and its decay products are compared with the corresponding experimental alpha half-lives [15]. The calculations are done for zero angular momentum transfers.

Parent nuclei	Q_α (expt.) MeV	T_{SF} (s)	$T_{1/2}^{\alpha}(ms)$					Mode Of Decay
			Expt.	CPPM	CPPMDN	VSS	Royer [67]	
^{294}118	11.81±0.06	3.048x10^{8}	$0.69^{+0.64}_{-0.22}$	$2.58^{-0.75}_{+1.06}$	$0.53^{-0.16}_{+0.22}$	$0.64^{-0.18}_{+0.24}$	$0.39^{-0.11}_{+0.14}$	α1
^{290}Lv	11.00±0.08	6.392x10^{3}	$8.3^{+3.5}_{-1.9}$	$73.6^{-28.8}_{+48.1}$	$20.8^{-8.2}_{+13.8}$	$15.2^{-5.7}_{+9.0}$	$8.94^{-3.31}_{+5.33}$	α2
^{286}Fl$^{\#}$	10.33±0.06	2.372x10^{0}	$0.12^{+0.04}_{-0.02}$	$1.19^{-0.40}_{+0.59}$	$0.17^{-0.06}_{+0.09}$	$0.21^{-0.06}_{+0.10}$	$0.12^{-0.04}_{+0.06}$	α3
^{282}Cn	≤ 10.69	8.200x10^{-4*}	-	23.51	4.89	5.71	3.29	SF

$^{\#}$ Half-lives are in seconds.
* Experimental spontaneous fission half life taken from Ref. [15].

On comparison of the experimental half-lives with the half-lives evaluated using CPPMDN, it can be seen that the calculated values are in good agreement with the experimental values. The alpha half lives evaluated using the semi-empirical VSS formula and the analytical formulae of Royer have been given in column 7 and column 8 respectively. The mode of decay of the isotopes is shown in column 9. In column 3 of the **Table 2.1**, we have shown the spontaneous fission half lives of the corresponding isotopes, evaluated using the phenomenological formula of Xu *et al.,* [62]. As the isotopes with smaller α decay half lives than the spontaneous fission half lives survive fission and could be detected through α decay in the laboratory, a comparison of the α half-lives with the corresponding spontaneous fission half-lives leads us to predict the mode of decay and thereby identify the nuclei (both parent and decay products) that will survive fission. Thus, through such a comparison, we have predicted 3α chains from ^{294}118 and it is noteworthy that, our predictions go hand in hand with the observation of Oganessian *et al.,* [15, 16].

As we could successfully reproduce the experimental data for ^{294}118 using our formalism, we have confidently extended our study to predict the α half lives and the mode of decay of the isotopes of Z = 118 ranging from 271 ≤ A ≤ 310. The entire work is presented in **Figures 2.1-2.10**, where we have plotted the $\log_{10}(T_{1/2})$ against the mass number of the parent nuclei in the corresponding α chain. The plots for the decay half lives calculated using both CPPM and CPPMDN has been shown in these figures and it can be seen that, the alpha half-lives decreases when the deformation values are included. Along with these, we have plotted the decay half-lives evaluated using the VSS formula, the UNIV and the analytical formulae of Royer for comparison and these values agrees well with our theoretical calculations. The spontaneous fission half-lives computed using the phenomenological formula of Xu *et al.,* are also given in these figures. The evaluated spontaneous fission half-lives have been compared with the experimental spontaneous fission half-lives [70] and were found to be in agreement with each other. For example, in the case of ^{253}Rf, $T_{sf}^{expt.} = 4.800\times10^{-5}s$ and $T_{sf}^{calc.} = 3.451\times10^{-5}s$; and in the case of ^{250}Cm, $T_{sf}^{expt.} = 3.537\times10^{11}s$ and $T_{sf}^{calc.} = 8.109\times10^{11}s$, which shows the agreement between the experimental and the evaluated spontaneous fission half lives.

Figure 2.1 represents the plot of $\log_{10}(T_{1/2})$ versus mass number for the nuclei $^{271\text{-}274}$118. A comparison of alpha half-life with the corresponding spontaneous fission half-life makes it clear that none of these isotopes survive fission. The plots for the nuclei $^{275\text{-}278}$118 and $^{279\text{-}282}$118 are given in **Figures 2.2** and **2.3** respectively. It can be seen that, except for the ^{275}118 isotope, all these nuclei survive fission and 1α chain can be observed from ^{276}118, 2α from ^{277,278}118, 3α from ^{279,280}118, 4α from ^{281}118 and 6α from ^{282}118.

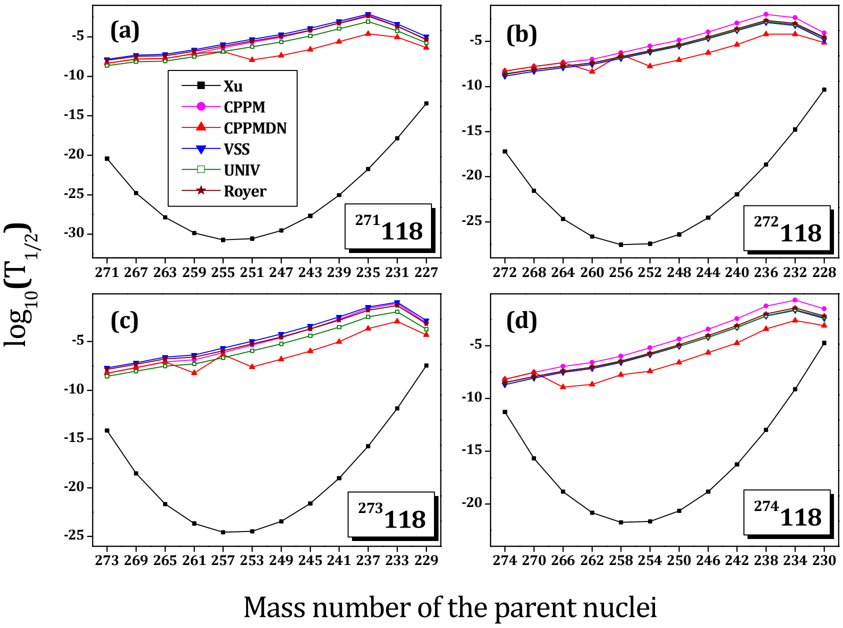

Figure 2.1. Plot for the comparison of the calculated α decay half-lives with the corresponding spontaneous fission half lives of the isotopes $^{271-274}118$ and their decay products.

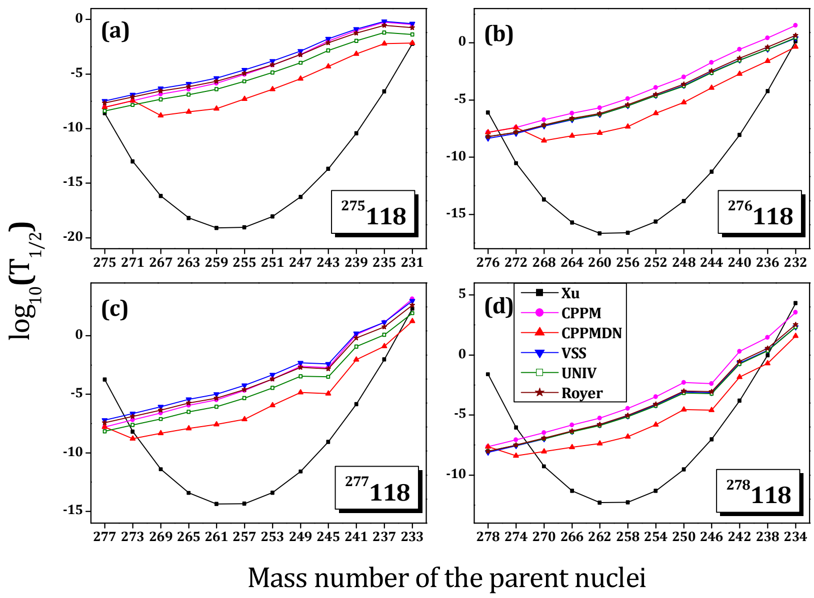

Figure 2.2. Plot for the comparison of the calculated α decay half-lives with the corresponding spontaneous fission half-lives of the isotopes $^{275-278}118$ and their decay products.

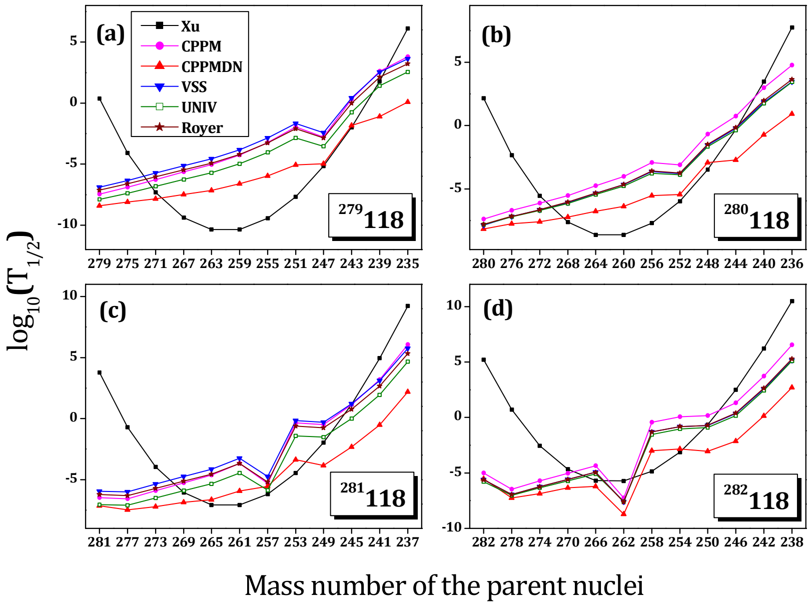

Figure 2.3. Plot for the comparison of the calculated α decay half-lives with the corresponding spontaneous fission half-lives of the isotopes $^{279\text{-}282}118$ and their decay products.

Figures 2.4 and **2.5** represent the plot for $^{283\text{-}286}118$ and $^{287\text{-}290}118$ respectively. These figures clearly depicts that all these isotopes survive fission and 6α chains can be observed from $^{283}118$. However, it can be seen from these figures that the alpha half-lives, evaluated using CPPMDN, of both the parent and the daughter isotopes of Z = 118 in the range 284 ≤ A ≤ 288 are much below the millisecond region (for eg. $T_{1/2}^{\alpha} = 2.650\times10^{-6}s$ for $^{284}118$, $T_{1/2}^{\alpha} = 7.444\times10^{-6}s$ for $^{285}118$ and for $^{274}112$, $T_{1/2}^{\alpha} = 8.609\times10^{-9}s$) and their decay chain do not end with SF. Hence these isotopes cannot be predicted to be detectable in laboratories, through alpha decay. The isotopes $^{289}118$ and $^{290}118$ shown in **Figure 2.5(c)** and **2.5(d)** survive fission and 5α chains can be observed from these isotopes.

The plot of $\log_{10}(T_{1/2})$ versus mass number for the nuclei $^{291\text{-}294}118$ and $^{295\text{-}298}118$, which includes the experimentally synthesized nuclei $^{294}118$, is shown in the **Figures 2.6** and **2.7** respectively. As seen, 5α chains can be observed from $^{291\text{-}293}118$ and thus these isotopes survive fission.

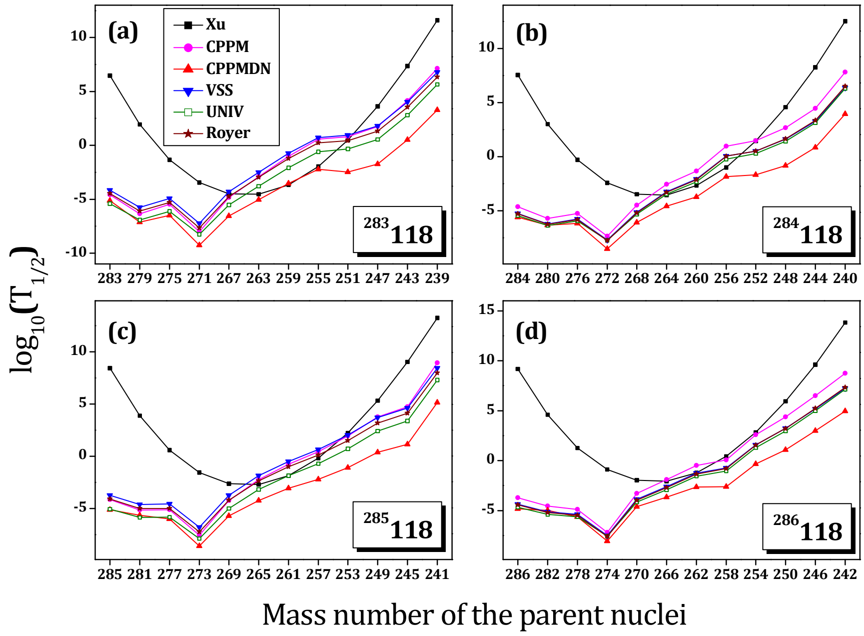

Figure 2.4. Plot for the comparison of the calculated α decay half-lives with the corresponding spontaneous fission half-lives of the isotopes $^{283\text{-}286}118$ and their decay products.

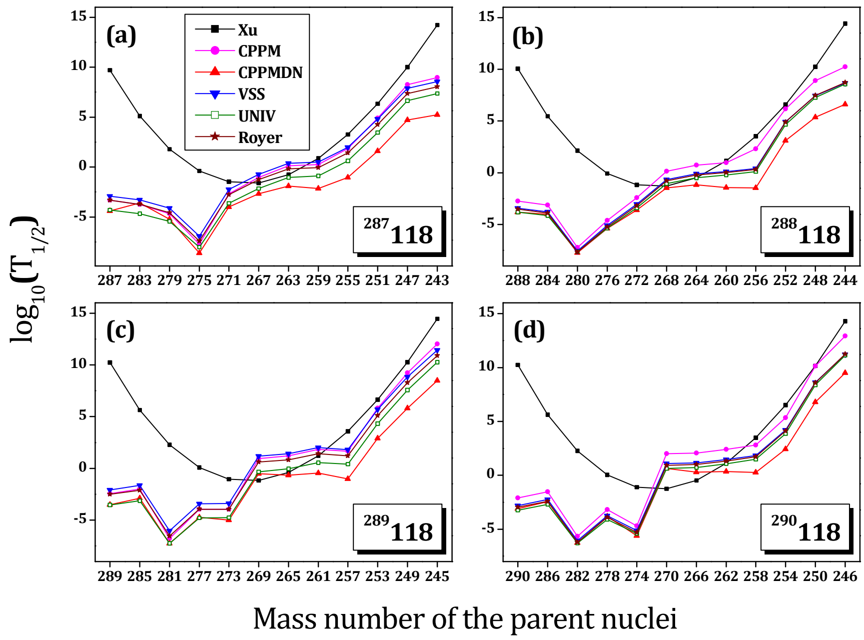

Figure 2.5. Plot for the comparison of the calculated α decay half-lives with the corresponding spontaneous fission half-lives of the isotopes $^{287\text{-}290}118$ and their decay products.

The **Figure 2.6(d)** gives the calculations done for the experimentally synthesized nuclei ^{294}118 and as the experimental Q values were available for the nuclei and its decay products, we have used these Q values for the calculation of the alpha decay half lives and have already presented in the **Table 2.1**. In the case of ^{294}118, as the experimental Q values were available only up to the decay product ^{282}112, in **Figure 2.6(d)**, we have plotted the alpha decay half-lives that were calculated using the experimental Q values up to the decay product ^{282}112. The alpha decay half-lives for the remaining decay products have been evaluated using the Q values that were calculated using the mass excess values taken from Ref. [56, 57]. A comparison of the T_{sf} values calculated using the semi empirical relation given by Xu *et al*., and the alpha decay half lives predicts 3α chains for ^{294}118 which closely agrees with the experimentally observed facts [15, 16]. The experimental alpha decay values have been represented as scattered points in this figure. Also from our calculations we have predicted two alpha chains from the nuclei $^{295\text{-}297}$118 and one alpha chain to be seen from the isotope ^{298}118.

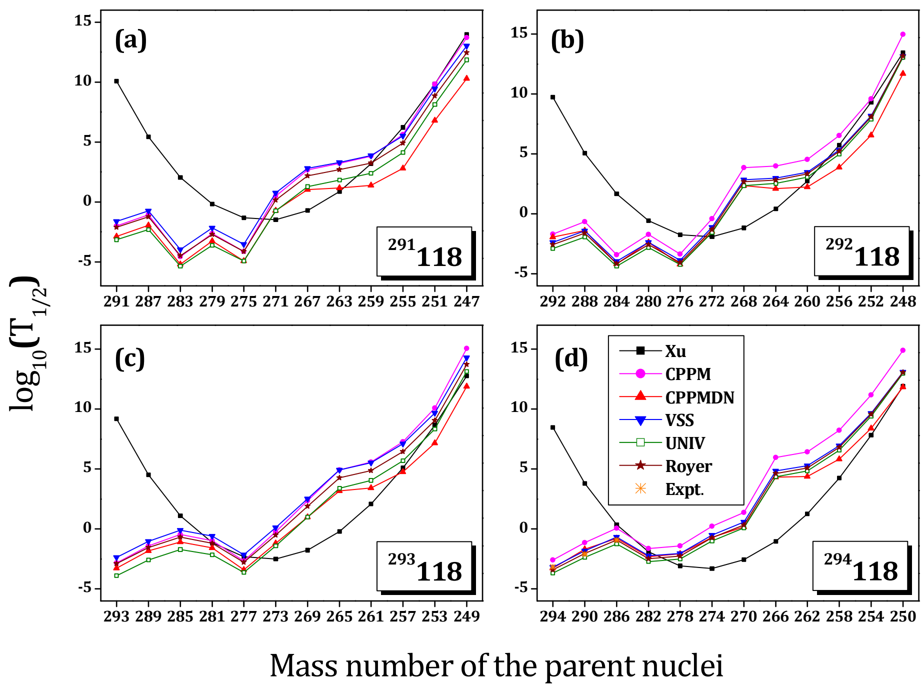

Figure 2.6. Plot for the comparison of the calculated α decay half-lives with the corresponding spontaneous fission half-lives of the isotopes $^{291\text{-}294}$118 and their decay products.

As we could observe 5α chains consistently from the nuclei $^{289-293}$118, we have predicted that these nuclei could be synthesized and detected experimentally via alpha decay. However, even though we could observe a consistent 3α, 4α and 6α chains from ^{279,280}118, ^{281}118 and ^{282,283}118 respectively, these nuclei could not be predicted to be synthesized in the laboratories as their decay half lives are too small, which span the order 10^{-9}s to 10^{-6}s. Most of the predicted, unknown nuclei in the range 289 ≤ A ≤ 293 were found to have relatively long half-lives and hence could be sufficient to detect them if synthesized in a laboratory. These predictions are highlighted in **Tables 2.2** and **2.3** as we hope this observation to provide a new guide to the experiments progressing on Z = 118. In the tables, the Q_α values represent the difference in the mass excess of the parent and the fragments.

Table 2.2. Comparison of the alpha half-lives and spontaneous fission half-lives of ^{289,290}118 and their decay products. A prediction on the mode of decay is given by comparing the alpha decay half-lives with the spontaneous fission half lives. The calculations are done for zero angular momentum transfers.

Parent nuclei	Q_α (cal) MeV	T_{SF} (s)	$T^{\alpha}_{1/2}$ (s)					Mode of Decay
			CPPM	CPPMDN	VSS	UNIV	Royer [67]	
^{289}118	11.785	1.776x10^{10}	3.614x10^{-3}	3.055x10^{-4}	8.478x10^{-3}	2.833x10^{-4}	3.116x10^{-3}	α1
^{285}Lv	11.355	4.357x10^{5}	1.021x10^{-2}	1.311x10^{-3}	2.352x10^{-2}	7.673x10^{-4}	7.993x10^{-3}	α2
^{281}Fl	13.165	1.894x10^{2}	1.655x10^{-7}	5.575x10^{-8}	9.174x10^{-7}	5.493x10^{-8}	2.951x10^{-7}	α3
^{277}Cn	11.625	1.195x10^{0}	1.111x10^{-4}	1.920x10^{-5}	3.912x10^{-4}	1.644x10^{-5}	1.168x10^{-4}	α4
^{273}Ds	11.365	9.016x10^{-2}	1.096x10^{-4}	9.909x10^{-6}	4.014x10^{-4}	1.749x10^{-5}	1.130x10^{-4}	α5
^{269}Hs	9.365	6.707x10^{-2}	9.131x10^{0}	3.011x10^{-1}	1.497x10^{1}	4.795x10^{-1}	4.051x10^{0}	SF
^{290}118	11.645	1.792x10^{10}	7.817x10^{-3}	8.213x10^{-4}	1.548x10^{-3}	5.601x10^{-4}	1.112x10^{-3}	α1
^{286}Lv	11.175	4.263x10^{5}	2.909x10^{-2}	3.711x10^{-3}	5.548x10^{-3}	1.945x10^{-3}	3.887x10^{-3}	α2
^{282}Fl	12.625	1.795x10^{2}	2.221x10^{-6}	5.391x10^{-7}	8.949x10^{-7}	5.077x10^{-7}	6.197x10^{-7}	α3
^{278}Cn	11.305	1.098x10^{0}	6.607x10^{-4}	1.533x10^{-4}	1.813x10^{-4}	7.871x10^{-5}	1.239x10^{-4}	α4
^{274}Ds	11.665	8.017x10^{-2}	1.990x10^{-5}	2.518x10^{-6}	7.388x10^{-6}	3.913x10^{-6}	5.006x10^{-6}	α5
^{270}Hs	9.045	5.776x10^{-2}	9.952x10^{1}	4.371x10^{0}	1.227x10^{1}	4.217x10^{0}	8.583x10^{0}	SF
^{266}Sg	8.805	3.398x10^{-1}	1.124x10^{2}	1.986x10^{0}	1.389x10^{1}	5.143x10^{0}	9.931x10^{0}	SF

The plots for the nuclei $^{299\text{-}302}118$, $^{303\text{-}306}118$ and $^{307\text{-}310}118$ are given in **Figures 2.8**, **2.9** and **2.10** respectively. Of these nuclei, $^{299\text{-}300}118$ isotopes survive fission and give one alpha chain, whereas the nuclei $^{301\text{-}310}118$ are found to undergo spontaneous fission completely and thus will not survive fission. Hence, our calculations on the heavy mass isotopes of Z = 118 punctuates the fact, as no isotope below A ≤ 275 and above A ≥ 301 survives fission, the alpha decay is restricted within the range 276 ≤ A ≤ 300.

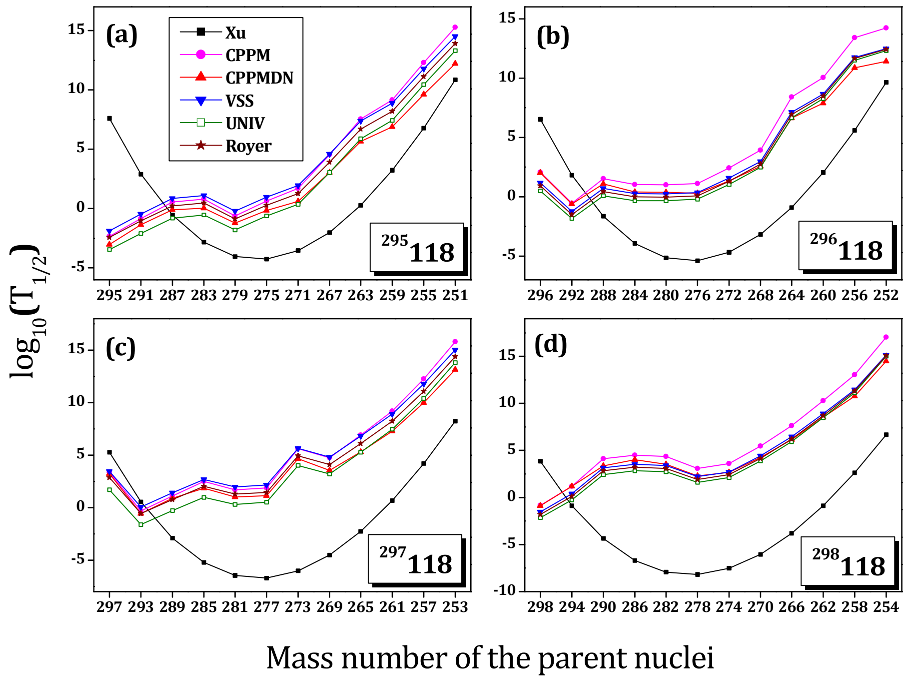

Figure 2.7. Plot for the comparison of the calculated α decay half-lives with the corresponding spontaneous fission half-lives of the isotopes $^{295\text{-}298}118$ and their decay products.

Table 2.3. Comparison of the alpha half-lives and spontaneous fission half-lives of $^{291-293}118$ and their decay products. A prediction on the mode of decay is given by comparing the alpha decay half-lives with the spontaneous fission half-lives. The calculations are done for zero angular momentum transfers.

Parent nuclei	Q_α (cal) MeV	T_{SF} (s)	$T_{1/2}^{\alpha}$ (s)					Mode of Decay
			CPPM	CPPMDN	VSS	UNIV	Royer [67]	
$^{291}118$	11.595	1.199x10^{10}	1.008x10^{-2}	1.305x10^{-3}	2.367x10^{-2}	7.000x10^{-4}	8.001x10^{-3}	α1
^{287}Lv	10.995	2.764x10^{5}	8.511x10^{-2}	1.104x10^{-2}	1.817x10^{-1}	5.061x10^{-3}	5.671x10^{-2}	α2
^{283}Fl	12.135	1.128x10^{2}	2.702x10^{-5}	6.419x10^{-6}	1.085x10^{-4}	4.415x10^{-6}	3.199x10^{-5}	α3
^{279}Cn	11.085	6.679x10^{-1}	2.326x10^{-3}	5.677x10^{-4}	7.016x10^{-3}	2.387x10^{-4}	1.929x10^{-3}	α4
^{275}Ds	11.425	4.725x10^{-2}	7.244x10^{-5}	1.204x10^{-5}	2.935x10^{-4}	1.206x10^{-5}	7.617x10^{-5}	α5
^{271}Hs	9.505	3.297x10^{-2}	3.042x10^{0}	1.880x10^{-1}	5.785x10^{0}	1.751x10^{-1}	1.441x10^{0}	SF
^{267}Sg	8.625	1.878x10^{-1}	4.629x10^{2}	1.072x10^{1}	6.240x10^{2}	1.874x10^{1}	1.514x10^{2}	SF
$^{292}118$	11.465	5.319x10^{9}	2.096x10^{-2}	1.161x10^{-2}	4.165x10^{-3}	1.339x10^{-3}	2.739x10^{-3}	α1
^{288}Lv	10.835	1.188x10^{5}	2.251x10^{-1}	4.056x10^{-2}	4.001x10^{-2}	1.206x10^{-2}	2.566x10^{-2}	α2
^{284}Fl	11.645	4.696x10^{1}	3.833x10^{-4}	6.826x10^{-5}	1.125x10^{-4}	4.490x10^{-5}	7.130x10^{-5}	α3
^{280}Cn	10.735	2.694x10^{-1}	1.907x10^{-2}	4.365x10^{-3}	4.392x10^{-3}	1.546x10^{-3}	2.756x10^{-3}	α4
^{276}Ds	11.105	1.846x10^{-2}	4.383x10^{-4}	6.203x10^{-5}	1.378x10^{-4}	5.851x10^{-5}	8.593x10^{-5}	α5
^{272}Hs	9.785	1.247x10^{-2}	4.039x10^{-1}	3.486x10^{-2}	7.892x10^{-2}	2.805x10^{-2}	5.004x10^{-2}	SF
^{268}Sg	8.295	6.880x10^{-2}	7.214x10^{3}	2.221x10^{2}	7.137x10^{2}	2.336x10^{2}	4.733x10^{2}	SF
$^{293}118$	11.915	1.564x10^{9}	1.475x10^{-3}	5.267x10^{-4}	4.260x10^{-3}	1.270x10^{-4}	1.337x10^{-3}	α1
^{289}Lv	11.105	3.384x10^{4}	3.983x10^{-2}	1.516x10^{-2}	9.628x10^{-2}	2.550x10^{-3}	2.777x10^{-2}	α2
^{285}Fl	10.515	1.296x10^{1}	3.605x10^{-1}	8.117x10^{-2}	7.819x10^{-1}	1.984x10^{-2}	2.100x10^{-1}	α3
^{281}Cn	10.465	7.205x10^{-2}	1.029x10^{-1}	2.601x10^{-2}	2.532x10^{-1}	6.957x10^{-3}	6.409x10^{-2}	α4
^{277}Ds	10.835	4.782x10^{-3}	2.116x10^{-3}	3.846x10^{-4}	7.126x10^{-3}	2.346x10^{-4}	1.707x10^{-3}	α5
^{273}Hs	9.725	3.129x10^{-3}	5.913x10^{-1}	6.499x10^{-2}	1.354x10^{0}	3.936x10^{-2}	3.104x10^{-1}	SF
^{269}Sg	8.705	1.671x10^{-2}	2.244x10^{2}	1.002x10^{1}	3.407x10^{2}	9.535x10^{0}	7.611x10^{1}	SF

Recently, within the dinuclear system model with dynamical potential energy surface (DNS-DyPES model), Wang *et al.,* [71] have studied the excitation functions for producing superheavy nuclei with Z = 118 in some ^{48}Ca induced reactions and the possibilities for producing the same element with other entrance channels at different mass asymmetries such as ^{50}Ti + ^{248}Cm and ^{54}Cr + ^{244}Pu were also investigated.

The authors have evaluated and predicted the excitation functions for ^{48}Ca + ^{250,251,252}Cf and the dependence of the evaporation residue (ER) cross sections for producing the residue nuclei ^{293,294,295,296,297}118. Their study revealed that the maximum effective ER cross sections for the productions of ^{294}118, ^{295}118 and ^{296}118 were about 0.2-0.5 pb, close to the current experimental limit, and that for ^{293}118 and ^{297}118 were about 0.1 pb. It can be seen that the study aims at making predictions for the experiment being under way at the Flerov Laboratory of Joint Institute for Nuclear Research in Dubna, Russia and the predictions highlights the isotopes ^{293,294,295,296,297}118.

In the present work, as we have predicted 5α, 3α and 2α chains consistently from the nuclei $^{289\text{-}293}$118, ^{294}118 and $^{295\text{-}297}$118 respectively, which includes the isotopes highlighted by Wang *et al.,* we hope that our studies will also accelerate the experiments in progress at JINR, FLNR, Dubna.

We would also like to lay emphasis on the fact that the present work, whereby a comparison of the alpha decay half lives and spontaneous fission half lives predicts the mode of decay of a vast range of isotopes, is the first theoretical work done on the alpha decay properties of Z = 118.

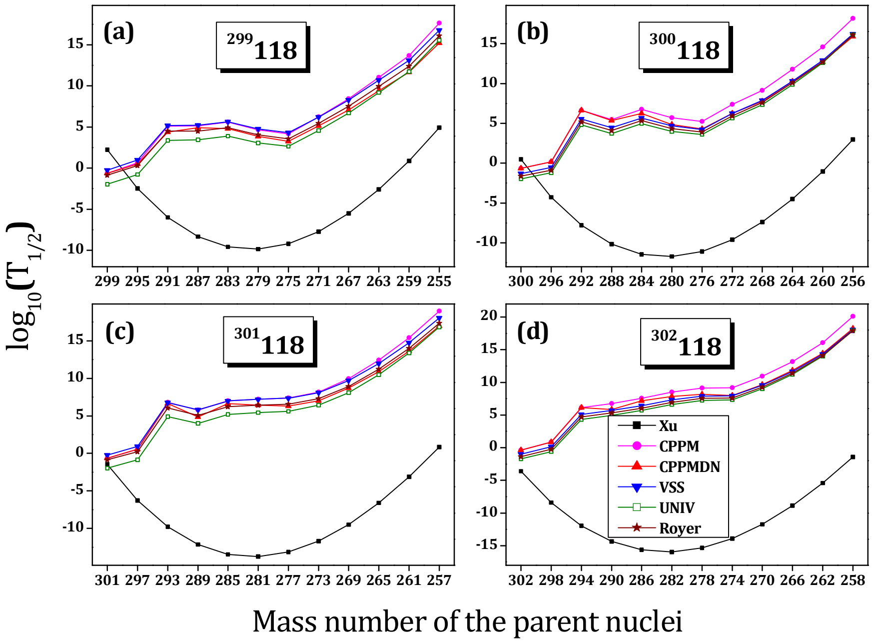

Figure 2.8. Plot for the comparison of the calculated α decay half-lives with the corresponding spontaneous fission half-lives of the isotopes $^{299-302}118$ and their decay products.

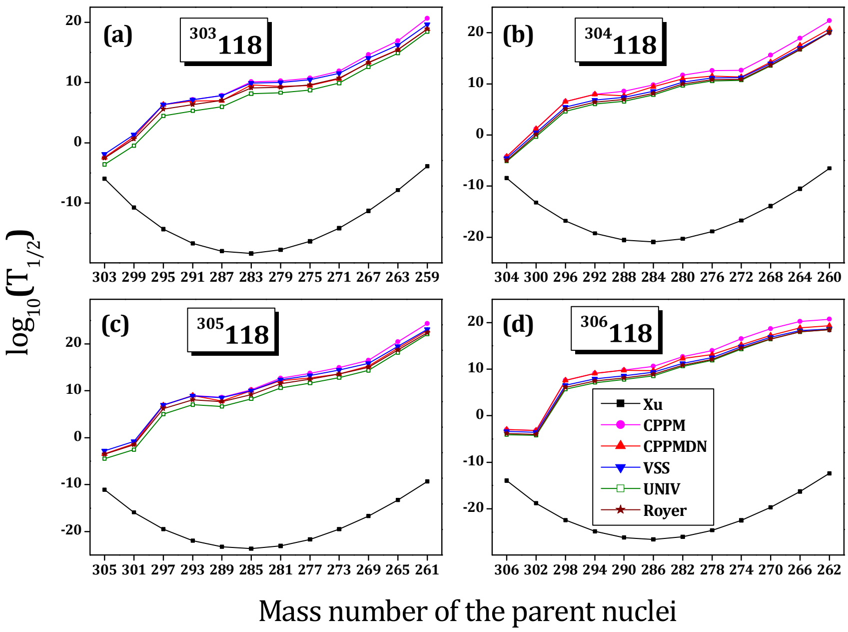

Figure 2.9. Plot for the comparison of the calculated α decay half-lives with the corresponding spontaneous fission half-lives of the isotopes $^{303-306}118$ and their decay products.

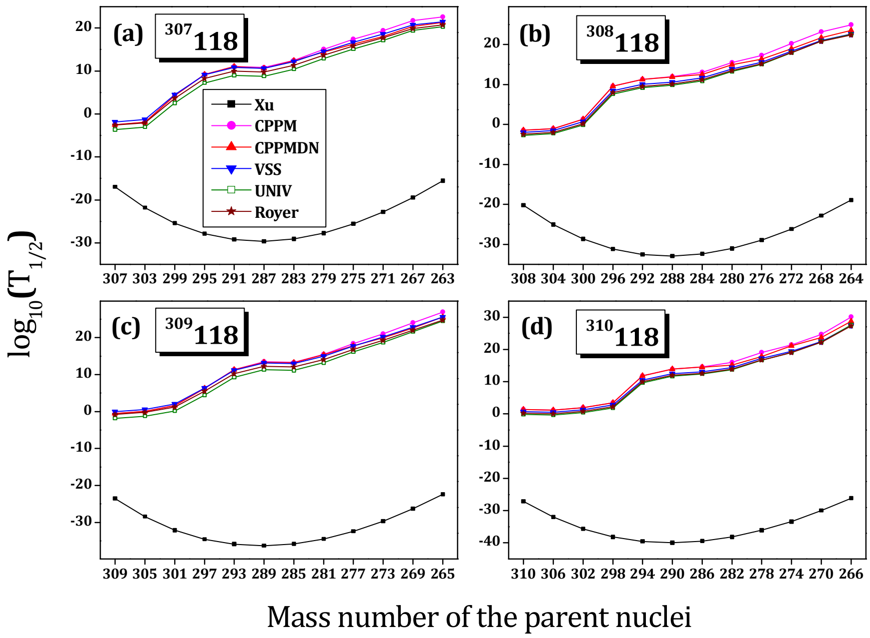

Figure 2.10. Plot for the comparison of the calculated α decay half-lives with the corresponding spontaneous fission half-lives of the isotopes $^{307\text{-}310}118$ and their decay products.

2.5.1 Summary

The formalism CPPMDN could be considered unimpeachable, for the study of alpha decay from the isotopes of the superheavy nuclei with Z=118, which span the range $271 \leq A \leq 310$, as we were successful in reproducing the experimental alpha half-lives and the decay chains observed for $^{294}118$. We, thus confidently counted in 39 more isotopes of Z = 118, with an aim of predicting the alpha decay chains of all the isotopes in this region. Through our study, we have lightened the fact that those isotopes of Z = 118 with $A \geq 301$ and with $A \leq 275$, do not survive fission and thus the alpha decay is retrenched to the range $276 \leq A \leq 300$. We anticipate that our predictions of 5α chains consistently from $^{289\text{-}293}118$, 3α chains from $^{294}118$ and 2α chains from $^{295\text{-}297}118$ would accelerate the experiments in progress for the synthesis of new isotopes of Z = 118.

2.6 Heavy particle radioactivity from superheavy nuclei leading to ^{298}114 daughter nuclei

The decay half lives in the emission of even-even clusters ^{4}He, ^{8}Be, ^{10}Be, ^{14}C, ^{20}O and ^{24}Ne from the various even-even superheavy parent isotopes $^{290\text{-}314}$Lv, $^{294\text{-}318}$118, $^{296\text{-}320}$118, $^{300\text{-}324}$120, $^{306\text{-}330}$122 and $^{310\text{-}334}$124 leading to the predicted [72-76] doubly magic ^{298}114 (Z=114, N=184) and the neighbouring nuclei have been calculated by using the Coulomb and proximity potential model (CPPM).

Figures 2.11-2.13 represent the plot for $\log_{10}(S)$ vs. neutron number of the parent nuclei, for the cluster emission of ^{4}He, ^{8}Be, ^{10}Be, ^{14}C, ^{20}O and ^{24}Ne respectively from $^{290\text{-}314}$Lv, $^{294\text{-}318}$118, $^{296\text{-}320}$118, $^{300\text{-}324}$120, $^{306\text{-}330}$122, $^{310\text{-}334}$124. The behaviour of the cluster formation probability with the neutron number of the parent nuclei can be clearly seen from these figures. In **Figure 2.11**, the plot for the cluster formation probability of ^{4}He from $^{290\text{-}314}$Lv and ^{8}Be from $^{294\text{-}318}$118 isotopes have been given and it is to be noticed that the cluster formation probability is the maximum for the emission of ^{4}He and ^{8}Be accompanied by ^{298}114 (Z=114, N=184) daughter nuclei. The plots for the cluster formation probability of ^{10}Be from $^{296\text{-}320}$118 and ^{14}C from $^{300\text{-}324}$120 isotopes have been given respectively in **Figure 2.12**. It should be noticed that the cluster formation probability is the maximum for the emission of ^{10}Be and ^{14}C accompanied by ^{298}114 (N = 84, Z = 114) daughter nuclei. In **Figure 2.13**, the plot for the cluster formation probability of ^{20}O from $^{306\text{-}330}$122 and ^{24}Ne from $^{310\text{-}334}$124 isotopes have been given and it can be clearly seen that the cluster formation probability is the maximum for the emission of ^{20}O and ^{24}Ne accompanied by ^{298}114 (Z = 114, N = 184) daughter nuclei. Thus it is clearly evident from the **Figures 2.11-2.13** that, the cluster formation probability is maximum for the decay accompanying ^{298}114, which reveal the role of neutron magicity in cluster radioactivity. The cluster decay half lives have been evaluated using CPPM, UNIV, UDL and the scaling law of Horoi and their comparisons are shown in **Figures 2.14-2.16**. The plots for $\log_{10}(T_{1/2})$ against the neutron number of the daughter in the corresponding decay are given in these figures.

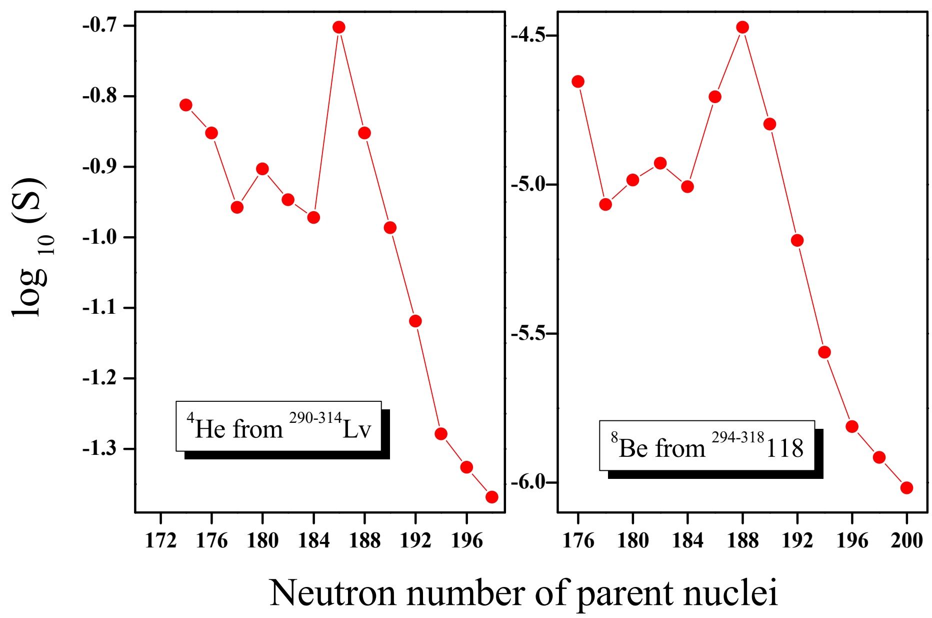

Figure 2.11. The computed $\log_{10}(S)$ values plotted against the neutron number of the parent, for the emission of clusters ^{4}He and ^{8}Be from $^{290-314}Lv$ and $^{294-318}118$ isotopes respectively.

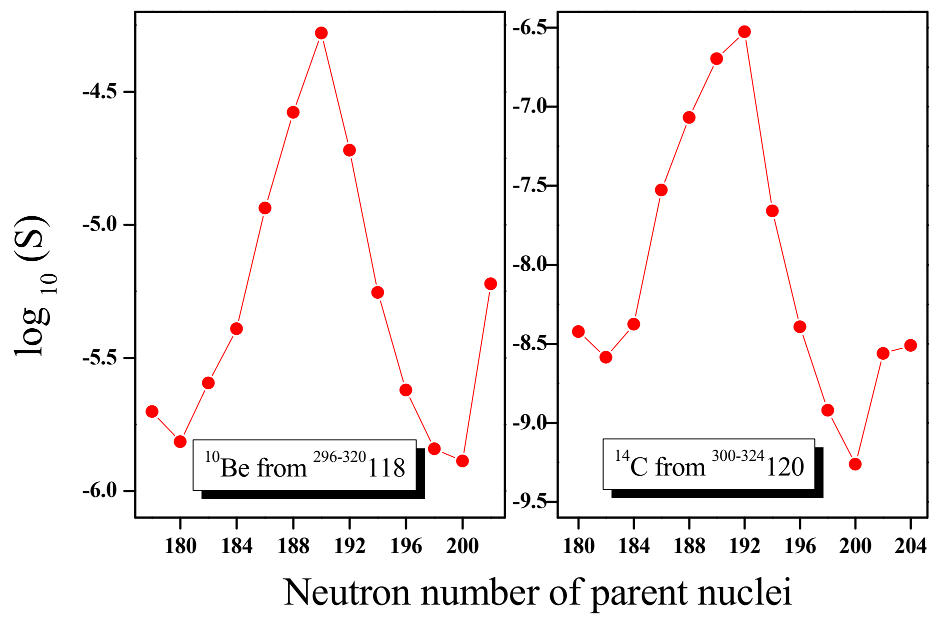

Figure 2.12. The computed $\log_{10}(S)$ values plotted against the neutron number of the parent, for the emission of clusters ^{10}Be and ^{14}C from $^{296-320}118$ and $^{300-324}120$ isotopes respectively.

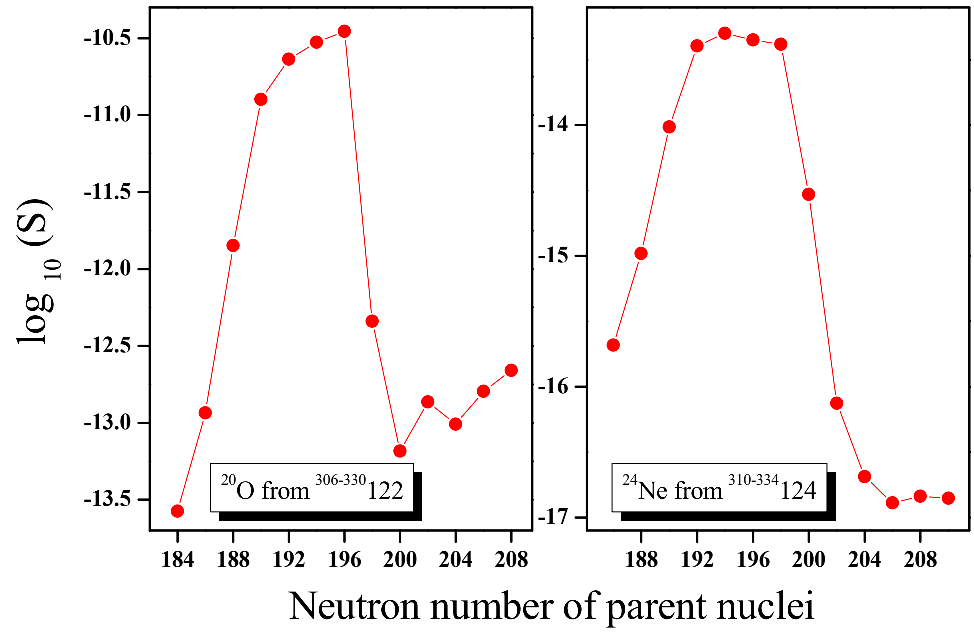

Figure 2.13. The computed $\log_{10}(S)$ values plotted against the neutron number of the parent, for the emission of clusters ^{20}O and ^{24}Ne from $^{306-330}122$ and $^{310-334}124$ isotopes respectively.

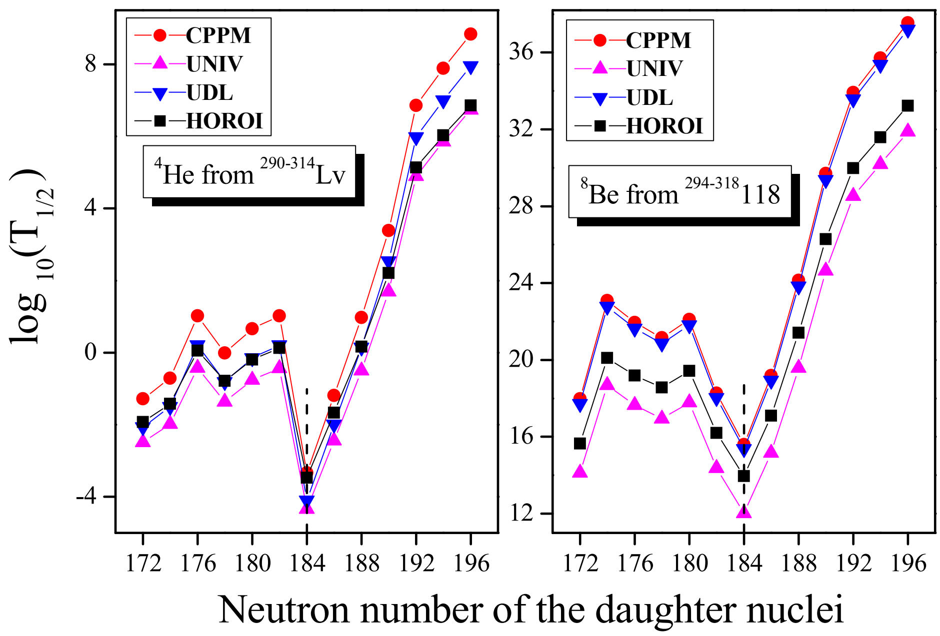

Figure 2.14. The computed $\log_{10}(T_{1/2})$ values vs. neutron number of daughter for the emission of clusters ^{4}He and ^{8}Be from $^{290-314}Lv$ and $^{294-318}118$ isotopes respectively. $T_{1/2}$ is in seconds.

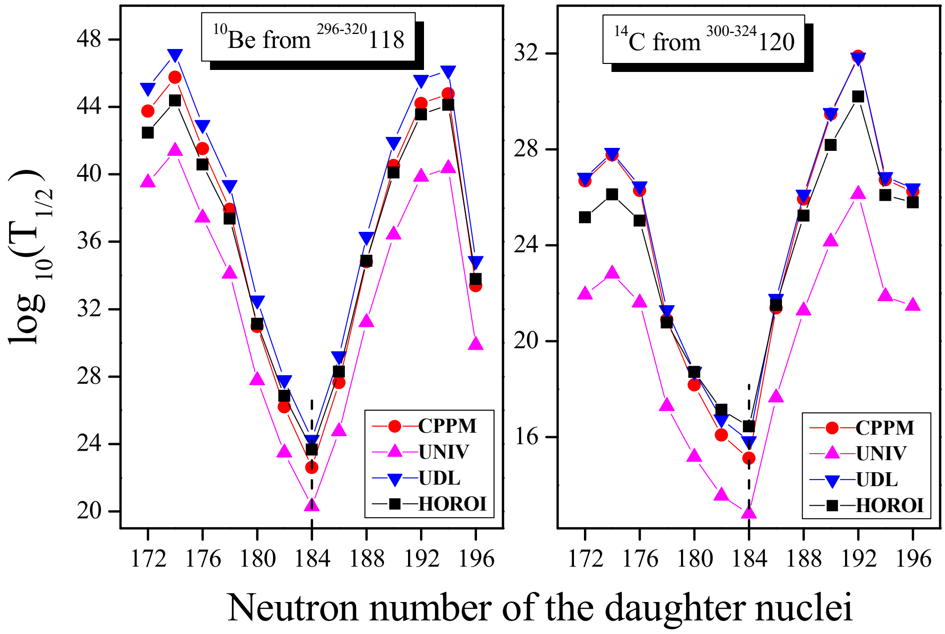

Figure 2.15. The computed $\log_{10}(T_{1/2})$ values vs. neutron number of daughter for the emission of clusters ^{10}Be and ^{14}C from $^{296-320}$118 and $^{300-344}$120 isotopes respectively. $T_{1/2}$ is in seconds.

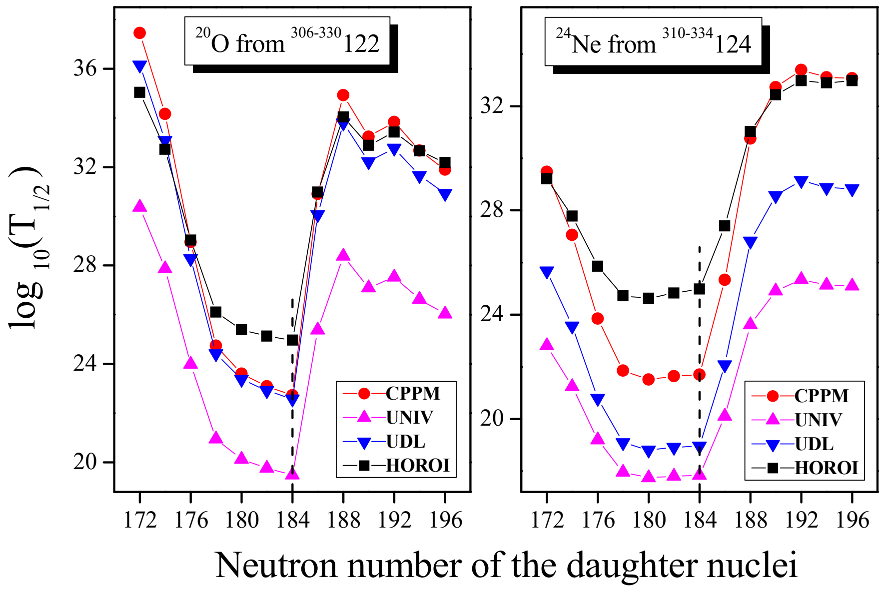

Figure 2.16. The computed $\log_{10}(T_{1/2})$ values vs. neutron number of daughter for the emission of clusters ^{20}O and ^{24}Ne from $^{306-330}$120 and $^{310-334}$124 isotopes respectively. $T_{1/2}$ is in seconds.

Figure 2.14 gives the plot for the cluster emission of ^{4}He and ^{8}Be from $^{290-314}Lv$ and $^{294-318}118$ isotopes respectively. In **Figure 2.15** and **Figure 2.16**, the plots for the cluster emission of ^{10}Be from $^{296-320}118$, ^{14}C from $^{300-324}120$ and ^{20}O from $^{306-330}122$, ^{24}Ne from $^{310-334}124$ isotopes have been given respectively.

The minima of the logarithmic half-lives for all these cluster emission are found for the decay leading to $^{298}114$ (Z=114, N=184). A minimum in the decay half lives corresponds to the greater barrier penetrability, which in turn indicates the doubly magic behaviour of the daughter nuclei. In the cluster decay studies on heavy nuclei, it has been shown that the half life is minimum for the decays leading to the doubly magic daughter ^{208}Pb (Z=82, N=126) or its neighbouring nuclei. The present study on the cluster decay half lives of the superheavy nuclei gives a pronounced minima for the daughter $^{298}114$ (Z=114, N=184). This may be interpreted as a result of the strong shell effect of the assumed magic number of the neutrons and protons of $^{298}114$ and this reveal the role shell closures in the cluster decays of superheavy nuclei. It can be also be seen from the plots connecting $\log_{10}(T_{1/2})$ versus neutron number of daughter nuclei that the four calculations, CPPM, UNIV, UDL and Scaling law, show the same trend. It should be taken into consideration that the CPPM values matches well with the UDL values than that of the UNIV or the values obtained using the Scaling Law of Horoi. Thus, similar to UNIV, UDL and Scaling law, CPPM could be considered as a unified model for α-decay and cluster decay studies.

In **Tables 2.4-2.6**, the computed Q values, barrier penetrability, decay constant and half-lives for the emission of various cluster from the superheavy nuclei $^{290-314}Lv$, $^{294-318}118$, $^{296-320}118$, $^{300-324}120$, $^{306-330}122$, $^{310-334}124$ are given. The parent nuclei, the emitted clusters and the corresponding daughter nuclei are given in columns 1, 2 and 3 respectively of the tables mentioned above. Column 4 gives the respective Q values of these decays which are evaluated using equation (2.5.1). The penetrability and decay constants for the respective decays are calculated using CPPM and are included in columns 5 and 6 respectively. The cluster decay half-lives predicted within the CPPM for all the parent-cluster combinations are arranged in column 7.

Most of the predicted half lives are well within the present upper limit for measurements $(T_{1/2} < 10^{30} s)$. Moreover, the alpha half lives calculated using our model give closer values with the experimental alpha half lives [68]. For example, in the case of ^{290}Lv, the $T_{\alpha}^{\exp} = 1.500 \times 10^{-2} s$ and $T_{\alpha}^{calc.}(CPPM) = 5.259 \times 10^{-2} s$ and in the case of ^{292}Lv, the $T_{\alpha}^{\exp} = 1.800 \times 10^{-2} s$ and $T_{\alpha}^{calc.}(CPPM) = 1.951 \times 10^{-1} s$. Spontaneous fission, being an important mode of decay in the superheavy region, we have computed the spontaneous fission half lives of all the parent nuclei under study, using the semi-empirical formula of Santhosh *et al.,* [61] and the corresponding values have been given in the columns 8. Thus the present study on the cluster decay half lives for the emission of various clusters from the superheavy nuclei $^{290-314}$Lv, $^{294-318}$118, $^{296-320}$118, $^{300-324}$120, $^{306-330}$122, $^{310-334}$124 reveals that the cluster decay half lives is the minimum for those decays leading to the daughter nuclei ^{298}114, which stress the role of neutron magicity (N=184) in cluster decays. We would like to mention that, the results obtained through our study closely agree with that of the early predictions [72-76]. Thus, through our study, we have indicated towards a new island for the cluster radioactivity, after the experimentally observed doubly magic ^{208}Pb and ^{100}Sn, leading to the residual superheavy isotope ^{298}114 and its neighbours and have established the role of neutron shell closure in cluster radioactivity.

Table 2.4. The Q value, penetrability, decay constant and the predicted half lives for the emission of the cluster ^{4}He from $^{290-314}$Lv isotopes and the cluster ^{8}Be from $^{294-318}$118 isotopes. The half lives are calculated for zero angular momentum transfers.

Parent nuclei	Emitted cluster	Daughter nuclei	Q value (MeV)	Penetrability P	Decay constant λ (s^{-1})	$T^{\alpha}_{1/2}$(s) CPPM	$T^{sf}_{1/2}$(s) KPS [61]
^{290}Lv	^{4}He	^{286}114	11.054	2.595x10^{-20}	1.318x10^{1}	5.259x10^{-2}	7.831x10^{0}
^{292}Lv	^{4}He	^{288}114	10.834	7.136x10^{-21}	3.552x10^{0}	1.951x10^{-1}	3.293x10^{-1}
^{294}Lv	^{4}He	^{290}114	10.224	1.395x10^{-22}	6.553x10^{-2}	1.058x10^{1}	5.090x10^{-3}
^{296}Lv	^{4}He	^{292}114	10.564	1.457x10^{-21}	7.073x10^{-1}	9.798x10^{-1}	3.015x10^{-5}
^{298}Lv	^{4}He	^{294}114	10.324	3.171x10^{-22}	1.504x10^{-1}	4.608x10^{0}	7.117x10^{-8}
^{300}Lv	^{4}He	^{296}114	10.194	1.398x10^{-22}	6.549x10^{-2}	1.058x10^{1}	6.957x10^{-11}
^{302}Lv	^{4}He	^{298}114	11.784	2.772x10^{-18}	1.501x10^{3}	4.617x10^{-4}	2.921x10^{-14}
^{304}Lv	^{4}He	^{300}114	10.944	2.135x10^{-20}	1.073x10^{1}	6.457x10^{-2}	5.453x10^{-18}
^{306}Lv	^{4}He	^{302}114	10.184	1.586x10^{-22}	7.420x10^{-2}	9.339x10^{0}	4.684x10^{-22}
^{308}Lv	^{4}He	^{304}114	9.424	6.597x10^{-25}	2.856x10^{-4}	2.426x10^{3}	1.912x10^{-26}
^{310}Lv	^{4}He	^{306}114	8.474	2.494x10^{-28}	9.708x10^{-8}	7.139x10^{6}	3.824x10^{-31}
^{312}Lv	^{4}He	^{308}114	8.214	2.384x10^{-29}	8.998x10^{-9}	7.702x10^{7}	3.862x10^{-36}
^{314}Lv	^{4}He	^{310}114	7.984	2.730x10^{-30}	1.001x10^{-9}	6.920x10^{8}	2.027x10^{-41}
^{294}118	^{8}Be	^{286}114	22.837	1.022x10^{-39}	7.209x10^{-19}	9.613x10^{17}	5.915x10^{3}
^{296}118	^{8}Be	^{288}114	20.927	8.592x10^{-45}	5.554x10^{-24}	1.248x10^{23}	2.369x10^{2}
^{298}118	^{8}Be	^{290}114	21.307	1.192x10^{-43}	7.843x10^{-23}	8.836x10^{21}	3.590x10^{0}
^{300}118	^{8}Be	^{292}114	21.567	7.256x10^{-43}	4.834x10^{-22}	1.434x10^{21}	2.140x10^{-2}
^{302}118	^{8}Be	^{294}114	21.207	8.370x10^{-44}	5.483x10^{-23}	1.264x10^{22}	5.217x10^{-5}
^{304}118	^{8}Be	^{296}114	22.597	5.225x10^{-40}	3.647x10^{-19}	1.900x10^{18}	5.392x10^{-8}
^{306}118	^{8}Be	^{298}114	23.647	2.421x10^{-37}	1.769x10^{-16}	3.918x10^{15}	2.447x10^{-11}
^{308}118	^{8}Be	^{300}114	22.207	6.660x10^{-41}	4.568x10^{-20}	1.517x10^{19}	5.045x10^{-15}
^{310}118	^{8}Be	^{302}114	20.427	8.049x10^{-46}	5.079x10^{-25}	1.365x10^{24}	4.879x10^{-19}
^{312}118	^{8}Be	^{304}114	18.667	2.370x10^{-51}	1.367x10^{-30}	5.070x10^{29}	2.284x10^{-23}
^{314}118	^{8}Be	^{306}114	17.477	1.552x10^{-55}	8.377x10^{-35}	8.272x10^{33}	5.331x10^{-28}
^{316}118	^{8}Be	^{308}114	16.997	2.585x10^{-57}	1.357x10^{-36}	5.106x10^{35}	6.385x10^{-33}
^{318}118	^{8}Be	^{310}114	16.527	3.936x10^{-59}	2.010x10^{-38}	3.447x10^{37}	4.035x10^{-38}

Table 2.5. The Q value, penetrability, decay constant and the predicted half lives for the emission of the cluster ^{10}Be from $^{296-320}$118 isotopes and the cluster ^{14}C from $^{300-324}$120 isotopes. The half lives are calculated for zero angular momentum transfers.

Parent nuclei	Emitted cluster	Daughter nuclei	Q value (MeV)	Penetrability P	Decay constant λ (s^{-1})	$T^{\alpha}_{1/2}$(s) CPPM	$T^{sf}_{1/2}$(s) KPS [61]
^{296}118	^{10}Be	^{286}114	16.371	2.682x10^{-65}	1.264x10^{-44}	5.481x10^{43}	2.369x10^{2}
^{298}118	^{10}Be	^{288}114	15.931	2.635x10^{-67}	1.209x10^{-46}	5.733x10^{45}	3.590x10^{0}
^{300}118	^{10}Be	^{290}114	16.831	4.450x10^{-63}	2.156x10^{-42}	3.214x10^{41}	2.140x10^{-2}
^{302}118	^{10}Be	^{292}114	17.651	1.690x10^{-59}	8.591x10^{-39}	8.066x10^{37}	5.217x10^{-5}
^{304}118	^{10}Be	^{294}114	19.421	1.311x10^{-52}	7.332x10^{-32}	9.451x10^{30}	5.392x10^{-8}
^{306}118	^{10}Be	^{296}114	20.791	7.359x10^{-48}	4.406x10^{-27}	1.573x10^{26}	2.447x10^{-11}
^{308}118	^{10}Be	^{298}114	21.911	2.737x10^{-44}	1.726x10^{-23}	4.014x10^{22}	5.045x10^{-15}
^{310}118	^{10}Be	^{300}114	20.321	2.692x10^{-49}	1.575x10^{-28}	4.399x10^{27}	4.879x10^{-19}
^{312}118	^{10}Be	^{302}114	18.341	2.028x10^{-56}	1.071x10^{-35}	6.470x10^{34}	2.284x10^{-23}
^{314}118	^{10}Be	^{304}114	16.961	4.444x10^{-62}	2.170x10^{-41}	3.193x10^{40}	5.331x10^{-28}
^{316}118	^{10}Be	^{306}114	16.141	9.339x10^{-66}	4.340x10^{-45}	1.597x10^{44}	6.385x10^{-33}
^{318}118	^{10}Be	^{308}114	16.011	2.551x10^{-66}	1.176x10^{-45}	5.893x10^{44}	4.035x10^{-38}
^{320}118	^{10}Be	^{310}114	18.651	5.270x10^{-55}	2.830x10^{-34}	2.449x10^{33}	1.381x10^{-43}
^{300}120	^{14}C	^{286}114	40.330	1.261x10^{-48}	1.395x10^{-27}	4.969x10^{26}	9.776x10^{5}
^{302}120	^{14}C	^{288}114	39.800	1.090x10^{-49}	1.190x10^{-28}	5.824x10^{27}	1.394x10^{4}
^{304}120	^{14}C	^{290}114	40.420	3.171x10^{-48}	3.516x10^{-27}	1.971x10^{26}	8.038x10^{1}
^{306}120	^{14}C	^{292}114	42.950	7.627x10^{-43}	8.985x10^{-22}	7.713x10^{20}	1.943x10^{-1}
^{308}120	^{14}C	^{294}114	44.270	3.749x10^{-40}	4.552x10^{-19}	1.523x10^{18}	2.038x10^{-4}
^{310}120	^{14}C	^{296}114	45.320	4.587x10^{-38}	5.702x10^{-17}	1.215x10^{16}	9.605x10^{-8}
^{312}120	^{14}C	^{298}114	45.790	4.232x10^{-37}	5.315x10^{-16}	1.304x10^{15}	2.099x10^{-11}
^{314}120	^{14}C	^{300}114	42.520	2.424x10^{-43}	2.827x10^{-22}	2.452x10^{21}	2.195x10^{-15}
^{316}120	^{14}C	^{302}114	40.330	7.254x10^{-48}	8.024x10^{-27}	8.637x10^{25}	1.132x10^{-19}
^{318}120	^{14}C	^{304}114	38.720	2.158x10^{-51}	2.291x10^{-30}	3.024x10^{29}	2.962x10^{-24}
^{320}120	^{14}C	^{306}114	37.670	8.882x10^{-54}	9.177x10^{-33}	7.552x10^{31}	4.043x10^{-29}
^{322}120	^{14}C	^{308}114	39.860	1.189x10^{-48}	1.300x10^{-27}	5.333x10^{26}	2.957x10^{-34}
^{324}120	^{14}C	^{310}114	40.040	3.561x10^{-48}	3.911x10^{-27}	1.772x10^{26}	1.188x10^{-39}

Table 2.6. The Q value, penetrability, decay constant and the predicted half lives for the emission of the cluster ^{20}O from $^{306\text{-}330}122$ isotopes and the cluster ^{24}Ne from $^{310\text{-}334}124$ isotopes. The half lives are calculated for zero angular momentum transfers.

Parent nuclei	Emitted cluster	Daughter nuclei	Q value (MeV)	Penetrability P	Decay constant λ (s^{-1})	$T^{\alpha}_{1/2}$(s) CPPM	$T^{sf}_{1/2}$(s) KPS [61]
$^{306}122$	^{20}O	$^{286}114$	57.317	1.575x10^{-59}	2.448x10^{-38}	2.831x10^{37}	3.088x10^{8}
$^{308}122$	^{20}O	$^{288}114$	58.847	2.983x10^{-56}	4.759x10^{-35}	1.456x10^{34}	1.656x10^{6}
$^{310}122$	^{20}O	$^{290}114$	61.417	4.567x10^{-51}	7.605x10^{-30}	9.112x10^{28}	3.817x10^{3}
$^{312}122$	^{20}O	$^{292}114$	63.587	7.282x10^{-47}	1.256x10^{-25}	5.520x10^{24}	3.912x10^{0}
$^{314}122$	^{20}O	$^{294}114$	64.137	1.000x10^{-45}	1.739x10^{-24}	3.985x10^{23}	1.841x10^{-3}
$^{316}122$	^{20}O	$^{296}114$	64.347	3.240x10^{-45}	5.653x10^{-24}	1.226x10^{23}	4.103x10^{-7}
$^{318}122$	^{20}O	$^{298}114$	64.477	7.446x10^{-45}	1.302x10^{-23}	5.324x10^{22}	4.463x10^{-11}
$^{320}122$	^{20}O	$^{300}114$	60.087	5.248x10^{-53}	8.550x10^{-32}	8.105x10^{30}	2.439x10^{-15}
$^{322}122$	^{20}O	$^{302}114$	58.037	5.226x10^{-57}	8.224x10^{-36}	8.427x10^{34}	6.884x10^{-20}
$^{324}122$	^{20}O	$^{304}114$	58.807	2.520x10^{-55}	4.018x10^{-34}	1.725x10^{33}	1.030x10^{-24}
$^{326}122$	^{20}O	$^{306}114$	58.457	6.357x10^{-56}	1.008x10^{-34}	6.878x10^{33}	8.393x10^{-30}
$^{328}122$	^{20}O	$^{308}114$	58.977	9.225x10^{-55}	1.475x10^{-33}	4.698x10^{32}	3.813x10^{-35}
$^{330}122$	^{20}O	$^{310}114$	59.307	5.413x10^{-54}	8.704x10^{-33}	7.962x10^{31}	9.895x10^{-41}
$^{310}124$	^{24}Ne	$^{286}114$	84.800	9.910x10^{-52}	2.276x10^{-30}	3.044x10^{29}	4.029x10^{13}
$^{312}124$	^{24}Ne	$^{288}114$	86.140	2.611x10^{-49}	6.093x10^{-28}	1.137x10^{27}	1.937x10^{11}
$^{314}124$	^{24}Ne	$^{290}114$	87.980	4.136x10^{-46}	9.858x10^{-25}	7.030x10^{23}	4.102x10^{8}
$^{316}124$	^{24}Ne	$^{292}114$	89.100	4.032x10^{-44}	9.733x10^{-23}	7.120x10^{21}	3.956x10^{5}
$^{318}124$	^{24}Ne	$^{294}114$	89.200	8.736x10^{-44}	2.111x10^{-22}	3.283x10^{21}	1.791x10^{2}
$^{320}124$	^{24}Ne	$^{296}114$	89.020	6.640x10^{-44}	1.601x10^{-22}	4.328x10^{21}	3.922x10^{-2}
$^{322}124$	^{24}Ne	$^{298}114$	88.880	5.788x10^{-44}	1.394x10^{-22}	4.973x10^{21}	4.276x10^{-6}
$^{324}124$	^{24}Ne	$^{300}114$	86.560	1.364x10^{-47}	3.198x10^{-26}	2.167x10^{25}	2.386x10^{-10}
$^{326}124$	^{24}Ne	$^{302}114$	83.260	5.387x10^{-53}	1.215x10^{-31}	5.704x10^{30}	7.000x10^{-15}
$^{328}124$	^{24}Ne	$^{304}114$	82.040	5.877x10^{-55}	1.306x10^{-33}	5.306x10^{32}	1.108x10^{-19}
$^{330}124$	^{24}Ne	$^{306}114$	81.580	1.286x10^{-55}	2.842x10^{-34}	2.438x10^{33}	9.686x10^{-25}
$^{332}124$	^{24}Ne	$^{308}114$	81.660	2.458x10^{-55}	5.438x10^{-34}	1.274x10^{33}	4.796x10^{-30}
$^{334}124$	^{24}Ne	$^{310}114$	81.600	2.647x10^{-55}	5.851x10^{-34}	1.184x10^{33}	1.375x10^{-35}

2.6.1 Summary

Calculations on the cluster decay half lives for the emission of ^{4}He, ^{8}Be, ^{10}Be, ^{14}C, ^{20}O and ^{24}Ne from the various superheavy parents $^{290-314}$Lv, $^{294-318}$118, $^{296-320}$118, $^{300-324}$120, $^{306-330}$122 and $^{310-334}$124 leading to ^{298}114 (Z=114, N=184) and the neighboring nuclei have been by taking the barrier potential as the sum of Coulomb and proximity potential (within CPPM). A comparison of our calculated alpha and cluster half lives with that of the values evaluated within the Universal formula for cluster decay (UNIV) of Poenaru *et al.,* the Universal Decay Law (UDL) and the Scaling Law of Horoi *et al.,* show a similar trend. The spontaneous fission half lives of the corresponding parents have also been evaluated using the semi-empirical formula of Santhosh *et al.,*. The behavior of the cluster formation probability with the neutron number of the parent nuclei can be clearly seen from the plots for $\log_{10}(S)$ vs. neutron number of the parent nuclei. The role of neutron magicity in cluster decays is clearly revealed from the low values of the cluster decay half-lives at N=184, as seen in the plots for $\log_{10}(T_{1/2})$ versus neutron number of daughter nuclei. We have thus established and have indicated towards a new island for the cluster radioactivity leading to the residual superheavy isotope ^{298}114 and its neighbors.

2.7 Probable cluster decays from $^{270-318}$118 superheavy nuclei

The cluster decay process in $^{270-318}$118 superheavy nuclei has been studied extensively within the Coulomb and proximity potential model (CPPM), thereby investigating the probable cluster decays from the various isotopes of Z = 118. The behaviour of the cluster half-lives computed within CPPM, with the neutron number of the daughter nuclei can be clearly seen from the **Figures 2.17** and **2.18** which represents the plot for $\log_{10}(T_{1/2})$ vs. neutron number of the daughter nuclei, for the cluster emission of various clusters from $^{286-318}$118 superheavy nuclei. **Figure 2.17** represents the plot for the cluster emission of ^{4}He, ^{8,10}Be, ^{12,14,16,18}C, ^{16,18,20,22,24}O and ^{22,24}Ne from $^{286-318}$118 superheavy nuclei and the plot for the cluster emission of ^{26,28}Ne, ^{26,28,30,32,34}Mg, ^{30,32,34,36,38}Si and ^{38,40,42,44}S has been given in **Figure 2.18**. It can be seen clearly from **Figure 2.17**, that the minima of the logarithmic half-lives for most of these cluster emission are found for the decay leading to a daughter with N = 184. For example, in the case of ^{4}He emission from ^{304}118, the minima of the logarithmic half lives is found for the decay leading to ^{300}116 (N=184) and in the case of ^{10}Be emission from ^{308}118, the minima of the logarithmic half-lives is found for the decay leading to ^{298}114 (N = 184). A minimum in the decay half lives corresponds to the greater barrier penetrability, which in turn indicates the neutron/proton shell closure of the daughter nuclei. This indicates the role of neutron magicity N = 184 in cluster radioactivity. The present experimental upper and lower limits of half lives favourable for the cluster decay measurements, are 10^{30}s and 10^{-6}s respectively and have been represented as dotted line in these figures. As can be seen from the figures, most of the decays in **Figure 2.17** and a few decays in **Figure 2.18** are well within these experimental limits and are hence favourable for measurements. The comparison of the predicted cluster decay half-lives with that of the cluster half-lives evaluated using various theoretical models, for the emission of various clusters from $^{286-318}$118 has been given in the **Tables 2.7-2.10**. Only the most probable cluster emissions, most of those with $T_{1/2} < 10^{30}$s, are given here. The parent nuclei, emitted cluster and the daughter nuclei are given in column 1, 2 and 3 respectively and the energy released in the decay has been given in column 4. In column 5, the cluster decay half lives evaluated within CPPM have been arranged. The decay half-lives evaluated using the Universal Decay Law (UDL) of Qi *et al.,* the Universal (UNIV) curve of Poenaru *et al.,* and the Scaling Law of Horoi *et al.,* are given in columns 6, 7 and 8 respectively. The alpha decay half-life of the experimentally synthesized isotope ^{294}118 has been evaluated within CPPM and is included in **Table 2.9**. On comparison with the experimental half life, $T_{1/2} = 0.69\text{x}10^{-3}$s [15], it can be seen that our value ($T_{1/2} = 2.508\text{x}10^{-3}$s) matches well with the experimental value. In the recent study [77] on the investigation of the alpha decay half lives of $^{271-310}$118 superheavy nuclei, we had shown that, on inclusion of the deformations of both the parent and daughter nuclei, the predicted alpha decay half life of ^{294}118 ($T_{1/2}$=$0.53\text{x}10^{-3}$s) is in better agreement with the experimental value.

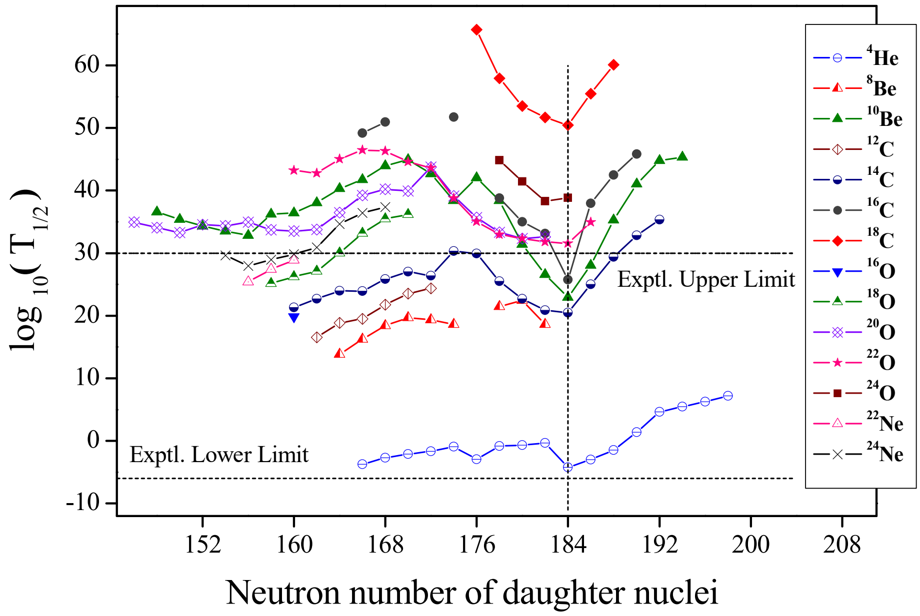

Figure 2.17. The computed $\log_{10}(T_{1/2})$ values versus neutron number of daughter nuclei for the emission of various clusters from $^{286-318}118$ SHN. $T_{1/2}$ is in seconds.

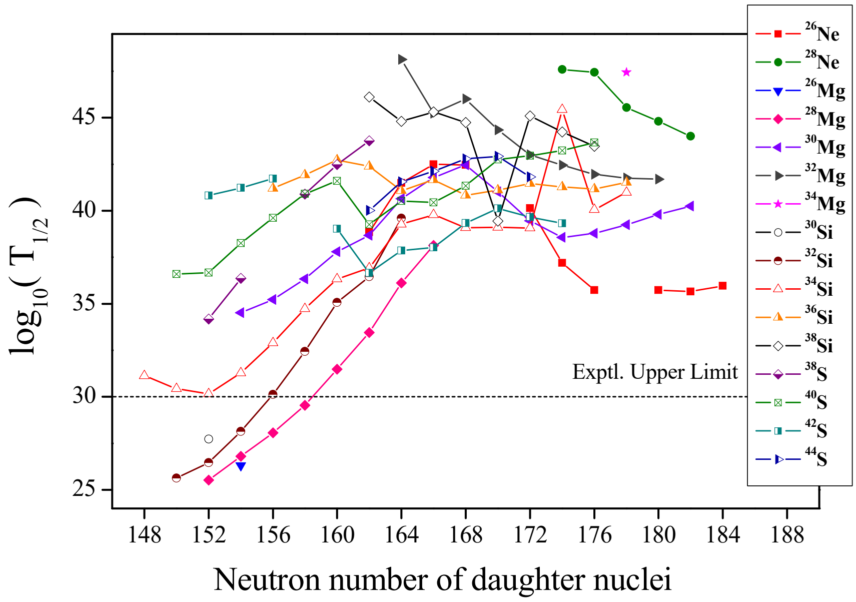

Figure 2.18. The computed $\log_{10}(T_{1/2})$ values versus neutron number of daughter nuclei for the emission of various clusters from $^{286-318}118$ SHN. $T_{1/2}$ is in seconds.

Table 2.7. Comparison of the predicted cluster decay half-lives with that of the cluster half-lives evaluated using various theoretical models, for the emission of various clusters from $^{286, 288}118$ SHN. The half-lives are calculated for zero angular momentum transfers.

Parent Nuclei	Emitted Cluster	Daughter Nuclei	Q value (MeV)	$T_{1/2}$ (s)			
				CPPM	UNIV	UDL	Horoi
$^{286}118$	^{4}He	$^{282}116$	12.335	1.919×10^{-4}	2.148×10^{-5}	3.452×10^{-5}	8.588×10^{-5}
	^{8}Be	$^{278}114$	24.678	6.791×10^{13}	3.160×10^{10}	3.875×10^{13}	7.002×10^{11}
	^{12}C	$^{274}112$	44.350	3.477×10^{16}	7.199×10^{11}	2.272×10^{15}	9.617×10^{13}
	^{14}C	$^{272}112$	42.260	1.992×10^{21}	5.611×10^{17}	4.872×10^{21}	2.108×10^{20}
	^{16}O	$^{270}110$	64.617	4.345×10^{19}	2.598×10^{13}	3.528×10^{16}	3.415×10^{16}
	^{18}O	$^{268}110$	61.693	4.404×10^{24}	1.251×10^{19}	6.138×10^{22}	2.725×10^{22}
	^{22}Ne	$^{264}108$	83.021	2.158×10^{25}	4.257×10^{18}	7.969×10^{20}	1.085×10^{23}
	^{24}Ne	$^{262}108$	80.242	4.159×10^{29}	3.325×10^{23}	1.671×10^{26}	1.018×10^{28}
	^{26}Mg	$^{260}106$	104.227	1.815×10^{26}	3.687×10^{18}	8.131×10^{18}	1.449×10^{24}
	^{28}Mg	$^{258}106$	104.339	1.712×10^{25}	1.066×10^{20}	3.827×10^{19}	4.188×10^{25}
	^{30}Si	$^{256}104$	124.769	5.016×10^{27}	9.685×10^{18}	1.279×10^{17}	6.072×10^{25}
	^{32}Si	$^{254}104$	125.438	2.746×10^{25}	7.269×10^{19}	7.122×10^{16}	3.929×10^{26}
	^{34}Si	$^{252}104$	121.157	1.352×10^{31}	6.956×10^{24}	5.027×10^{22}	3.721×10^{31}
$^{288}118$	^{4}He	$^{284}116$	11.905	1.897×10^{-3}	1.606×10^{-4}	3.301×10^{-4}	6.073×10^{-4}
	^{8}Be	$^{280}114$	23.628	1.687×10^{16}	3.832×10^{12}	9.001×10^{15}	9.030×10^{13}
	^{12}C	$^{276}112$	44.390	2.289×10^{16}	5.280×10^{11}	1.587×10^{15}	8.601×10^{13}
	^{14}C	$^{274}112$	41.510	5.277×10^{22}	7.674×10^{18}	1.141×10^{23}	3.704×10^{21}
	^{18}O	$^{270}110$	60.843	9.719×10^{25}	1.228×10^{20}	1.120×10^{24}	3.444×10^{23}
	^{22}Ne	$^{266}108$	81.625	2.292×10^{27}	9.560×10^{19}	5.207×10^{22}	3.257×10^{24}
	^{24}Ne	$^{264}108$	81.128	7.700×10^{27}	2.459×10^{22}	5.443×10^{24}	1.045×10^{27}
	^{28}Mg	$^{260}106$	103.211	5.721×10^{26}	8.514×10^{20}	7.514×10^{20}	4.935×10^{26}
	^{32}Si	$^{256}104$	124.595	2.762×10^{26}	2.459×10^{20}	4.549×10^{17}	2.032×10^{27}
	^{34}Si	$^{254}104$	121.497	1.753×10^{30}	2.485×10^{24}	1.139×10^{22}	1.969×10^{31}

Table 2.8. Comparison of the predicted cluster decay half-lives with that of the cluster half-lives evaluated using various theoretical models, for the emission of various clusters from $^{290, 292}$118 SHN. The half-lives are calculated for zero angular momentum transfers.

Parent Nuclei	Emitted Cluster	Daughter Nuclei	Q value (MeV)	$T_{1/2}$ (s)			
				CPPM	UNIV	UDL	Horoi
^{290}118	^{4}He	^{286}116	11.645	$7.817x10^{-3}$	$5.601x10^{-4}$	$1.337x10^{-3}$	$2.091x10^{-3}$
	^{8}Be	^{282}114	22.728	$2.511x10^{18}$	$3.120x10^{14}$	$1.279x10^{18}$	$7.600x10^{15}$
	^{12}C	^{278}112	42.720	$1.744x10^{19}$	$1.011x10^{14}$	$9.304x10^{17}$	$1.944x10^{16}$
	^{14}C	^{276}112	42.260	$1.170x10^{21}$	$3.775x10^{17}$	$3.160x10^{21}$	$2.191x10^{20}$
	^{18}O	^{272}110	60.393	$4.358x10^{26}$	$3.778x10^{20}$	$4.708x10^{24}$	$1.365x10^{24}$
	^{22}Ne	^{268}108	80.825	$2.872x10^{28}$	$5.342x10^{20}$	$5.226x10^{23}$	$2.415x10^{25}$
	^{24}Ne	^{266}108	80.442	$7.219x10^{28}$	$1.113x10^{23}$	$4.144x10^{25}$	$6.484x10^{27}$
	^{28}Mg	^{262}106	102.279	$9.792x10^{27}$	$4.693x10^{21}$	$8.576x10^{21}$	$3.938x10^{27}$
	^{32}Si	^{258}104	123.368	$1.123x10^{28}$	$1.758x10^{21}$	$8.787x10^{18}$	$2.241x10^{28}$
	^{34}Si	^{256}104	121.364	$1.379x10^{30}$	$2.309x10^{24}$	$1.049x10^{22}$	$2.732x10^{31}$
^{292}118	^{4}He	^{288}116	11.465	$2.096x10^{-2}$	$1.339x10^{-3}$	$3.545x10^{-3}$	$5.049x10^{-3}$
	^{8}Be	^{284}114	22.208	$4.850x10^{19}$	$4.302x10^{15}$	$2.435x10^{19}$	$1.118x10^{17}$
	^{12}C	^{280}112	41.220	$9.058x10^{21}$	$1.566x10^{16}$	$3.925x10^{20}$	$3.352x10^{18}$
	^{14}C	^{278}112	40.990	$3.868x10^{23}$	$3.833x10^{19}$	$8.116x10^{23}$	$2.906x10^{22}$
	^{18}O	^{274}110	58.523	$8.300x10^{29}$	$1.064x10^{23}$	$5.442x10^{27}$	$4.552x10^{26}$
	^{24}Ne	^{268}108	80.042	$2.243x10^{29}$	$2.421x10^{23}$	$1.191x10^{26}$	$1.930x10^{28}$
	^{28}Mg	^{264}106	101.159	$3.537x10^{29}$	$4.095x10^{22}$	$1.837x10^{23}$	$4.922x10^{28}$
	^{32}Si	^{260}104	121.848	$1.359x10^{30}$	$2.343x10^{22}$	$4.157x10^{20}$	$4.559x10^{29}$
	^{34}Si	^{258}104	120.537	$1.535x10^{31}$	$8.803x10^{24}$	$7.675x10^{22}$	$1.575x10^{32}$

A comparison of the cluster decay half-lives evaluated within CPPM with the half-lives evaluated using various theoretical models shows that, for most of the decays, the CPPM values matches well with the UDL values than that of the UNIV or the values obtained using the Scaling Law of Horoi. As most of the cluster decay half-lives predicted through our study are much below the experimental limit ($T_{1/2}$ < 10^{30}s), these decays could be treated as favourable for measurements and hence we hope these observations serve as a guide for the future experiments.

Table 2.9. Comparison of the predicted cluster decay half-lives with that of the cluster half-lives evaluated using various theoretical models, for the emission of various clusters from $^{294-304}118$ SHN. The half-lives are calculated for zero angular momentum transfers.

Parent Nuclei	Emitted Cluster	Daughter Nuclei	Q value (MeV)	$T_{1/2}$ (s)			
				CPPM	UNIV	UDL	Horoi
$^{294}118$	^{4}He	$^{290}116$	11.815	2.508×10^{-3}	2.022×10^{-4}	4.381×10^{-4}	9.347×10^{-4}
	^{8}Be	$^{286}114$	22.718	1.937×10^{18}	2.490×10^{14}	1.029×10^{18}	8.171×10^{15}
	^{12}C	$^{282}112$	40.450	2.271×10^{23}	2.181×10^{17}	9.074×10^{21}	5.309×10^{19}
	^{14}C	$^{280}112$	40.550	2.608×10^{24}	1.779×10^{20}	5.146×10^{24}	1.689×10^{23}
	^{24}Ne	$^{270}108$	80.132	1.003×10^{29}	1.442×10^{23}	6.154×10^{25}	1.578×10^{28}
	^{28}Mg	$^{266}106$	100.669	1.269×10^{30}	9.060×10^{22}	5.709×10^{23}	1.543×10^{29}
	^{32}Si	$^{262}104$	120.958	1.749×10^{31}	9.683×10^{22}	3.422×10^{21}	2.791×10^{30}
$^{296}118$	^{4}He	$^{292}116$	10.125	1.157×10^{2}	3.118×10^{0}	1.781×10^{1}	7.230×10^{0}
	^{8}Be	$^{288}114$	20.808	2.764×10^{23}	9.796×10^{18}	1.323×10^{23}	2.530×10^{20}
	^{12}C	$^{284}112$	38.240	6.232×10^{27}	1.040×10^{21}	1.896×10^{26}	2.262×10^{23}
	^{14}C	$^{282}112$	38.630	3.677×10^{28}	4.246×10^{23}	5.027×10^{28}	4.840×10^{26}
$^{298}118$	^{4}He	$^{294}116$	11.115	1.424×10^{-1}	7.246×10^{-3}	2.355×10^{-2}	2.989×10^{-2}
	^{14}C	$^{284}112$	37.890	1.516×10^{30}	9.116×10^{24}	1.846×10^{30}	1.239×10^{28}
$^{300}118$	^{4}He	$^{296}116$	11.035	2.192×10^{-1}	1.057×10^{-2}	3.601×10^{-2}	4.547×10^{-2}
	^{8}Be	$^{292}114$	21.448	3.069×10^{21}	1.714×10^{17}	1.568×10^{21}	6.970×10^{18}
	^{14}C	$^{286}112$	37.780	2.189×10^{30}	1.226×10^{25}	2.669×10^{30}	2.061×10^{28}
$^{302}118$	^{4}He	$^{298}116$	10.915	4.389×10^{-1}	1.950×10^{-2}	7.135×10^{-2}	8.590×10^{-2}
	^{8}Be	$^{294}114$	21.088	2.757×10^{22}	1.215×10^{18}	1.395×10^{22}	5.282×10^{19}
	^{14}C	$^{288}112$	37.920	8.194×10^{29}	5.359×10^{24}	1.043×10^{30}	1.133×10^{28}
$^{304}118$	^{4}He	$^{300}116$	12.435	5.793×10^{-5}	7.025×10^{-6}	1.057×10^{-5}	5.664×10^{-5}
	^{8}Be	$^{296}114$	22.478	3.868×10^{18}	4.448×10^{14}	2.143×10^{18}	2.933×10^{16}
	^{10}Be	$^{294}114$	19.303	2.538×10^{31}	1.472×10^{28}	8.722×10^{32}	3.235×10^{31}
	^{14}C	$^{290}112$	39.810	3.343×10^{25}	1.331×10^{21}	6.240×10^{25}	3.720×10^{24}

Table 2.10. Comparison of the predicted cluster decay half-lives with that of the cluster half-lives evaluated using various theoretical models, for the emission of various clusters from $^{306-318}118$ SHN. The half-lives are calculated for zero angular momentum transfers.

Parent Nuclei	Emitted Cluster	Daughter Nuclei	Q value (MeV)	$T_{1/2}$ (s)			
				CPPM	UNIV	UDL	Horoi
$^{306}118$	^{4}He	$^{302}116$	11.895	$1.046x10^{-3}$	$8.778x10^{-5}$	$1.815x10^{-4}$	$6.527x10^{-4}$
	^{10}Be	$^{296}114$	20.673	$3.846x10^{26}$	$6.796x10^{23}$	$1.530x10^{28}$	$1.590x10^{27}$
	^{14}C	$^{292}112$	41.080	$4.989x10^{22}$	$6.939x10^{18}$	$1.228x10^{23}$	$2.333x10^{22}$
$^{308}118$	^{4}He	$^{304}116$	11.295	$3.332x10^{-2}$	$1.867x10^{-3}$	$5.492x10^{-3}$	$1.209x10^{-2}$
	^{10}Be	$^{298}114$	21.793	$9.191x10^{22}$	$4.108x10^{20}$	$4.153x10^{24}$	$9.685x10^{23}$
	^{14}C	$^{294}112$	41.920	$7.264x10^{20}$	$2.356x10^{17}$	$2.160x10^{21}$	$9.301x10^{20}$
$^{310}118$	^{4}He	$^{306}116$	10.275	$2.463x10^{1}$	$7.060x10^{-1}$	$3.774x10^{0}$	$3.066x10^{0}$
	^{10}Be	$^{300}114$	20.203	$1.109x10^{28}$	$1.300x10^{25}$	$4.137x10^{29}$	$4.432x10^{28}$
	^{14}C	$^{296}112$	42.070	$2.927x10^{20}$	$1.118x10^{17}$	$8.972x10^{20}$	$5.359x10^{20}$
	^{20}O	$^{290}110$	56.934	$2.182x10^{32}$	$6.978x10^{26}$	$4.355x10^{31}$	$6.311x10^{31}$
$^{312}118$	^{4}He	$^{308}116$	9.275	$4.432x10^{4}$	$6.680x10^{2}$	$6.392x10^{3}$	$1.656x10^{3}$
	^{14}C	$^{298}112$	39.880	$1.035x10^{25}$	$4.647x10^{20}$	$1.956x10^{25}$	$3.011x10^{24}$
	^{16}C	$^{296}112$	36.976	$1.438x10^{33}$	$2.678x10^{29}$	$7.546x10^{34}$	$7.440x10^{33}$
	^{22}O	$^{290}110$	57.030	$2.308x10^{32}$	$8.319x10^{28}$	$1.869x10^{33}$	$1.892x10^{34}$
$^{314}118$	^{4}He	$^{310}116$	9.035	$3.061x10^{5}$	$3.931x10^{3}$	$4.338x10^{4}$	$8.767x10^{3}$
	^{14}C	$^{300}112$	37.920	$2.400x10^{29}$	$1.671x10^{24}$	$3.073x10^{29}$	$1.282x10^{28}$
	^{22}O	$^{292}110$	57.240	$6.239x10^{31}$	$3.001x10^{28}$	$5.405x10^{32}$	$8.995x10^{33}$
$^{316}118$	^{4}He	$^{312}116$	8.815	$1.922x10^{6}$	$2.129x10^{4}$	$2.680x10^{5}$	$4.289x10^{4}$
	^{22}O	$^{294}110$	57.300	$3.577x10^{31}$	$1.886x10^{28}$	$3.111x10^{32}$	$7.450x10^{33}$
$^{318}118$	^{4}He	$^{314}116$	8.575	$1.559x10^{7}$	$1.470x10^{5}$	$2.136x10^{6}$	$2.597x10^{5}$

In the cluster decay studies on heavy nuclei, it has been shown that the half-life is minimum for the decays leading to the doubly magic daughter ^{208}Pb (Z=82, N=126) or its neighbouring nuclei. The present study on the cluster decay half-lives of the superheavy nuclei gives a pronounced minima for the daughter with N = 184. This may be interpreted as a result of the strong shell effect of the assumed magic number of the neutrons and this reveal that neutron shell closure plays a decisive role in the cluster decays of superheavy nuclei.

2.7.1 Summary

Taking the interacting barrier as the sum of Coulomb and proximity potential (within CPPM), the feasibility for the emission of ^{4}He, $^{8,10}Be$, $^{12,14,16,18}C$, $^{16,18,20,22,24}O$, $^{22,24,26,28}Ne$, $^{26,28,30,32,34}Mg$, $^{30,32,34,36,38}Si$ and $^{38,40,42,44}S$, from the superheavy nuclei with Z=118 within the range $270 \leq A \leq 318$ has been investigated. The cluster decay half lives have also been calculated using the Universal formula for cluster decay (UNIV) of Poenaru *et al.,* the Universal Decay Law (UDL) and the Scaling Law of Horoi *et al.,*. A comparison of our calculated alpha and cluster half lives with the values evaluated within these theoretical models show a similar trend. The experimental and the predicted half life of the experimentally synthesized superheavy isotope $^{294}118$ are also found to be in agreement with each other. The plots for $\log_{10}(T_{1/2})$ against the neutron number of the daughter in the corresponding decay reveals that, for most of the decays, the half life is minimum for the decay leading to a daughter with N = 184. The predictions on the cluster decay half-lives of Z = 118, performed within CPPM, may be of great use for further experimental investigation on cluster decay in the superheavy region, as most of the predicted half-lives are well within the present upper limit for measurements.

References

[1] E. Rutherford and H. Geiger, Proc. R. Soc. London, Ser. A. **81**, 162 (1908).
[2] E. Rutherford and T. Royds, Phil. Mag. **17**, 281 (1909).
[3] P. Moller and J. R. Nix, Nucl. Phys. A **549**, 84 (1992).
[4] H. F. Zhang and G. Royer, Phys. Rev. **C 76**, 047304 (2007).
[5] P. R. Chowdhury, D. N. Basu and C. Samanta, Phys. Rev. **C 75**, 047306 (2007).
[6] D. S. Delion, R. J. Liotta and R. Wyss, Phys. Rev. **C 76**, 044301 (2007).
[7] Z. Ren and C. Xu, J. Phys.: Conf. Ser. **111**, 012040 (2008).
[8] V. Yu. Denisov and A. A. Khudenko, At. Data Nucl. Data Tables **95**, 815 (2009).
[9] A. I. Budaca and I. Silişteanu, Phys. Rev. **C 88**, 044618 (2013).
[10] Y. Qian, Z. Ren and D. Ni, Phys. Rev. **C 89**, 024318 (2014).
[11] P. Jachimowicz, M. Kowal and J. Skalski, Phys. Rev. **C 89**, 024304 (2014).
[12] Niyti and R. K. Gupta, Phys. Rev. **C 89**, 014603 (2014).
[13] Y. J. Liang, M. Zhu, Z. H. Liu and W. Z. Wang, Phys. Rev. **C 89**, 034627 (2014).
[14] L. Zhu, W. J. Xie and F. S. Zhang, Phys. Rev. **C 89**, 024615 (2014).
[15] Yu. Ts. Oganessian, F. Sh. Abdullin, C. Alexander, J. Binder, R. A. Boll, S. N. Dmitriev,J. Ezold, K. Felker, J. M. Gostic, R. K. Grzywacz, J. H. Hamilton, R. A. Henderson, M. G. Itkis, K. Miernik, D. Miller, K. J. Moody, A. N. Polyakov, A. V. Ramayya, J. B. Roberto, M. A. Ryabinin, K. P. Rykaczewski, R. N. Sagaidak, D. A. Shaughnessy, I. V. Shirokovsky, M. V. Shumeiko, M. A. Stoyer, N. J. Stoyer, V. G. Subbotin, A. M. Sukhov, Yu. S. Tsyganov, V. K. Utyonkov, A. A. Voinov and G. K. Vostokin, Phys. Rev. Lett. **109**, 162501 (2012).
[16] Yu. Ts. Oganessian, V. K. Utyonkov, Yu. V. Lobanov, F. Sh. Abdullin, A. N. Polyakov, R. N. Sagaidak, I. V. Shirokovsky, Yu. S. Tsyganov, A. A. Voinov, G. G. Gulbekian, S. L. Bogomolov, B. N. Gikal, A. N. Mezentsev, S. Iliev, V. G. Subbotin, A. M. Sukhov, K. Subotic, V. I. Zagrebaev, G. K. Vostokin, M. G. Itkis, K. J. Moody, J. B. Patin, D. A. Shaughnessy, M. A. Stoyer, N. J. Stoyer, P. A. Wilk, J. M. Kenneally, J. H. Landrum, J. F. Wild and R. W. Lougheed, Phys. Rev. **C 74**, 044602 (2006).
[17] M. A. Stoyer, Nature **442**, 876 (2006).
[18] Yu. Ts. Oganessian, V. K. Utyonkov, S. N. Dmitriev, Yu. V. Lobanov, M. G. Itkis, A. N. Polyakov, Yu. S. Tsyganov, A. N. Mezentsev, A. V. Yeremin, A. A. Voinov, E. A. Sokol, G. G. Gulbekian, S. L. Bogomolov, S. Iliev, V. G. Subbotin, A. M. Sukhov, G. V. Buklanov, S. V. Shishkin, V. I. Chepygin, G. K. Vostokin, N. V. Aksenov, M. Hussonnois, K. Subotic, V. I. Zagrebaev, K. J. Moody, J. B. Patin, J. F. Wild, M. A. Stoyer, N. J. Stoyer, D. A. Shaughnessy, J. M. Kenneally, P. A. Wilk, R. W. Lougheed, H. W. Gäggeler,

D. Schumann, H. Bruchertseifer and R. Eichler, Phys. Rev. **C 72**, 034611 (2005).

[19] Yu. Ts. Oganessian, V. K. Utyonkov, Yu. V. Lobanov, F. Sh. Abdullin, A. N. Polyakov, I. V. Shirokovsky, Yu. S. Tsyganov, G. G. Gulbekian, S. L. Bogomolov, B. N. Gikal, A. N. Mezentsev, S. Iliev, V. G. Subbotin, A. M. Sukhov, O. V. Ivanov, G. V. Buklanov, K. Subotic, M. G. Itkis, K. J. Moody, J. F. Wild, N. J. Stoyer, M. A. Stoyer and R. W. Lougheed, Phys. Rev. **C 62**, 041604(R) (2000).

[20] Yu. Ts. Oganessian, V. K. Utyonkov, Yu. V. Lobanov, F. Sh. Abdullin, A. N. Polyakov, I. V. Shirokovsky, Yu. S. Tsyganov, G. G. Gulbekian, S. L. Bogomolov, B. N. Gikal, A. N. Mezentsev, S. Iliev, V. G. Subbotin, A. M. Sukhov, O. V. Ivanov, G. V. Buklanov, K. Subotic, A. A. Voinov, M. G. Itkis, K. J. Moody, J. F. Wild, N. J. Stoyer, M. A. Stoyer, R. W. Lougheed and C. A. Laue, Eur. Phys. J. **A 15**, 201 (2002).

[21] Yu. Ts. Oganessian, V. K. Utyonkov, Yu. V. Lobanov, F. Sh. Abdullin, A. N. Polyakov, I. V. Shirokovsky, Yu. S. Tsyganov, G. G. Gulbekian, S. L. Bogomolov, B. N. Gikal, A. N. Mezentsev, S. Iliev, V. G. Subbotin, A. M. Sukhov, A. A. Voinov, G. V. Buklanov, K. Subotic, V. I. Zagrebaev, M. G. Itkis, J. B. Patin, K. J. Moody, J. F. Wild, M. A. Stoyer, N. J. Stoyer, D. A. Shaughnessy, J. M. Kenneally and R. W. Lougheed, Nucl. Phys. A **734**, 109 (2004).

[22] S. Hofmann and G. Münzenberg, Rev. Mod. Phys.**72**, 733 (2000).

[23] Yu. Ts. Oganessian, J. Phys. G: Nucl. Part. Phys. **34**, R165 (2007).

[24] Yu. Ts. Oganessian, Nucl. Phys. A **685**, 17c (2001).

[25] P. Armbruster, Annu. Rev .Nucl. Part. Sci. **35** 135 (1985).

[26] P. Armbruster, Annu. Rev. Nucl. Part. Sci. **50** 411 (2000).

[27] G. Münzenberg, S. Hofmann, F. P. Heßberger, W. Reisdorf, K. H. Schmidt, J. H. R. Schneider, P. Armbruster, C. C. Sahm, B. Thuma, Z. Phys. A **300**, 107 (1981).

[28] Yu. Ts. Oganessian, F. Sh. Abdullin, P. D. Bailey, D. E. Benker, M. E. Bennett, S. N. Dmitriev, J. G. Ezold, J. H. Hamilton, R. A. Henderson, M. G. Itkis, Yu. V. Lobanov, A. N. Mezentsev, K. J. Moody, S. L. Nelson, A. N. Polyakov, C. E. Porter, A. V. Ramayya, F. D. Riley, J. B. Roberto, M. A. Ryabinin, K. P. Rykaczewski, R. N. Sagaidak, D. A. Shaughnessy, I. V. Shirokovsky, M. A. Stoyer, V. G. Subbotin, R. Sudowe, A. M. Sukhov, Yu. S. Tsyganov, V. K. Utyonkov, A. A. Voinov, G. K. Vostokin and P. A. Wilk, Phys. Rev. Lett. **104**, 142502 (2010).

[29] Yu. Ts. Oganessian, F. Sh. Abdullin, P. D. Bailey, D. E. Benker, M. E. Bennett, S. N. Dmitriev, J. G. Ezold, J. H. Hamilton, R. A. Henderson, M. G. Itkis, Yu. V. Lobanov, A. N. Mezentsev, K. J. Moody, S. L. Nelson, A. N. Polyakov, C. E. Porter, A. V. Ramayya, F. D. Riley, J. B. Roberto, M. A. Ryabinin, K. P. Rykaczewski, R. N. Sagaidak, D. A. Shaughnessy, I. V.

Shirokovsky, M. A. Stoyer, V. G. Subbotin, R. Sudowe, A. M. Sukhov, R. Taylor, Yu. S. Tsyganov, V. K. Utyonkov, A. A. Voinov, G. K. Vostokin and P. A. Wilk, Phys. Rev. **C 83**, 054315 (2011).

[30] Yu. Ts. Oganessian, A. S. Iljinov, A. G. Demin, S. P. Tretyakova, Nucl. Phys. A **239**, 353 (1975).

[31] G. Münzenberg, P. Armbruster, F. P. Heßberger, S. Hofmann, K. Poppensieker, W. Reisdorf, J. H. R. Schneider, W. F. W. Schneider, K. H. Schmidt, C. C. Sahm and D. Vermeulen, Z. Phys. **A 309**, 89 (1982).

[32] D. Ackermann, Nucl. Phys. A **787**, 353c (2007).

[33] S. Hofmann, D. Ackermann, S. Antalic, H. G. Burkhard, V. F. Comas, R. Dressler, Z. Gan, S. Heinz, J. A. Heredia, and F. P. Heßberger, Eur. Phys. J. **A 32**, 251 (2007).

[34] S. Hofmann, F. P. Heßberger, D. Ackermann, S. Antalic, P. Cagarda, B. Kindler, P. Kuusiniemi, M. Leino, B. Lommel, O. N. Malyshev, R. Mann, G. Münzenberg, A. G. Popeko, S. Saro, B. Streicher, and A. V. Yeremin, Nucl. Phys. A **734**, 93 (2004).

[35] S. Hofmann, G. Munzenberg and M. Schadel, Nucl. Phys. News **14**, 5 (2004).

[36] K. Morita, K. Morimoto, D. Kaji, T. Akiyama, S. Goto, H. Haba, E. Ideguchi, K. Katori, H. Koura, H. Kikunaga, H. Kudo, T. Ohnishi, A. Ozawa, N. Sato, T. Suda, K. Sueki, F. Tokanai, T. Yamaguchi, A. Yoneda and A. Yoshida, J. Phys. Soc. Jpn. **76**, 045001 (2007).

[37] K. Morita, K. Morimoto, D. Kaji, T. Akiyama, S. Goto, H. Haba, E. Ideguchi, R. Kanungo, K. Katori, H. Koura, H. Kudo, T. Ohnishi, A. Ozawa, T. Suda, K. Sueki, H. S. Xu, T. Yamaguchi, A. Yoneda, A. Yoshida and Y. L. Zhao, J. Phys. Soc. Jpn. **73**, 2593 (2004).

[38] K. Morita, K. Morimoto, D. Kaji, S. Goto, H. Haba, E. Ideguchi, R. Kanungo, K. Katori, H. Koura, H. Kudo, T. Ohnishi, A. Ozawa, J. C. Peter, T. Suda, K. Sueki, I. Tanihata, F. Tokanai, H. Xu, A. V. Yeremin, A. Yoneda, A. Yoshida, Y. L. Zhao, T. Zheng, Nucl. Phys. A **734**, 101 (2004).

[39] K. Morita, K. Morimoto, D. Kaji, T. Akiyama, Sin-ichi Goto, H. Haba, E. Ideguchi, K. Katori, H. Koura, H. Kudo, T. Ohnishi, A. Ozawa, T. Suda, K. Sueki, F. Tokanai, T. Yamaguchi, A. Yoneda and A. Yoshida, J. Phys. Soc. Jpn. **76**, 043201 (2007).

[40] J. Blocki, J. Randrup, W. J. Swiatecki, C. F. Tsang, Ann. Phys. NY **105**, 427 (1977).

[41] J. Blocki, W. J. Swiatecki, Ann. Phys. NY **132**, 53 (1981).

[42] D. N. Poenaru, M. Ivascu, A. Sandulescu, W. Greiner, Phys. Rev. C **32**, 572 (1985).

[43] N. Malhotra and R. K. Gupta, Phys. Rev. **C 31**, 1179 (1985).

[44] R. K. Gupta, M. Balasubramaniam, R. Kumar, N. Singh, M. Manhas and W. Greiner, J. Phys. G: Nucl. Part. Phys. **31**, 631 (2005).

[45] C. Y. Wong, Phys. Rev. Lett. **31**, 766 (1973).

[46] N. V. Antonenko and R. V. Jolos, Z. Phys. A **339**, 453 (1991).
[47] N. V. Antonenko, E. A. Cherepanov, A. K. Nasirov, V. P. Permjakov and V. Volkov, Phys. Rev. C **51**, 2635 (1995).
[48] A. J. Baltz and B. F. Bayman, Phys. Rev. C **26**, 1969 (1982).
[49] D. N. Poenaru and W. Greiner, J. Phys. G: Nucl. Part. Phys. **17**, S443 (1991).
[50] D. N. Poenaru and W. Greiner, Phys. Scr. **44**, 427 (1991).
[51] D. N. Poenaru, I. H. Plonski and W. Greiner, Phys. Rev. **C 74**, 014312 (2006).
[52] D. N. Poenaru, I. H. Plonski, R. A. Gherghescu and W. Greiner, J. Phys. G: Nucl. Part. Phys. **32**, 1223 (2006).
[53] R. Blendowske and H. Walliser, Phys. Rev. Lett. **61**, 1930 (1988).
[54] R. Blendowske, T. Fliessbach, H. Walliser, Nuclear Decay Modes, Institute of Physics Publishing, Bristol, 1996, Chap. 7, p. 337.
[55] M. Iriondo, D. Jerrestam and R. J. Liotta, Nucl. Phys. A **454**, 252 (1986).
[56] M. Wang, G. Audi, A. H. Wapstra, F. G. Kondev, M. Mac Cormick, X. Xu and B. Pfeiffer, Chin. Phys. **C 36**, 1603 (2012).
[57] H. Koura, T. Tachibana, M. Uno and M. Yamada, Prog. Theor. Phys. **113**, 305 (2005).
[58] C. Qi, F. R. Xu, R. J. Liotta, R. Wyss, Phys. Rev. Lett. **103**, 072501 (2009).
[59] C. Qi, F. R. Xu, R. J. Liotta, R. Wyss, M.Y. Zhang, C. Asawatangtrakuldee, D. Hu, Phys. Rev. C **80**, 044326 (2009).
[60] M. Horoi, A. Brown, A. Sandulescu, arXiv:nucl-th/9403008v1, 1994.
[61] K. P. Santhosh, R. K. Biju, S. Sabina, Nucl. Phys. A **832**, 220 (2009).
[62] C. Xu, Z. Ren, and Y. Guo, Phys. Rev. C **78**, 044329 (2008).
[63] A. Sobiczewski, Z. Patyk, and S. Cwiok, Phys. Lett. **B 224**, 1 (1989).
[64] V. E. Viola, Jr. and G. T. Seaborg, J. Inorg. Nucl. Chem. **28**, 741 (1966).
[65] Z. Patyk, A. Sobiczewski, P. Armbruster and K. H. Schmidt, Nucl. Phys. A **491**, 267 (1989).
[66] H. Geiger and J. M. Nutall, Phil. Mag. **22**, 613(1911).
[67] G. Royer, J. Phys. G: Nucl. Part. Phys. **26**, 1149 (2000).
[68] V. Yu. Denisov, H. Ikezoe, Phys. Rev. C **72**, 064613 (2005).
[69] K. N. Huang, M. Aoyagi, M H. Chen, B. Crasemann, H. Mark, At. Data Nucl. Data Tables **18**, 243 (1976).
[70] National Nuclear Data Centre, NuDat2.5, http://www.nndc.bnl.gov
[71] N. Wang, E. G. Zhao and W. Scheid, Phys. Rev. C **89**, 037601 (2014).
[72] R. K. Gupta, S. K. Patra, W. Greiner, Mod. Phys. Lett. A **12**, 1727 (1997).
[73] P. R. Chowdhury, C. Samanta, D. N. Basu, Phys. Rev. C **77** 044603 (2008).
[74] R. K. Gupta, S. Kumar, R. Kumar, M. Balasubramaniam, W. Scheid, J. Phys. G: Nucl. Part. Phys. **28**, 2875 (2002).
[75] K. P. Santhosh, R. K. Biju, J. Phys. G: Nucl. Part. Phys. **36**, 015107 (2009).
[76] K. P. Santhosh, R. K. Biju, Pramana. J. Phys. **72**, 689 (2009).
[77] K. P. Santhosh and B. Priyanka, Phys. Rev. C **89**, 064604 (2014).

CHAPTER 3

Binary Fission

Binary fission is a common radioactive decay process, where the fissioning nucleus ends up into two fission fragments. In 1939, Hahn *et al.,* [1] discovered that the uranium atom was fragmented into two parts, which are more or less equal in size. Bohr and Wheeler [2] developed a theory of fission based on the liquid drop model. The authors gave a theory based on the usual ideas of penetration of potential barrier. Experimental studies of cold fission started in the early 80's by Signarbieux *et al.,* [3] Armbruster *et al.,* [4] and found that the relative yields of different fragmentation modes are governed by the available phase space of the system at scission, determined by the nuclear structure properties of the fragments. The cold spontaneous fission of many actinide nuclei into fragments with masses from 70 to 160 were observed and studied [5-9] and found that in these cold decays both the final fragments were in the ground states and confirmed the theoretical predictions by Sandulescu *et al.,* [10,11]. The first direct observation of cold fragmentation in the spontaneous fission of ^{252}Cf was carried out [7, 8] using the multiple Ge-detector Compact Ball facility at Oak Ridge National Laboratory where four pairs of neutronless fragmentations that of ^{104}Zr-^{148}Ce, ^{104}Mo-^{148}Ba, ^{106}Mo-^{146}Ba and ^{108}Mo-^{144}Ba were observed. Further in 1996 Sandulescu *et al.,* [12] and Dardenne *et al.,* [13] observed cold fragmentation in the spontaneous fission of ^{252}Cf with the Gammasphere consisting of 72 detectors where the correlations between the two fragments was observed clearly. Sandulescu *et al.,* [12] using a simple cluster model predicted correctly the most significant cold fragmentations observed in the spontaneous cold fission of the nucleus ^{252}Cf, where the double-folding potential barrier with the M3Y nucleon-nucleon forces gave the relative isotopic yields. The results were in good agreement with the experimental data [12, 14].

Ramayya *et al.,* [15] observed cold binary and ternary fission in the spontaneous fission of ^{252}Cf using triple gamma coincidence technique with Gammasphere and identified several correlated pairs whose yields were extracted. Gonnenwein *et al.,* [16] observed the presence of doubly magic ^{132}Sn fragment in the cold fission of ^{252}Cf, which was predicted some years ago by Kumar *et al.,* [17]. Moller *et al.,* [16,18] reported spontaneous decay of ^{252}Cf using a twin ionization chamber where two distinct mass regions of cold fission were observed: the first region includes the mass split 96/156 up to 114/138 and second one comprises only a narrow mass range around the mass split 120/132. Mirea *et al.,* [19] computed the cold fission path in the potential energy surface of ^{252}Cf by using the two-center shell model, based on the idea of the cold rearrangements of nucleons during the cold fission process and obtained a satisfactory agreement with experimental yields by considering variable mass and charge asymmetry beyond the first barrier of the potential surface. Mirea *et al.,* [19] analyzed the data obtained by Hambsch *et al.,* [5] from the cold fission yields of ^{252}Cf, and showed that the cold fission of ^{252}Cf is strongly connected with the cold valley of the doubly magic isotope ^{132}Sn.

The ground state decay properties (nuclear mass, deformation, α decay energy, α decay half-life, spontaneous fission half life etc.) of even-even isotopes of superheavy (SH) elements with Z = 104-170 has been studied by Smolanczuk [20] based on the macroscopic-microscopic model in which a multi dimensional deformation space describing axially symmetric nuclear shapes are used. Within the Hartree-Fock-Bogoliubov (HFB) approach with the finite-range and density-dependent Gogny force with the D1S parameter, a systematic study of 160 heavy and superheavy nuclei was performed by Warda *et al.,* [21] and the relevant properties of the ground state such as fission barrier, α decay energy, fission and α half lives were discussed. Staszczak *et al.,* [22] carried out self-consistent Skyrme-HFB calculations to predict main decay modes of even-even superheavy nuclei with $108 \leq Z \leq 126$ and $148 \leq N \leq 188$, to assess their lifetimes and estimated the center of enhanced stability in the superheavy region, thereby predicted the reflection-symmetric mode and the reflection-asymmetric mode as two spontaneous fission modes in superheavy nuclei. Poenaru *et al.,* [23] improved the accuracy of alpha and cluster decay half-life of superheavy element with Z >121 by using a semi-empirical formula for α decay and changing the parameters of analytical super asymmetric fission and of the universal curve for cluster decay. The authors improved the spontaneous fission half lives by using nuclear dynamics based on potential barriers computed by the macroscopic–microscopic method and employing various nuclear inertia variation laws. Poenaru *et al.,* [24,25] analyzed a way to improve the accuracy of evaluated spontaneous fission of nuclei in superheavy region by using the action integral based on cranking inertia and a potential barrier computed within the two-center shell model. The calculations in our work was done for Californium (Cf) nuclei which offer interesting possibilities for decay studies due to the closed shell effects of the daughter nucleus (^{48}Ca, ^{208}Pb, ^{132}Sn) that has been observed [26,27] and predicted [28-30]. On the other hand the usual (not cold) mass asymmetric fission of transuranium isotopes [31-33] has a very special property which was not entirely reproduced until now by any theoretical work. The mass of the heavier fraction of daughter products centers on a mass number of 136-144 regardless of the mass of the nuclei undergoing fission.

The formalism used for our calculations based on binary fission process is briefly described in the following section.

3.1 The Model

The binary fission is energetically possible only if Q value of the reaction is positive.

$$Q = M - \sum_{i=1}^{2} m_i > 0 \qquad (3.1.1)$$

Here M is the mass excess of the parent, m_i is the mass excess of the fragments. The interacting potential for a parent nucleus exhibiting binary fission is given by,

$$V = \frac{Z_1 Z_2 e^2}{r} + V_p(z) + \frac{\hbar^2 \ell(\ell+1)}{2\mu r^2} \quad \text{, for z > 0.} \qquad (3.1.2)$$

Here Z_1 and Z_2 are the atomic numbers of the binary fission fragments, 'z' is the distance between the near surfaces of the fragments, 'r' is the distance between fragment centers and is given as $r = z + C_1 + C_2$, where, C_1 and C_2 are the Süsmann central radii of fragments. The term ℓ represents the angular momentum, μ the reduced mass and V_P is the proximity potential. The proximity potential V_P is given by Blocki *et al.,* [34, 35] as,

$$V_p(z) = 4\pi\gamma b\left[\frac{C_1C_2}{(C_1+C_2)}\right]\Phi\left(\frac{z}{b}\right), \quad (3.1.3)$$

with the nuclear surface tension coefficient,

$$\gamma = 0.9517[1-1.7826(N-Z)^2/A^2] \text{ MeV/fm}^2, \quad (3.1.4)$$

where *N*, *Z* and *A* represent neutron, proton and mass number of parent respectively, Φ represents the universal proximity potential [35] given as,

$$\Phi(\varepsilon) = -4.41e^{-\varepsilon/0.7176}, \text{ for } \varepsilon > 1.947, \quad (3.1.5)$$

$$\Phi(\varepsilon) = -1.7817 + 0.9270\varepsilon + 0.0169\varepsilon^2 - 0.05148\varepsilon^3, \text{ for } 0 \le \varepsilon \le 1.9475 \quad (3.1.6)$$

with ε = *z/b*, where the width (diffuseness) of the nuclear surface $b \approx 1$ fm and Süsmann central radii C_i of fragments related to sharp radii R_i as,

$$C_i = R_i - \left(\frac{b^2}{R_i}\right) \quad (3.1.7)$$

For R_i we use semi empirical formula in terms of mass number A_i as [34],

$$R_i = 1.28A_i^{1/3} - 0.76 + 0.8A_i^{-1/3} \quad (3.1.8)$$

The potential for the internal part (overlap region) of the barrier is given as,

$$V = a_0(L-L_0)^n, \text{ for } z < 0 \quad (3.1.9)$$

Here $L = z + 2C_1 + 2C_2$ and $L_0 = 2C$, the diameter of the parent nuclei. The constants a_0 and *n* are determined by the smooth matching of the two potentials at the touching point.

Using one-dimensional WKB approximation, the barrier penetrability P is given as,

$$P = \exp\left\{-\frac{2}{\hbar}\int_a^b \sqrt{2\mu(V-Q)}dz\right\}$$

(3.1.10)

Here the mass parameter is replaced by $\mu = mA_1A_2/A$, where '*m*' is the nucleon mass and A_1, A_2 are the mass numbers of binary fission fragments respectively. The turning points 'a' and 'b' are determined from the equation $V(a) = V(b) = Q$.

The relative yield can be calculated as the ratio between the penetration probability of a given fragmentation over the sum of penetration probabilities of all possible fragmentation as follows,

$$Y(A_i, Z_i) = \frac{P(A_i, Z_i)}{\sum P(A_i, Z_i)} \quad (3.1.11)$$

3.2 Isotopic yield in cold binary fission of even-even $^{244-258}$Cf isotopes

Using the concept of cold reaction valley the binary fission of even-even $^{244-258}$Cf isotopes has been studied. In the study, the structure of minima in the driving potential is considered. The driving potential is defined as the difference between the interaction potential, V and the decay energy, Q of the reaction. Most of the Q values are calculated using experimental mass excesses of Wang *et al.,* [36] and some masses are taken from the table of KTUY [37]. The interaction potential is calculated as the sum of Coulomb and proximity potential. Next the driving potential ($V-Q$) for a particular parent nuclei is calculated for all possible fission fragments as a function of mass and charge asymmetries respectively given as $\eta = \frac{A_1 - A_2}{A_1 + A_2}$ and $\eta_Z = \frac{Z_1 - Z_2}{Z_1 + Z_2}$, at the touching configuration. For every fixed mass pair (A_1, A_2) a pair of charges is singled out for which the driving potential is minimized.

3.2.1 Cold reaction valley of even–even $^{244-258}$Cf isotopes

The driving potential for the touching configuration of fragments are calculated for the binary fragmentation of even-even $^{244-258}$Cf isotopes as the representative parent nucleus. **Figure 3.1 – Figure 3.4** represent the plots for driving potential versus A_1 (mass of one fragment) for even-even $^{244-258}$Cf isotopes respectively. The occurrences of the mass-asymmetry valleys in these figures are due to the shell effects of one or both the fragments. The fragment combinations corresponding to the minima in the potential energy will be the most probable binary fission fragments.

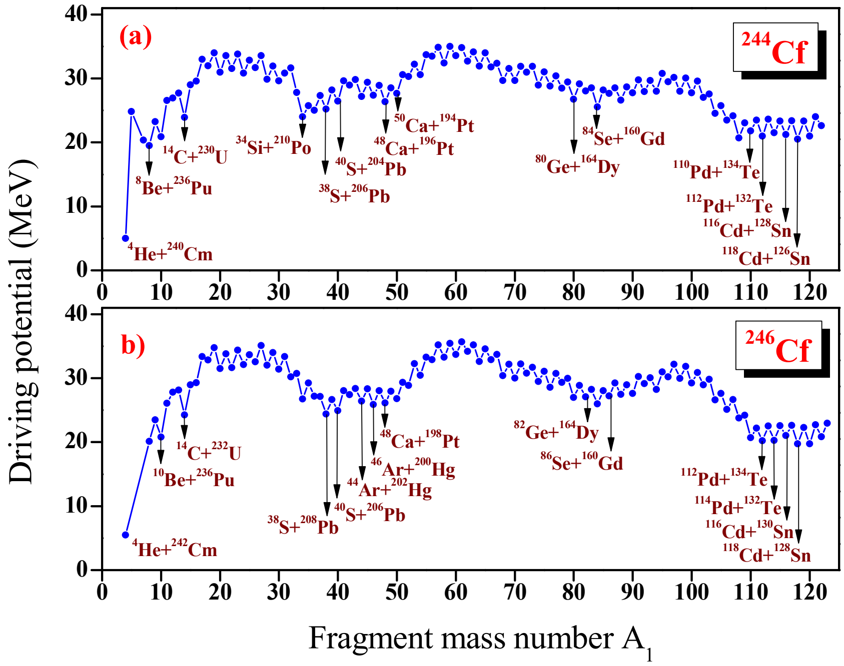

Figure 3.1. The driving potential for ^{244}Cf and ^{246}Cf isotope plotted as a function of mass number A_1.

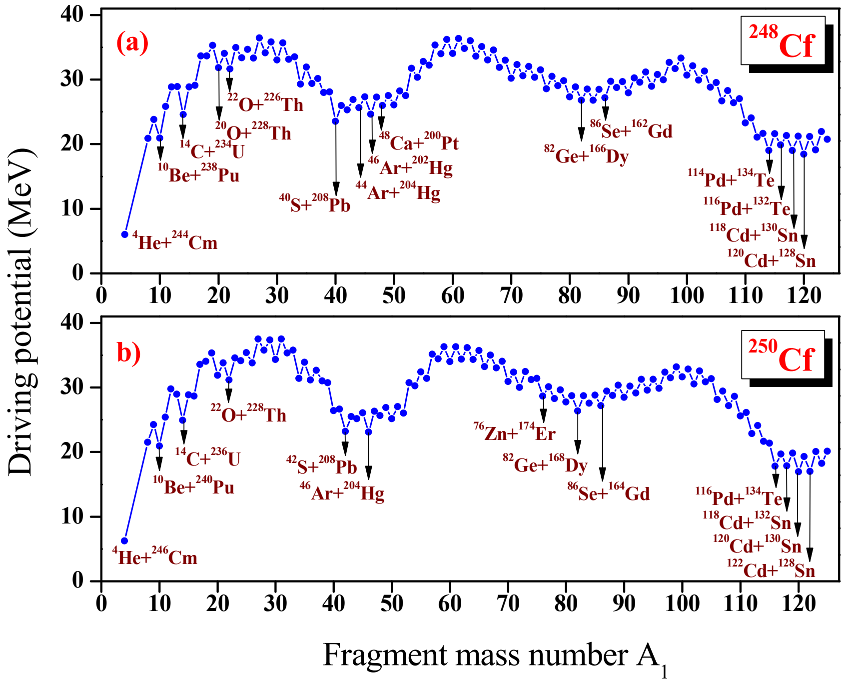

Figure 3.2. The driving potential for ^{248}Cf and ^{250}Cf isotope plotted as a function of mass number A_1.

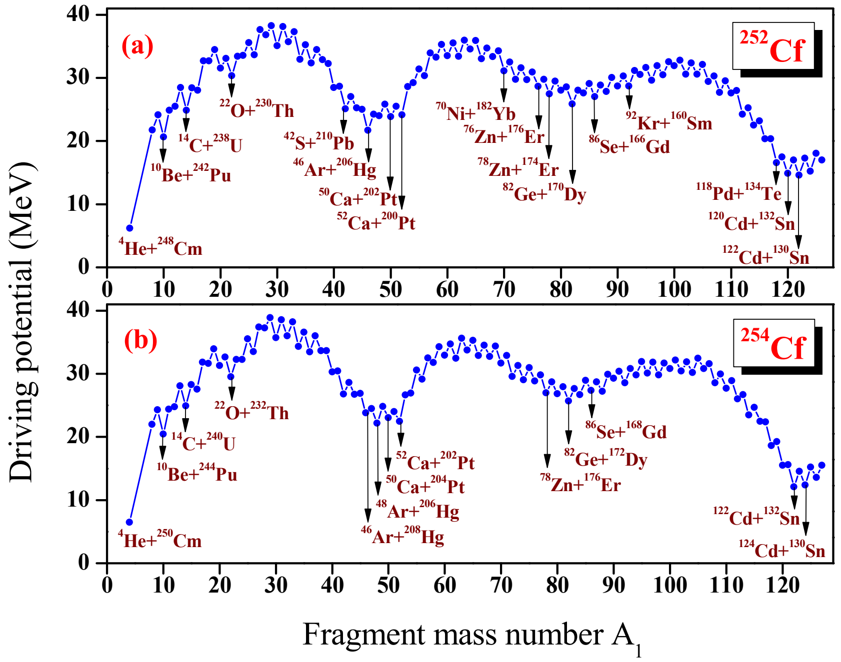

Figure 3.3. The driving potential for ^{252}Cf and ^{254}Cf isotope plotted as a function of mass number A_1.

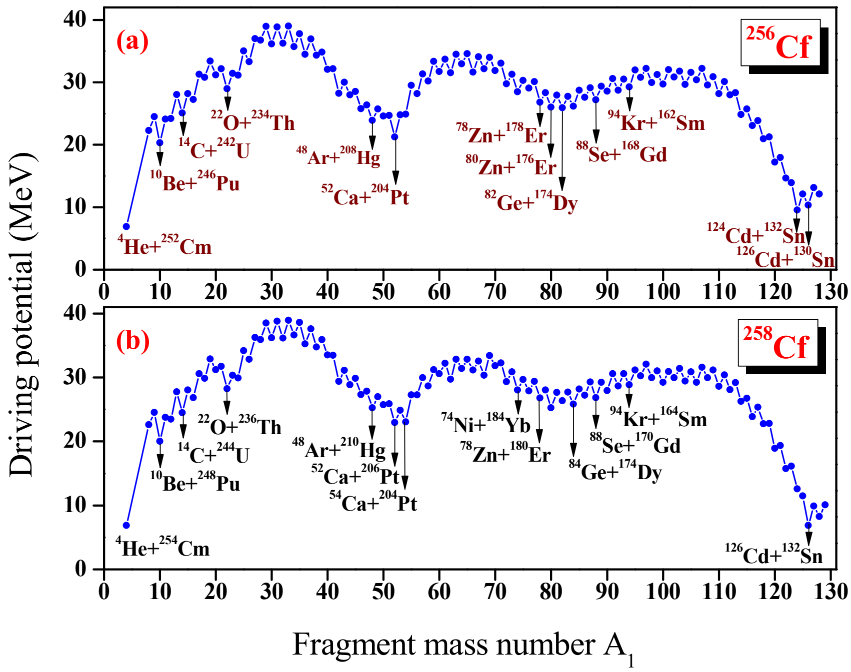

Figure 3.4. The driving potential for ^{256}Cf and ^{258}Cf isotope plotted as a function of mass number A_1.

From **Figure 3.1 – Figure 3.4** we found that the first minimum in each plot corresponds to the splitting ^{4}He+^{240}Cm, ^{4}He+^{242}Cm, ^{4}He+^{244}Cm, ^{4}He+^{246}Cm, ^{4}He+^{248}Cm, ^{4}He+^{250}Cm, ^{4}He+^{252}Cm and ^{4}He+^{254}Cm for even-even $^{244\text{-}258}$Cf isotopes respectively and these fragment combination shows the deepest minimum in the cold valley.

For ^{244}Cf in addition to the alpha particle ^{8,10}Be, ^{14}C, ^{34}Si, ^{38,40}S, ^{44}Ar, ^{48,50}Ca, ^{80}Ge, ^{84}Se, ^{88}Kr etc. are found to be the possible candidates for emission. Moving on to the fission region, there are three deep regions each consisting of few minima. For the first valley as one can see from **Figure 3.1 (a)**, the first minimum corresponds to the splitting ^{34}Si+^{210}Po, while the second and third minima correspond to the splitting ^{38}S+^{206}Pb and ^{40}S+^{204}Pb. The first minimum is due to the magic neutron shell N = 126 of ^{210}Po and magic neutron shell N = 20 of ^{34}Si, the second and third minimum is occurring due to the magic proton shell Z = 82 of ^{206}Pb and ^{204}Pb respectively. Other fragment combinations in this region are ^{48}Ca+^{196}Pt and ^{50}Ca+^{194}Pt, due to the presence of doubly magic ^{48}Ca (N = 28 and Z = 20) and proton shell closure Z = 20 of ^{50}Ca. In second valley the splitting ^{84}Se+^{160}Gd is due to the presence of magic shell N = 50 of ^{84}Se. In the case of the third valley, the first two minima involve ^{108}Ru+^{136}Xe and ^{110}Pd+^{134}Te splitting and therefore their occurrence is attributed to the presence of magic neutron shell N = 82 of ^{136}Xe and ^{134}Te. Other minima in this valley comes from the splitting ^{116}Cd+^{128}Sn, ^{118}Cd+^{126}Sn, ^{120}Cd+^{124}Sn and ^{122}Cd+^{122}Sn, due to the presence of Z = 50 magic shell.

Just as in the case of ^{244}Cf, even-even $^{246\text{-}258}$Cf isotopes also has three deep valleys in the fission regions each consisting of several comparable minima. In the first region the minima obtained for ^{246}Cf isotope is centered on doubly magic ^{208}Pb. For ^{248,250}Cf isotope, the minima is obtained for near doubly magic ^{204}Hg and doubly magic ^{208}Pb whereas for ^{252,254}Cf isotope the minima is obtained for ^{206}Hg and ^{50,52}Ca possessing magic shell N = 126 and Z = 20 respectively. The minima for ^{256}Cf isotope are at ^{208}Hg and ^{52}Ca whereas for ^{258}Cf isotope the minima are at ^{210}Hg and ^{52,54}Ca. In the second region the minima at ^{82}Ge and ^{84}Se due to magic shell N = 50 are found for ^{246,248,250}Cf isotope. For ^{252,254,256}Cf isotope, the minimum is found for ^{82}Ge whereas minimum at ^{80}Zn is obtained for ^{254,256,258}Cf isotopes. The minimum around Ni due to magic shell Z = 28 is obtained for ^{252,258}Cf isotope.

Finally, in the third valley the minimum at ^{132}Te is found for ^{246,248}Cf isotope whereas a nearly doubly magic nucleus ^{134}Te is obtained for ^{246,248,250,252}Cf isotope. Also in this region the minima is obtained around ^{126,128}Sn due to magic shell Z=50 for ^{246}Cf and around ^{132}Sn for ^{250,252,254,256,258}Cf isotope.

It is clear from **Figure 3.1 – Figure 3.4** that, as we move towards the symmetric fission region, we can see that the driving potential decreases with increase in mass number (ie. due to the increase in neutron number) of the parent nuclei. This is because in this region there is a chance for symmetric fission to occur (for e.g. ^{124}Sn + ^{124}Cd, ^{130}Sn + ^{128}Cd). This also stresses the role of double or near double magicity of the fragments. It is evident from **Figure 3.4 (a)** that in the case of ^{256}Cf isotope the minimum observed at ^{124}Cd+^{132}Sn is almost near to the deepest minimum found at ^{4}He+^{252}Cm whereas in the case of ^{258}Cf isotope it is clear from **Figure 3.4 (b)** that the minimum found at ^{126}Cd+^{132}Sn is comparable with that obtained at ^{4}He+^{254}Cm.

3.2.2 Barrier penetrability and yield calculation

The barrier penetrability for each charge minimized fragment combinations found in the cold valley for even–even $^{244\text{-}258}$Cf isotopes are calculated using the formalism described above. The relative yield is calculated and is plotted as a function of fragment mass number A_1 and A_2 in **Figure 3.5 – Figure 3.8**. The most favourable fragment combinations for all the eight isotopes mentioned above are obtained by calculating their relative yield. From **Figure 3.5(a)**, it is clear that for ^{244}Cf, the combination ^{36}S+^{208}Pb possesses highest yield due to the presence of doubly magic nuclei ^{208}Pb (N = 126, Z = 82). The next higher yield can be observed for the ^{34}Si+^{210}Po combination and is due to the near doubly magic ^{210}Po (N = 126, Z = 84). The various other fragment combinations observed in this binary fission of parent nuclei ^{244}Cf are ^{68}Ni+^{176}Yb, ^{70}Ni+^{174}Yb, ^{108}Ru+^{136}Xe, ^{110}Pd+^{134}Te. Of these the first and second one are attributed to the magic shell Z = 28 of Ni while the third fragment combination is due to the presence of neutron shell closure at N = 82 of ^{136}Xe. The fragment combination with ^{134}Te is due to the near double magicity Z = 52 and N = 82. The splitting ^{116}Cd+^{128}Sn, ^{118}Cd+^{126}Sn and ^{120}Cd+^{124}Sn are due to the presence of magic number Z = 50 of Sn.

In the case of ^{246}Cf isotope, ^{38}S+^{208}Pb is the most favoured binary splitting and it is due to the presence of doubly magic ^{208}Pb (Z = 82, N = 126). The next higher yield is observed for the ^{40}S+^{206}Pb combination and is due to the near doubly magic ^{206}Pb (N = 124, Z = 82). The various fragment combinations found in the binary fission process are ^{34}Si+^{212}Po, ^{46}Ar+^{200}Hg, ^{48}Ca+^{198}Pt, ^{110}Ru+^{136}Xe, ^{112}Pd+^{134}Te, ^{114}Pd+^{132}Te ^{118}Cd+^{128}Sn, ^{120}Cd+^{126}Sn and ^{122}Cd+^{124}Sn. The first combination is due to the near doubly magic ^{212}Po (N = 128, Z = 84). The second combination is due to neutron shell closure N= 28 of ^{46}Ar and also due to near proton shell closure Z= 80 of ^{200}Hg. The third combination is due to doubly magic ^{48}Ca (Z = 20, N = 28). The fourth combination is due to neutron shell closure N=82 of ^{136}Xe. The fifth and sixth combinations are due to the near doubly magic ^{134}Te (N = 82, Z = 52) and ^{132}Te (N = 80, Z = 52) respectively. The last three combinations are attributed to the magic shell closure at Z = 50 of ^{128}Sn, ^{126}Sn and ^{124}Sn respectively.

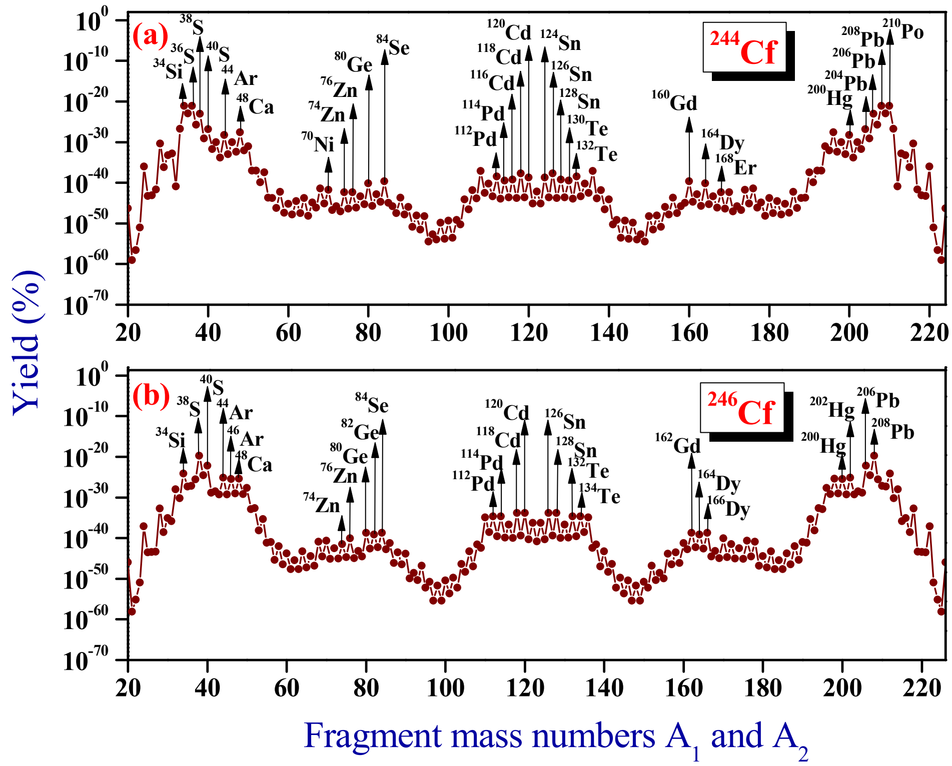

Figure 3.5. The relative yields plotted as a function of mass numbers A_1 and A_2 for ^{244}Cf and ^{246}Cf isotope. The fragment combinations with higher yields are labelled.

For ^{248}Cf isotope, the highest yield is obtained for the fragment combination $^{40}S+^{208}Pb$ due to the presence of doubly magic ^{208}Pb (N = 126, Z = 82). The next higher yields are for the fragment combinations $^{46}Ar+^{202}Hg$, $^{44}Ar+^{204}Hg$ and $^{48}Ca+^{200}Pt$ which possess the neutron shell closure N = 28 of ^{46}Ar, near proton shell closure Z = 80 of ^{202}Hg, near doubly magic shell of ^{204}Hg (N = 124, Z = 80) and the doubly magic ^{48}Ca (N = 28, Z = 20). The various fragment combinations that occur in this binary fission process are $^{34}Si+^{214}Po$, $^{70}Ni+^{178}Yb$, $^{72}Ni+^{176}Yb$ and $^{78}Zn+^{170}Er$. These splitting are due to the neutron shell closure at N = 20 of ^{34}Si, near proton shell closure at Z = 84 of ^{214}Po, proton shell closure at Z = 28 of Ni and near neutron shell closure N = 48 of ^{78}Zn respectively.

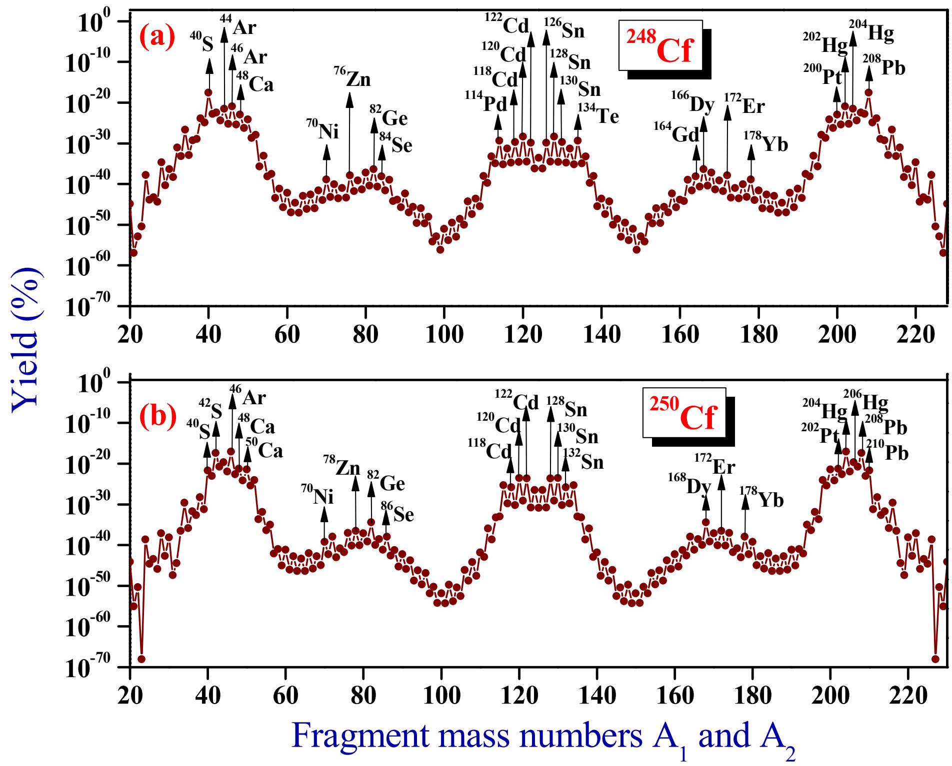

Figure 3.6. The relative yields plotted as a function of mass numbers A_1 and A_2 for ^{248}Cf and ^{250}Cf isotope. The fragment combinations with higher yields are labelled.

In the case of ^{250}Cf isotope, the highest yield is obtained for the fragment combination $^{46}Ar+^{204}Hg$ due to the presence of nearly doubly magic ^{204}Hg (N = 124, Z = 80). The next higher yields are for the fragment combinations $^{42}S+^{208}Pb$, $^{44}Ar+^{206}Hg$, $^{40}S+^{210}Pb$, $^{48}Ca+^{202}Pt$ and $^{50}Ca+^{200}Pt$. It is due to the doubly magic ^{208}Pb

(N = 126, Z = 82), magic shell N = 126 of ^{206}Hg, magic shell Z=82 of ^{210}Pb, doubly magic ^{48}Ca (N = 28, Z = 20), magic shell Z = 20 of ^{50}Ca. For ^{252}Cf isotope, the highest yield is obtained for the fragment combination ^{46}Ar+^{206}Hg due to the presence of nearly doubly magic ^{206}Hg (N = 126, Z = 80). The next higher yields are for the fragment combinations ^{122}Cd+^{130}Sn, ^{120}Cd+^{132}Sn, ^{50}Ca+^{202}Pt, ^{124}Cd+^{128}Sn and ^{42}S+^{210}Pb. It is due to the magic shell Z = 50 of ^{130}Sn, doubly magic ^{132}Sn (N = 82, Z = 50), magic shell Z = 20 of ^{50}Ca, Z = 50 of ^{128}Sn, Z = 82 of ^{210}Pb.

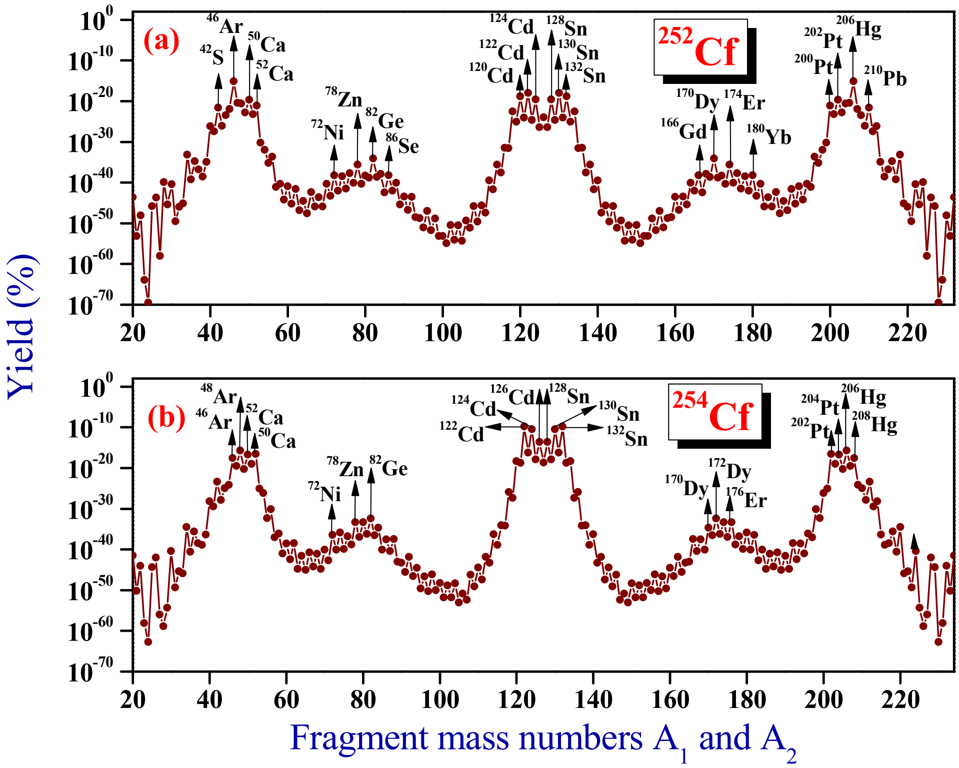

Figure 3.7. The relative yields plotted as a function of mass numbers A_1 and A_2 for ^{252}Cf and ^{254}Cf isotope. The fragment combinations with higher yields are labelled.

In the case of ^{254}Cf isotope, the highest yield is obtained for the fragment combination ^{122}Cd+^{132}Sn due to the presence of doubly magic ^{132}Sn (N = 82, Z = 50). The next higher yields are for the fragment combinations ^{124}Cd+^{130}Sn, ^{126}Cd+^{128}Sn, ^{48}Ar+^{206}Hg, ^{50}Ca+^{204}Pt, ^{52}Ca+^{202}Pt and ^{46}Ar+^{208}Hg. The first two combinations are due to magic shell Z = 50 of ^{130}Sn and ^{128}Sn whereas third one is due to neutron shell closure N = 126 and near proton shell closure Z = 80 of ^{206}Hg. The combination ^{50}Ca+^{204}Pt is due to proton shell closure Z = 20 of ^{50}Ca and neutron shell closure

N= 126 of ^{204}Pt. The splitting ^{52}Ca+^{202}Pt is due to proton shell closure Z = 20 of ^{52}Ca and near neutron shell closure N=124 of ^{202}Pt. The last combination is due to near doubly magic ^{208}Hg (N=128, Z=80). For ^{256}Cf isotope, the highest yield is obtained for the fragment combination ^{124}Cd+^{132}Sn due to the presence of doubly magic ^{132}Sn (N = 82, Z = 50). The next higher yields are for the fragment combinations ^{126}Cd+^{130}Sn, ^{128}Cd+^{128}Sn, ^{52}Ca+^{204}Pt, ^{122}Pd+^{134}Te, ^{48}Ar+^{208}Hg and ^{46}Ar+^{210}Hg. The first two combinations are due to magic shell Z = 50 of ^{130}Sn and ^{128}Sn. The splitting ^{52}Ca+^{204}Pt and ^{122}Pd+^{134}Te are due to proton shell closure Z = 20 of ^{52}Ca, neutron shell closure N = 126 of ^{204}Pt and near doubly magic ^{134}Te (N = 82, Z = 52). The last combinations are due to near proton shell closure (Z=80) of ^{208,210}Hg.

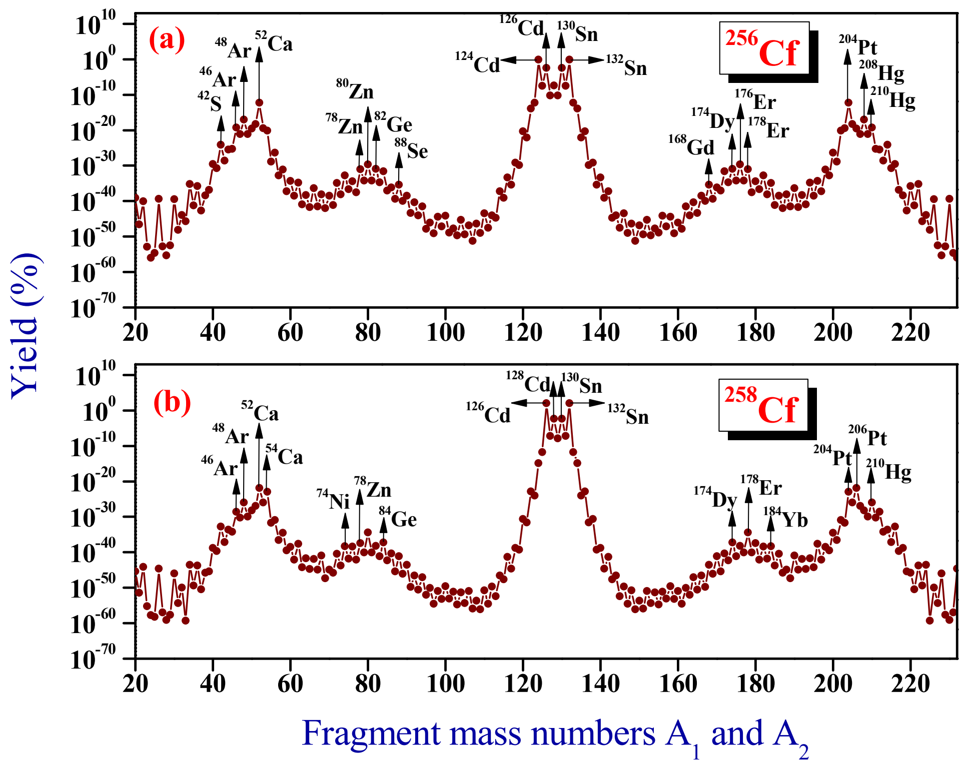

Figure 3.8. The relative yields plotted as a function of mass numbers A_1 and A_2 for ^{256}Cf and ^{258}Cf isotope. The fragment combinations with higher yields are labelled.

In the case of ^{258}Cf isotope, the fragment combination ^{126}Cd+^{132}Sn possesses the highest yield due to the presence of doubly magic ^{132}Sn (N = 82, Z = 50). The next higher yields are for the fragment combinations ^{128}Cd+^{130}Sn, ^{124}Cd+^{134}Sn, ^{52}Ca+^{206}Pt, ^{54}Ca+^{204}Pt, ^{48}Ar+^{210}Hg and ^{46}Ar+^{212}Hg. The first two combinations are due to magic shell Z = 50 of ^{130}Sn and ^{134}Sn. The combination ^{52}Ca+^{206}Pt is due to proton shell closure Z = 20 of ^{52}Ca and near neutron shell closure N = 128 of ^{206}Pt. The splitting ^{54}Ca+^{204}Pt is due to proton shell closure Z = 20 of ^{54}Ca and neutron shell closure N = 126 of ^{204}Pt. The last two combinations are due to near proton shell closure Z = 80 of ^{210,212}Hg and neutron shell closure N = 28 of ^{46}Ar.

In **Figure 3.9**, we have compared the individual yields obtained for the cold fission of ^{252}Cf isotope with the experimental data taken from the γ-γ-γ coincidences technique using Gammasphere [12, 14].

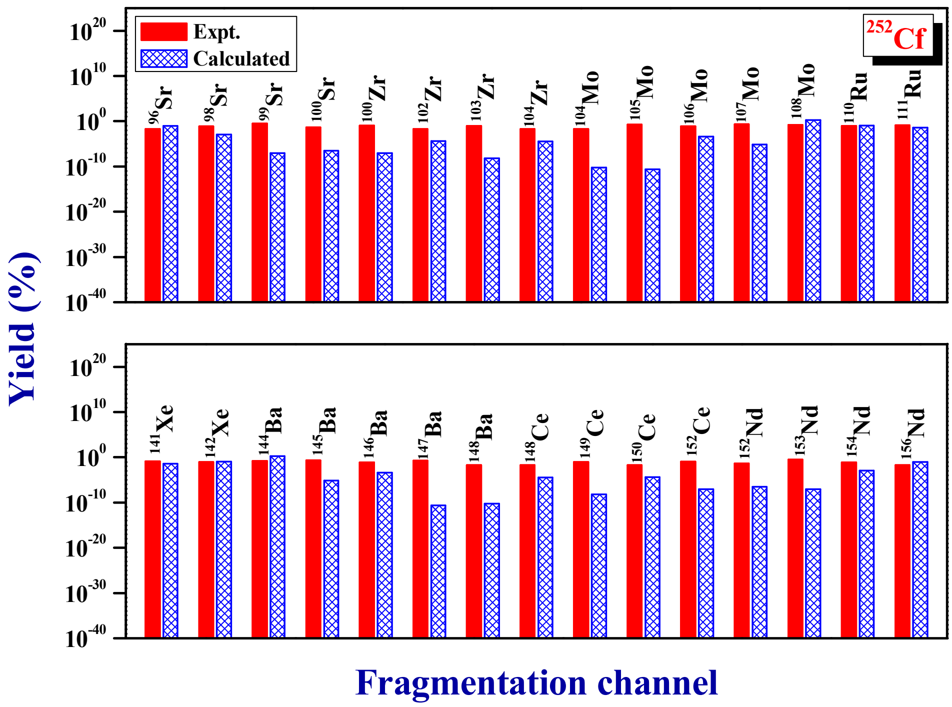

Figure 3.9. The yields obtained for the cold fission of ^{252}Cf isotope and their comparison with the experimental data [12, 14].

Our work reveals that, the presence of doubly magic or near doubly magic nuclei plays an important role in the binary fission of even-even $^{244\text{-}258}$Cf isotopes. It is found that the magnitude of the relative yield increases with increase in mass number (ie. due to the increase in neutron number) of the parent nuclei. Also it is found that highest yield for ^{244,246,248}Cf isotopes are for the fragments with isotope of Pb (Z=82) as one fragment, whereas for ^{250}Cf and ^{252}Cf isotopes the highest yield is for the fragments with isotope of Hg (Z=80) as one fragment. The highest yield (or minima in the cold reaction valley) associated with ^{208}Pb daughter can be interpreted as a heavy particle radioactivity [38-41]. In the case of ^{254,256,258}Cf isotopes the highest yield is for the fragments with Sn (Z=50) as one fragment. It is found that for the binary fragmentation of ^{244,246,248,250}Cf isotopes, asymmetric splitting is dominant and in the case of ^{254,256,258}Cf isotopes symmetric splitting is dominant. In the case of ^{252}Cf isotope, the highest yield is for the fragment combination ^{46}Ar+^{206}Hg, which corresponds to asymmetric splitting whereas the second highest yield is obtained for the fragmentation ^{122}Cd+^{130}Sn that corresponds to symmetric splitting. Hence, we can say that both asymmetric splitting and symmetric splitting are favourable for the binary fission of ^{252}Cf isotope.

3.2.3 Summary

The binary fragmentation of even-even $^{244-258}$Cf isotopes has been studied by taking Coulomb and proximity potential as interacting barrier. In each case, the fragmentation potential and Q-values are calculated for all possible fission components, which reveal that, the even mass number fragments are more favoured than odd mass number fragments. The favourable fragment combinations are obtained by calculating the relative yield. It is found that highest yield for ^{244,246,248}Cf isotopes are for the fragments with isotope of Pb (Z=82) as one fragment, whereas for ^{250}Cf and ^{252}Cf isotopes the highest yield is for the fragments with isotope of Hg (Z=80) as one fragment. In the case of ^{254,256,258}Cf isotopes, the highest yield are for the fragments with Sn (Z=50) as one fragment. This reveals the role of doubly magic and near doubly magic shell closures (of ^{48}Ca, ^{132}Sn, ^{134}Te, ^{204}Hg and ^{208}Pb) in binary fission.

3.3 Studies on cold binary fragmentation of even–even $^{238-248}$Pu isotopes

In this work, we have considered even-even plutonium isotopes with the mass numbers A = 238, 240, 242, 244, 246 and 248, and estimated the yield in the binary fragmentation of above isotopes using two version of nuclear proximity potential, proximity 1977 and proximity 2000, by minimizing the fragmentation potential with respect to the mass and charge asymmetries. The calculations in this work have been carried out for plutonium (Pu) nuclei, where the plutonium isotopes, provide a very valuable set of nuclides to investigate the influence of the neutron number of the compound nucleus on the mass and energy characteristics of the fission fragments, including shell effects. The calculated relative yield using Proximity 1977 and Proximity 2000 are compared with the experimental values obtained from Wagemans *et al.,* [42]. The formalism used in the Proximity 2000 is briefly described in the following section.

3.3.1 Proximity potential 2000

Myers and Swiatecki [43] modified equation (3.1.3) by using the latest knowledge of nuclear radii and surface tension coefficients using their concept of droplet model. The important aim behind this effort was to eliminate the disagreement in the case of barrier height between the results of Proximity 1977 and experimental data [43]. Using the droplet model [44], matter radius C_i was calculated as,

$$C_i = c_i + \frac{N_i}{A_i} t_i \qquad (i = 1, 2), \qquad (3.3.1)$$

where c_i denotes the half-density radii of the charge distribution and t_i is the neutron skin of the nucleus. The nuclear charge radius (denoted as R_{00} in Ref. [45]), is given by the relation:

$$R_{00i} = \sqrt{5/3}\left\langle r^2 \right\rangle^{1/2}$$

$$= 1.240\, A_i^{1/3} \left\{ 1 + \frac{1.646}{A_i} - 0.191 \left(\frac{A_i - 2Z_i}{A_i} \right) \right\} \text{fm} \quad (i=1, 2) \qquad (3.3.2)$$

where $\langle r^2 \rangle$ represents the mean-square nuclear charge radius. According to Ref. [45], equation (3.3.2) was valid for the even-even nuclei with $8 \le Z < 38$ only. For nuclei with $Z \ge 38$, the above equation was modified by Pomorski *et al.,* [45] as

$$R_{00i} = 1.256\, A_i^{1/3} \left\{ 1 - 0.202 \left(\frac{A_i - 2Z_i}{A_i} \right) \right\} \text{ fm} \qquad (i = 1, 2) \tag{3.3.3}$$

These expressions give good estimate of the measured mean square nuclear charge radius $\langle r^2 \rangle$. The half-density radius, c_i was obtained from the relation:

$$c_i = R_{00i} \left(1 - \frac{7}{2} \frac{b^2}{R_{00i}{}^2} - \frac{49}{8} \frac{b^4}{R_{00i}{}^4} + ... \right), \qquad (i = 1, 2) \tag{3.3.4}$$

Using the droplet model [44], neutron skin t_i reads as

$$t_i = \frac{3}{2} r_0 \left(\frac{JI_i - \frac{1}{12} c_1 Z_i A_i^{-1/3}}{Q + \frac{9}{4} J A_i^{-1/3}} \right), \qquad (i = 1, 2) \tag{3.3.5}$$

Here r_0 is 1.14 fm, the value of nuclear symmetric energy coefficient J = 32.65 MeV, and $c_1 = 3e_2/5r_0$ = 0.757895 MeV. The neutron skin stiffness coefficient Q was taken to be 35.4 MeV. The nuclear surface energy coefficient γ in terms of neutron skin was given as,

$$\gamma = \frac{1}{4\pi r_0^2} \left[18.63(MeV) - Q \frac{(t_1^2 + t_2^2)}{2r_0^2} \right], \tag{3.3.6}$$

where t_1 and t_2 were calculated using equation (3.3.5). The universal function $\Phi(\xi)$ was reported as,

$$\Phi(\xi) = \left\{ -0.1353 + \sum_{n=0}^{5} \left[\frac{c_n}{n+1} \right] (2.5 - \xi)^{n+1} \right\} \quad \text{for} \quad 0 < \xi \le 2.5$$
$$\Phi(\xi) = -0.09551 \exp[(2.75 - \xi)/0.7176] \quad \text{for} \quad \xi \ge 2.5 \tag{3.3.7}$$

The values of different constants c_n were $c_0 = -0.1886$, $c_1 = -0.2628$, $c_2 = -0.15216$, $c_3 = -0.04562$, $c_4 = 0.069136$, and $c_5 = -0.011454$. For $\xi > 2.74$, the above exponential expression is the exact representation of the Thomas-Fermi extension of the proximity potential. This potential is labelled as Proximity 2000.

3.3.2 Cold reaction valley of even–even $^{238\text{-}248}$Pu isotopes

In the case of binary fission of even-even $^{238\text{-}248}$Pu isotopes, its driving potential for the touching configuration of fragment combinations are calculated. **Figure 3.10 – Figure 3.12** represent the plots for driving potential versus A_1 (mass of one fragment) for all the above isotopes. The occurrences of the mass-asymmetry valleys in these figures are due to the shell effects of one or both the fragments. The fragment combinations having minima in the potential energy are the most probable binary fission fragments. From **Figure 3.10 – Figure 3.12**, we noticed that the first minimum in each plot corresponds to the splitting ^{4}He+^{234}U, ^{4}He+^{236}U, ^{4}He+^{238}U, ^{4}He+^{240}U, ^{4}He+^{242}U and ^{4}He+^{244}U and these fragment combination shows the deepest minimum in the cold valley. For ^{238}Pu apart from the alpha particle ^{10}Be, ^{26}Ne, ^{28,30}Mg, ^{34}Si, ^{46}Ar, ^{50,52}Ca, ^{80,82}Ge, ^{84,86}Se, ^{104}Mo, ^{108,110}Ru etc. are seen to be possible for emission. Two deep regions are observed in the fission region both having comparable minima. The minimum in the first region corresponds to the splitting ^{30}Mg+^{208}Pb and ^{34}Si+^{204}Hg, whereas, that in the second region is due to the splitting ^{104}Mo+^{134}Te and ^{108}Ru+^{130}Sn. The driving potential values for the above combinations lies very close to each other. We noticed that the four mentioned combinations include doubly or nearly doubly magic nuclei, ^{208}Pb (N = 126, Z = 82), ^{204}Hg (N = 124, Z = 80), ^{134}Te (N = 82, Z = 52) and ^{130}Sn (N = 80, Z = 50). All the other isotopes also have deep valleys in the fission regions each having several comparable minima. The minima obtained for ^{240,242}Pu isotope in the first region are at ^{208,210,212}Pb and ^{204,206}Hg where these minima corresponds to the doubly magic ^{208}Pb (N = 126, Z = 82) and near doubly magic ^{204}Hg (N = 124, Z = 80), ^{206}Hg (N = 126, Z = 80) and ^{210}Pb (N = 128, Z = 82). For ^{242,244,246}Pu isotope, the minima are observed at ^{46}Ar (N = 28), ^{204}Pt (N = 126) that possesses neutron shell closure and also at ^{206,208}Hg, a near doubly magic nuclei. For ^{246,248}Pu isotope, minima are obtained at ^{52}Ca, ^{46}Ar and ^{200,202}Os. In the second region the minima at ^{82}Ge, ^{84}Se and ^{80}Zn due to magic shell N=50 are found for various isotopes. Other minima are found at ^{78}Zn, ^{84}Ge and ^{86}Se for ^{242,244,246}Pu isotopes. Finally, in the third valley the minimum at ^{134}Te is found for ^{240,242,244}Pu isotope whereas a doubly magic nucleus ^{132}Sn is obtained for ^{240,242,244,246,248}Pu isotope. Also in this region the minima is obtained around ^{128,130}Sn due to magic shell Z=50 for plutonium isotopes.

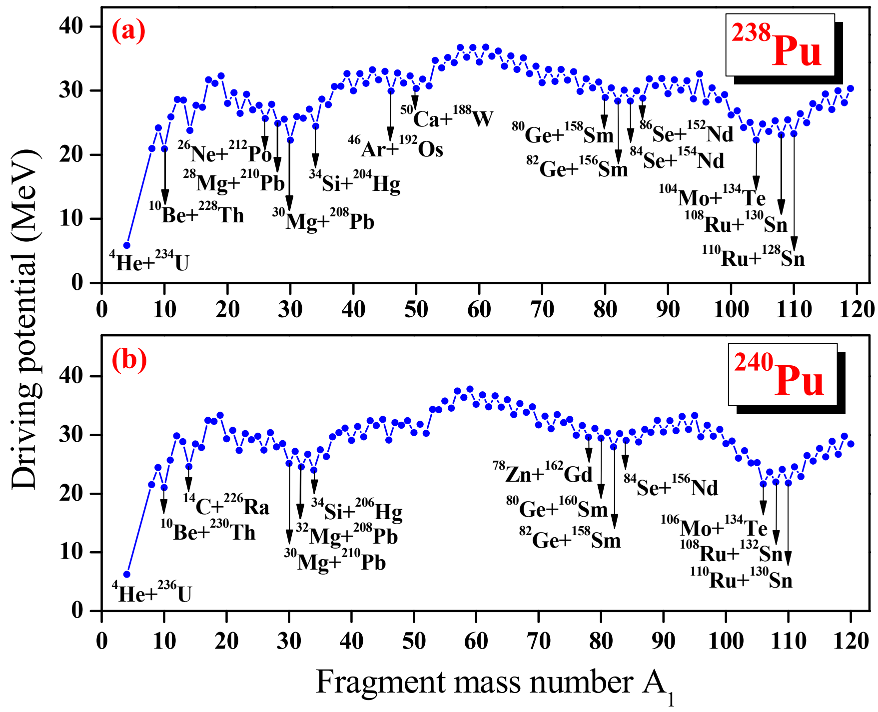

Figure 3.10. The driving potential for ^{238}Pu and ^{240}Pu isotope plotted as a function of mass number A_1.

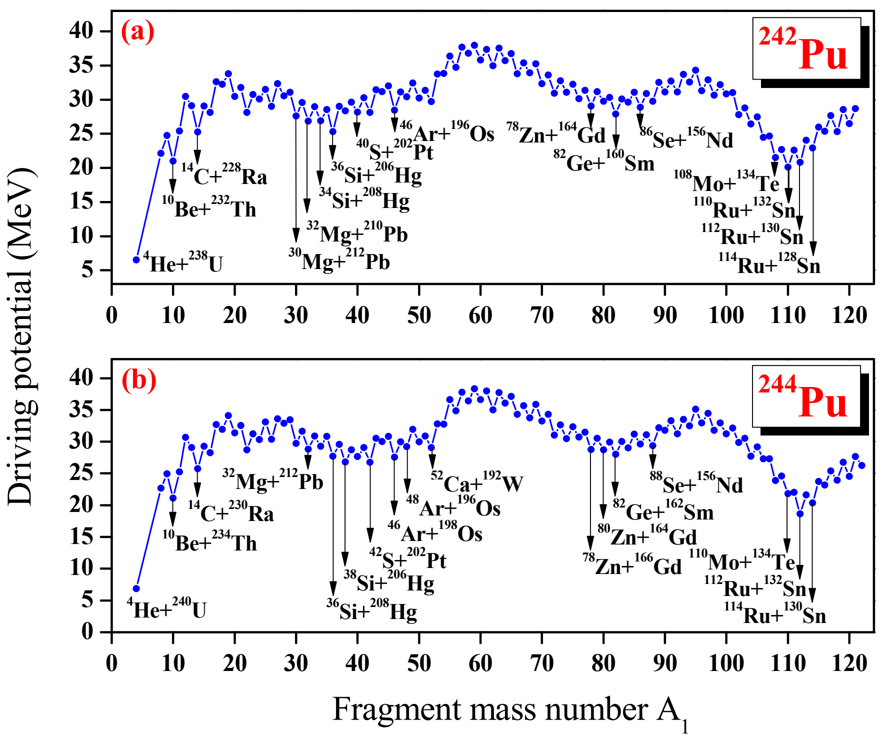

Figure 3.11. The driving potential for ^{242}Pu and ^{244}Pu isotope plotted as a function of mass number A_1.

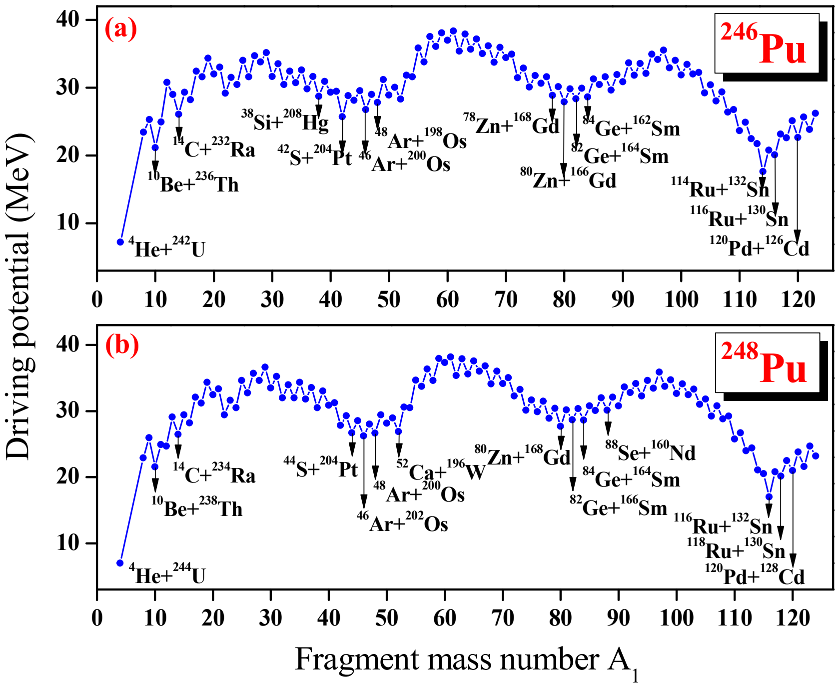

Figure 3.12. The driving potential for ^{246}Pu and ^{248}Pu isotope plotted as a function of mass number A_1.

From **Figure 3.10 – Figure 3.12**, it is clear that, towards the symmetric fission region, the driving potential decreases with increase in mass number (i.e. due to the increase in neutron number) of the parent nuclei. Also a noticeable difference in driving potential was observed for the combinations of different isotopes in the cold fission valleys.

3.3.3 Barrier penetrability and yield calculation

The barrier penetrability for each fragment combinations found in the cold valley for even-even $^{238\text{-}248}$Pu isotopes are calculated using Proximity 1977. The most favourable fragment combinations for all the six isotopes mentioned above are obtained by calculating their relative yield. For a better comparison of barrier penetrability and relative yield, calculations are carried out for all the isotopes using proximity 2000 also. The relative yield is calculated and is plotted as a function of fragment mass number A_1 and A_2 and is shown in **Figure 3.13 – Figure 3.18**.

For ^{238}Pu, the combination ^{30}Mg+^{208}Pb possesses highest yield due to the presence of doubly magic nuclei ^{208}Pb (N = 126, Z = 82).

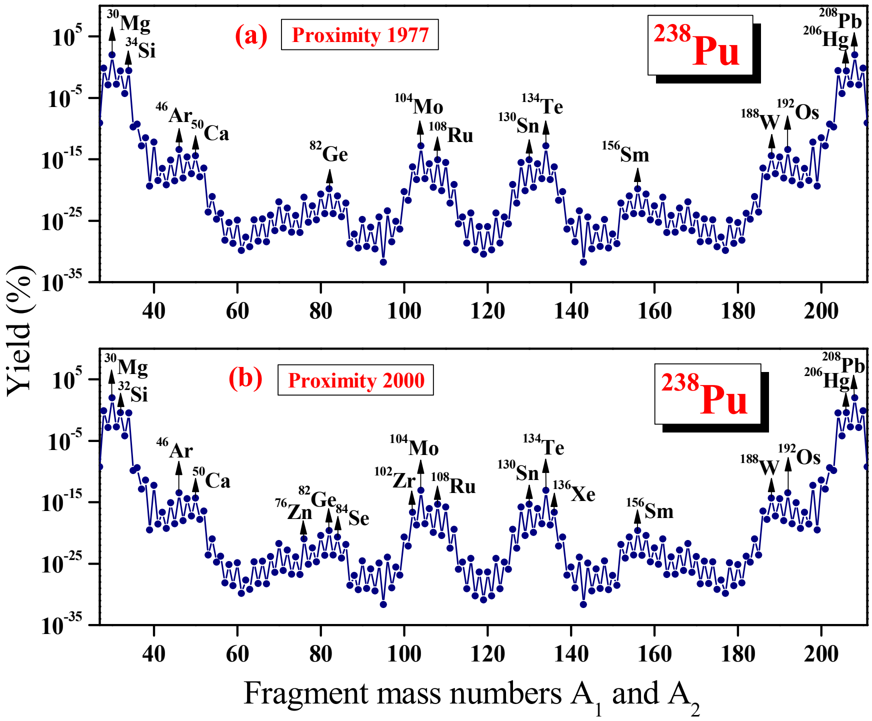

Figure 3.13. The relative yield plotted as a function of mass numbers A_1 and A_2 for ^{238}Pu isotope using proximity 1977 and proximity 2000. The fragment combinations with higher yields are labelled.

The next higher yield can be observed for the ^{28}Mg+^{210}Pb due to the near doubly magic ^{210}Pb (N = 128, Z = 82). The various other fragment combinations observed in this binary fission of parent nuclei ^{238}Pu are ^{34}Si+^{204}Hg, ^{32}Si+^{206}Hg, ^{36}Si+^{202}Hg, ^{38}S+^{200}Pt, ^{40}S+^{198}Pt, ^{46}Ar+^{192}Os and ^{50}Ca+^{188}W. Of these, the first three are attributed to the near proton shell closure Z = 80 of Hg. The splitting ^{46}Ar+^{192}Os and ^{50}Ca+^{188}W are due to the presence of magic number N=28 of Ar and Z= 20 of Ca respectively.

In the case of ^{240}Pu isotope, ^{34}Si+^{206}Hg is the most favoured binary splitting and it is due to the presence of near doubly magic ^{206}Hg (N =126, Z = 80). Other favoured channels for the binary fission of ^{240}Pu isotope are, ^{30}Mg+^{210}Pb, ^{32}Mg+^{208}Pb, ^{28}Mg+^{212}Pb, ^{36}Si+^{204}Hg, ^{40}S+^{200}Pt, ^{38}S+^{202}Pt, ^{46}Ar+^{194}Os and ^{24}Ne+^{216}Po as ordered from the most to the less probable ones. As can be noticed, these favoured channels include the doubly magic ^{208}Pb, near doubly magic ^{210}Pb, proton shell closure Z=82 of ^{212}Pb, near doubly magic ^{204}Hg, neutron shell closure N=28 of ^{46}Ar.

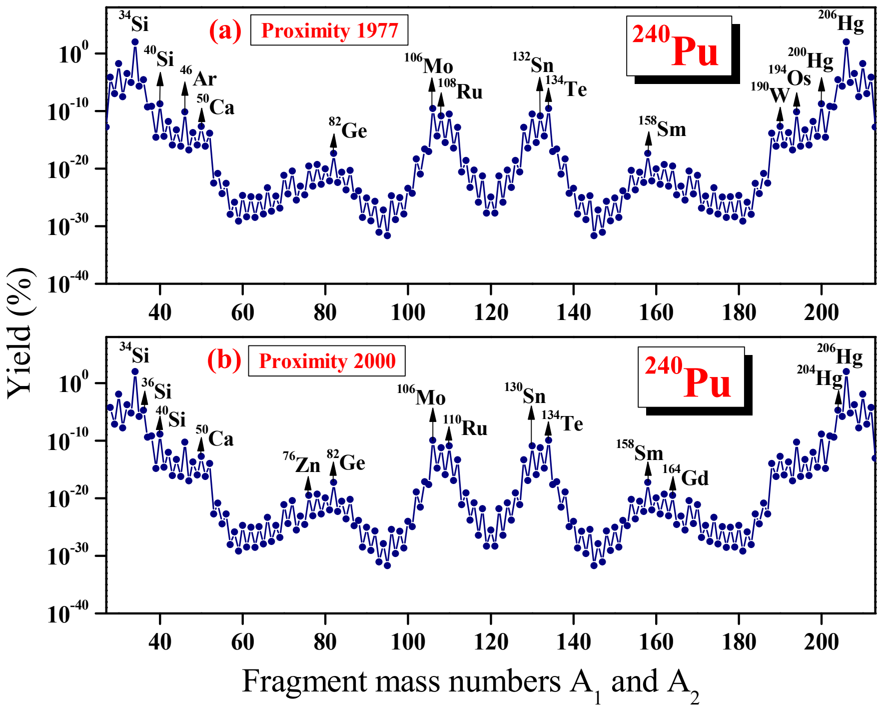

Figure 3.14. The relative yield plotted as a function of mass numbers A_1 and A_2 for ^{240}Pu isotope using proximity 1977 and proximity 2000. The fragment combinations with higher yields are labelled.

The fragmentation channels that are predicted to be the most favourable ones in the binary fission of ^{242}Pu isotope are ^{36}Si+^{206}Hg, ^{34}Si+^{208}Hg, ^{110}Ru+^{132}Sn, ^{30}Mg+^{212}Pb, ^{40}S+^{202}Pt, ^{112}Ru+^{130}Sn, ^{32}Mg+^{210}Pb, ^{42}S+^{200}Pt and ^{46}Ar+^{196}Os as ordered from the most to the less probable ones. It is noticed that these channels contain a near doubly magic ^{206,208}Hg, doubly magic nuclei ^{132}Sn, proton shell closure Z=82 of ^{210,212}Pb and proton shell closure Z=50 of ^{130}Sn.

In the case of ^{244}Pu isotope, more yield is obtained for the symmetric fragment combination ^{112}Ru+^{132}Sn due to the presence of doubly magic ^{132}Sn (N = 82, Z = 50). The next higher yields are for the fragment splitting ^{40}S+^{204}Pt, ^{42}S+^{202}Pt, ^{114}Ru+^{130}Sn, ^{46}Ar+^{198}Os, ^{36}Si+^{208}Hg, ^{38}Si+^{206}Hg, ^{110}Mo+^{134}Te, ^{30}Mg+^{214}Pb and ^{48}Ar+^{196}Os. It is due to the neutron shell closure of ^{204}Pt (N = 126, Z = 78) and ^{46}Ar (N = 28, Z = 18), near doubly magic ^{130}Sn, ^{206,208}Hg and ^{134}Te, proton shell closure Z=82 of ^{214}Pb.

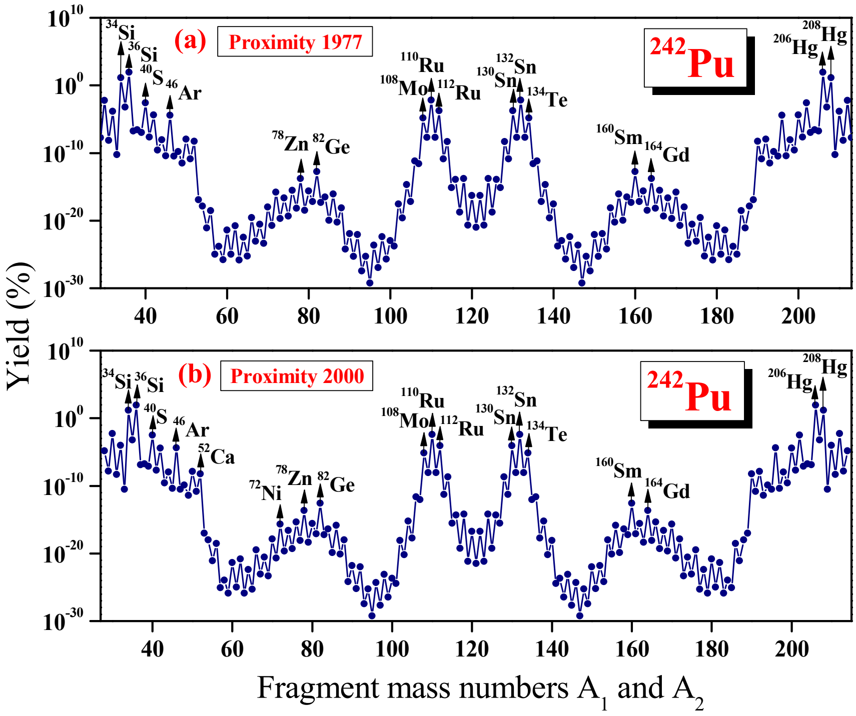

Figure 3.15. The relative yield plotted as a function of mass numbers A_1 and A_2 for ^{242}Pu isotope using proximity 1977 and proximity 2000. The fragment combinations with higher yields are labelled.

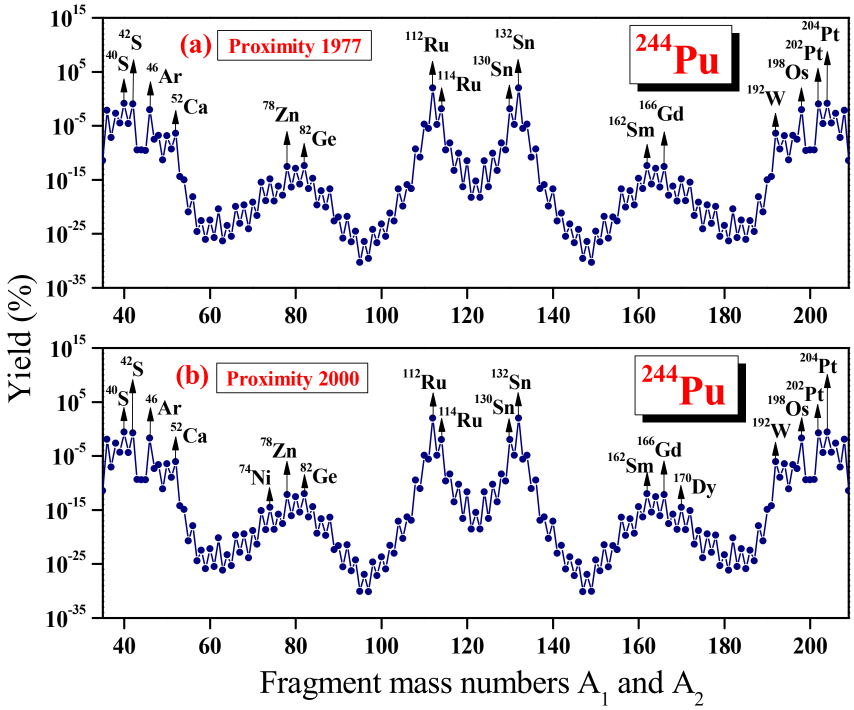

Figure 3.16. The relative yield plotted as a function of mass numbers A_1 and A_2 for ^{244}Pu isotope using proximity 1977 and proximity 2000. The fragment combinations with higher yields are labelled.

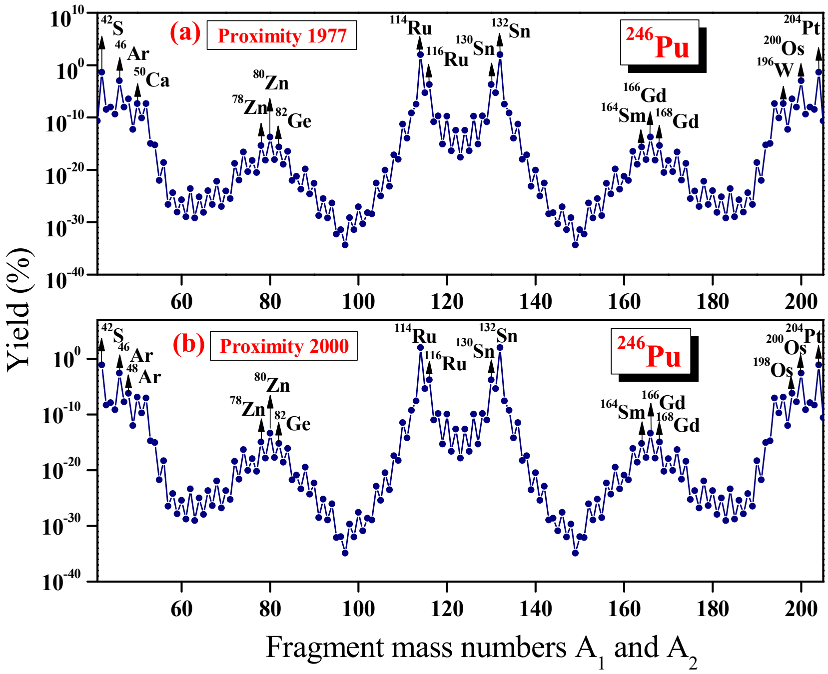

Figure 3.17. The relative yield plotted as a function of mass numbers A_1 and A_2 for ^{246}Pu isotope using proximity 1977 and proximity 2000. The fragment combinations with higher yields are labelled.

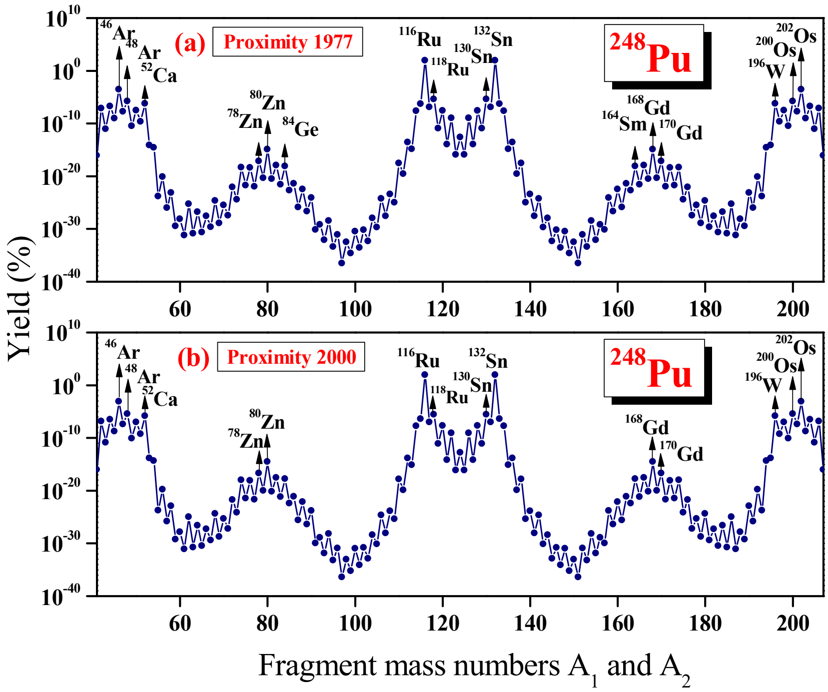

Figure 3.18. The relative yield plotted as a function of mass numbers A_1 and A_2 for ^{248}Pu isotope using proximity 1977 and proximity 2000. The fragment combinations with higher yields are labelled.

For ^{246}Pu isotope, the highest yield is obtained for the symmetric fragment combination ^{114}Ru+^{132}Sn as it possesses a doubly magic ^{132}Sn (N = 82, Z = 50). The next higher yields are for the fragment combinations ^{42}S+^{204}Pt, ^{46}Ar+^{200}Os, ^{116}Ru+^{130}Sn, ^{48}Ar+^{198}Os, ^{50}Ca+^{196}W, ^{52}Ca+^{194}W and ^{44}S+^{202}Pt. The occurrence of these fragment combinations are attributed to the presence of neutron shell closure N=126 and N=28 of ^{204}Pt and ^{46}Ar respectively, near neutron shell closure N=124 of ^{200}Os, near doubly magic ^{130}Sn and magic shell Z=20 of ^{50,52}Ca.

In the case of ^{248}Pu isotope, the highest yield is obtained for the symmetric fragment combination ^{116}Ru+^{132}Sn as it contains a doubly magic ^{132}Sn (N = 82, Z = 50). The next higher yields are for the fragment combinations ^{46}Ar+^{202}Os, ^{118}Ru+^{130}Sn, ^{48}Ar+^{200}Os, ^{52}Ca+^{196}W, ^{50}Ca+^{198}W, ^{120}Pd+^{128}Cd, ^{114}Ru+^{134}Sn and ^{122}Pd+^{126}Cd. The first two combinations are due to the neutron shell closure N=28 and N=126 of ^{46}Ar and ^{202}Os respectively and near doubly magic ^{130}Sn. The other combinations are due to near neutron shell closure N=124 of ^{200}Os, magic shell Z=20 of ^{50,52}Ca, magic shell Z=50 of ^{134}Sn.

From **Figure 3.13 – Figure 3.18**, it becomes clear that on using the potentials, proximity 1977 and proximity 2000, we get the highest yield for the same fragment combination for the binary fission of all the chosen plutonium isotopes. At the same time, other fragment combinations, as ordered from the most probable to the least probable ones were also same from both the potential calculations. It is also noticed that our predicted relative yield values using two different potentials are almost same and were able to compare with the experimental data.

The relative yield obtained using two different proximity potential, for all possible neutronless binary fission of ^{238,240,242}Pu are compared with the available experimental value obtained using double energy method by Wagemans *et al.,* [42] and are shown in **Figure 3.19 – Figure 3.21**.

Our work reveals that, the presence of doubly magic or near doubly magic nuclei plays an important role in the binary fission of even-even $^{238\text{-}248}$Pu isotopes. It is found that the magnitude of the relative yield increases with increase in mass number (i.e. due to the increase in neutron number) of the parent nuclei.

Also it is found that the highest yield for ^{238}Pu isotope is for the fragments with isotope of Pb (Z=82) as one fragment, whereas for ^{240,242}Pu isotopes the highest yield is for the fragments with isotope of Hg (Z=80) as one fragment. The highest yield (or minima in the cold reaction valley) associated with ^{208}Pb and ^{206}Hg daughter can be interpreted as a heavy particle radioactivity [46-48]. Fragments with Sn (Z=50) as one fragment has the highest yield in the case of ^{244,246,248}Pu isotopes. It is found that for the binary fragmentation of ^{238,240,242}Pu isotopes, asymmetric splitting is superior and in the case of ^{244,246,248}Pu isotopes symmetric splitting is superior.

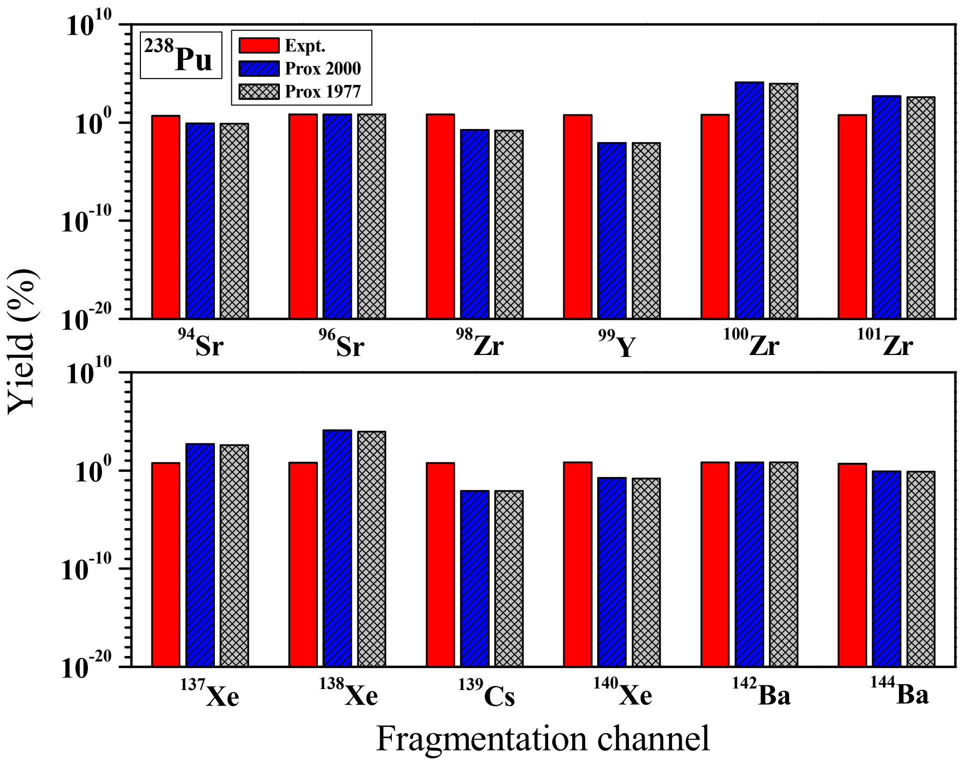

Figure 3.19. The yields obtained for the cold fission of ^{238}Pu isotope and their comparison with the experimental data [42].

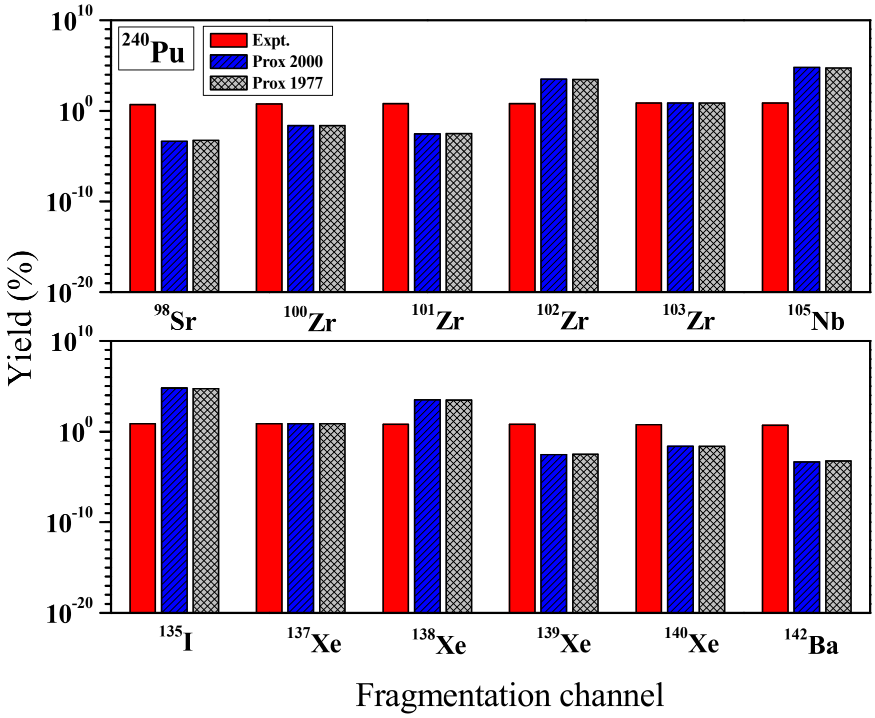

Figure 3.20. The yields obtained for the cold fission of ^{240}Pu isotope and their comparison with the experimental data [42].

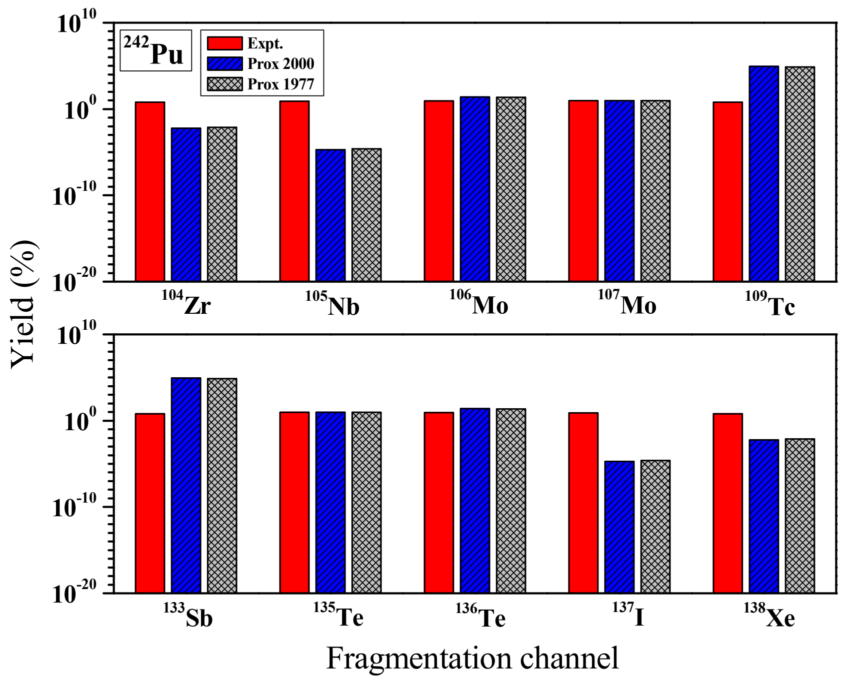

Figure 3.21. The yields obtained for the cold fission of ^{242}Pu isotope and their comparison with the experimental data [42].

3.3.4 Summary

To study the binary fragmentation of even-even $^{238-248}$Pu isotopes, Coulomb and proximity potential is taken as the interacting barrier. In each case, the fragmentation potential and Q-values are calculated for all possible fission components. The relative yields are calculated using proximity 1977 and proximity 2000. The favourable fragment combinations for the binary fission are discussed in detail. For ^{238}Pu isotope, the highest yield is predicted for the fragments with isotope of Pb (Z=82) as one fragment, whereas for ^{240,242}Pu isotopes, fragments with isotope of Hg (Z=80) as one fragment possesses the highest yield. In the case of ^{244,246,248}Pu isotopes, the highest yield are for the fragments with Sn (Z=50) as one fragment. The double magicity and near double magicity of the predicted heavy fragment (^{208,210}Pb, ^{204,206,208}Hg, ^{204}Pt, ^{200,202}Os and ^{130,132}Sn) are found to play the key role for the most favourable fragment combinations. The relative yield obtained using two different proximity potential for all possible neutronless binary fission of ^{238,240,242}Pu are compared with the experimental value of Wagemans *et al.,* [42] and were found to be in good agreement.

3.4 Isotopic yield in cold binary fission of even-even $^{230-250}$U isotopes

Within the frame work of Coulomb and proximity potential model (CPPM), the cold binary fission of even-even uranium isotopes with the mass numbers A=230, 232, 234, 236, 238, 240, 242, 244, 246, 248 and 250 have been studied.

3.4.1 Cold reaction valley of even–even $^{230-250}$U isotopes

In the case of binary fission of even-even $^{230-250}$U isotopes, its driving potential for the touching configuration (z=0) of fragment combinations are calculated. **Figures 3.22 - Figures 3.27** represent the plots for driving potential versus A_1 (mass of one fragment) for all the above isotopes. Observed mass-asymmetry valleys in these figures are because of the shell effects of one or both the fragments. The fragment combinations having minima in the potential energy are the most probable binary fission fragments.

From **Figures 3.22 - Figures 3.27**, we noticed that for ^{230}U apart from the alpha particle ^{10}Be, ^{14}C, ^{20}O, ^{24}Ne, ^{28}Mg, ^{48,50}Ca, ^{68,70}Ni, ^{94}Sr, ^{96}Zr etc. are seen to be possible for emission. Two deep regions are observed in the fission region both having comparable minima. The minimum in the first region corresponds to the splitting ^{20}O+^{210}Po and ^{24}Ne+^{206}Pb, whereas, that in the second region is due to the splitting ^{94}Sr+^{136}Xe and ^{96}Zr+^{134}Te. The driving potential values for the above combinations lies very close to each other. It was found that the four mentioned combinations include doubly or nearly doubly magic nuclei viz, ^{210}Po (N = 126, Z = 84), ^{206}Pb (N = 124, Z = 82), ^{134}Te (N = 82, Z = 52) and ^{136}Xe (N = 82, Z = 54).

All the other isotopes also have deep valleys in the fission regions each having several comparable minima. The minima obtained for ^{232,234,236}U isotope in the first region are at ^{210,212,214}Po and ^{208,210}Pb and they are due to the doubly magic ^{208}Pb (N = 126, Z = 82), near doubly magic ^{210}Po (N = 126, Z = 84), ^{212}Po (N = 128, Z = 84) and ^{210}Pb (N = 128, Z = 82). For ^{238,240,242}U isotope, a deep minimum is observed at ^{106}Mo+^{132}Sn, ^{108}Mo+^{132}Sn and ^{110}Mo+^{132}Sn respectively, due to the presence of doubly magic ^{132}Sn.

For ^{244,246,248,250}U first minima are observed at ^{202}Os (N=126), ^{198}W (N=124), ^{200}W (N=126), ^{198}Hf (N = 126). In the second region the minima at ^{84}Ge, ^{78}Ni and ^{80}Zn are due to presence of the magic shell N=50, N=52. Finally, in the third valley a minimum at doubly magic ^{132}Sn (N = 82, Z = 50) is found for the splitting ^{112}Mo+^{132}Sn, ^{114}Mo+^{132}Sn, ^{116}Mo+^{132}Sn and ^{118}Mo+^{132}Sn respectively.

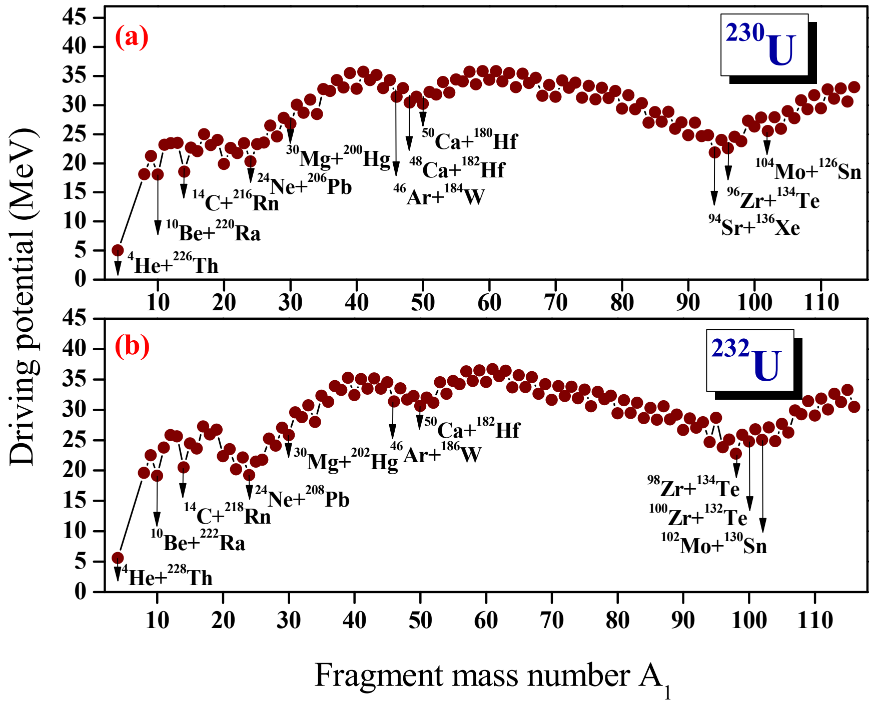

Figure 3.22. The driving potential for ^{230}U and ^{232}U isotope plotted as a function of mass number A_1.

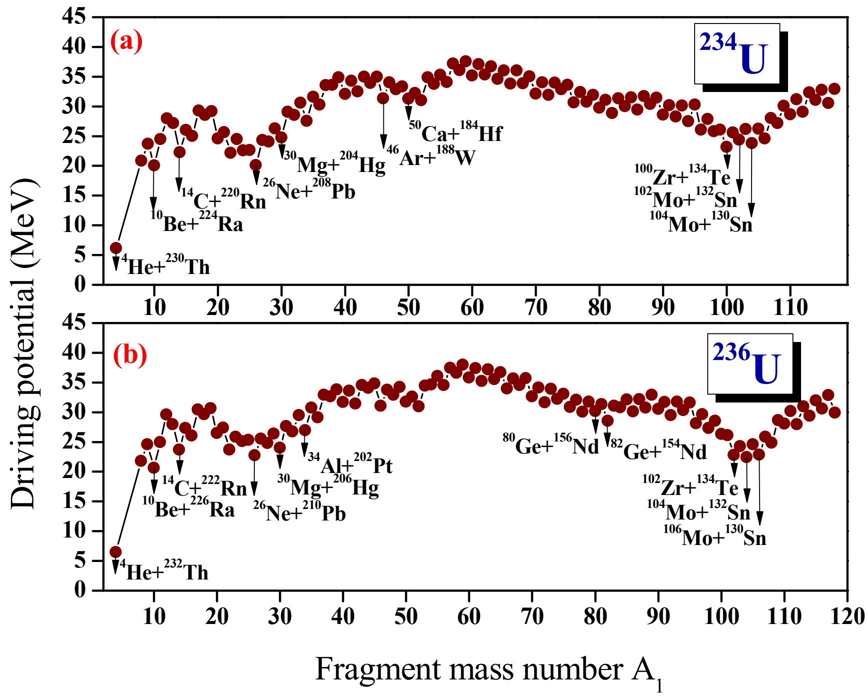

Figure 3.23. The driving potential for ^{234}U and ^{236}U isotope plotted as a function of mass number A_1.

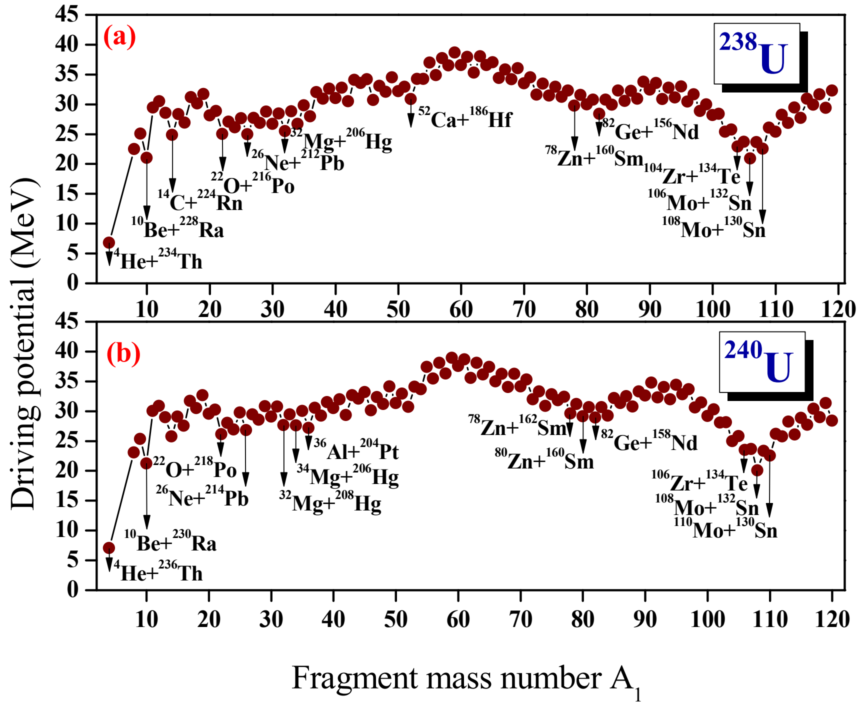

Figure 3.24. The driving potential for ^{238}U and ^{240}U isotope plotted as a function of mass number A_1.

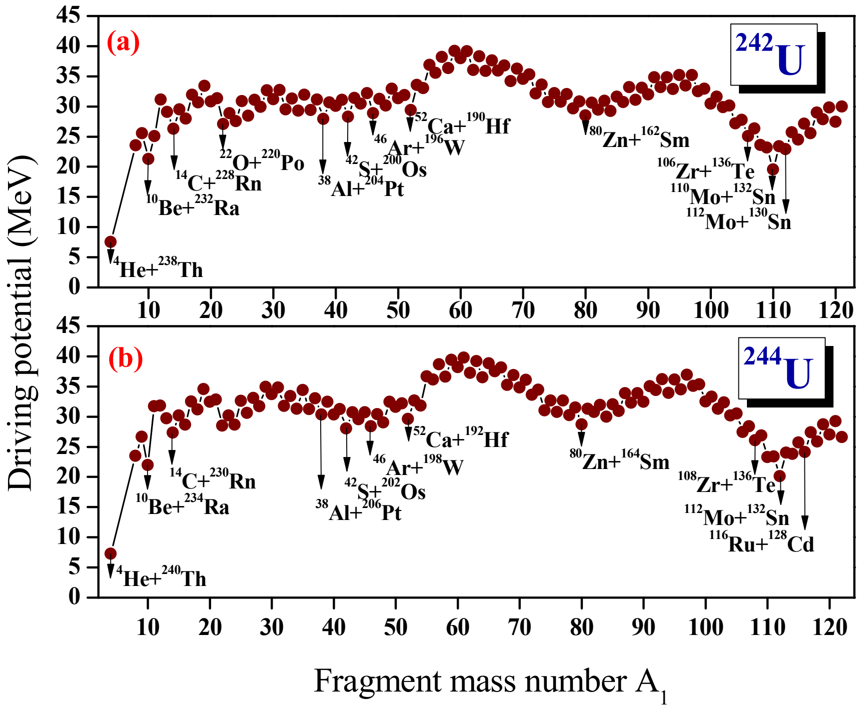

Figure 3.25. The driving potential for ^{242}U and ^{244}U isotope plotted as a function of mass number A_1.

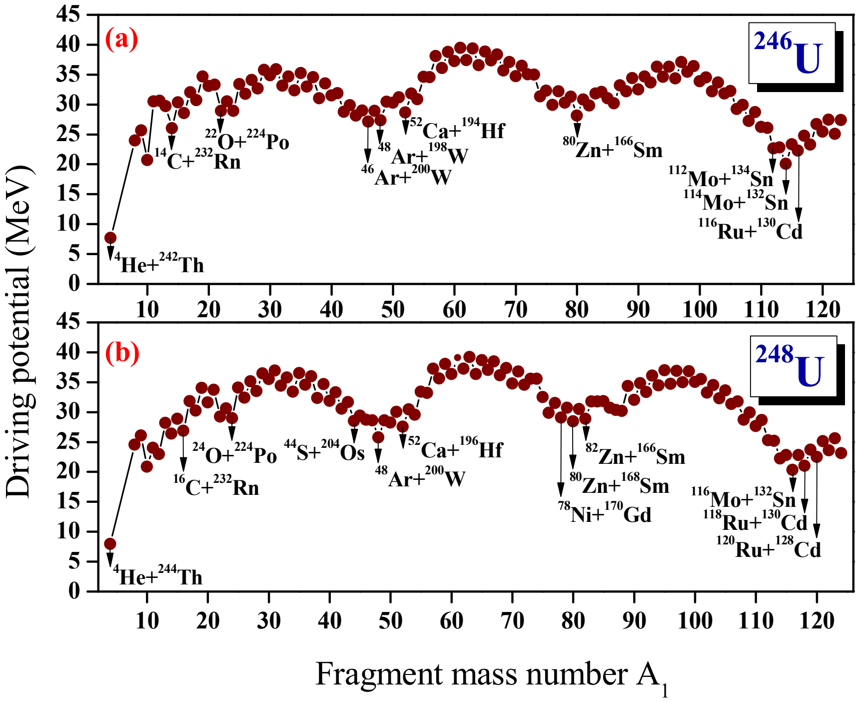

Figure 3.26. The driving potential for ^{246}U and ^{248}U isotope plotted as a function of mass number A_1.

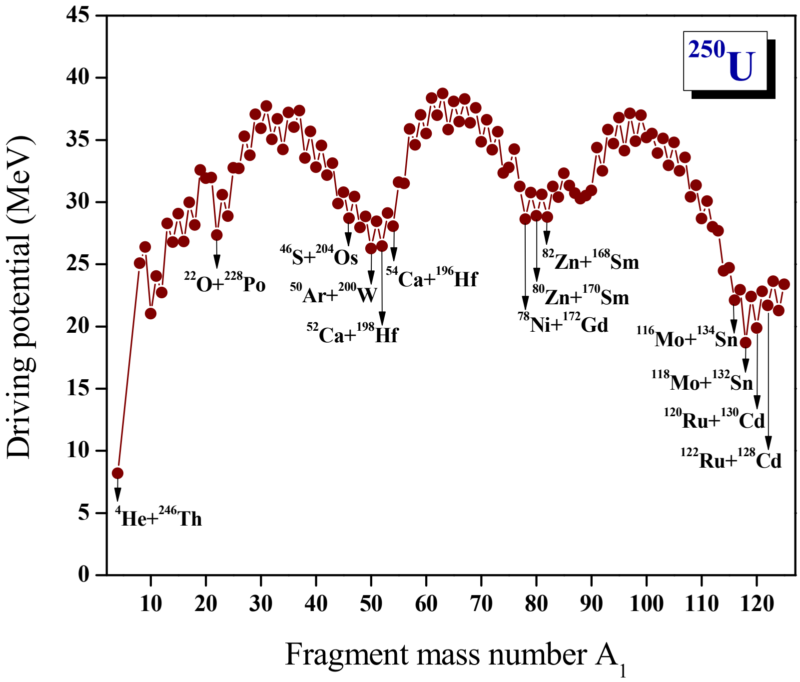

Figure 3.27. The driving potential for ^{250}U isotope plotted as a function of mass number A_1.

3.4.2 Barrier penetrability and yield calculation

The barrier penetrability for each fragment combinations found in the cold valley for even-even $^{230\text{-}250}U$ isotopes are calculated using Proximity 1977. The most favorable fragment combinations for all the six isotopes mentioned above are obtained by calculating their relative yields. For a better comparison of barrier penetrability and relative yields, calculations are carried out for all the isotopes using proximity 2000 also. The relative yield is calculated and is plotted as a function of fragment mass number A_1 and A_2 and is shown in **Figures 3.28 - Figures 3.38**.

For ^{230}U, the combination $^{24}Ne+^{206}Pb$ possesses the highest yield due to the presence of near doubly magic nuclei ^{206}Pb (N = 124, Z = 82). The next higher yield can be observed for the $^{28}Mg+^{202}Hg$ due to the near doubly magic ^{202}Hg (N = 122, Z = 80). The various other fragment combinations observed in this binary fission of ^{230}U are $^{32}Si+^{198}Pt$, $^{34}Si+^{196}Pt$, $^{94}Sr+^{136}Xe$, $^{96}Zr+^{134}Te$ and $^{98}Zr+^{132}Te$. These splitting are due to the presence of magic number N= 20 of ^{34}Si, N=82 of ^{136}Xe, ^{134}Te and near proton shell closure Z=52 of ^{132}Te.

In the case of ^{232}U isotope, $^{24}Ne+^{208}Pb$ possesses the highest yield due to the presence of doubly magic nuclei ^{208}Pb (N = 124, Z = 82). Other favored channels for the binary fission of ^{232}U isotope are, $^{28}Mg+^{204}Hg$, $^{32}Si+^{200}Pt$, $^{34}Si+^{198}Pt$, $^{98}Zr+^{134}Te$, $^{96}Sr+^{136}Xe$ and $^{94}Sr+^{138}Xe$, as ordered from the most probable to the less probable ones. As can be noticed, these favored channels include the near doubly magic ^{204}Hg, neutron shell closure Z=20 of ^{34}Si, neutron shell closure N=82 of ^{136}Xe and ^{134}Te. The fragmentation channels that are predicted to be the most favorable ones in the binary fission of ^{234}U isotope are $^{26}Ne+^{208}Pb$, $^{28}Mg+^{206}Hg$, $^{30}Mg+^{204}Hg$, $^{34}Si+^{200}Pt$, $^{100}Zr+^{134}Te$, $^{104}Mo+^{130}Sn$ and $^{102}Mo+^{132}Sn$ as ordered from the most to the less probable ones. It is noticed that these channels contain near doubly magic $^{206,204}Hg$, doubly magic nuclei ^{132}Sn and ^{208}Pb, neutron shell closure N=82 of ^{134}Te and proton shell closure Z=50 of ^{130}Sn. In the case of ^{236}U isotope, more yield is obtained for the fragment combination $^{30}Mg+^{206}Hg$ due to the presence of near doubly magic ^{206}Hg (N = 126, Z = 80). The next higher yields are for the fragment splitting $^{26}Ne+^{210}Pb$, $^{34}Si+^{202}Pt$, $^{104}Mo+^{132}Sn$, $^{102}Zr+^{134}Te$, $^{106}Mo+^{130}Sn$ and $^{36}Si+^{200}Pt$. It is due to the near doubly magic ^{210}Pb and ^{132}Sn, near doubly magic ^{130}Sn. For ^{238}U isotope, the highest yield is obtained for the fragment combination $^{34}Si+^{204}Pt$. The next higher yields are for the fragment combinations $^{30}Mg+^{208}Hg$, $^{32}Mg+^{206}Hg$, $^{106}Mo+^{132}Sn$, $^{36}Si+^{202}Pt$, $^{108}Mo+^{130}Sn$ and $^{104}Zr+^{134}Te$. The occurrence of these fragment combinations are attributed to the presence of near doubly magic ^{130}Sn, ^{208}Hg, ^{206}Hg, ^{134}Te and doubly magic ^{132}Sn.

In the case of ^{240}U isotope, the highest yield is obtained for the symmetric fragment combination $^{108}Mo+^{132}Sn$ as it contains a doubly magic ^{132}Sn (N = 82, Z = 50). The next higher yields are for the fragment combinations $^{36}Si+^{204}Pt$, $^{110}Mo+^{130}Sn$, $^{42}S+^{198}Os$, $^{40}S+^{200}Os$, $^{46}Ar+^{194}W$ and $^{50}Ca+^{190}Hf$. The occurrence of these fragment combinations are attributed to the presence near doubly magic ^{130}Sn, neutron shell closure N=28 and N=126 of ^{46}Ar and ^{204}Pt respectively, near neutron shell closure N=124 of ^{200}Os and magic shell Z=20 of ^{50}Ca. For ^{242}U isotope, the highest yield is obtained for the fragment combination $^{110}Mo+^{132}Sn$ as it contains a doubly magic ^{132}Sn (N = 82, Z = 50). The next higher yields are for the fragment combinations $^{42}S+^{200}Os$, $^{46}Ar+^{196}W$, $^{112}Mo+^{130}Sn$, $^{52}Ca+^{190}Hf$ and $^{106}Zr+^{136}Te$. The occurrence of these fragment combinations are attributed to the presence of near doubly magic ^{130}Sn, ^{136}Te, ^{46}Ar and near neutron shell closure ^{200}Os.

In the case of ^{244}U isotope, the highest yield is obtained for the symmetric fragment combination $^{112}Mo+^{132}Sn$ as it contains a doubly magic ^{132}Sn (N = 82, Z = 50). The next higher yields are for the fragment combinations $^{42}S+^{202}Os$, $^{48}Ar+^{196}W$, $^{46}Ar+^{198}W$ and $^{52}Ca+^{192}Hf$. For ^{246}U isotope, the highest yield is obtained for the fragment combination $^{114}Mo+^{132}Sn$ as it contains a doubly magic ^{132}Sn (N = 82, Z = 50). The next higher yields are for the fragment combinations $^{46}Ar+^{200}W$, $^{48}Ar+^{198}W$, $^{116}Ru+^{130}Cd$ and $^{52}Ca+^{194}Hf$. For ^{248}U isotope, the highest yield is obtained for the fragment combination $^{116}Mo+^{132}Sn$ as it contains a doubly magic ^{132}Sn (N = 82, Z = 50). The next higher yields are for the fragment combinations $^{48}Ar+^{200}W$, $^{118}Ru+^{130}Cd$ and $^{52}Ca+^{196}Hf$ and $^{114}Mo+^{134}Sn$. For ^{250}U isotope, the highest yield is obtained for the fragment combination $^{118}Mo+^{132}Sn$ as it contains a doubly magic ^{132}Sn (N = 82, Z = 50). The next higher yields are for the fragment combinations $^{120}Ru+^{130}Cd$, $^{52}Ca+^{198}Hf$, $^{50}Ar+^{200}W$, $^{116}Mo+^{134}Sn$ and $^{48}Ar+^{202}W$.

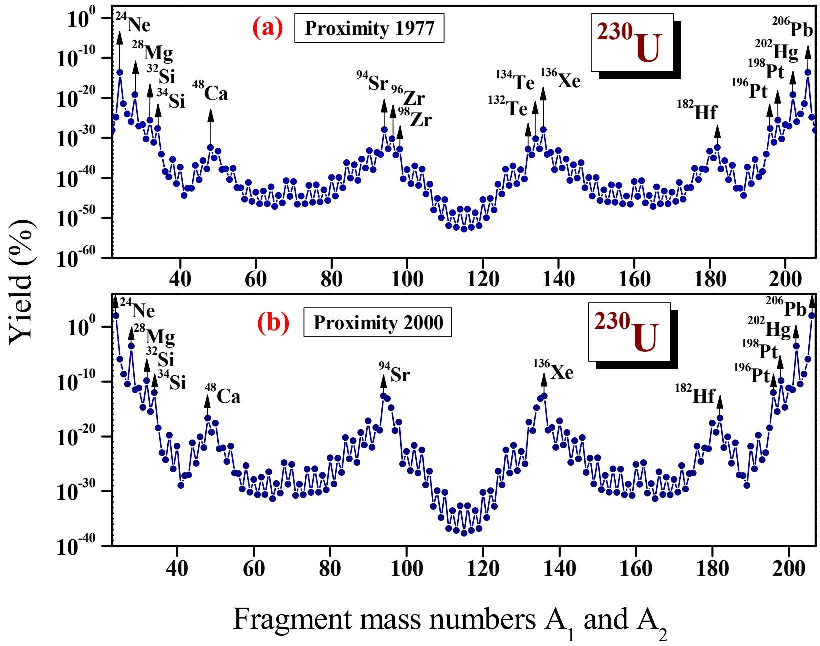

Figure 3.28. The relative yield plotted as a function of mass numbers A₁ and A₂ for ^{230}U isotope using proximity 1977 and proximity 2000. The fragment combinations with higher yields are labelled.

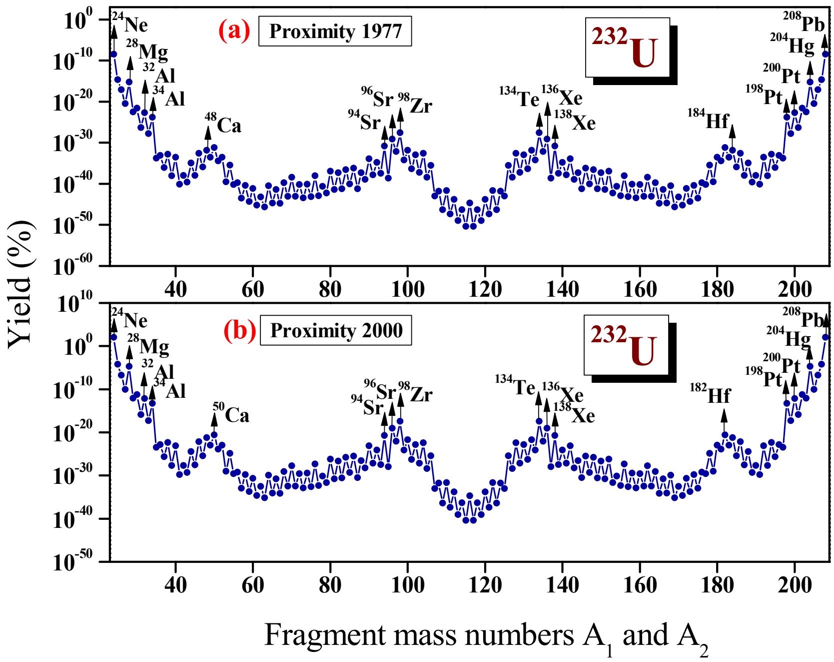

Figure 3.29. The relative yield plotted as a function of mass numbers A_1 and A_2 for ^{232}U isotope using proximity 1977 and proximity 2000. The fragment combinations with higher yields are labelled.

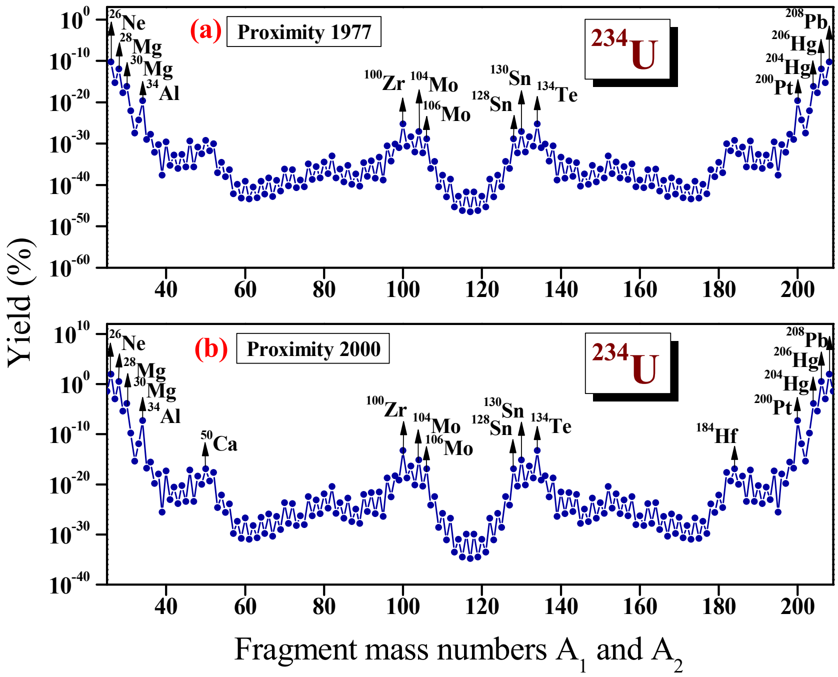

Figure 3.30. The relative yield plotted as a function of mass numbers A_1 and A_2 for ^{234}U isotope using proximity 1977 and proximity 2000. The fragment combinations with higher yields are labelled.

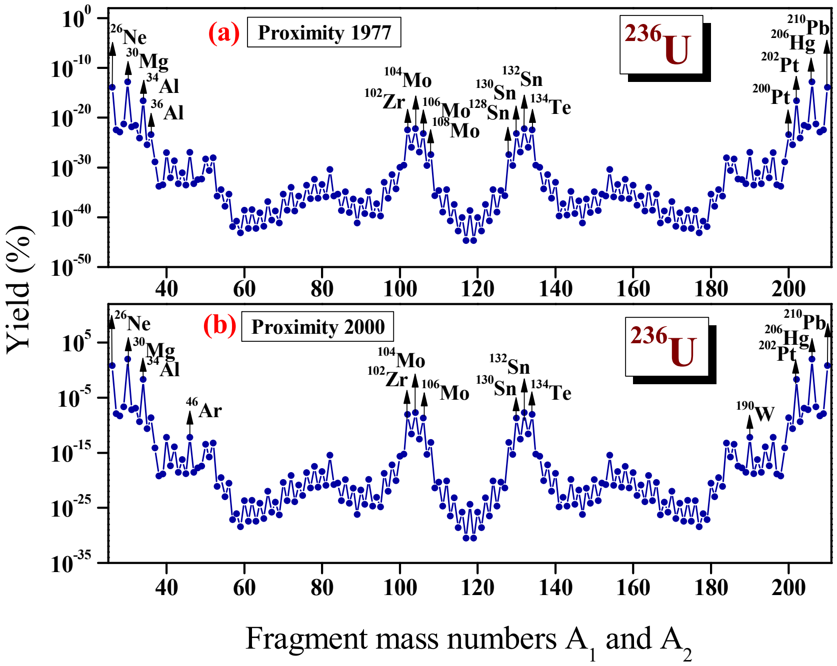

Figure 3.31. The relative yield plotted as a function of mass numbers A_1 and A_2 for ^{236}U isotope using proximity 1977 and proximity 2000. The fragment combinations with higher yields are labelled.

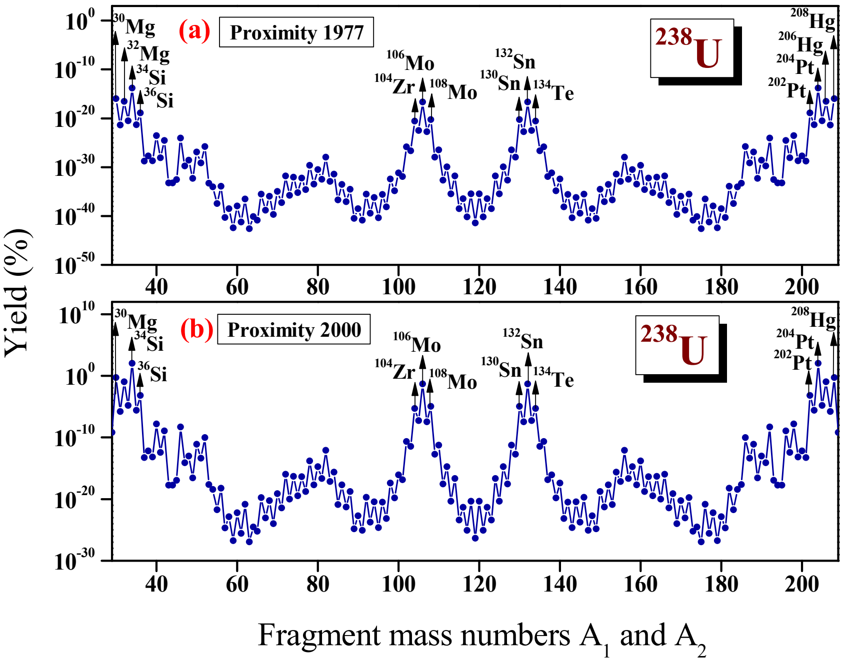

Figure 3.32. The relative yield plotted as a function of mass numbers A_1 and A_2 for ^{238}U isotope using proximity 1977 and proximity 2000. The fragment combinations with higher yields are labelled.

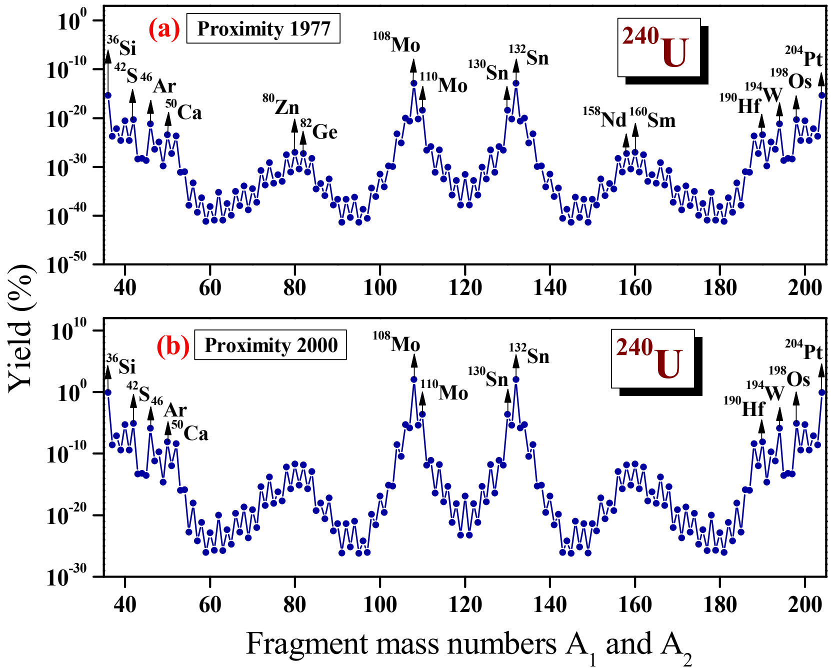

Figure 3.33. The relative yield plotted as a function of mass numbers A_1 and A_2 for ^{240}U isotope using proximity 1977 and proximity 2000. The fragment combinations with higher yields are labelled.

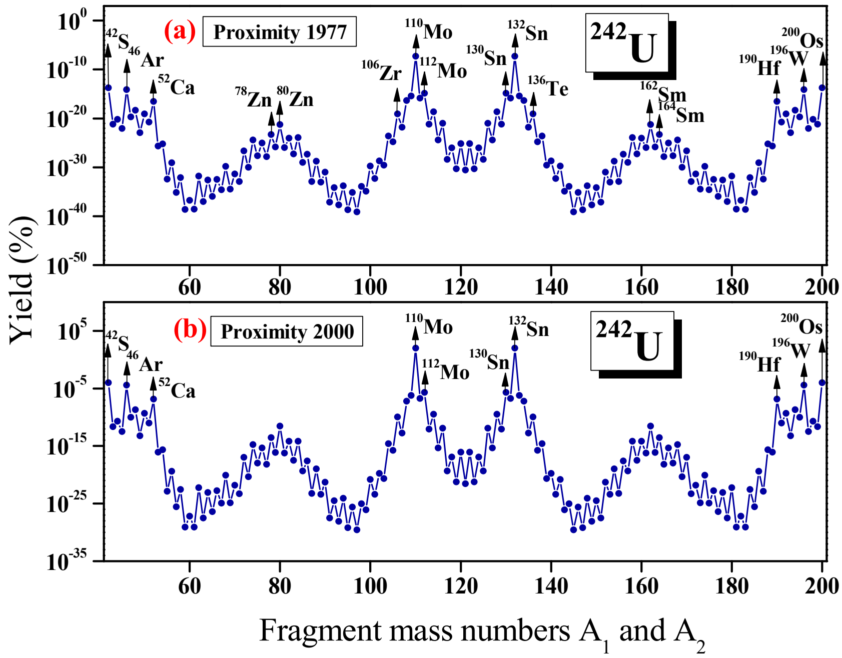

Figure 3.34. The relative yield plotted as a function of mass numbers A_1 and A_2 for ^{242}U isotope using proximity 1977 and proximity 2000. The fragment combinations with higher yields are labelled.

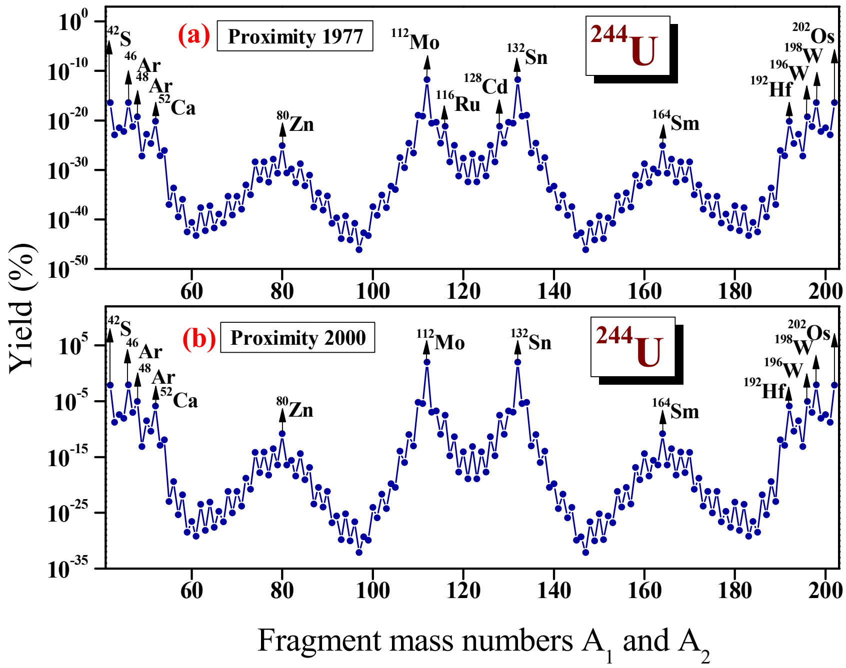

Figure 3.35. The relative yield plotted as a function of mass numbers A_1 and A_2 for ^{244}U isotope using proximity 1977 and proximity 2000. The fragment combinations with higher yields are labelled.

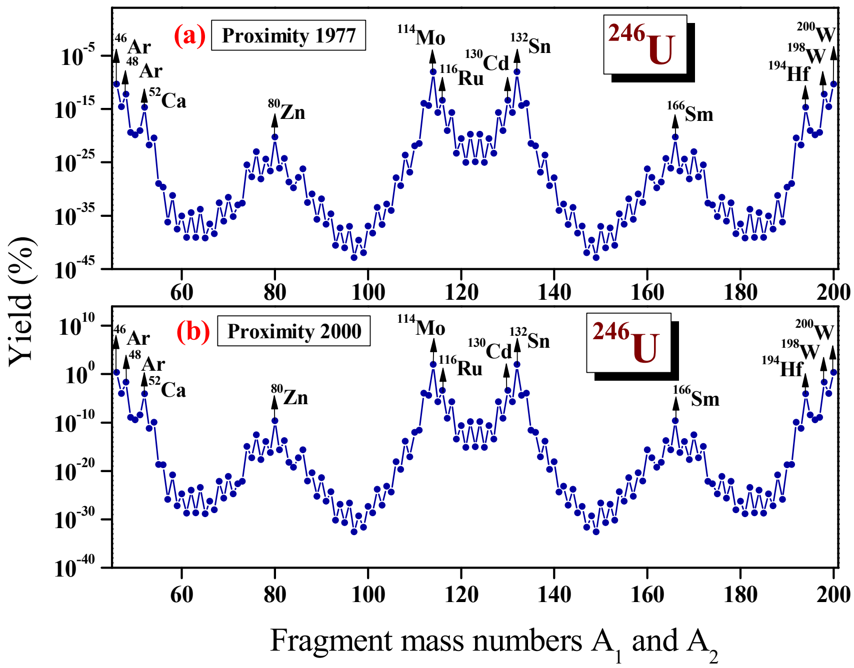

Figure 3.36. The relative yield plotted as a function of mass numbers A1 and A2 for ^{246}U isotope using proximity 1977 and proximity 2000. The fragment combinations with higher yields are labelled.

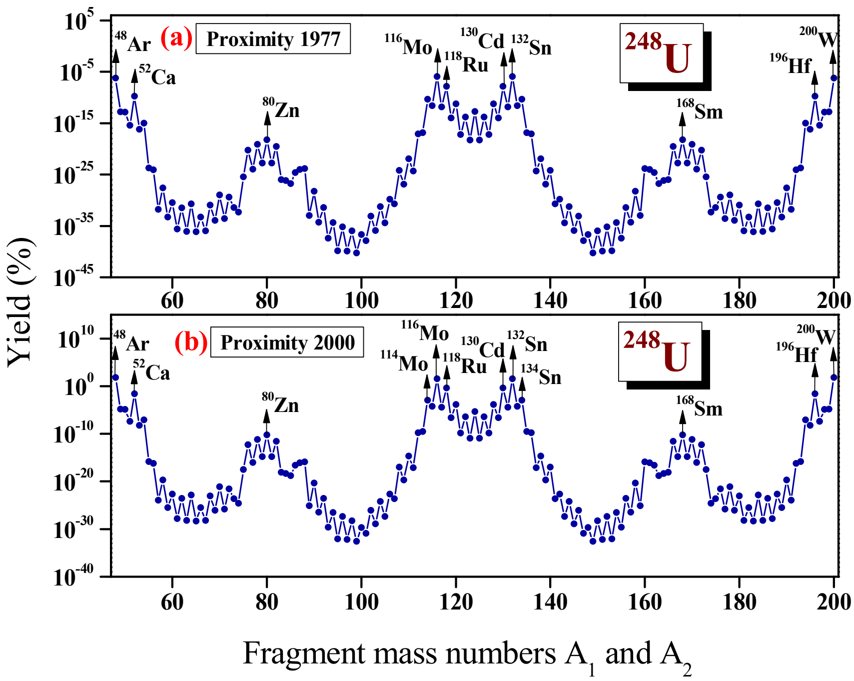

Figure 3.37. The relative yield plotted as a function of mass numbers A1 and A2 for ^{248}U isotope using proximity 1977 and proximity 2000. The fragment combinations with higher yields are labelled.

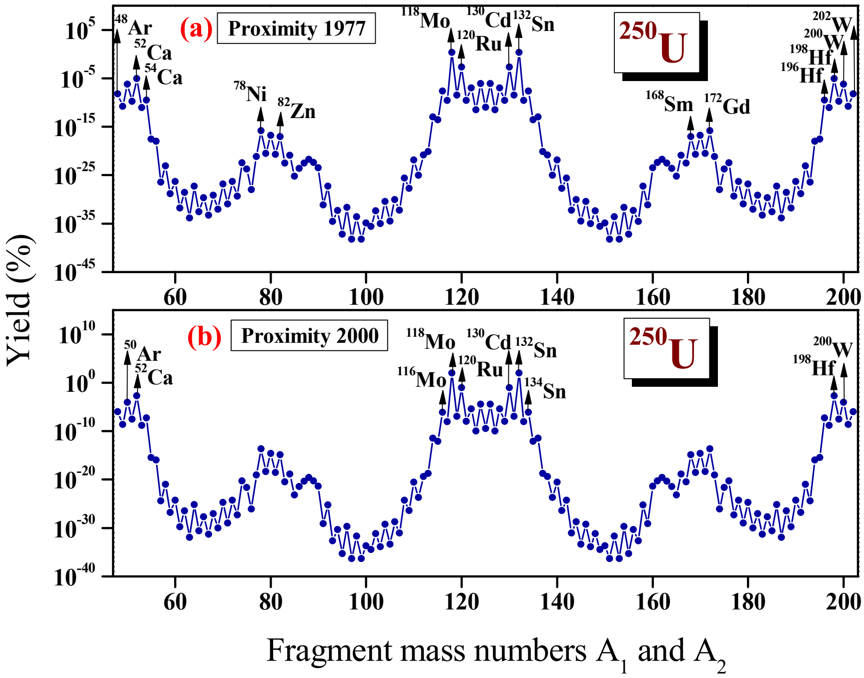

Figure 3.38. The relative yield plotted as a function of mass numbers A_1 and A_2 for ^{250}U isotope using proximity 1977 and proximity 2000. The fragment combinations with higher yields are labelled.

3.4.3 Summary

The binary fragmentations of even-even $^{230-250}U$ isotopes are studied with Coulomb and proximity potential taken as the interacting potential barrier. In each case, the fragmentation potential and Q-values are calculated for all possible fission components. The relative yield is calculated and the predicted favourable fragment combinations for the binary fission of all isotopes are discussed in detail. The role of the nuclear shell structure in the formation of fission products is revealed through our study. The presence of doubly magic or near doubly magic nuclei plays an important role in the fission process of even-even $^{230-250}U$ isotopes.

References

[1] O. Hahn and F. Strassmann, Naturwissenschaften **27**, 11 (1939).

[2] N. Bohr and J. A. Wheeler, Phys. Rev. **56**, 426 (1939).

[3] C. Signarbieux, J. Phys. Lett, **42**, L437 (1981).

[4] P. Armbruster, International Conference "Nuclei far from stability", Helsingor, DK, CERN 81-09,675 (1981).

[5] F. J. Hambsch, H. H. Knitter, and C. Budtz-Jorgensen, Nucl. Phys. A **554**, 209 (1993).

[6] A. Benoufella, G. Barreau, M. Asghar, P. Audouard, F. Brisard, T.P. Doan, M. Hussonnois, B. Leroux, J. Trochon,and M.S. Moore, Nucl. Phys. A **565**, 563 (1993).

[7] J. H. Hamilton, A.V. Ramayya, J. Kormicki, W.C. Ma, Q. Lu, D. Shi, J.K. Deng, S.J. Zhu, A. Sandulescu, W. Greiner, G.M. Ter-Akopian, Yu.Ts. Oganessian, G.S. Popeko, A.V. Daniel, J. Kliman, V. Polhorsky, M. Morhac, J.D. Cole, R. Aryaeinejad, I.Y. Lee, N.R. Johnson, and F.K. McGowan, J. Phys. G **20**, L85(1994).

[8] G.M. Ter-Akopian, J.H. Hamilton, Yu.Ts. Oganessian, J. Kormicki, G.S. Popeko, A.V. Daniel, A.V. Ramayya, Q. Lu, K. Butler-Moore, W.-C. Ma, J.K. Deng, D. Shi, J. Kliman, V. Polhorsky, M. Morhac, W. Greiner, A. Sandulescu, J.D. Cole, R. Aryaeinejad, N.R. Johnson, I.Y. Lee, and F.K. McGowan, Phys. Rev. Lett. **73**, 1477(1994).

[9] W. Schwab, H. G. Clerc, M. Mutterer, J.P. Theobald, and H. Faust, Nucl. Phys. A **577**, 674 (1994).

[10] A. Sandulescu and W. Greiner, J. Phys. G. Nucl. Phys. **3**, L189 (1977).

[11] A. Sandulescu and W. Greiner, Rep. Prog. Phys. **55**, 1423 (1992).

[12] A. Sandulescu, A. Florescu, F. Carstoiu, W. Greiner, J. H. Hamilton, A. V. Ramayya, and B. R. S. Babu, Phys. Rev. C **54**, 258 (1996).

[13] Y. X. Dardenne, R. Aryaeinejad, S. J. Asztalos, B. R. S. Babu, K. Butler-Moore, S. Y. Chu, J. D. Cole, M. W. Drigert, K. E. Gregorich, J. H. Hamilton, J. Kormicki, I. Y. Lee, R. W. Lougheed, Q. H. Lu, W.-C. Ma, M. F. Mohar, K. J. Moody, S. G. Prussin, A. V. Ramayya, J. O. Rasmussen, M. A. Stoyer, and J. F. Wild, Phys. Rev. C **54**, 206 (1996).

[14] J.H. Hamilton, A.V. Ramayya, J. K. Hwang, J. Kormicki, B.R.S. Babu, A. Sandulescu, A. Florescu, W. Greiner, G.M. Ter-Akopian, Yu.Ts. Oganessian, A. V. Daniel, S.J. Zhu, M. G. Wang, T. Ginter, J. K. Deng, W.C. Ma, G. S. Popeko, Q. H. Lu, E. Jones, R. Dodder, P. Gore, W. Nazarewicz, J.O. Rasmussen, S. Asztalos, I.Y. Lee, S.Y. Chu, K.E. Gregorich, A.O. Macchiavelli, M.F. Mohar, S. Prussin, M.A. Stoyer, R.W. Lougheed, K.J. Moody, J.F. Wild, L. A. Bernstein, J. A. Becker, J.D. Cole, R. Aryaeinejad,

Y.X. Dardenne, M.W. Drigert, K. Butler-Moore, R. Donangelo and H. C. Griffin, Prog. Part. Nucl. Phys. **38**, 273 (1997).

[15] A. V. Ramayya, J. H. Hamilton, J. K. Hwang, L. K. Peker, J. Kormicki, B. R. S. Babu, T. N. Ginter, A. Sandulescu, A. Florescu, F. Carstoiu, W. Greiner, G. M. Ter-Akopian, Yu. Ts. Oganessian, A. V. Daniel, W. C. Ma, P. G. Varmette, J. O. Rasmussen, S. J. Asztalos, S. Y. Chu, K. E. Gregorich, A. O. Macchiavelly, R. W. Macleod, J. D. Cole, R. Aryaeinjad, K. Butler-Moore, M. W. Drigest, M. A. Stoyer, L. A. Bernstein, R. W. Longheed, K. J. Moody, S. G. Prussin, S. J. Zhu, H. C. Griffin, and R. Donangelo, Phys. Rev. C **57**, 2370 (1998).

[16] F. Gonnenwein, A. Moller, M. Cronni, M. Hesse, M. Wostheinrich, H. Faust, G. Fioni, and S. Oberstedt, Nuovo Cimento **A110**, 1089 (1997).

[17] S. Kumar, R. K. Gupta and W. Scheid, Int. J. Mod. Phys. E, **3**, 195 (1994).

[18] A. Moller, M. Cronni, F. Gonnenwein, and G. Petrov, International Conference on Large Scale Collective Motion of Atomic Nuclei, Brolo, (1996).

[19] M. Mirea, D. S. Delion and A. Sandulescu, Phys. Rev. C **81**, 044317 (2010).

[20] R. Smolanczuk, Phys. Rev. C **56**, 812 (1997).

[21] M. Warda and J. L. Egido, Phys. Rev. C **86**, 014322 (2012).

[22] A. Staszczak, A. Baran and W. Nazarewicz, Phys. Rev. C **87**, 024320 (2013).

[23] D. N. Poenaru R. A. Gherghescu and W. Greiner, J. Phys. G: Nucl. Part. Phys. **40**, 105105 (2013).

[24] D. N. Poenaru and R. A. Gherghescu, J. Phys. G: Nucl. Part. Phys. **41**, 125104 (2014).

[25] D. N. Poenaru, Nuclear Decay Modes, Institute of Physics Publishing, Bristol, Ed. D. N. Poenaru, p.393 (1996).

[26] R. K. Gupta and W. Greiner, Int. J. Mod. Phys. E**3**, 335 (1994).

[27] R. Bonetti and A. Guglielmetti, in Heavy Elements and Related New Phenomena, edited by W. Greiner and R. K. Gupta (World Scientific, Singapore, 1999), Vol. II, p. 643.

[28] S. Kumar and R. K. Gupta, Phys. Rev. C **49**, 1922 (1994).

[29] S. Kumar, D. Bir, and R. K. Gupta, Phys. Rev. C **51**, 1762 (1995).

[30] S. Kumar, J. S. Batra, and R. K. Gupta, J. Phys. G **22**, 215 (1996).

[31] B. D.Wilkins, E. P.Steinberg and R. R.Chasman, Phys. Rev. C **14**, 1832 (1976).

[32] A. C. Wahl, At. Data Nucl. Data Table **39,** 1 (1988).

[33] P. Moller, D. G. Madland, A. J. Sierk and A. Iwamoto, Nature, **409**, 785 (2001).

[34] J. Blocki, J. Randrup, W. J. Swiatecki and C. F. Tsang, Ann. Phys. NY **105**, 427 (1977).

[35] J. Blocki and W. J. Swiatecki, Ann. Phys. NY **132**, 53 (1981).

[36] M. Wang, G. Audi, F. G. Kondev, W. J. Huang, S. Naimi and X. Xu, Chin.

Phys. C **41**, 030002 (2017).

[37] H. Koura, T. Tachibana, M. Uno and M. Yamada, Prog. Theor. Phys. **113**, 305 (2005).
[38] D. N. Poenaru and W. Greiner, Handbook of Nuclear Properties, Clarendon Press, Oxford (1996).
[39] C. Qi, F. R. Xu, R. J. Liotta and R. Wyss, Phys. Rev. Lett. **103**, 072501 (2009).
[40] D. N. Poenaru R. A. Gherghescu and W. Greiner, Phys. Rev. Lett. **107**, 062503 (2011).
[41] E. Hourani, M. Hussonnois and D.N. Poenaru**,** Annales de Physique (Paris) **14,** 311 (1989).
[42] C. Wagemans and P. Schillebeeckx, Nucl. Phys. **A 502**, 287c (1989).
[43] W. D. Myers and W. J. Swiatecki, Phys. Rev. C **62**, 044610 (2000).
[44] W. D. Myers and W. J. Swiatecki, Ann. Phys. **55**, 395 (1969); **84**, 186 (1974); Nucl. Phys. A **336**, 267 (1980).
[45] B. Nerlo-Pomorska and K. Pomorski, Z. Phys. A **348**, 169 (1994).
[46] A. Sandulescu, D. N. Poenaru and W. Greiner, Fiz. Elem. Chastits At. Yadra **11**, 1334 (1980); Sov. J. Part. Nucl **11**, 528 (1980).
[47] H. J. Rose and G. A. Jones, Nature (London) **307**, 245 (1984).
[48] D. N. Poenaru, R. A. Gherghescu and W. Greiner, Phys. Rev. Lett. **107**, 062503 (2011).

CHAPTER 4

Ternary Fission

The breakup of radioactive nuclei into more than two fission fragments has been considered as a very rare process and the formation of three fission fragments through the spontaneous fission of a radioactive nucleus is usually referred to as ternary fission. Usually, one of the ternary fission fragments is very light compared to the main fission fragments and hence the ternary fission is often referred to as light charged particle (LCP) accompanied fission. In most cases of ternary fission, the light charged particle is an alpha particle emitted in a direction perpendicular to the other two fission fragments. Such long range emission of alpha particle with an average energy of 16MeV through ternary fission was reported for the first time by Alvarez *et al.,* (see Ref. [1]), where the authors have computed the number of alpha particles emitted in coincidence with the fission of ^{235}U and ^{239}Pu isotopes. Later Perfilov *et al.,* [2-4] have studied the energy spectra of alpha particles for ternary fission of different isotopes of uranium, plutonium and curium isotopes and in 1964 Malkin *et al.,* [5] have studied the spectrum of long range alpha particle from the spontaneous fission of ^{244}Cm isotope and obtained the most probable energy of the alpha particle as 15.8MeV. The angular distributions and the energy distributions of long range alpha particles emitted from the spontaneous ternary fission of ^{252}Cf isotope have been studied using the statistical theory of nuclear fission by Vitta [6] and the multi-parameter measurements are performed by Theobald *et al.,* in order to compute the kinetic energies and relative angles of the three particles emitted in the ternary fission process [7]. Using triple gamma coincidence technique, the alpha accompanied ternary fission of ^{252}Cf isotope has been studied by Ramayya *et al.,* [8,9] and the correlated pairs Kr-Nd, Sr-Ce, Zr-Ba, Mo-Xe, Ru-Te and Pd-Sn were found to be the favorable fragment combinations.

During the last decades the ternary decay mode has been studied in detail theoretically [10-14]. Without including the pre-formation factors, a coplanar three cluster model was developed by Sandulescu *et al.,* [15] to study the cold alpha accompanied ternary fission of ^{252}Cf. Later in the beginning of the twenty-first century Florescu *et al.,* [16] calculated the pre-formation amplitude for ^{4}He and ^{10}Be clusters formed in the ternary fission of ^{252}Cf. In terms of spheroidal co-ordinates, Delion *et al.,* [17] studied the dynamics of cold ternary fission of ^{252}Cf isotope with light charged particle as ^{4}He and ^{10}Be. The clusters heavier than alpha particles like ^{5}He, ^{7}He and ^{8}Li that formed during the spontaneous ternary fission of ^{252}Cf has been studied by Kopatch *et al.,* [18].

The studies on the emission probabilities and yield of long range alpha particle (LRA) emitted during the spontaneous fission of ^{238,240,242,244}Pu isotopes have been measured by Serot and Wagemans [19], where the authors demonstrated that, the LRA emission strongly depended on alpha cluster preformation probability S_α. Later, the authors [20] have also studied the long range alpha emission probability using one dimensional sudden approximation. Recently, the emission probability of long range alpha particle emitted during the spontaneous ternary fission of ^{250,252}Cf and ^{244,246,248}Cm isotopes was studied by Vermote *et al.,* [21-22].

The three cluster model (TCM) developed by Manimaran *et al.,* [23-26] has been extensively used by the authors for the ternary fission of ^{252}Cf isotope for all fragment combinations, with fission fragments in both the equatorial and collinear configurations. Later, Vijayaraghavan *et al.,* [27] studied the ternary fission of ^{252}Cf isotope for different positioning of the fragments starting from collinear configuration to the triangular configuration. Various theoretical groups [28-30] have developed several theoretical models to study the collinear cluster tri-partition, a new decay mode of heavy nuclei, for the spontaneous ternary fission of ^{252}Cf and ^{236}U nuclei.

4.1 Unified Ternary Fission Model (UTFM)

The light charged particle accompanied ternary fission is energetically possible only if Q value of the reaction is positive. ie.

$$Q = M - \sum_{i=1}^{3} m_i > 0 \tag{4.1.1}$$

Here M is the mass excess of the parent and m_i is the mass excess of the fragments. The interacting potential barrier for a parent nucleus exhibiting cold ternary fission consists of Coulomb potential and nuclear proximity potential of Blocki *et al.,* [31, 32]. The proximity potential was first used by Shi and Swiatecki [33] in an empirical manner and has been quite extensively used by Gupta *et al.,* [34] in the preformed cluster model (PCM) and is based on pocket formula of Blocki *et al.,* [31]. But in the present work, another formulation of proximity potential (eqn (21a) and eqn (21b) of Ref. [32]) is used as given by equations (4.1.7) and (4.1.8). The interacting potential barrier is given by,

$$V = \sum_{i=1}^{3} \sum_{j>i}^{3} (V_{Cij} + V_{Pij}) \tag{4.1.2}$$

with $V_{Cij} = \frac{Z_i Z_j e^2}{r_{ij}}$, the Coulomb interaction between the fragments. Here Z_i and Z_j are the atomic numbers of the fragments and r_{ij} is the distance between fragment centres. The nuclear proximity potential [31] between the fragments is,

$$V_{Pij}(z) = 4\pi\gamma b \left[\frac{C_i C_j}{(C_i + C_j)} \right] \Phi\left(\frac{z}{b} \right) \tag{4.1.3}$$

Here Φ is the universal proximity potential and z is the distance between the near surfaces of the fragments. The distance between the near surfaces of the fragments for equatorial configuration is considered as $z_{12} = z_{23} = z_{13} = z$ and for collinear configuration the distance of separation are $z_{12} = z_{23} = z$ and $z_{13} = 2(C_2+z)$. In collinear configuration the light charged particle is considered to lie in between the first and third fragment. The Süssmann central radii C_i of the fragments related to sharp radii R_i is,

$$C_i = R_i - \left(\frac{b^2}{R_i}\right) \quad (4.1.4)$$

For R_i we use semi empirical formula in terms of mass number A_i as [31]

$$R_i = 1.28A_i^{1/3} - 0.76 + 0.8A_i^{-1/3} \quad (4.1.5)$$

The nuclear surface tension coefficient called Lysekil mass formula [35] is

$$\gamma = 0.9517[1 - 1.7826(N-Z)^2 / A^2] \text{ MeV/fm}^2 \quad (4.1.6)$$

where N, Z and A represents neutron, proton and mass number of the parent, Φ, the universal proximity potential (eqn. (21a) and eqn. (21b) of Ref. [32]) is given as,

$$\Phi(\varepsilon) = -4.41e^{-\varepsilon/0.7176}, \text{ for } \varepsilon > 1.9475 \quad (4.1.7)$$

$$\Phi(\varepsilon) = -1.7817 + 0.9270\varepsilon + 0.0169\varepsilon^2 - 0.05148\varepsilon^3, \text{ for } 0 \le \varepsilon \le 1.9475 \quad (4.1.8)$$

with $\varepsilon = z/b$, where the width (diffuseness) of the nuclear surface $b \approx 1$ fermi.

Using one-dimensional WKB approximation, barrier penetrability P, the probability which the ternary fragments cross the three body potential barrier is given as,

$$P = \exp\left\{-\frac{2}{\hbar}\int_{z_1}^{z_2}\sqrt{2\mu(V-Q)}\,dz\right\} \quad (4.1.9)$$

The turning points $z_1 = 0$ represent touching configuration and z_2 is determined from the equation $V(z_2) = Q$, where Q is the decay energy. The potential V in equation (4.1.9), which is the sum of Coulomb and proximity potential given by equation (4.1.2), are computed by varying the distance between the near surfaces of the fragments. In equation (4.1.9) the mass parameter is replaced by reduced mass μ and is defined as, $\mu = m\left(\frac{\mu_{12}A_3}{\mu_{12}+A_3}\right)$ where $\mu_{12} = \frac{A_1A_2}{A_1+A_2}$ (4.1.10)

Here m is the nucleon mass and A_1, A_2 and A_3 are the mass numbers of the three fragments.

The relative yield can be calculated as the ratio between the penetration probability of a given fragmentation over the sum of penetration probabilities of all possible fragmentation as follows,

$$Y(A_i, Z_i) = \frac{P(A_i, Z_i)}{\sum P(A_i, Z_i)} \tag{4.1.11}$$

The schematic diagram for the touching configuration of three spherical fragments in equatorial and collinear configuration is shown in **Figure 4.1**.

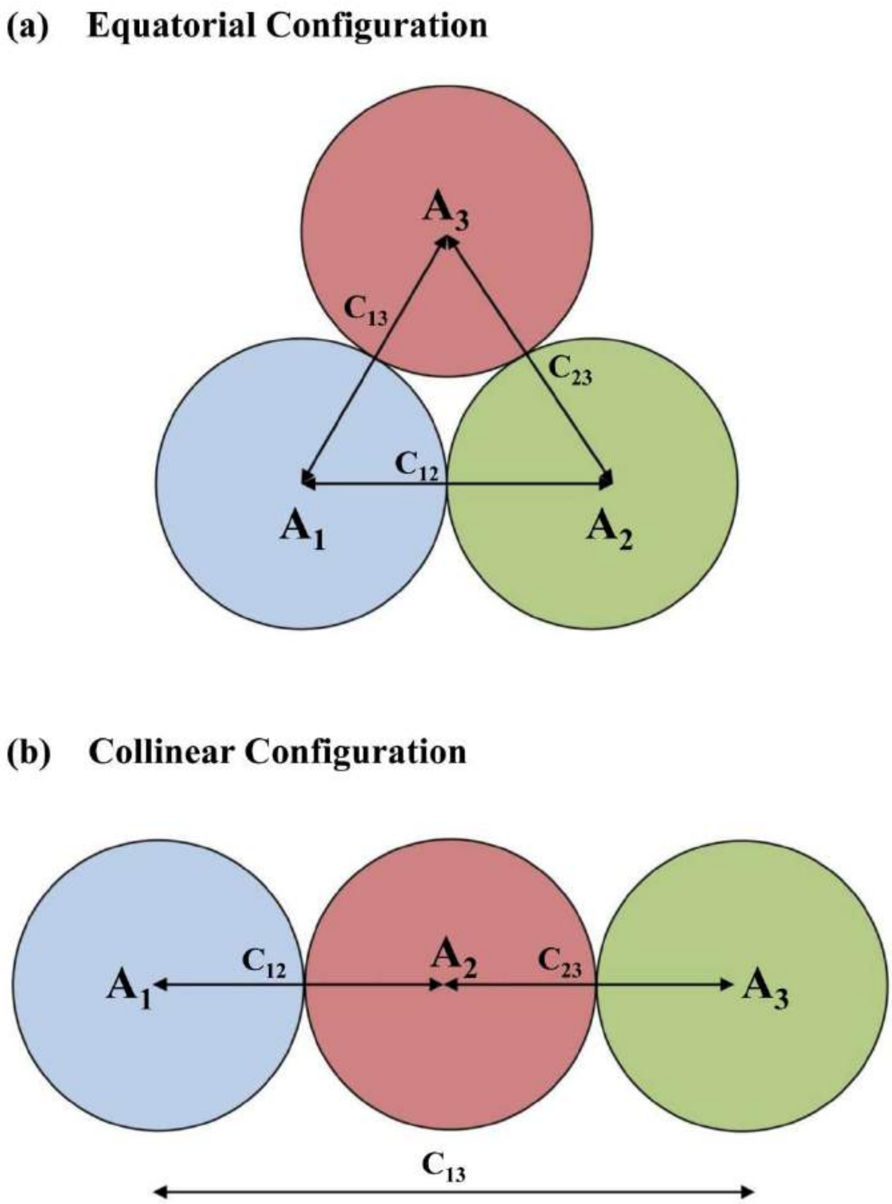

Figure 4.1 The touching configuration of three spherical fragments in (a) equatorial configuration (b) collinear configuration.

4.2 Light charged particle accompanied ternary fission of ^{242}Cm using the Coulomb and proximity potential.

The study is based on the concept of cold reaction valley, introduced in relation to the structure of minima in the so-called driving potential. The driving potential is defined as the difference between the interaction potential V and the decay energy Q of the reaction. The Q values are calculated using the recent mass tables of Wang *et al.,* [36] and KTUY [37]. The driving potential (V-Q) for a particular parent is calculated (with keeping third fragment A_3 as fixed) for all possible fragments as a function of mass and charge asymmetries respectively given as $\eta = \frac{A_1 - A_2}{A_1 + A_2}$ and $\eta_Z = \frac{Z_1 - Z_2}{Z_1 + Z_2}$, at the touching configuration. For every fixed mass pair (A_1, A_2) a pair of charges is singled out for which driving potential is minimized. Taking the interaction barrier as the sum of Coulomb and proximity potential all the possible fragment combinations formed in the ternary fission of ^{242}Cm is studied with the light charged particle (LCP) as ^{4}He, ^{10}Be and ^{14}C.

In the present work we have taken the distance of separation between fragments as equal, but in actual situation the light charged particle (third fragment) will move faster than the other two fragments i.e. the distance of surface separation between the first and second fragment, z_{12} is less than z_{13} and z_{23}. We would like to mention that Manimaran *et al.,* have studied the relative yield (see Fig.7 of Ref [23]) for alpha accompanied ternary fragmentation of ^{252}Cf with equatorial configuration, taking distance of separation between the fragments, $z_{12} = z_{23} = z_{13}$. The authors have also computed the yield by keeping distance $z_{13} = z_{23}$ and reducing the distance between the first and second fragment, z_{12} as 0.5, 0.33, 0.25 and 0.2 of z_{13} and z_{23} respectively. It can be seen from the figure that the position (trend) of yield for various fragmentation channel is not changed when different distances of separation are taken between the fragments. This justifies our notion of taking equal distance between the fragments i.e. $z_{12} = z_{23} = z_{13}$, in equatorial configuration. The interesting aspects of the experimental observations on the cold ternary fission of ^{252}Cf

accompanying ^{4}He [8], ^{10}Be and ^{14}C [38, 39] was that, in some cases not only the heavy fragments but also the light fragments can be born in excited states. But in such decays, the excitation energies of the three fragments are found to be very low and hence the total kinetic energy (TKE) has high values close to the Q value of the ternary fission. According to Sandulescu *et al.,* [15, 40], so as to achieve such large TKE values, the final fragments should have very compact shapes at the scission points and hence the ground state deformations can be taken as in the case of binary fission.

4.2.1 ^{4}He accompanied ternary fission

The driving potential for the touching configuration of fragments is calculated for the ternary fragmentation of ^{242}Cm as the representative parent nucleus with ^{4}He as light charged particle (LCP) and is plotted as a function of fragment mass number A_1, shown in **Figure 4.2**. In the **Figure 4.2**, fragments in the cold valley will be the most probable ternary fission fragments. The minima in the cold valley keeping ^{4}He as light charged particle are at ^{4}He, ^{10}Be, ^{14}C, ^{16}C, ^{18}O, ^{22}O, ^{24}Ne, ^{26}Ne, ^{28}Mg, ^{30}Mg, ^{34}Si, ^{36}Si, ^{40}S, ^{42}S, ^{44}Ar, ^{46}Ar, ^{48}Ca, ^{50}Ca, ^{52}Ca etc.

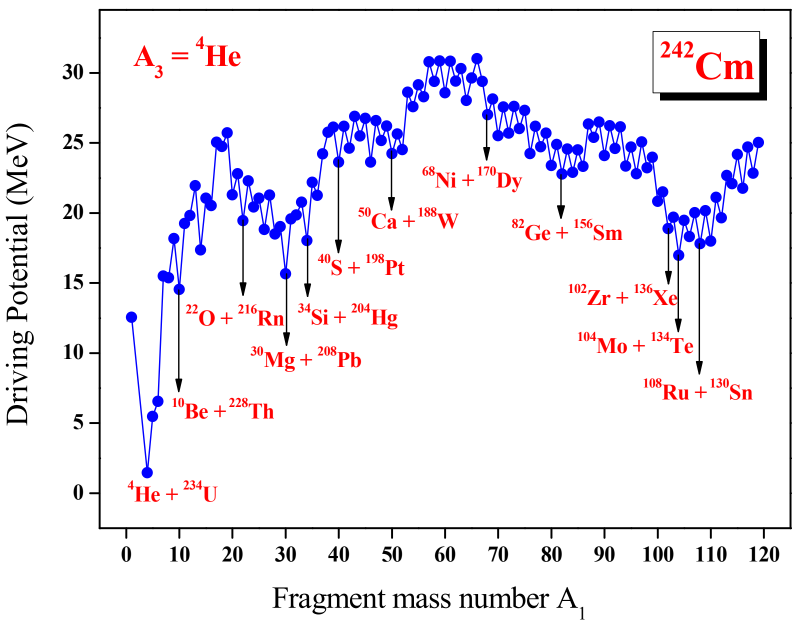

Figure 4.2. The driving potential for ^{242}Cm isotope with ^{4}He as light charged particle, plotted as a function of mass number A_1.

Here the deepest minima for the fragmentation ^{4}He+^{234}U+^{4}He is due to the doubly magic ^{4}He (N = 2, Z = 2) which proves the emission of α-particle in ternary fission as more fundamental. The minimum found for the splitting ^{14}C+^{224}Ra+^{4}He is due to the shell closure at N = 8 of ^{14}C. The next deepest minimum for fragment configuration ^{30}Mg+^{208}Pb+^{4}He is due to the doubly magic ^{208}Pb (N = 126, Z = 82). The second minimum valley is found around ^{82}Ge for the fragment combinations ^{76}Zn+^{162}Gd+^{4}He, ^{78}Zn+^{160}Gd+^{4}He, ^{80}Ge+^{158}Sm+^{4}He, ^{82}Ge+^{156}Sm+^{4}He, ^{84}Se+^{154}Nd+^{4}He, ^{86}Se+^{152}Nd+^{4}He and is likely to be the possible fission fragments. Here the minima for ^{82}Ge+^{158}Sm+^{4}He and ^{84}Se+^{154}Nd+^{4}He is due to the neutron shell closure at N = 50 of Ge and Se respectively. Another deep valley occurs around ^{134}Te for the fragment combinations ^{102}Zr+^{136}Xe+^{4}He, ^{104}Mo+^{134}Te+^{4}He, ^{106}Mo+^{132}Te+^{4}He, ^{108}Ru+^{130}Sn+^{4}He, ^{110}Ru+^{128}Sn+^{4}He, ^{112}Ru+^{126}Sn+^{4}He. Here the minima found for ^{102}Zr+^{136}Xe+^{4}He is due to the presence of the neutron shell closure at N = 82 of ^{136}Xe. The fragment combination with ^{104}Mo+^{134}Te+^{4}He and ^{106}Mo+^{132}Te+^{4}He is due to the presence of the near doubly magic ^{134}Te (N = 82, Z = 52) and ^{132}Te (N = 80, Z = 52) respectively. The splitting ^{108}Ru+^{130}Sn+^{4}He is due to the near doubly magic ^{130}Sn (N = 80, Z = 50). The minima found for the fragment combinations ^{110}Ru+^{128}Sn+^{4}He and ^{112}Ru+^{126}Sn+^{4}He is due to the proton shell closure at Z = 50 of ^{128}Sn and ^{126}Sn respectively. The computed Q value and driving potential (V-Q) for various ternary fragmentations in the cold valley plot are given in **Table 4.1**. The barrier penetrability is calculated for each charge minimized fragment combinations found in the cold ternary fission of ^{242}Cm using the formalism described above. The relative yield is calculated and is plotted as a function of fragment mass number A_1 and A_2 in the **Figure 4.3**. From the figure it is clear that the combination ^{104}Mo+^{134}Te+^{4}He with ^{4}He as LCP possess highest yield due to the presence of near doubly magic nuclei ^{134}Te (N = 82, Z = 52). The next higher yield can be observed for the ^{108}Ru+^{130}Sn+^{4}He combination and is due to the near doubly magic ^{130}Sn (N = 80, Z = 50). The various other fragment combinations observed in this α-accompanied ternary fission of parent nuclei ^{242}Cm are ^{110}Ru+^{128}Sn+^{4}He, ^{106}Mo+^{132}Te+^{4}He, ^{102}Zr+^{136}Xe+^{4}He, ^{100}Zr+^{138}Xe+^{4}He. Of these the first one is attributed to the magic shell Z = 50 of ^{128}Sn, while the second fragment combination is due to the near doubly closed shell Z = 52 and N = 82 of ^{132}Te. The fragment combinations with ^{136}Xe and ^{138}Xe are due to the presence of neutron shell closure at N = 82 and near neutron shell closure at N = 84 respectively.

Table 4.1. The fragments occur in the cold valley with ^{4}He accompanied ternary fission of ^{242}Cm. The corresponding Q-values and (V-Q) for the touching configuration of fragments are listed.

First Fragment (A_1)	LCP (A_3)	Second Fragment (A_2)	Q-value (MeV)	V-Q (MeV)	First Fragment (A_1)	LCP (A_3)	Second Fragment (A_2)	Q-value (MeV)	V-Q (MeV)
^{4}He	^{4}He	^{234}U	11.808	1.4536	^{62}Cr	^{4}He	^{176}Yb	146.760	29.401
^{6}He	^{4}He	^{232}U	0.177	6.5438	^{64}Fe	^{4}He	^{174}Er	159.300	28.036
^{8}Be	^{4}He	^{230}Th	16.574	15.375	^{66}Fe	^{4}He	^{172}Er	158.932	27.491
^{10}Be	^{4}He	^{228}Th	13.000	14.535	^{68}Ni	^{4}He	^{170}Dy	169.504	27.013
^{12}Be	^{4}He	^{226}Th	4.105	19.823	^{70}Ni	^{4}He	^{168}Dy	170.154	25.521
^{14}C	^{4}He	^{224}Ra	30.533	17.358	^{72}Ni	^{4}He	^{166}Dy	169.190	25.694
^{16}O	^{4}He	^{222}Ra	24.364	20.515	^{74}Zn	^{4}He	^{164}Gd	177.907	26.024
^{18}O	^{4}He	^{220}Rn	42.549	24.737	^{76}Zn	^{4}He	^{162}Gd	178.963	24.243
^{20}O	^{4}He	^{218}Rn	43.366	21.288	^{78}Zn	^{4}He	^{160}Gd	177.804	24.724
^{22}O	^{4}He	^{216}Rn	42.847	19.452	^{80}Ge	^{4}He	^{158}Sm	187.165	23.379
^{24}Ne	^{4}He	^{214}Po	62.801	20.431	^{82}Ge	^{4}He	^{156}Sm	187.158	22.773
^{26}Ne	^{4}He	^{212}Po	62.270	18.822	^{84}Se	^{4}He	^{154}Nd	194.008	22.902
^{28}Mg	^{4}He	^{210}Pb	82.127	18.503	^{86}Se	^{4}He	^{152}Nd	193.032	23.329
^{30}Mg	^{4}He	^{208}Pb	83.012	15.654	^{88}Kr	^{4}He	^{150}Ce	196.918	25.393
^{32}Si	^{4}He	^{206}Hg	97.403	19.472	^{90}Kr	^{4}He	^{148}Ce	197.737	24.089
^{34}Si	^{4}He	^{204}Hg	97.027	18.032	^{92}Kr	^{4}He	^{146}Ce	196.784	24.596
^{36}Si	^{4}He	^{202}Hg	92.115	21.260	^{94}Sr	^{4}He	^{144}Ba	202.993	23.341
^{38}S	^{4}He	^{200}Pt	105.842	24.470	^{96}Sr	^{4}He	^{142}Ba	203.153	22.797
^{40}S	^{4}He	^{198}Pt	105.124	23.619	^{98}Zr	^{4}He	^{140}Xe	206.659	23.230
^{42}S	^{4}He	^{196}Pt	102.665	24.612	^{100}Zr	^{4}He	^{138}Xe	208.734	20.835
^{44}Ar	^{4}He	^{194}Os	117.490	25.501	^{102}Zr	^{4}He	^{136}Xe	210.403	18.882
^{46}Ar	^{4}He	^{192}Os	117.994	23.626	^{104}Mo	^{4}He	^{134}Te	215.272	16.969
^{48}Ca	^{4}He	^{190}W	130.985	25.166	^{106}Mo	^{4}He	^{132}Te	213.709	18.310
^{50}Ca	^{4}He	^{188}W	130.639	24.231	^{108}Ru	^{4}He	^{130}Sn	216.172	17.798
^{52}Ca	^{4}He	^{186}W	129.151	24.516	^{110}Ru	^{4}He	^{128}Sn	215.813	17.995
^{54}Ti	^{4}He	^{184}Hf	139.480	27.573	^{112}Ru	^{4}He	^{126}Sn	214.024	19.659
^{56}Ti	^{4}He	^{182}Hf	137.642	28.287	^{114}Pd	^{4}He	^{124}Cd	212.573	22.085
^{58}Cr	^{4}He	^{180}Yb	148.810	29.382	^{116}Pd	^{4}He	^{122}Cd	212.824	21.768
^{60}Cr	^{4}He	^{178}Yb	148.574	28.572	^{118}Pd	^{4}He	^{120}Cd	211.726	22.836

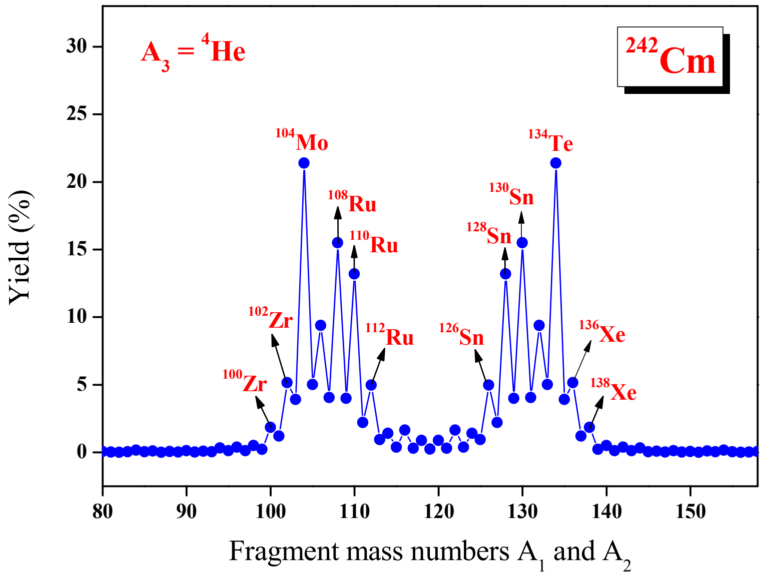

Figure 4.3. The calculated yields for the charge minimized third fragment ^{4}He, plotted as a function of mass numbers A_1 and A_2.

In order to make the yield of the fragments more comprehensive, we plotted a bar graph as shown in **Figure 4.4**, where the hatched bars represent odd mass numbers and the black ones belong to even mass numbers. The splitting $^{68}Ni+^{170}Dy+^{4}He$, $^{70}Ni+^{168}Dy+^{4}He$ and $^{72}Ni+^{166}Dy+^{4}He$ is due to the presence of magic number Z = 28 of Ni. The fragment combination $^{82}Ge+^{156}Sm+^{4}He$ and $^{84}Se+^{154}Nd+^{4}He$ is due to the presence of magic shell N = 50 of ^{82}Ge and ^{84}Se respectively.

The emission probability of Long Range Alpha particle can be defined as the ratio of penetrability of Long Range Alpha particle through the potential barrier (both internal and external barrier) to the disintegration per second of the alpha particle in spontaneous binary fission process.

$$Emission\ Probability = \frac{P_{LRA}^{Total}}{\lambda} = \frac{P_{LRA}^{int.} \cdot P_{LRA}^{ext.}}{\nu P} \qquad (4.2.1)$$

Here P_{LRA}^{Total} is the penetrability of the Long range Alpha particle through the potential barrier. λ, ν and P are the disintegration constant, assault frequency and the penetrability of the alpha particle respectively. $P_{LRA}^{ext.}$ is the penetrability of the Long

Range Alpha particle through the external potential barrier as given in the equation (4.1.9) and $P_{LRA}^{int.}$ is the penetrability of the Long Range Alpha particle through the internal potential barrier (overlap region) and is given as,

$$P_{LRA}^{int.} = \exp\left\{-\frac{2}{\hbar}\int_{z_0}^{z_1}\sqrt{2\mu(V-Q)}dz\right\}$$

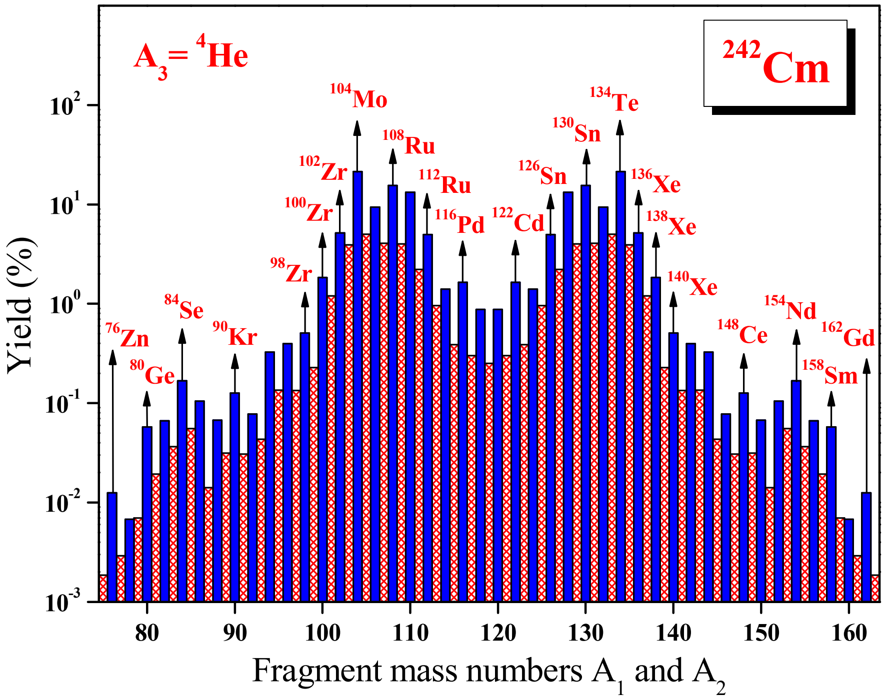

Figure 4.4. The calculated yields for the charge minimized third fragment ^{4}He, plotted as a function of mass numbers A_1 and A_2.

For the internal (overlap) region, the potential is taken as a simple power law interpolation. Here the first turning point is determined from the equation $V(z_0)=Q$, where Q is the decay energy, and the second turning point $z_1 = 0$ represent the touching configuration. The emission probability of the Long Range Alpha particle in the various ternary fragmentations of ^{242}Cm has been evaluated and is given in **Table 4.2**. Thus, we have shown that our formalism is able to compute the emission probability of the Long Range Alpha particle.

Table 4.2. The emission probability of the long range alpha particle for the various fragmentation channels in ternary fission of ^{242}Cm isotope.

Fragmentation channel	$P_{LRA}^{int.}$	$P_{LRA}^{ext.}$	P_{LRA}^{Total}	Emission Probability
^{102}Zr+^{4}He+^{136}Xe	7.96 x 10^{-2}	5.52 x 10^{-11}	4.39 x 10^{-12}	0.28 x 10^{-3}
^{104}Mo+^{4}He+^{134}Te	1.23 x 10^{-1}	2.29 x 10^{-10}	2.82 x 10^{-11}	1.83 x 10^{-3}
^{106}Mo+^{4}He+^{132}Te	9.08 x 10^{-2}	1.00 x 10^{-10}	9.08 x 10^{-12}	0.59 x 10^{-3}
^{108}Ru+^{4}He+^{130}Sn	9.16 x 10^{-2}	1.66 x 10^{-10}	1.52 x 10^{-11}	0.98 x 10^{-3}
^{110}Ru+^{4}He+^{128}Sn	9.88 x 10^{-2}	1.41 x 10^{-10}	1.39 x 10^{-11}	0.90 x 10^{-3}
^{112}Ru+^{4}He+^{126}Sn	7.01 x 10^{-2}	5.32 x 10^{-11}	3.72 x 10^{-12}	0.24 x 10^{-3}

4.2.2 ^{10}Be accompanied ternary fission

With ^{10}Be as the light charged particle, we get the potential energy surface as shown in the **Figure 4.5**. In the cold valley region, the minima occur for A_1 = ^{10}Be, ^{14}C, ^{16}C, ^{18}O, ^{20}O, ^{22}O, ^{24}Ne, ^{28}Mg, ^{32}Si, ^{34}Si, ^{36}Si, ^{38}S, ^{40}S, ^{42}S, ^{44}Ar, ^{46}Ar, ^{48}Ca, ^{50}Ca etc. The fragment combination ^{24}Ne+^{208}Pb+^{10}Be shows the deepest minimum in the cold valley which is due to the doubly magic ^{208}Pb (N = 126, Z = 82). The next minimum is found for the splitting ^{22}O+^{210}Po+^{10}Be which is due to the presence of the near doubly magic ^{210}Po (N = 126, Z = 84) and also due to ^{22}O, the nucleus with neutron shell closure at N = 8. The next minima is found for the fragment combination ^{10}Be+^{222}Ra+^{10}Be and ^{14}C+^{218}Rn+^{10}Be, of which minima for ^{14}C+^{218}Rn+^{10}Be is due to the neutron closed shell N = 8 of ^{14}C.

The minima found for the splitting ^{34}Si+^{200}Pt+^{10}Be and ^{50}Ca+^{182}Hf+^{10}Be is due to the presence of ^{34}Si (N = 20) and ^{50}Ca (Z = 20) respectively. The next deep valley occurs around ^{98}Zr for the fragment combination ^{94}Sr+^{138}Xe+^{10}Be, ^{96}Sr+^{136}Xe+^{10}Be, ^{98}Zr+^{134}Te+^{10}Be, ^{100}Zr+^{132}Te+^{10}Be, ^{102}Mo+^{130}Sn+^{10}Be. Here the minima observed for ^{98}Zr+^{134}Te+^{10}Be is due to the presence of near doubly magic ^{134}Te (N = 82, Z = 52). The next minima is due to the neutron shell closure at N = 82 of ^{136}Xe. The minima found for the fragment combinations ^{100}Zr+^{132}Te+^{10}Be and ^{102}Mo+^{130}Sn+^{10}Be is due to the near double magic ^{132}Te (N = 80, Z = 52) and ^{130}Sn

(N=80, Z=50) respectively. The computed Q value and driving potential (V-Q) for various ternary fragmentations in the cold valley plot are given in **Table 4.3**.

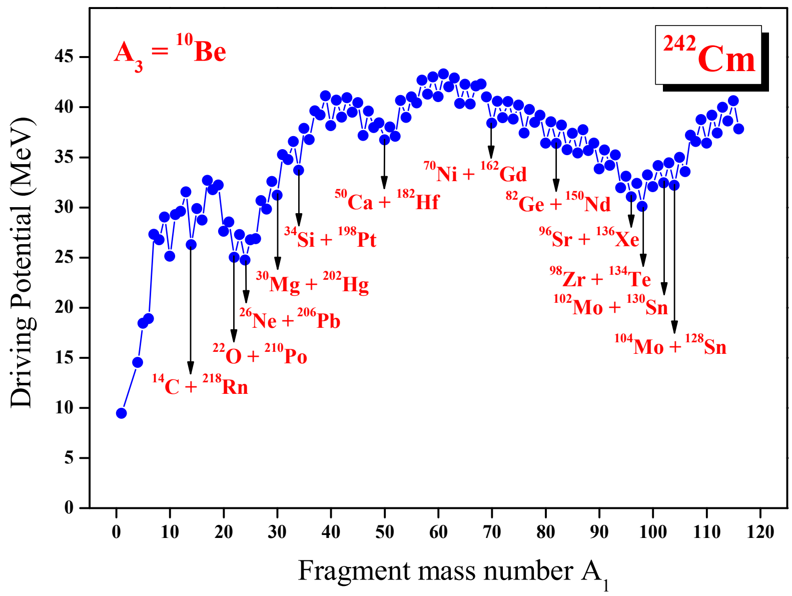

Figure 4.5. The driving potential for ^{242}Cm isotope with ^{10}Be as light charged particle, plotted as a function of mass number A_1.

The barrier penetrability is calculated for each charge minimized fragment combinations found in the cold ternary fission of ^{242}Cm using the formalism described above. The relative yield is calculated and is plotted as a function of fragment mass number A_1 and A_2 as shown in the **Figure 4.6**. From the figure it is clear that the fragment combination ^{98}Zr+^{134}Te+^{10}Be is the most favoured ternary splitting and it is due to the presence of near doubly magic ^{134}Te (Z = 52, N = 82). The various fragment combinations found in the ternary fission process are ^{106}Mo+^{126}Sn+^{10}Be, ^{104}Mo+^{128}Sn+^{10}Be, ^{102}Mo+^{130}Sn+^{10}Be, ^{100}Zr+^{132}Te+^{10}Be, ^{98}Zr+^{134}Te+^{10}Be, ^{96}Sr+^{136}Xe+^{10}Be and ^{94}Sr+^{138}Xe+^{10}Be. The first three combinations are attributed to the magic shell closure at Z = 50 of ^{126}Sn, ^{128}Sn and ^{130}Sn respectively. The fourth and fifth combinations is due to the near doubly magic ^{132}Te (N = 80, Z = 52) and ^{134}Te (N = 82, Z = 52) respectively. The last two fragment combinations are attributed to the presence of neutron shell closure at N = 82 and near neutron shell closure at N = 84 in ^{136}Xe and ^{138}Xe respectively. In order to make the yield of the fragments more comprehensive, we plotted a bar graph as shown in

Figure 4.7, where the hatched bars represent odd mass numbers and the black ones belong to even mass numbers. The splitting ^{82}Ge+^{150}Nd+^{10}Be and ^{84}Se+^{148}Ce+^{10}Be is due to the presence of magic shell closure at N = 50 of ^{82}Ge and ^{84}Se respectively.

Table 4.3. The fragments occur in the cold valley with ^{10}Be accompanied ternary fission of ^{242}Cm. The corresponding Q-values and (V-Q) for the touching configuration of fragments are listed.

First Fragment (A_1)	LCP (A_3)	Second Fragment (A_2)	Q-value (MeV)	V-Q (MeV)	First Fragment (A_1)	LCP (A_3)	Second Fragment (A_2)	Q-value (MeV)	V-Q (MeV)
^{4}He	^{10}Be	^{228}Th	13.006	14.535	^{62}Cr	^{10}Be	^{170}Er	143.197	42.022
^{6}He	^{10}Be	^{226}Th	1.408	18.903	^{64}Fe	^{10}Be	^{168}Dy	155.728	40.364
^{8}Be	^{10}Be	^{224}Ra	18.428	26.773	^{66}Fe	^{10}Be	^{166}Dy	154.849	40.319
^{10}Be	^{10}Be	^{222}Ra	15.268	25.118	^{68}Ni	^{10}Be	^{164}Gd	165.431	42.310
^{12}Be	^{10}Be	^{220}Ra	6.849	29.615	^{70}Ni	^{10}Be	^{162}Gd	165.691	38.404
^{14}C	^{10}Be	^{218}Rn	33.960	26.266	^{72}Ni	^{10}Be	^{160}Gd	164.364	38.938
^{16}C	^{10}Be	^{216}Rn	28.251	28.734	^{74}Zn	^{10}Be	^{158}Sm	173.204	38.809
^{18}O	^{10}Be	^{214}Po	47.450	31.753	^{76}Zn	^{10}Be	^{156}Sm	173.863	37.428
^{20}O	^{10}Be	^{212}Po	48.771	27.623	^{78}Zn	^{10}Be	^{154}Sm	172.135	38.486
^{22}O	^{10}Be	^{210}Po	48.870	25.018	^{80}Ge	^{10}Be	^{152}Nd	181.882	36.403
^{24}Ne	^{10}Be	^{208}Pb	69.897	24.742	^{82}Ge	^{10}Be	^{150}Nd	181.292	36.390
^{26}Ne	^{10}Be	^{206}Pb	65.504	26.872	^{84}Se	^{10}Be	^{148}Ce	188.543	35.748
^{28}Mg	^{10}Be	^{204}Hg	81.906	29.813	^{86}Se	^{10}Be	^{146}Ce	188.336	35.421
^{30}Mg	^{10}Be	^{202}Hg	78.427	31.225	^{88}Kr	^{10}Be	^{144}Ba	193.656	35.665
^{32}Si	^{10}Be	^{200}Pt	92.876	34.778	^{90}Kr	^{10}Be	^{142}Ba	195.000	33.853
^{34}Si	^{10}Be	^{198}Pt	92.060	33.692	^{92}Kr	^{10}Be	^{140}Ba	194.237	34.192
^{36}Si	^{10}Be	^{196}Pt	87.234	36.759	^{94}Sr	^{10}Be	^{138}Xe	201.015	31.962
^{38}Si	^{10}Be	^{194}Os	101.496	39.213	^{96}Sr	^{10}Be	^{136}Xe	201.557	31.063
^{40}S	^{10}Be	^{192}Os	100.919	38.157	^{98}Zr	^{10}Be	^{134}Te	206.027	30.111
^{42}S	^{10}Be	^{190}Os	98.545	39.011	^{100}Zr	^{10}Be	^{132}Te	203.767	32.077
^{44}Ar	^{10}Be	^{188}W	113.541	39.493	^{102}Mo	^{10}Be	^{130}Sn	205.901	32.436
^{46}Ar	^{10}Be	^{186}W	114.438	37.179	^{104}Mo	^{10}Be	^{128}Sn	205.916	32.193
^{48}Ca	^{10}Be	^{184}Hf	127.922	37.972	^{106}Mo	^{10}Be	^{126}Sn	204.354	33.568
^{50}Ca	^{10}Be	^{182}Hf	127.839	36.737	^{108}Mo	^{10}Be	^{124}Sn	201.194	36.580
^{52}Ca	^{10}Be	^{180}Hf	126.239	37.101	^{110}Ru	^{10}Be	^{122}Cd	202.881	36.411
^{54}Ti	^{10}Be	^{178}Yb	137.491	38.966	^{112}Ru	^{10}Be	^{120}Cd	201.784	37.425
^{56}Ti	^{10}Be	^{176}Yb	134.897	40.411	^{114}Pd	^{10}Be	^{118}Pd	201.077	38.628
^{58}Cr	^{10}Be	^{174}Er	145.978	41.308	^{116}Pd	^{10}Be	^{116}Pd	201.862	37.825
^{60}Cr	^{10}Be	^{172}Er	145.182	41.037					

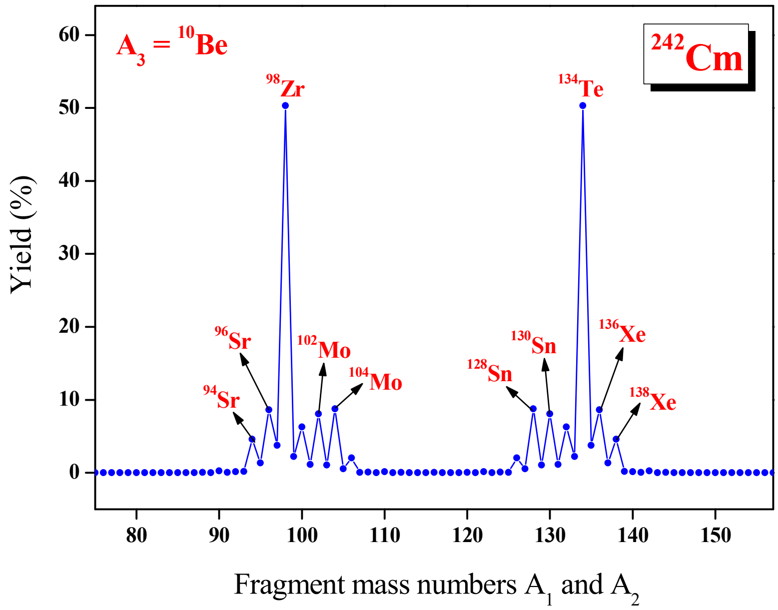

Figure 4.6. The calculated yields for the charge minimized third fragment ^{10}Be, plotted as a function of mass numbers A_1 and A_2.

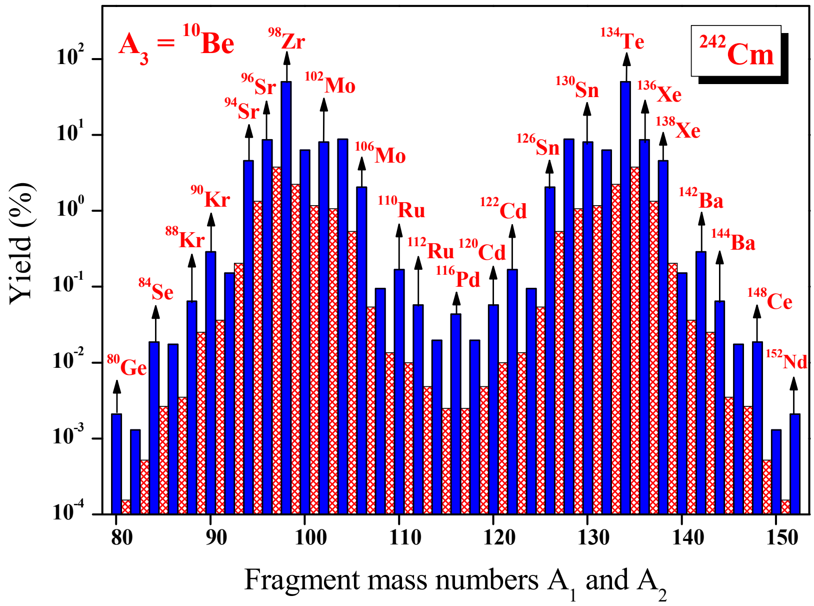

Figure 4.7. The calculated yields for the charge minimized third fragment ^{10}Be, plotted as a function of mass numbers A_1 and A_2.

4.2.3 ^{14}C accompanied ternary fission

In the case of ^{14}C as the light charged particle, the fragmentation potential is calculated and the driving potential is plotted as a function of A_1 in **Figure 4.8**. The minima in the cold valley is observed for A_1= ^{4}He, ^{10}Be, ^{12}Be, ^{14}C, ^{16}C, ^{20}O, ^{22}O, ^{26}Ne, ^{30}Mg, ^{32}Mg, ^{34}Si etc. Here the deepest minima is found for the fragment combination ^{4}He+^{224}Ra+^{14}C and is due to the doubly magic nuclei ^{4}He (N=2, Z=2).

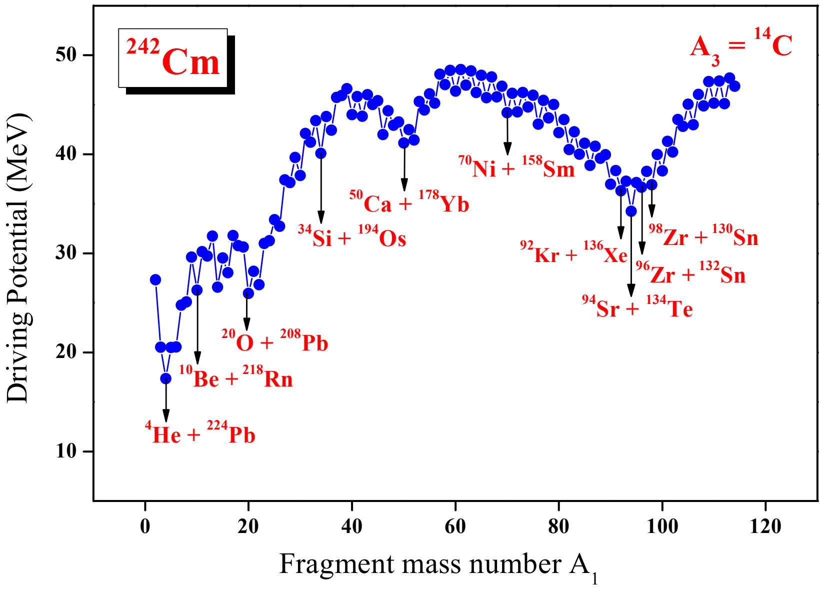

Figure 4.8. The driving potential for ^{242}Cm isotope with ^{14}C as light charged particle, plotted as a function of mass number A_1.

The second minima, due to the presence of doubly magic nuclei ^{208}Pb (N = 126 and Z = 82), is found for the fragment combination ^{20}O+^{208}Pb+^{14}C. The minima observed at ^{14}C+^{214}Po+^{14}C is due to the neutron shell closure at N = 8 of ^{14}C. The second minimum valley is found around ^{50}Ca for the fragment combinations ^{52}Ca+^{176}Yb+^{14}C, ^{50}Ca+^{178}Yb+^{14}C, ^{48}Ca+^{180}Yb+^{14}C and ^{46}Ar+^{182}Hf+^{14}C. The minima observed for ^{52}Ca, ^{50}Ca and ^{48}Ca is due to the presence of magic shell at Z = 20 and the minima seen for ^{46}Ar+^{182}Hf+^{14}C is due the neutron shell closure at N = 28 of ^{46}Ar. Another deep valley is found around ^{134}Te and is observed for the fragment combinations ^{138}Xe+^{90}Kr+^{14}C, ^{136}Xe+^{92}Kr+^{14}C, ^{134}Te+^{94}Sr+^{14}C, ^{132}Sn+^{96}Zr+^{14}C and ^{130}Sn+^{98}Zr+^{14}C. The deep minima found in fragment combination ^{134}Te+^{94}Sr+^{14}C is due to the near doubly magic nuclei ^{134}Te (N = 82 and Z = 52). The minima for ^{132}Sn+^{96}Zr+^{14}C is due to the doubly magic nuclei ^{132}Sn (N = 82 and Z = 50). The presence of the near doubly magic nuclei ^{130}Sn (N = 80, Z = 50) makes the fragment combination ^{130}Sn+^{98}Zr+^{14}C to be found at the minima of the cold valley. The computed Q value and driving potential $(V-Q)$ for various ternary fragmentations in the cold valley plot are given in **Table 4.4**.

The most possible fragment configuration to be observed in the ^{14}C accompanied ternary fission of ^{242}Cm can be obtained by calculating the relative yield and is plotted as a function of mass numbers A_1 and A_2 as shown in **Figure 4.9**. The most probable ternary fragment combination is obtained for ^{94}Sr+^{134}Te+^{14}C and is due to the presence of near double magic ^{134}Te (N = 82, Z = 52). The next higher yields are obtained for the fragment combinations ^{96}Zr+^{132}Sn+^{14}C and ^{98}Zr+^{130}Sn+^{14}C which possesses the doubly magic ^{132}Sn (N = 82, Z = 50) and near double magic shell of ^{130}Sn (N = 80, Z = 50) respectively. The fragment combinations ^{136}Xe+^{92}Kr+^{10}Be and ^{138}Xe+^{90}Kr+^{10}Be possesses the near doubly magic ^{134}Te (N = 82, Z = 52) and ^{138}Te (N = 84, Z = 52) respectively. For a better comparison of relative yield of all possible fragments, we have plotted a bar graph as shown in **Figure 4.10**, where the hatched one represents the fragments with odd mass number and the black histogram belongs to fragments with even mass number. The various fragment combinations that occur in this ternary fission process are ^{100}Zr+^{128}Sn+^{14}C, ^{102}Zr+^{126}Sn+^{14}C, ^{104}Mo+^{124}Cd+^{14}C, ^{106}Mo+^{122}Cd+^{14}C, ^{86}Se+^{142}Ba+^{14}C and ^{84}Se+^{144}Ba+^{14}C. The splitting found in fragment combinations ^{100}Zr+^{128}Sn+^{14}C and ^{102}Zr+^{126}Sn+^{14}C is due to the proton shell closure at Z = 50 of ^{128}Sn and ^{126}Sn respectively. The splitting for ^{86}Se+^{142}Ba+^{14}C and ^{84}Se+^{144}Ba+^{14}C is due to the neutron shell closure at N = 52 and N = 50 of ^{86}Se and ^{84}Se respectively.

The light particle accompanied ternary fission can occur only if the light charged particle is pre-formed inside the parent nucleus, as a cluster of nucleons (as in the α-decay process), before its emission [41]. Hence, we would like to point out that, our formalism is able to describe the emission of light clusters like ^{3}He, ^{3}H etc. It is also to be noted that, the present formalism could not be used in the case of protons and neutrons, as these particles are not preformed inside the parent nucleus before emission, but found on the surface of the parent nuclei.

Table 4.4. The fragments occur in the cold valley with ^{14}C accompanied ternary fission of ^{242}Cm. The corresponding Q-values and (V-Q) for the touching configuration of fragments are listed.

First Fragment (A_1)	LCP (A_3)	Second Fragment (A_2)	Q-value (MeV)	V-Q (MeV)	First Fragment (A_1)	LCP (A_3)	Second Fragment (A_2)	Q-value (MeV)	V-Q (MeV)
^{4}He	^{14}C	^{224}Ra	30.533	17.358	^{60}Cr	^{14}C	^{168}Dy	156.845	46.384
^{6}He	^{14}C	^{222}Ra	19.871	20.543	^{62}Cr	^{14}C	^{166}Dy	155.259	46.971
^{8}He	^{14}C	^{220}Ra	9.904	25.086	^{64}Fe	^{14}C	^{164}Gd	166.525	46.245
^{10}Be	^{14}C	^{218}Rn	33.960	26.266	^{66}Fe	^{14}C	^{162}Gd	166.133	45.716
^{12}Be	^{14}C	^{216}Rn	26.454	29.724	^{68}Ni	^{14}C	^{160}Sm	175.484	45.791
^{14}C	^{14}C	^{214}Po	53.235	26.591	^{70}Ni	^{14}C	^{158}Sm	176.249	44.182
^{16}C	^{14}C	^{212}Po	48.460	28.029	^{72}Ni	^{14}C	^{156}Sm	175.374	44.271
^{18}C	^{14}C	^{210}Po	42.818	30.770	^{74}Zn	^{14}C	^{154}Nd	183.222	44.768
^{20}O	^{14}C	^{208}Pb	69.737	25.943	^{76}Zn	^{14}C	^{152}Nd	184.237	43.039
^{22}O	^{14}C	^{206}Pb	66.290	26.822	^{78}Zn	^{14}C	^{150}Nd	182.947	43.671
^{24}Ne	^{14}C	^{204}Hg	82.427	31.266	^{80}Ge	^{14}C	^{148}Ce	191.718	42.178
^{26}Ne	^{14}C	^{202}Hg	78.652	32.727	^{82}Ge	^{14}C	^{146}Ce	192.835	40.472
^{28}Mg	^{14}C	^{200}Pt	93.405	37.125	^{84}Se	^{14}C	^{144}Ba	199.500	40.016
^{30}Mg	^{14}C	^{198}Pt	90.575	37.844	^{86}Se	^{14}C	^{142}Ba	200.131	38.864
^{32}Mg	^{14}C	^{196}Pt	85.261	41.223	^{88}Se	^{14}C	^{140}Ba	198.939	39.584
^{34}Si	^{14}C	^{194}Os	104.179	40.088	^{90}Kr	^{14}C	^{138}Xe	206.716	36.973
^{36}Si	^{14}C	^{192}Os	100.059	42.419	^{92}Kr	^{14}C	^{136}Xe	206.983	36.301
^{38}S	^{14}C	^{190}W	113.026	45.930	^{94}Sr	^{14}C	^{134}Te	213.167	34.231
^{40}S	^{14}C	^{188}W	113.293	44.006	^{96}Zr	^{14}C	^{132}Sn	213.774	36.670
^{42}S	^{14}C	^{186}W	111.934	43.826	^{98}Zr	^{14}C	^{130}Sn	213.211	36.915
^{44}Ar	^{14}C	^{184}Hf	125.958	45.020	^{100}Zr	^{14}C	^{128}Sn	211.529	38.325
^{46}Ar	^{14}C	^{182}Hf	127.567	41.979	^{102}Zr	^{14}C	^{126}Sn	209.394	40.233
^{48}Ca	^{14}C	^{180}Yb	140.610	42.937	^{104}Mo	^{14}C	^{124}Cd	208.843	42.829
^{50}Ca	^{14}C	^{178}Yb	141.068	41.146	^{106}Mo	^{14}C	^{122}Cd	208.538	42.971
^{52}Ca	^{14}C	^{176}Yb	139.535	41.436	^{108}Mo	^{14}C	^{120}Cd	206.504	44.887
^{54}Ti	^{14}C	^{174}Er	149.335	44.457	^{110}Ru	^{14}C	^{118}Pd	207.245	45.173
^{56}Ti	^{14}C	^{172}Er	147.479	45.157	^{112}Ru	^{14}C	^{116}Pd	207.246	45.118
^{58}Cr	^{14}C	^{170}Dy	157.275	47.025	^{114}Ru	^{14}C	^{114}Pd	205.498	46.855

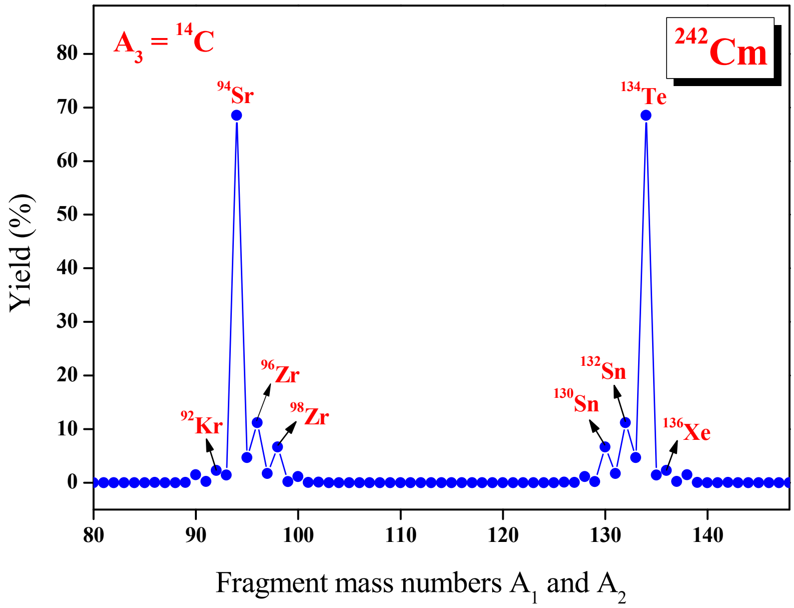

Figure 4.9. The calculated yields for the charge minimized third fragment ^{14}C, plotted as a function of mass numbers A_1 and A_2.

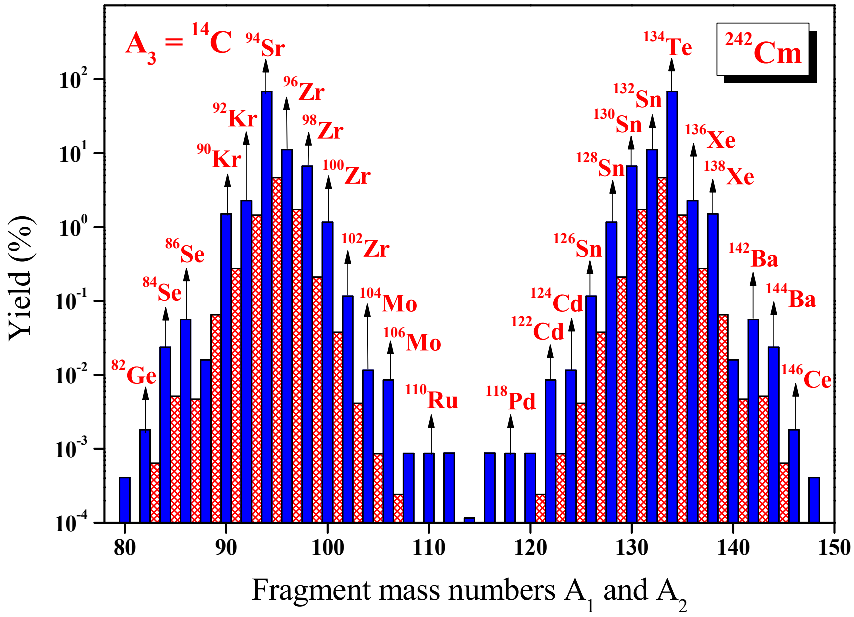

Figure 4.10. The calculated yields for the charge minimized third fragment ^{14}C, plotted as a function of mass numbers A_1 and A_2.

4.2.4 Summary

The ternary fragmentation of ^{242}Cm with light charged particle as ^{4}He, ^{10}Be, ^{14}C have been studied by taking Coulomb and proximity potential as interacting barrier with fragments in equatorial configuration. In each case, the fragmentation potential and Q-values are calculated for all possible fission components, which reveal that, the even mass number fragments are more favoured than odd mass number fragments. The favourable fragment combination is obtained by calculating the relative yield. For α- accompanied ternary fission the maximum yield is obtained for the fragmentation $^{104}Mo+^{4}He+^{134}Te$ and in the case of ^{10}Be as LCP, the maximum yield is found for the fragment combination $^{98}Zr+^{10}Be+^{134}Te$. In the case of ^{14}C accompanied ternary fission, the fragmentation combination $^{94}Sr+^{14}C+^{134}Te$ gives maximum yield and next higher yield is obtained for the fragment combination $^{96}Zr+^{132}Sn+^{14}C$. This reveals the role of doubly magic and near doubly magic shell closures (of ^{132}Sn and ^{134}Te) in light charged particle accompanied ternary fission.

4.3 Isotopic yield in alpha accompanied ternary fission of ^{252}Cf isotope

Taking the interacting barrier as the sum of Coulomb and proximity potential we have studied the relative yield in the ^{4}He accompanied ternary fragmentation of ^{252}Cf with fragments in the equatorial and collinear configuration. The relative yields obtained for the equatorial and collinear configuration are compared with the experimental yield reported by Ramayya *et al.,* [8]. In the present work we have considered the distance of separation between the fragments as equal i.e. $z_{12} = z_{23} = z_{13}$ in equatorial configuration, and the distance $z_{12} = z_{23}$ in collinear configuration.

4.3.1 Ternary fission with fragments in equatorial configuration

The driving potential for the alpha accompanied ternary fission of ^{252}Cf in the equatorial emission of fragments is calculated and plotted as a function of mass number A_1 and is shown in **Figure 4.11**. Here the first minimum is found for the fragment combination $^{4}He+^{4}He+^{244}Pu$ which possess a lower Q value of 11.3782

MeV. In addition to alpha particle, the fragment configuration with A_1= ^{10}Be, ^{14}C, ^{16}C, ^{18}C, ^{20}O, ^{22}O, ^{24}O, ^{26}Ne, ^{28}Ne, ^{30}Mg, ^{32}Mg, ^{34}Si, ^{36}Si etc. occurs at the minimum of the cold valley. Moving on to the fission region, three deep valleys are found, one at ^{42}S+^{4}He+^{206}Hg, second at ^{82}Ge+^{4}He+^{166}Gd and the third valley occurs at ^{116}Pd+^{4}He+^{132}Sn. The fragment combinations with lower mass numbers (A<80) may not be significant because of their lower Q value but the fission fragments occurs around ^{116}Pd+^{4}He+^{132}Sn may be the most probable fission fragments because of their higher Q values. The fragment combination ^{116}Pd+^{4}He+^{132}Sn possess the double magicity of ^{132}Sn (N=82, Z=50) and hence may be energetically the most favoured fission fragments than the others which can be verified through the calculation of penetrability.

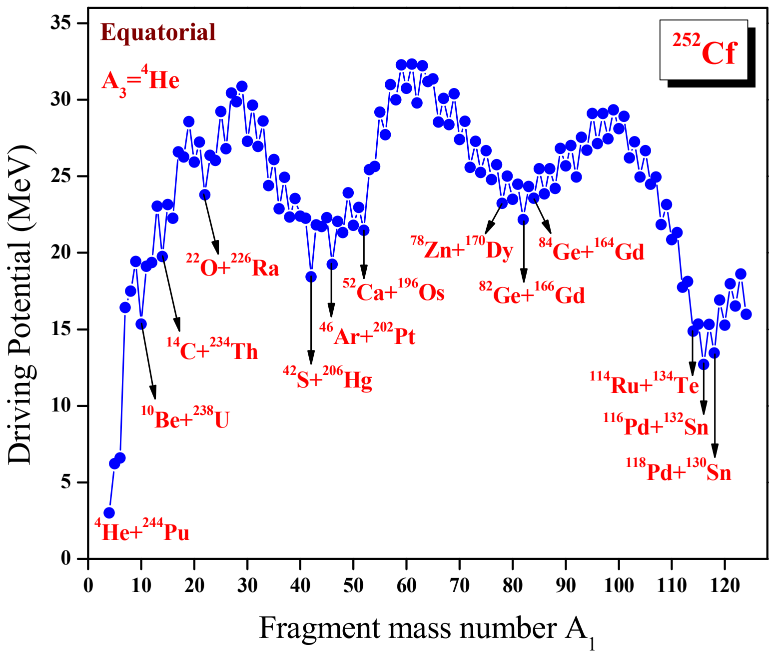

Figure 4.11. The driving potential for the ternary fission of ^{252}Cf isotope keeping ^{4}He as light charged particle, with fragments in the equatorial configuration, plotted as a function of mass number A_1.

The barrier penetrability is calculated for each charge minimized fragment combinations found in the cold ternary fission of ^{252}Cf using the formalism described above. The relative yield is calculated and plotted as a function of mass number A_1 and A_2 as shown in **Figure 4.12(a)**.

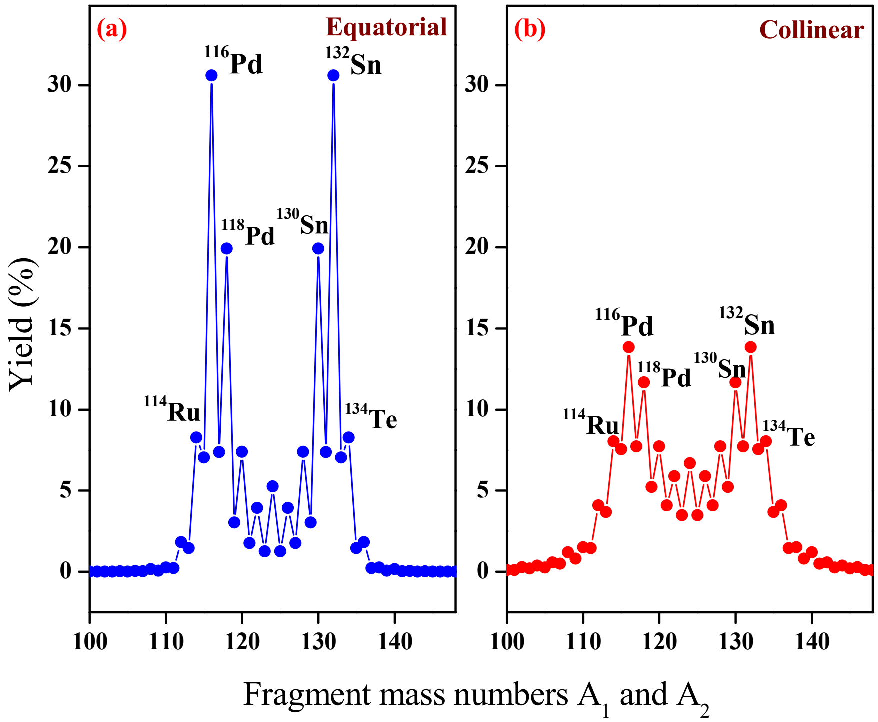

Figure 4.12. The calculated yields for the ternary fission of ^{252}Cf isotope keeping the third fragment as ^{4}He, is plotted as a function of mass numbers A_1 and A_2 with fragments in (a) equatorial configuration (b) collinear configuration.

The highest yield is obtained for the fragment combination ^{116}Pd+^{4}He+^{132}Sn which possess doubly magic nuclei ^{132}Sn (N=82, Z=50). The next higher yield is found for the splitting ^{118}Pd+^{4}He+^{130}Sn which is due to the near double magic nuclei ^{130}Sn (N=80, Z=50). The fragment combination ^{114}Ru+^{4}He+^{134}Te and ^{120}Pd+^{4}He+^{128}Sn have a probable yield due to the near doubly closed shell effect of ^{134}Te (N=82, Z=52) and proton shell closure of ^{128}Sn (Z=50) respectively. These results indicate that the fragment combinations with doubly or near doubly closed shell and with higher Q values are the most probable one in the ^{4}He accompanied ternary fission of ^{252}Cf with the fragments in the equatorial configuration. In order to get a better view of the result, a histogram is plotted in which the hatched bars belongs to odd mass numbers and dark ones belongs to even mass numbers as shown in **Figure 4.13**.

Table 4.5. The fragments in the cold reaction valley for the ^{4}He accompanied ternary fission of ^{252}Cf in equatorial configuration. The corresponding Q-values and (V-Q) for the touching configuration of fragments are listed.

First Fragment (A_1)	LCP (A_3)	Second Fragment (A_2)	Q-value (MeV)	V-Q (MeV)	First Fragment (A_1)	LCP (A_3)	Second Fragment (A_2)	Q-value (MeV)	V-Q (MeV)
^{4}He	^{4}He	^{244}Pu	11.3782	3.0027	^{66}Fe	^{4}He	^{182}Yb	162.748	28.551
^{6}He	^{4}He	^{242}Pu	1.29939	6.5880	^{68}Fe	^{4}He	^{180}Yb	162.040	28.362
^{8}Be	^{4}He	^{240}U	15.9524	17.486	^{70}Ni	^{4}He	^{178}Er	173.474	27.406
^{10}Be	^{4}He	^{238}U	13.6935	15.350	^{72}Ni	^{4}He	^{176}Er	174.466	25.582
^{12}Be	^{4}He	^{236}U	6.08578	19.362	^{74}Ni	^{4}He	^{174}Er	174.020	25.244
^{14}C	^{4}He	^{234}Th	29.9762	19.748	^{76}Zn	^{4}He	^{172}Dy	183.923	24.779
^{16}C	^{4}He	^{232}Th	24.4674	22.247	^{78}Zn	^{4}He	^{170}Dy	184.753	23.227
^{18}C	^{4}He	^{230}Th	17.8258	26.254	^{80}Zn	^{4}He	^{168}Dy	183.818	23.484
^{20}O	^{4}He	^{228}Ra	40.8716	25.931	^{82}Ge	^{4}He	^{166}Gd	193.555	22.163
^{22}O	^{4}He	^{226}Ra	40.6604	23.782	^{84}Ge	^{4}He	^{164}Gd	191.528	23.572
^{24}O	^{4}He	^{224}Ra	36.2828	26.028	^{86}Se	^{4}He	^{162}Sm	198.643	23.845
^{26}Ne	^{4}He	^{222}Rn	56.7571	26.786	^{88}Se	^{4}He	^{160}Sm	197.729	24.201
^{28}Ne	^{4}He	^{220}Rn	51.7064	29.869	^{90}Kr	^{4}He	^{158}Nd	202.629	25.671
^{30}Mg	^{4}He	^{218}Po	74.1353	27.291	^{92}Kr	^{4}He	^{156}Nd	202.849	24.952
^{32}Mg	^{4}He	^{216}Po	72.6551	26.944	^{94}Kr	^{4}He	^{154}Nd	200.638	26.701
^{34}Si	^{4}He	^{214}Pb	93.7478	24.385	^{96}Sr	^{4}He	^{152}Ce	205.600	27.121
^{36}Si	^{4}He	^{212}Pb	93.5472	22.882	^{98}Sr	^{4}He	^{150}Ce	204.883	27.435
^{38}Si	^{4}He	^{210}Pb	92.5081	22.336	^{100}Sr	^{4}He	^{148}Ce	203.838	28.112
^{40}S	^{4}He	^{208}Hg	109.718	22.392	^{102}Zr	^{4}He	^{146}Ba	210.144	26.208
^{42}S	^{4}He	^{206}Hg	112.192	18.428	^{104}Zr	^{4}He	^{144}Ba	211.107	24.935
^{44}S	^{4}He	^{204}Hg	107.504	21.723	^{106}Mo	^{4}He	^{142}Xe	214.981	24.466
^{46}Ar	^{4}He	^{202}Pt	126.032	19.246	^{108}Mo	^{4}He	^{140}Xe	217.358	21.835
^{48}Ar	^{4}He	^{200}Pt	122.651	21.314	^{110}Mo	^{4}He	^{138}Xe	218.131	20.844
^{50}Ca	^{4}He	^{198}Os	137.039	21.805	^{112}Ru	^{4}He	^{136}Te	223.665	17.745
^{52}Ca	^{4}He	^{196}Os	136.150	21.462	^{114}Ru	^{4}He	^{134}Te	226.368	14.879
^{54}Ca	^{4}He	^{194}Os	130.827	25.623	^{116}Pd	^{4}He	^{132}Sn	229.986	12.708
^{56}Ti	^{4}He	^{192}W	142.470	27.723	^{118}Pd	^{4}He	^{130}Sn	229.132	13.456
^{58}Ti	^{4}He	^{190}W	139.100	30.003	^{120}Pd	^{4}He	^{128}Sn	227.252	15.263
^{60}Cr	^{4}He	^{188}Hf	150.990	30.742	^{122}Cd	^{4}He	^{126}Cd	226.479	16.518
^{62}Cr	^{4}He	^{186}Hf	150.920	29.792	^{124}Cd	^{4}He	^{124}Cd	227.013	15.967
^{64}Cr	^{4}He	^{184}Hf	148.570	31.180					

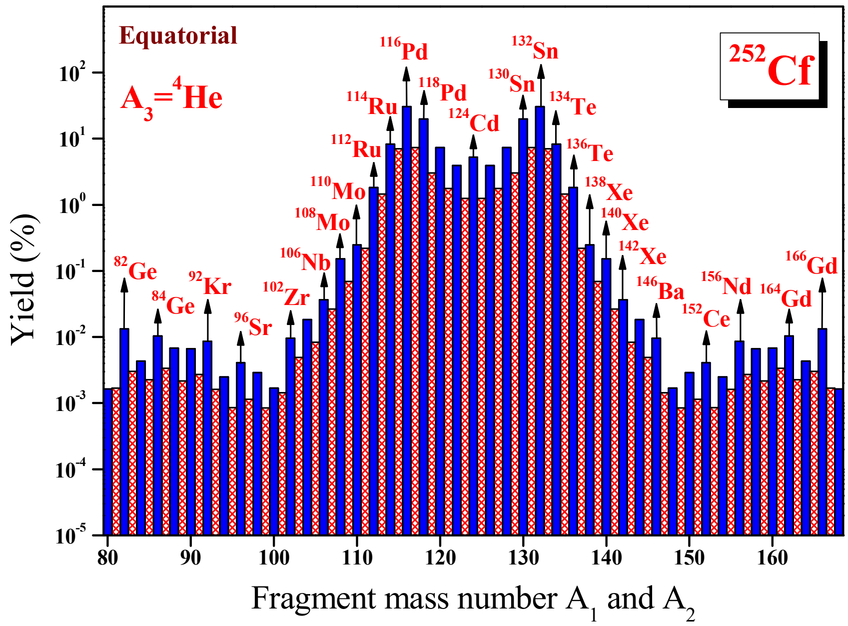

Figure 4.13. The calculated yields for the ternary fission of ^{252}Cf isotope keeping the third fragment as ^{4}He, with fragments in equatorial configuration is plotted as a function of mass numbers A_1 and A_2.

4.3.2 Ternary fission with fragments in collinear configuration

For collinear configuration, the light charged particle ^{4}He (A_2) is considered in between the other two fragments A_1 and A_3. The driving potential is calculated for each fragment combinations and plotted as a function of mass number A_1 as shown in **Figure 4.14**. The first minimum is found for the fragment combination with ^{4}He. The other minima is found for the fragment combination with A_1 = ^{4}He, ^{8}Be, ^{10}Be, ^{14}C, ^{18}O, ^{20}O, ^{22}O, ^{24}Ne, ^{26}Ne, ^{28}Mg, ^{30}Mg, ^{32}Si, ^{34}Si etc. The fragment combination ^{116}Pd+^{4}He+^{132}Sn which possesses the doubly magic nuclei ^{132}Sn (N=82, Z=50) lies deepest in the cold valley plot. It is to be noted that the minima for the fragment combination ^{116}Pd+^{4}He+^{132}Sn lies deeper than the minima found for the splitting ^{4}He+^{4}He+^{244}Pu. Other deep valleys are found around the fragment combinations ^{82}Ge+^{4}He+^{166}Gd and ^{42}S+^{4}He+^{206}Hg which is due to the neutron closure of ^{82}Ge (N=50) and near double magicity of ^{206}Hg (N=126, Z=80) respectively.

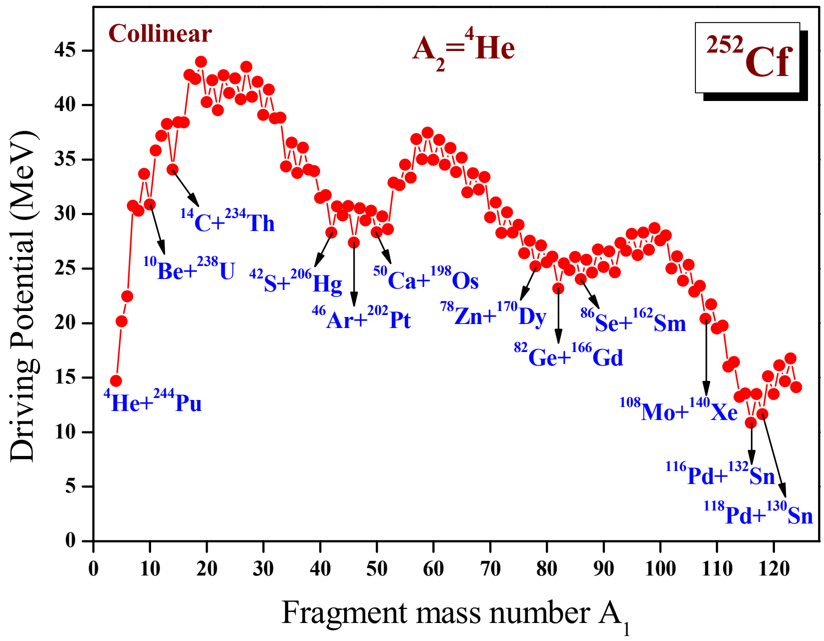

Figure 4.14. The driving potential for the ternary fission of ^{252}Cf isotope, keeping ^{4}He as light charged particle, with fragments in the collinear configuration is plotted as a function of mass number A_1.

For each charge minimized fragment combinations, the barrier penetrability is calculated. The relative yield is calculated and plotted as function of mass numbers A_1 and A_3 as shown in **Figure 4.12(b)**. The highest yield is found for the fragment combination ^{116}Pd+^{4}He+^{132}Sn, which possess doubly magic nuclei ^{132}Sn (N=82, Z=50). The yield obtained for the fragment combinations ^{118}Pd+^{4}He+^{130}Sn and ^{120}Pd+^{4}He+^{128}Sn are due to the presence of near double magicity of ^{130}Sn (N=80, Z=50) and proton shell closure of ^{128}Sn (Z=50) respectively. The presence of near doubly magic nuclei ^{134}Te (N=82, Z=52) makes the fragment combination ^{114}Ru+^{4}He+^{134}Te with relatively higher yield. For a better comparison of the yield for different fragment combinations, a histogram is plotted in which the yield as a function of mass numbers A_1 and A_3 is shown in **Figure 4.15**. The comparison of **Figures 4.12(a)** and **4.12(b)** reveals that in alpha accompanied ternary fission of ^{252}Cf the overall relative yield for equatorial configuration is higher than that of collinear configuration. This observation suggest that equatorial configuration is the preferred configuration for the light charged particle (^{4}He, ^{10}Be etc) accompanied ternary fission in ^{252}Cf isotope.

Table 4.6. The fragments in the cold reaction valley for the ^{4}He accompanied ternary fission of ^{252}Cf in collinear configuration. The corresponding Q-values and (V-Q) for the touching configuration of fragments are listed.

First Fragment (A_1)	LCP (A_2)	Third Fragment (A_3)	Q-value (MeV)	V-Q (MeV)	First Fragment (A_1)	LCP (A_2)	Third Fragment (A_3)	Q-value (MeV)	V-Q (MeV)
^{4}He	^{4}He	^{244}Pu	11.3781	14.698	^{66}Fe	^{4}He	^{182}Yb	162.748	31.991
^{6}He	^{4}He	^{242}Pu	1.29939	22.448	^{68}Fe	^{4}He	^{180}Yb	162.040	32.238
^{8}Be	^{4}He	^{240}U	15.9524	30.285	^{70}Ni	^{4}He	^{178}Er	173.474	29.686
^{10}Be	^{4}He	^{238}U	13.6934	30.877	^{72}Ni	^{4}He	^{176}Er	174.466	28.262
^{12}Be	^{4}He	^{236}U	6.08578	37.159	^{74}Ni	^{4}He	^{174}Er	174.020	28.302
^{14}C	^{4}He	^{234}Th	29.9761	34.082	^{76}Zn	^{4}He	^{172}Dy	183.923	26.397
^{16}C	^{4}He	^{232}Th	24.4673	38.396	^{78}Zn	^{4}He	^{170}Dy	184.753	25.190
^{18}O	^{4}He	^{230}Ra	39.8769	42.382	^{80}Ge	^{4}He	^{168}Gd	191.505	25.562
^{20}O	^{4}He	^{228}Ra	40.8716	40.278	^{82}Ge	^{4}He	^{166}Gd	193.555	23.164
^{22}O	^{4}He	^{226}Ra	40.6604	39.508	^{84}Ge	^{4}He	^{164}Gd	191.528	24.866
^{24}Ne	^{4}He	^{224}Rn	57.1166	41.096	^{86}Se	^{4}He	^{162}Sm	198.643	24.016
^{26}Ne	^{4}He	^{222}Rn	56.7571	40.516	^{88}Se	^{4}He	^{160}Sm	197.729	24.634
^{28}Mg	^{4}He	^{220}Po	73.3658	40.766	^{90}Kr	^{4}He	^{158}Nd	202.629	25.143
^{30}Mg	^{4}He	^{218}Po	74.1353	39.098	^{92}Kr	^{4}He	^{156}Nd	202.849	24.656
^{32}Si	^{4}He	^{216}Pb	90.2078	38.762	^{94}Kr	^{4}He	^{154}Nd	200.638	26.622
^{34}Si	^{4}He	^{214}Pb	93.7478	34.364	^{96}Sr	^{4}He	^{152}Ce	205.600	26.227
^{36}Si	^{4}He	^{212}Pb	93.5472	33.771	^{98}Sr	^{4}He	^{150}Ce	204.883	26.728
^{38}Si	^{4}He	^{210}Pb	92.5081	34.075	^{100}Sr	^{4}He	^{148}Ce	203.838	27.578
^{40}S	^{4}He	^{208}Hg	109.718	31.479	^{102}Zr	^{4}He	^{146}Ba	210.144	25.004
^{42}S	^{4}He	^{206}Hg	112.192	28.296	^{104}Zr	^{4}He	^{144}Ba	211.107	23.874
^{44}Ar	^{4}He	^{204}Pt	124.203	29.882	^{106}Mo	^{4}He	^{142}Xe	214.981	22.893
^{46}Ar	^{4}He	^{202}Pt	126.032	27.373	^{108}Mo	^{4}He	^{140}Xe	217.358	20.379
^{48}Ca	^{4}He	^{200}Os	136.614	29.400	^{110}Mo	^{4}He	^{138}Xe	218.131	19.489
^{50}Ca	^{4}He	^{198}Os	137.039	28.325	^{112}Ru	^{4}He	^{136}Te	223.665	16.022
^{52}Ca	^{4}He	^{196}Os	136.150	28.605	^{114}Ru	^{4}He	^{134}Te	226.368	13.231
^{54}Ti	^{4}He	^{194}W	143.740	32.655	^{116}Pd	^{4}He	^{132}Sn	229.986	10.845
^{56}Ti	^{4}He	^{192}W	142.470	33.343	^{118}Pd	^{4}He	^{130}Sn	229.132	11.641
^{58}Cr	^{4}He	^{190}Hf	151.480	35.037	^{120}Pd	^{4}He	^{128}Sn	227.252	13.482
^{60}Cr	^{4}He	^{188}Hf	150.990	34.975	^{122}Cd	^{4}He	^{126}Cd	226.479	14.665
^{62}Cr	^{4}He	^{186}Hf	150.920	34.526	^{124}Cd	^{4}He	^{124}Cd	227.013	14.122
^{64}Fe	^{4}He	^{184}Yb	161.370	33.859					

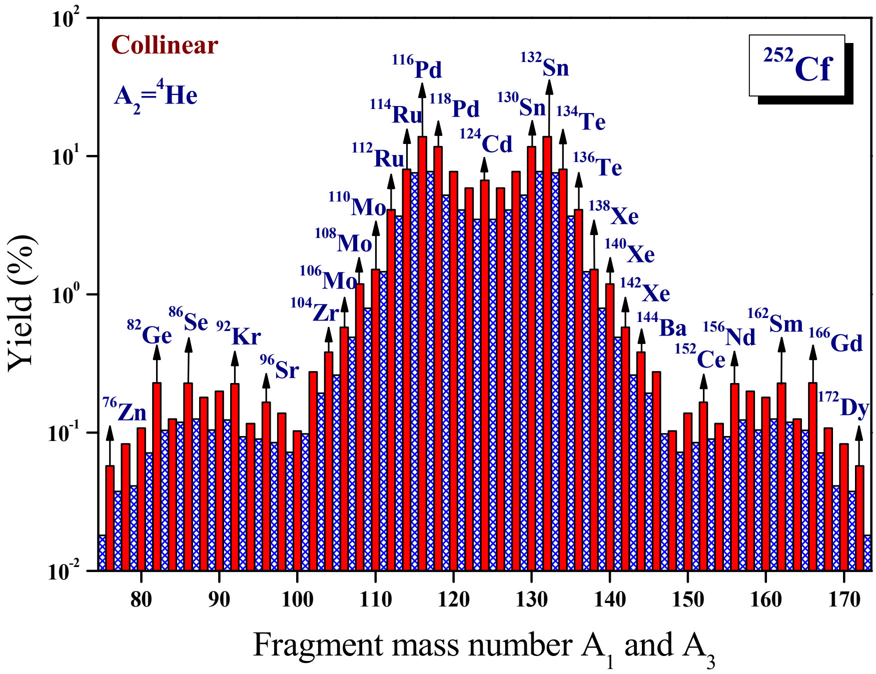

Figure 4.15. The calculated yields for the ternary fission of ^{252}Cf isotope keeping the third fragment as ^{4}He, with fragments in the collinear configuration is plotted as a function of mass numbers A_1 and A_3.

The experimental observation by Oertzen *et al.,* [29] suggest that the ternary fragmentation of heavy nuclei into three similar sized nuclei is only possible in a collinear geometry, which indicates to the fact that, for the ternary fission accompanied by light charged nuclei (^{4}He, ^{10}Be etc.), the most favourable mode of configuration is the triangular (equatorial) one. Using the Three Cluster Model (TCM), Manimaran *et al.,* have studied the overall relative yields for all the third fragments in the ternary fission of ^{252}Cf [26] and the authors have obtained that the light charged fragments (^{4}He, ^{10}Be etc.) prefer the equatorial configuration, while the heavy third fragments prefer the collinear configuration. In **Figure 4.16**, we have compared the individual yields obtained for the alpha accompanied ternary fission of ^{252}Cf in equatorial and collinear configuration with the experimental data [8]. It is to be noted from the figure that the yield for the equatorial configuration is more close to the experimental yield than that for the collinear configuration.

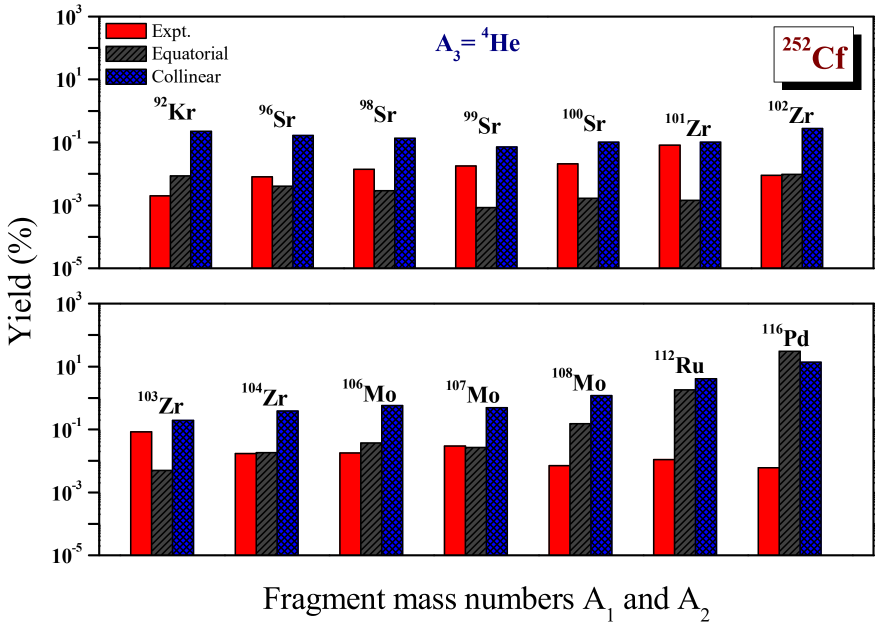

Figure 4.16. The yields obtained for the equatorial and collinear configuration of fragments in the ternary fission of ^{252}Cf isotope and their comparison with the experimental data.

According to Carjan [41] the long range alpha (LRA) emission is possible only if the α cluster is formed inside the fissioning nucleus and should gain enough energy to overcome the Coulomb barrier of the scission nucleus. Serot and Wagemans [19] demonstrated that the emission probability of long range alpha particle is strongly dependent on the spectroscopic factor or α cluster preformation factor S_α , which can be calculated in a semi-empirical way proposed by Blendowske *et al.,* [42] as, $S_\alpha = b\lambda_e / \lambda_{WKB}$ where *b* is the branching ratio for the ground state to ground state transition, λ_e is the experimental α decay constant and λ_{WKB} is the α decay constant calculated from the WKB approximation. Vermote *et al.,* [21] proved that ^{4}He emission probability in spontaneous fission is about 20% higher than for neutron induced fission. The absolute emission probability is given by,

$$\frac{LRA}{B} = S_\alpha P_{LRA} \qquad 4.3.1$$

With P_{LRA} as the probability of the alpha particle when it is already present in fissioning nucleus given as,

$$P_{LRA} = \exp\left\{ -\frac{2}{\hbar}\int_{z_0}^{z_1} \sqrt{2\mu(V-Q)}\,dz \right\} \qquad 4.3.2$$

Here the first turning point is determined from the equation $V(z_0)=Q$, where Q is the decay energy, and the second turning point $z_1=0$ represent the touching configuration. For the internal (overlap) region, the potential is taken as a simple power law interpolation. We have computed the emission probabilities of long range alpha particle *LRA/B* in the case of ^{252}Cf isotope and the predicted value is 6.0158x10^{-3}, which is comparable with the experimental value (3.06±0.11)x10^{-3} reported by Wild *et al.,* [43] and (2.56±0.07)x10^{-3} reported by Vermote *et al.,* [22].

4.3.3 Summary

The ternary fission of ^{252}Cf with ^{4}He as light charged particle for the equatorial and collinear emission of fragments is studied by taking the interacting barrier as the sum of Coulomb and proximity potential. In both equatorial and collinear mode of ternary fission, the highest yield is obtained for the fragment combination ^{116}Pd+^{4}He+^{132}Sn which is due to the presence of doubly magic nuclei ^{132}Sn (N=82, Z=50) and higher Q value. The yield obtained for the fragment combinations ^{118}Pd+^{4}He+^{130}Sn and ^{114}Ru+^{4}He+^{134}Te possess near doubly magic nuclei ^{130}Sn (N=80, Z=50) and ^{134}Te (N=82, Z=52) respectively. Hence we can conclude that the presence of doubly or near doubly magic nuclei (^{132}Sn, ^{130}Sn etc), and higher Q value plays an important role in the alpha accompanied ternary fission of ^{252}Cf. The comparison of the overall relative yield for equatorial configuration with that of collinear configuration points to the fact that equatorial configuration is the preferred configuration for the light charged particle (^{4}He, ^{10}Be etc) accompanied ternary fission in ^{252}Cf isotope. The individual yields obtained for the alpha accompanied ternary fission of ^{252}Cf in equatorial and collinear configuration are compared with the experimental data [8]. The emission probability of long range alpha particle from ^{252}Cf isotope, LRA/B is computed using our formalism, and is found to be in agreement with experimental value [22, 43].

4.4 Ternary fission of $^{250,252}Cf$ isotopes with ^{3}H and ^{6}He as light charged particle

The cold ternary fission of $^{250,252}Cf$ isotope with ^{3}H and ^{6}He as light charged particle in both equatorial and collinear configuration of fragments has studied using Unified ternary fission model.

4.4.1 ^{3}H accompanied ternary fission of $^{250,252}Cf$ isotopes with fragments in equatorial configuration.

The spontaneous cold ternary fission of ^{250}Cf and ^{252}Cf isotopes has been studied with ^{3}H as light charged particle using the Unified ternary fission model (UTFM). In the ^{3}H accompanied ternary fission of ^{250}Cf isotope, the driving potential is calculated for all possible fragment combinations. **Figure 4.17(a)** represents the plot of driving potential versus fragment mass number A_1 found in the ternary fission of ^{250}Cf isotope with ^{3}H as light charged particle. Here the minimum is found for the fragment combination with fragment mass number A_1 = ^{8}Be, ^{11}B, ^{12}B, ^{13}B, ^{14}C, ^{15}C, ^{16}C, ^{17}N, ^{18}C, ^{19}N, ^{20}O, ^{21}O, ^{22}O, ^{23}F, ^{24}Ne etc. The minimum found for the fragment combination $^{40}S+^{3}H+^{207}Tl$ is due to the presence of near doubly magic nucleus ^{207}Tl (N=126, Z=81). The minimum found around the fragment combination $^{82}Ge+^{3}H+^{165}Tb$ is due to the presence of neutron magic number N=50 of ^{82}Ge.

The deepest minimum found around the fragment combination $^{114}Pd+^{3}H+^{133}Sb$ is due to the presence of near doubly magic nucleus ^{133}Sb (N=82, Z=51), which may be the most suitable fragment combination in this ternary fission process. This can be verified through the calculation of barrier penetrability and the relative yield of fragment combinations obtained in the cold reaction valley. The barrier penetrability and hence the relative yield is calculated for each fragment combination found in the cold reaction valley plot. **Figure 4.18(a)** represents the relative yield plotted as a function of fragment mass numbers A_1 and A_2. From the plot, it is clear that the highest relative yield is obtained for the fragment combination $^{114}Pd+^{3}H+^{133}Sb$, which includes the presence of near doubly magic nucleus ^{133}Sb. The second highest relative yield is obtained for the fragment combination $^{117}Ag+^{3}H+^{130}Sn$, which includes the presence of near doubly magic nucleus ^{130}Sn (N=80, Z=50). The next highest relative yield is obtained for the fragment combination $^{119}Ag+^{3}H+^{128}Sn$ which includes the presence of proton shell closure Z=50 of ^{128}Sn.

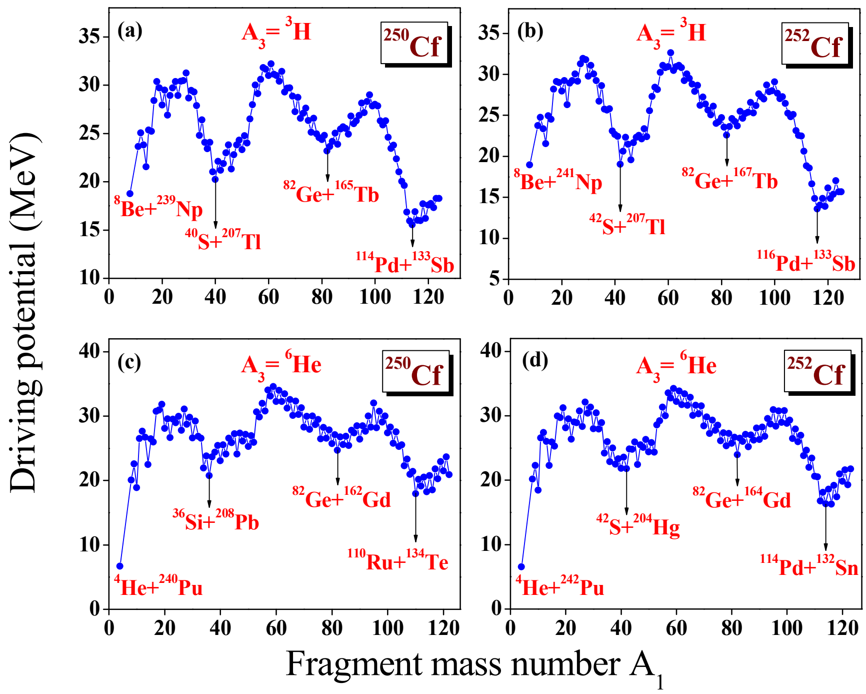

Figure 4.17. The driving potential is plotted as a function of fragment mass number A_1 in the case of ^{3}H and ^{6}He accompanied ternary fission of $^{250,252}Cf$ isotopes with fragments in equatorial configuration.

In the ^{3}H accompanied ternary fission of ^{252}Cf isotope, the driving potential is calculated and plotted as a function of fragment mass number A_1 as shown in **Figure 4.17(b)**. Here the deepest minimum is found for the fragment combination $^{116}Pd+^{3}H+^{133}Sb$, which includes the presence of near doubly magic nucleus ^{133}Sb (N=82, Z=51). The minima found around the fragment combinations $^{42}S+^{3}H+^{207}Tl$ and $^{82}Ge+^{3}H+^{167}Tb$ are due to the presence of near doubly magic nucleus ^{207}Tl (N=126, Z=81) and neutron shell closure N=50 of ^{82}Ge respectively. The relative yield is calculated for all possible fragmentations and plotted as a function of fragment mass numbers A_1 and A_2 as shown in **Figure 4.18(b)**. From the plot, it is clear that the highest relative yield is found for the fragment combination $^{116}Pd+^{3}H+^{133}Sb$, which is the same fragment combination with least driving potential in the cold reaction valley plot. Also the fragment combination possess the presence of near doubly magic nucleus ^{133}Sb (N=82, Z=51). The next highest relative yield found for the fragment combination $^{119}Ag+^{3}H+^{130}Sn$ is due to the presence of near doubly magic nucleus ^{130}Sn (N=80, Z=50). The presence of doubly magic nucleus ^{132}Sn and high Q value makes the fragment splitting $^{117}Ag+^{3}H+^{132}Sn$ a more probable one in this ternary fission process.

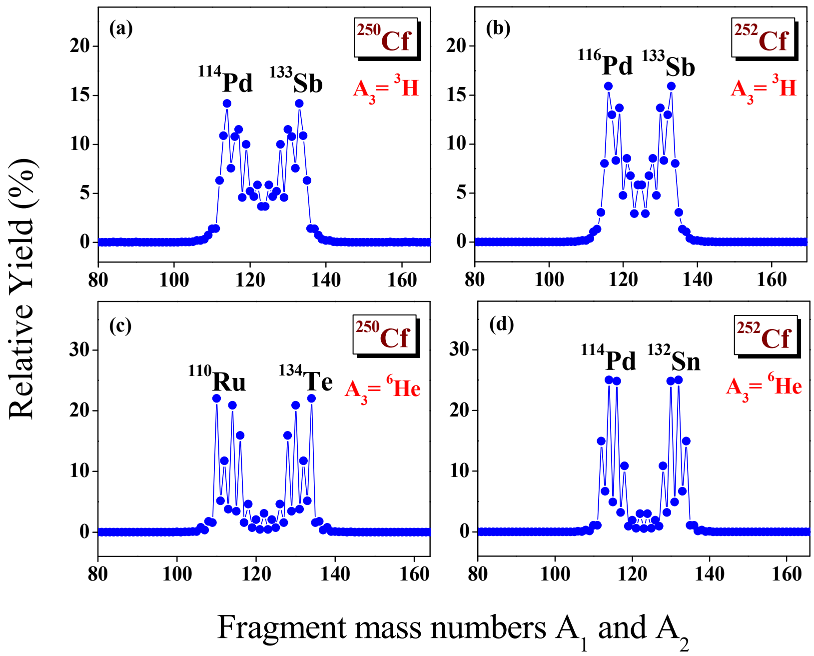

Figure 4.18. The relative yield is plotted as a function of fragment mass numbers A_1 and A_2 in the case of ^{3}H and ^{6}He accompanied ternary fission of $^{250,252}Cf$ isotopes with fragments in equatorial configuration.

4.4.2 ^{6}He accompanied ternary fission of $^{250,252}Cf$ isotopes with fragments in equatorial configuration.

For the ^{250}Cf isotope with ^{6}He as light charged particle, the driving potential is calculated for all possible fragmentations and potted as a function of fragment mass number A_1 as shown in **Figure 4.17(c)**. Here the deepest minimum is found for the fragment combination $^{4}He+^{6}He+^{240}Pu$, which possess doubly magic nucleus ^{4}He and a low Q value. The next minimum is found around the fragment combination $^{110}Ru+^{6}He+^{134}Te$, which includes the presence of near doubly magic nucleus ^{134}Te (N=82, Z=52). The same fragment combination possesses the highest Q value and hence may be the most suitable fragment splitting in this ternary fission process. The relative yield is calculated for all possible fragmentations and plotted as a function of fragment mass numbers A_1 and A_2 as shown in **Figure 4.18(c)**. In this case, the highest relative yield is found for the fragment combination $^{110}Ru+^{6}He+^{134}Te$, which includes the presence of near doubly magic nucleus ^{134}Te (N=82, Z=52). The next higher relative yields are found for the fragment combinations $^{114}Pd+^{6}He+^{130}Sn$ and $^{116}Pd+^{6}He+^{128}Sn$, which include the presence of near doubly magic nucleus ^{130}Sn (N=80, Z=50) and proton shell closure Z=50 of ^{128}Sn respectively.

In the ^{6}He accompanied ternary fission of ^{252}Cf isotope, the driving potential is calculated for all possible fragmentations and plotted as a function of fragment mass number A_1 as shown in **Figure 4.17(d)**. Here the deepest minimum is found for the fragment combination $^{4}He+^{6}He+^{242}Pu$. The next minimum found for the fragment combination around $^{114}Pd+^{6}He+^{132}Sn$ is due to the presence of doubly magic nucleus ^{132}Sn (N=82, Z=50). The relative yield is calculated and plotted as a function of fragment mass numbers A_1 and A_2 as shown in **Figure 4.18(d)**. From the plot, the highest relative yield is found for the fragment combination $^{114}Pd+^{6}He+^{132}Sn$, which is the same fragment combination with high Q value and also possess the presence of doubly magic nucleus ^{132}Sn (N=82, Z=50). The next higher relative yields are found for the ternary splitting $^{116}Pd+^{6}He+^{130}Sn$ and $^{112}Ru+^{6}He+^{134}Te$, of which ^{130}Sn (N=80, Z=50) and ^{134}Te (N=82, Z=52) are near doubly magic nuclei.

4.4.3 ^{3}H accompanied ternary fission of $^{250,252}Cf$ isotopes with fragments in collinear configuration.

In the ^{3}H accompanied ternary fission of ^{250}Cf and ^{252}Cf isotopes with fragments in collinear configuration the driving potential is plotted as a function of fragment mass number A_1 as shown in **Figure 4.19(a)** and **4.19(b)** respectively. The fragment combinations with least driving potential are also labelled. The relative yield in the case of ^{250}Cf and ^{252}Cf are calculated for all possible fragmentations found in the cold reaction valley and plotted as shown in **Figure 4.20(a)** and **4.20(b)** respectively. In the case of ^{250}Cf isotope, the highest relative yield is obtained for the ternary splitting $^{114}Pd+^{3}H+^{133}Sb$, which possess near doubly magic nucleus (N=82, Z=51). The next higher relative yields found in the ^{3}H accompanied ternary fission of ^{250}Cf are for the fragment combinations $^{117}Ag+^{3}H+^{130}Sn$ and $^{116}Pd+^{3}H+^{131}Sb$. In the case of ^{252}Cf isotope, the highest relative yield is found for the fragment combination ^{116}Pd+^{3}H+^{133}Sb, which includes the presence of doubly magic nucleus ^{133}Sb. The fragment combinations ^{119}Ag+^{3}H+^{130}Sn and ^{117}Ag+^{3}H+^{132}Sn also possess a higher relative yields in the ternary fission of ^{252}Cf isotope with ^{3}H as light charged particle formed in collinear configuration.

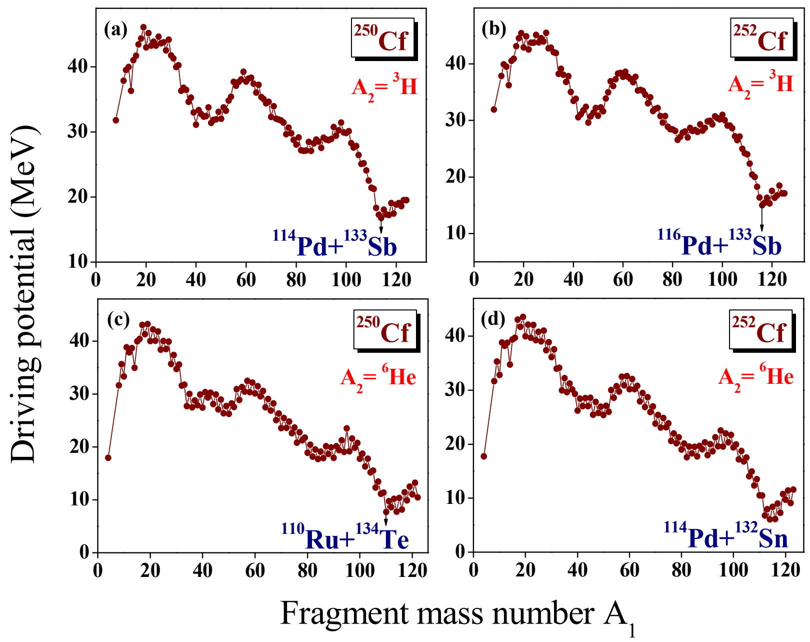

Figure 4.19. The driving potential is plotted as a function of fragment mass number A_1 in the case of ^{3}H and ^{6}He accompanied ternary fission of ^{250,252}Cf isotopes with fragments in collinear configuration.

4.4.4 ^{6}He accompanied ternary fission of ^{250,252}Cf isotopes with fragments in collinear configuration.

In the ^{6}He accompanied ternary fission of ^{250}Cf and ^{252}Cf isotopes with fragments in collinear configuration the driving potential is plotted as a function of fragment mass number A_1 as shown in **Figure 4.19(c)** and **4.19(d)** respectively. The relative yield is calculated for all fragment combinations found in the cold reaction valley plot. **Figure 4.20(c)** and **4.20(d)** represents the relative yield versus fragment mass numbers A_1 and A_3 in the case of ^{250}Cf and ^{252}Cf isotopes respectively. For ^{250}Cf isotope, the highest relative yield is found for the splitting ^{110}Ru+^{6}He+^{134}Te, which includes near doubly magic nucleus ^{134}Te. The next higher relative yields are found for $^{114}Pd+^{6}He+^{130}Sn$, $^{116}Pd+^{6}He+^{128}Sn$ and $^{112}Pd+^{6}He+^{132}Sn$. For the ^{252}Cf isotope, the fragment combination $^{114}Pd+^{6}He+^{132}Sn$ has the highest relative yield, which includes doubly magic nucleus ^{132}Sn. The next higher relative yields are found for the splitting $^{116}Pd+^{6}He+^{130}Sn$, $^{112}Ru+^{6}He+^{134}Te$, $^{118}Pd+^{6}He+^{128}Sn$.

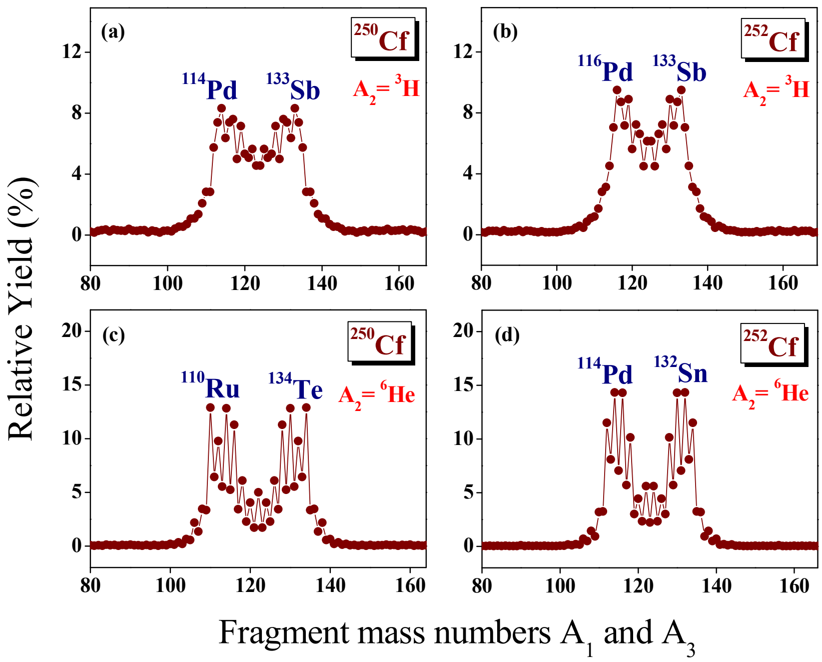

Figure 4.20. The relative yield is plotted as a function of fragment mass numbers A_1 and A_3 in the case of ^{3}H and ^{6}He accompanied ternary fission of $^{250,252}Cf$ isotopes with fragments in collinear configuration.

4.4.5 Summary

Using Unified ternary fission model (UTFM), the spontaneous cold ternary fission of $^{250,252}Cf$ isotopes with ^{3}H and ^{6}He as light charged particle with fragments in equatorial and collinear configuration has been studied. The fragment combinations with the highest relative yield are found to be the same in both equatorial and collinear configuration. In the ^{3}H accompanied ternary fission of ^{250}Cf and ^{252}Cf isotope, the most probable fragmentation is found for $^{114}Pd+^{3}H+^{133}Sb$ and $^{116}Pd+^{3}H+^{133}Sb$ respectively, in which ^{133}Sb (N=82, Z=51) is a near doubly magic nucleus. In the ternary fission of ^{250}Cf and ^{252}Cf isotope with ^{6}He as light charged particle, the most probable fragmentation is found for $^{110}Ru+^{6}He+^{134}Te$ and $^{114}Pd+^{6}He+^{132}Sn$ respectively, which is due to the presence of near doubly magic nucleus ^{134}Te (N=82, Z=52) and doubly magic nucleus ^{132}Sn (N=82, Z=50). Hence we can conclude that in the ternary fission of $^{250,252}Cf$ isotopes with ^{3}H and ^{6}He as light charged particle, the presence of doubly or near doubly magic nucleus and high Q value plays an important role.

4.5. Isotopic yield in the cold ternary fission of even-even $^{250\text{-}260}Cf$ isotopes with ^{14}C as light charged particle.

Using the UTFM, the cold ternary fission of even-even $^{250\text{-}260}Cf$ isotopes with ^{14}C as light charged particle has studied in detail in which the interacting barrier is taken as the sum of Coulomb and proximity potential.

The driving potential is calculated for all possible fragment combinations, in the ternary fission of ^{250}Cf isotope with ^{14}C as light charged particle and plotted as a function of fragment mass number A_1 as shown in **Figure 4.21(a)**. The minima are observed for the fragment combination with A_1 = ^{4}He, ^{10}Be, ^{28}Ne, ^{30}Mg, ^{36}Si, ^{42}S, ^{46}Ar, ^{52}Ca, ^{72}Ni, ^{76}Zn, ^{82}Ge etc. The fragment combination $^{4}He+^{232}Th+^{14}C$ possess the least driving potential in which ^{4}He (N=2, Z=2) nuclei is a doubly magic nuclei. The other minima are observed around the fragment combinations $^{26}Ne+^{210}Pb+^{14}C$, $^{52}Ca+^{184}Hf+^{14}C$, $^{82}Ge+^{154}Nd+^{14}C$ and $^{104}Mo+^{132}Sn+^{14}C$. The minima observed for the fragment combination $^{26}Ne+^{210}Pb+^{14}C$ is due to the presence of near doubly magic nuclei ^{210}Pb (N=128, Z=82). The minima found for the fragment combination $^{52}Ca+^{184}Hf+^{14}C$ is due to the proton shell closure Z=20 of ^{52}Ca. The fragment combinations around $^{104}Mo+^{132}Sn+^{14}C$, which includes the presence of ^{132}Sn (N=82, Z=50) may possess the highest yield, because it includes the presence of doubly or near doubly magic nuclei and high Q value. The barrier penetrability is calculated for all fragment combinations that obtained in the cold reaction valley and hence the relative yield is calculated and plotted as a function of fragment mass numbers A_1 and A_2 as shown in **Figure 4.22**. From the figure it is clear that, $^{104}Mo+^{132}Sn+^{14}C$ posses the highest yield which possess the presence of doubly magic nucleus ^{132}Sn (N=82, Z=50). The next highest yield is observed for the ternary fragmentation of $^{106}Mo+^{130}Sn+^{14}C$, in which ^{130}Sn (N=80, Z=50) is a near doubly magic nuclei. The fragment combinations $^{102}Zr+^{134}Te+^{14}C$ and $^{108}Mo+^{128}Sn+^{14}C$ possess a higher relative yield, in which ^{134}Te (N=82, Z=52) is a near doubly magic nuclei and ^{128}Sn possess proton shell closure Z=50. The various fragment combinations found in the ternary fission of ^{250}Cf isotope with ^{14}C as light charged particle are labelled in **Figure 4.22** in which, the black bars belong to the even mass numbers and hatched bars belong to odd mass numbers.

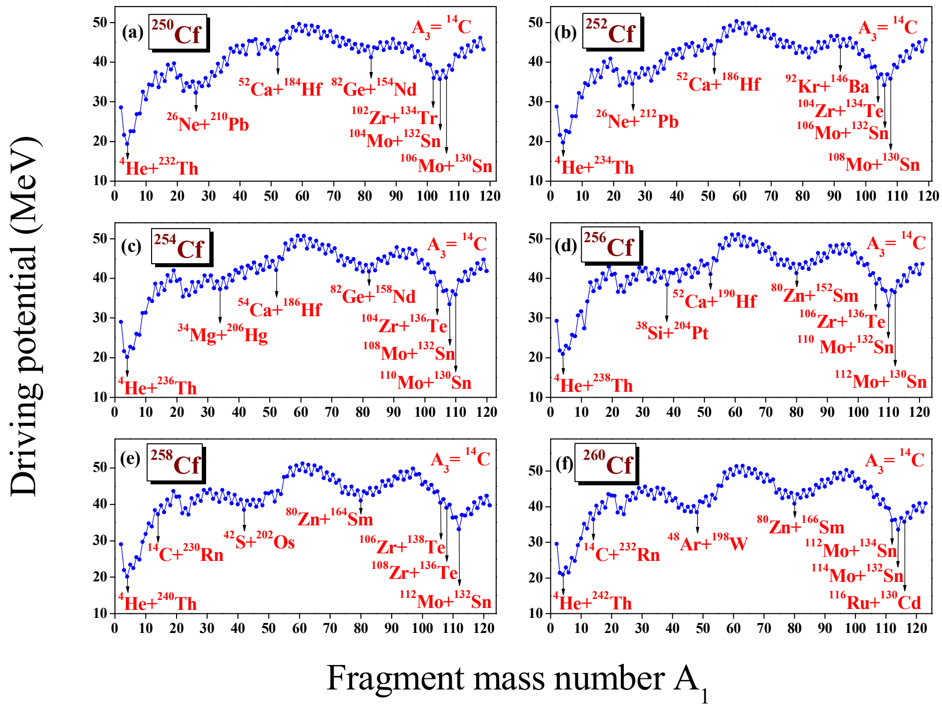

Figure 4.21. The driving potential is plotted as a function of fragment mass number A_1 for even-even $^{250\text{-}260}$Cf isotopes with ^{14}C as light charged particle.

In the ternary fission of ^{252}Cf isotope, the driving potential for the light charged particle ^{14}C is calculated and plotted as a function of fragment mass number A_1 is as shown in **Figure 4.21(b)**. The minima in the cold valley by keeping the light charged particle as ^{14}C are at ^{4}He, ^{26}Ne, ^{32}Mg, ^{34}Si, ^{40}S, ^{48}Ar, ^{52}Ca, ^{72}Ni etc. The various fragment combinations observed in the cold reaction valley for the ternary fission of ^{252}Cf are at ^{102}Zr+^{136}Te+^{14}C, ^{106}Mo+^{132}Sn+^{14}C and ^{110}Mo+^{128}Sn+^{14}C. Of these the first one is attributed to the near doubly closed shell N=84 and Z=52 of ^{134}Te, while the second fragment combination is due to the near doubly closed shell

N=82 and Z=50 of ^{132}Sn. The fragment combination $^{110}Mo+^{128}Sn+^{14}C$ possess proton shell closure Z=50 of ^{128}Sn nuclei.

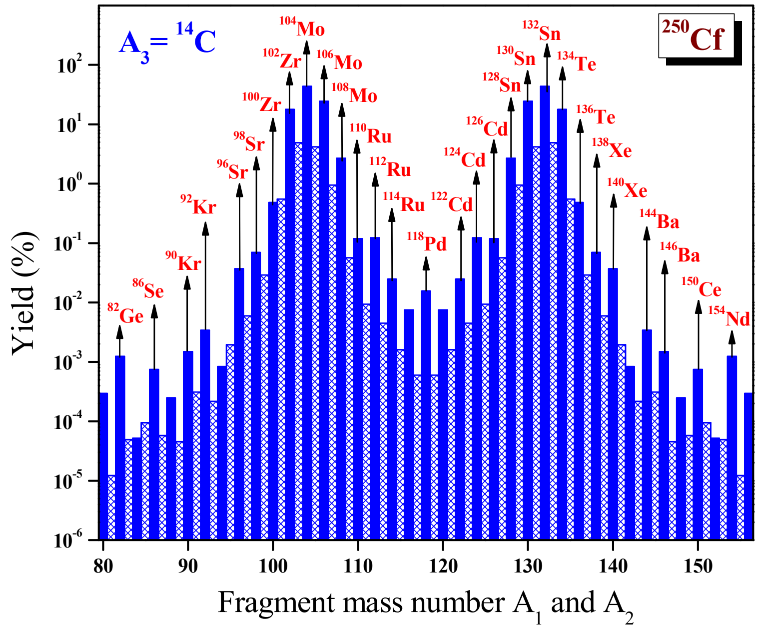

Figure 4.22. The calculated yields are plotted as a function of fragment mass numbers A_1 and A_2 for the ^{250}Cf isotope with ^{14}C as light charged particle.

The barrier penetrability is calculated for each fragment combination found in the cold reaction valley. The relative yield is hence calculated and plotted as a function of fragment mass number A_1 and A_2 as shown in **Figure 4.23**. From the figure it is clear that, the fragment combination $^{106}Mo+^{132}Sn+^{14}C$ has the highest yield which is due to the presence of doubly magic nuclei ^{132}Sn (N=82, Z=50) and a high Q value. The fragment combination $^{108}Mo+^{130}Sn+^{14}C$ shows the next highest yield in which ^{130}Sn (N=80, Z=50) is a near doubly magic nuclei. The fragment combinations $^{104}Zr+^{134}Te+^{14}C$ and $^{110}Mo+^{128}Sn+^{14}C$ possess a probable relative yield, in which ^{134}Te is a near doubly magic nuclei (N=82, Z=52) and ^{128}Sn possess proton shell closure Z=50. The relative yield obtained in the cold ternary fission of ^{252}Cf isotope with ^{14}C as light charged particle is compared with the experimental data [39] and plotted as a bar graph as shown in **Figure 4.24**. The relative yield obtained for all possible neutronless ^{14}C accompanied ternary fission of ^{252}Cf isotope is normalized with the experimental value.

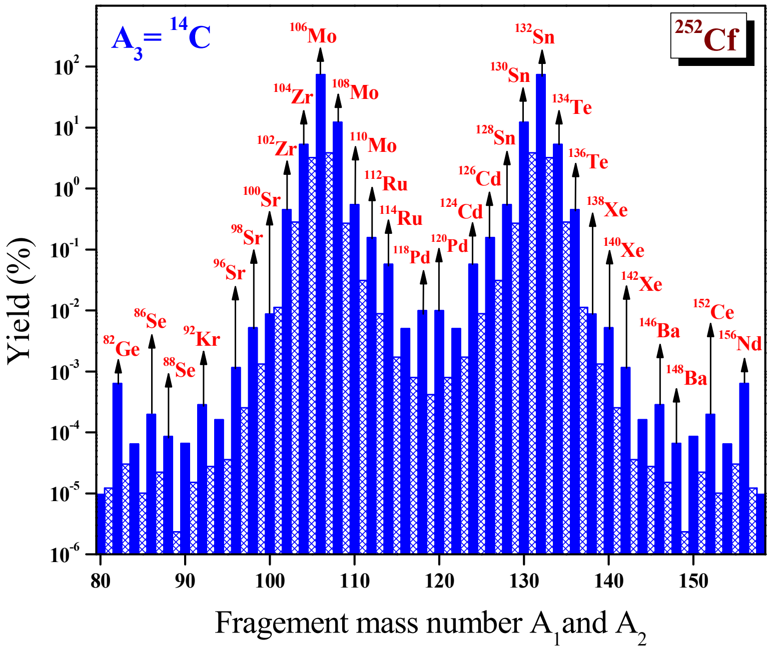

Figure 4.23. The calculated yields are plotted as a function of fragment mass numbers A_1 and A_2 for the ^{252}Cf isotope with ^{14}C as light charged particle.

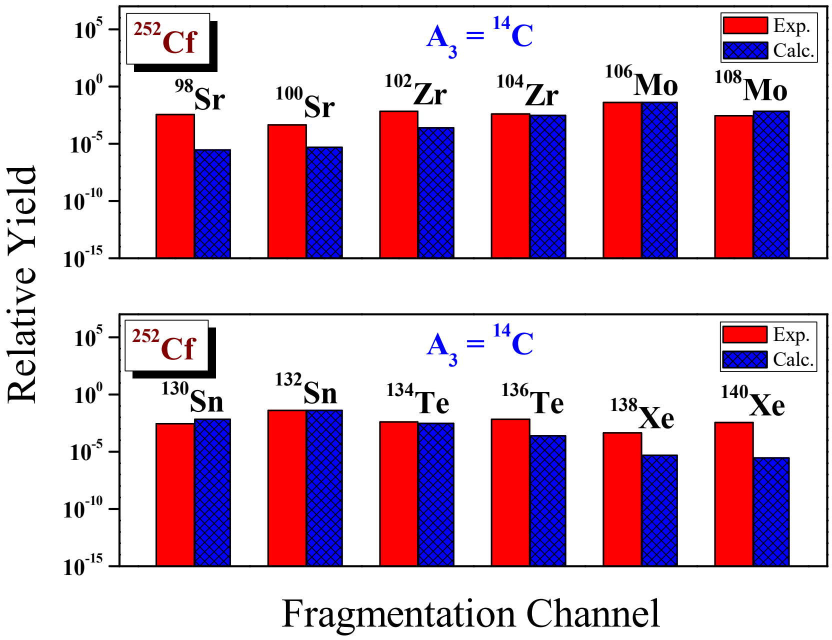

Figure 4.24. The relative yield obtained in the ternary fragmentation of ^{252}Cf isotope with ^{14}C as light charged particle is compared with the experimental data.

From the graph, it is clear that the relative yield obtained using our formalism are found to be in agreement with that obtained in the triple gamma coincidence technique at Gammasphere facility. Also, we would like to mention here that, the fragment combinations with relatively higher yield obtained using our formalism (UTFM) are found to be the same as that obtained using triple gamma coincidence technique at Gammasphere facility. For example, the relative yield found for the correlated pairs of fragment combinations like, ^{98}Sr+^{140}Xe+^{14}C, ^{100}Sr+^{138}Xe+^{14}C, ^{102}Zr+^{136}Te+^{14}C, ^{104}Zr+^{134}Te+^{14}C, ^{106}Mo+^{132}Sn+^{14}C and ^{108}Mo+^{130}Sn+^{14}C. It should also be noted that, the most favourable fragment combination ^{106}Mo+^{132}Sn+^{14}C, which possess the highest yield obtained using our formalism is found to be the same as that observed in the experiment using triple gamma coincidence technique at Gammasphere facility for the ^{14}C accompanied spontaneous cold ternary fission of ^{252}Cf isotope.

With ^{14}C as light charged particle the ternary fission of ^{254}Cf isotope is studied and the driving potential is calculated and plotted as a function of mass number A_1 as shown in **Figure 4.21(c)**. The minima found for the fragment combinations with mass number A_1 are at ^{4}He, ^{10}Be, ^{32}Mg, ^{34}Mg, ^{36}Si, ^{40}S, ^{60}Cr, ^{70}Ni, ^{72}Ni, ^{82}Ge etc. The relative yield is calculated and plotted as a function of fragment mass number A_1 and A_2 as shown in **Figure 4.25**. The most probable ternary fragmentation is obtained for ^{108}Mo+^{132}Sn+^{14}C which possess the presence of doubly magic nuclei ^{132}Sn (N=82, Z=50) and with high Q value. The next higher yields are obtained for the fragment combinations ^{110}Mo+^{130}Sn+^{14}C and ^{106}Mo+^{134}Te+^{14}C, which includes the presence of near doubly magic nuclei ^{130}Sn (N=80, Z=50) and near doubly magic nuclei ^{134}Te (N=52, Z=82) respectively. In the ternary fragmentation of ^{256}Cf with ^{14}C as the light charged particle, the driving potential is calculated and plotted as a function of fragment mass number A_1 as shown in **Figure 4.21(d)**. In the case of fragment combinations ^{108}Mo+^{134}Sn+^{14}C and ^{112}Mo+^{130}Sn+^{14}C, the minima obtained are due to the presence of near doubly magic nuclei ^{134}Sn (N=84, Z=50) and ^{130}Sn (N=80, Z=50) respectively. The relative yield for each charge minimized fragment combinations found in the cold reaction valley are calculated and plotted as a function of fragment mass numbers A_1 and A_2 as shown in **Figure 4.26**.

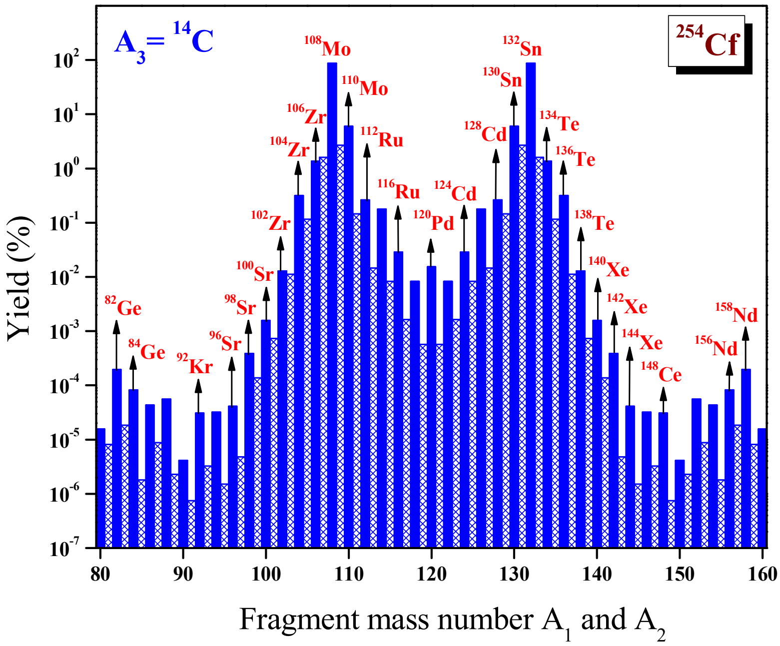

Figure 4.25. The calculated yields are plotted as a function of fragment mass numbers A_1 and A_2 for the ^{254}Cf isotope with ^{14}C as light charged particle.

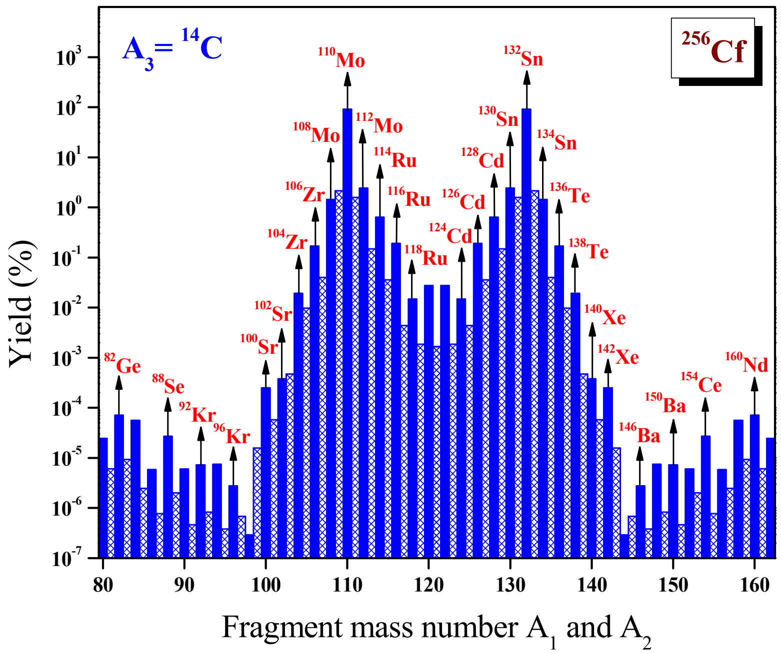

Figure 4.26. The calculated yields are plotted as a function of fragment mass numbers A_1 and A_2 for the ^{256}Cf isotope with ^{14}C as light charged particle.

From Figure 4.26 it can be seen that the highest yield is obtained for the fragment combination $^{110}Mo+^{132}Sn+^{14}C$, which is due to the doubly magic nuclei ^{132}Sn (N=82, Z=50). The next higher relative yields are found for the fragment combinations $^{112}Mo+^{130}Sn+^{14}C$ and $^{108}Mo+^{134}Sn+^{14}C$, of which the first fragment combination possess near doubly magic nuclei ^{130}Sn (N=80, Z=50) and the second one possess near doubly magic nuclei ^{134}Sn (N=84, Z=50).

In the case of ^{258}Cf isotope, with ^{14}C as the light charged particle, the driving potential is calculated and plotted as a function of mass number A_1 as shown in Figure 4.21(e). The minima is observed in the cold valley for the fragment mass number A_1 = ^{4}He, ^{14}C, ^{30}Ne, ^{34}Mg, ^{38}Si, ^{40}Si, ^{42}S, ^{60}Ti, ^{64}Cr, ^{72}Ni etc. The fragment combinations found around $^{112}Mo+^{132}Sn+^{14}C$ may be the most favourable splitting for the ternary fission process as it possess the presence of doubly magic nuclei ^{132}Sn (N=82, Z=50) and a high Q value. To obtain the most favourable fragment splitting in the ^{14}C accompanied ternary fission of ^{258}Cf; the relative yield is calculated and plotted as a function of mass numbers A_1 and A_2 as shown in Figure 4.27. The highest relative yield is obtained for the fragment combinations $^{112}Mo+^{132}Sn+^{14}C$ and is due to the doubly magic nucleus ^{132}Sn (N=82, Z=50). The next highest yield is found for the fragment combination $^{110}Mo+^{134}Sn+^{14}C$ and it possess the presence of near doubly magic nuclei ^{134}Sn (N=84, Z=50).

For the ^{14}C accompanied ternary fission of ^{260}Cf the driving potential is calculated and plotted as a function of mass number A_1 as shown in Figure 4.21(f). The fragment combinations found in the cold reaction valley around $^{114}Mo+^{132}Sn+^{14}C$ may possess higher relative yield, which can be clarified through the calculation of barrier penetrability. The barrier penetrability is calculated for each charge minimized fragment combinations found in the ^{14}C accompanied cold ternary fission of ^{260}Cf. The relative yield is hence calculated and plotted as a function of mass numbers A_1 and A_2 as shown in Figure 4.28. The highest yield is obtained for the fragment combination $^{114}Mo+^{132}Sn+^{14}C$, which is due to the doubly magic nucleus ^{132}Sn (N=82, Z=50). The next highest yields can be found for the fragment combinations $^{116}Ru+^{130}Cd+^{14}C$, which possess the presence of near doubly magic nuclei ^{130}Cd (N=82, Z=48) and $^{112}Mo+^{134}Sn+^{14}C$, which possess near doubly magic nuclei ^{134}Sn (N=84, Z=50).

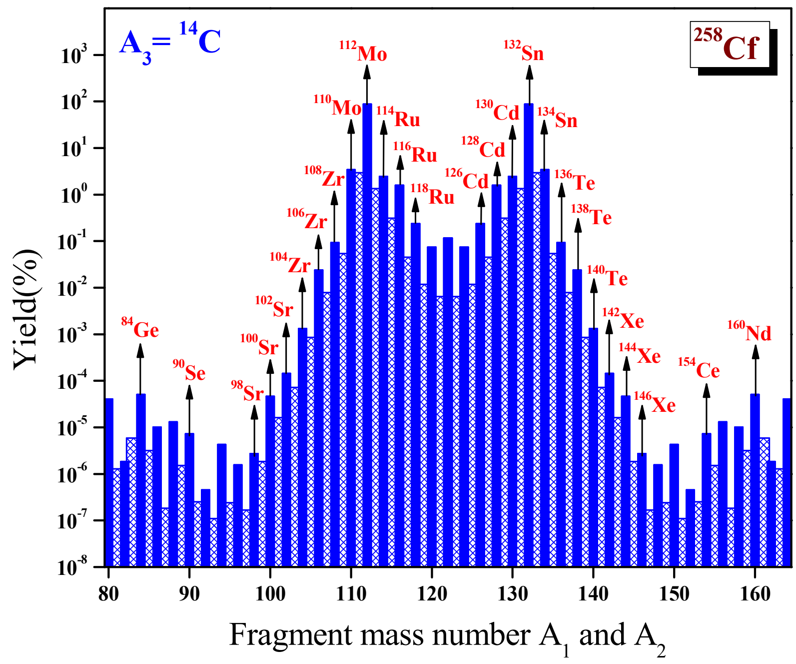

Figure 4.27. The calculated yields are plotted as a function of fragment mass numbers A_1 and A_2 for the ^{258}Cf isotope with ^{14}C as light charged particle.

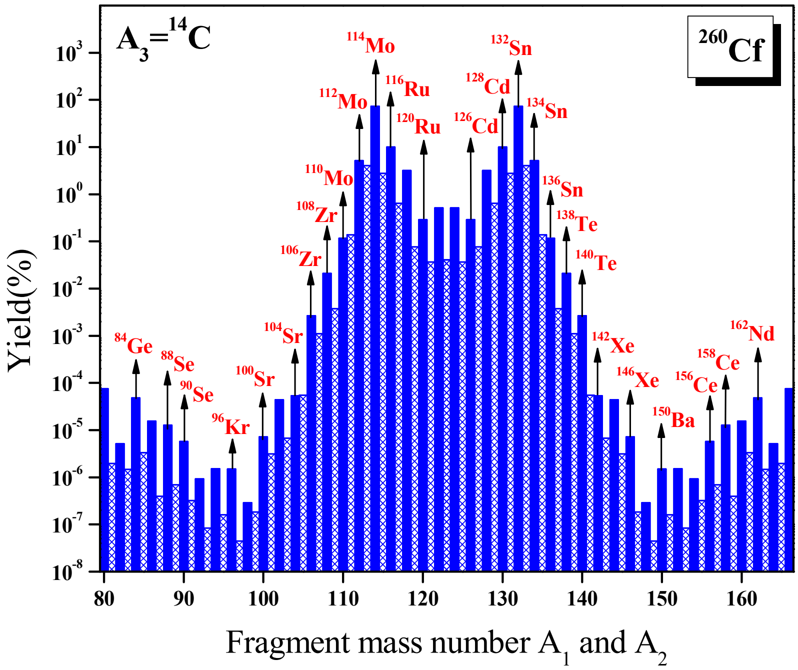

Figure 4.28. The calculated yields are plotted as a function of fragment mass numbers A_1 and A_2 for the ^{260}Cf isotope with ^{14}C as light charged particle.

In **Figure 4.29**, we have plotted the fragmentation potential as a function of the separation distance z for different fragmentations in ^{250}Cf isotope. In the figure, z_0 represents the inner turning point, $z_1=0$ represents the touching configuration of the fragments and z_2 represents the outer turning point. The penetration path for the various fragments splitting in the ^{14}C accompanied fission of ^{250}Cf isotope is also shown in **Figure 4.29**. From **Figure 4.29**, it is clear that the width and height of the barrier increases with the decreasing mass number of the lighter fragment. Here the fragmentation ^{104}Mo+^{132}Sn+^{14}C possess the highest barrier penetrability compared to the barrier penetrability for the fragmentation ^{28}Ne+^{208}Pb+^{14}C. We would like to mention that, the highest yield obtained in the ^{14}C accompanied ternary fission of ^{250}Cf is for ^{104}Mo+^{132}Sn+^{14}C which is the fragment combination with minimum height and width of the potential barrier (maximum barrier penetrability). Also in **Figure 4.30**, we have plotted the fragmentation potential as a function of distance of separation between the fragments z for different Cf isotopes, $^{250-260}$Cf, here the potential is shown for the fragmentation with maximum yield.

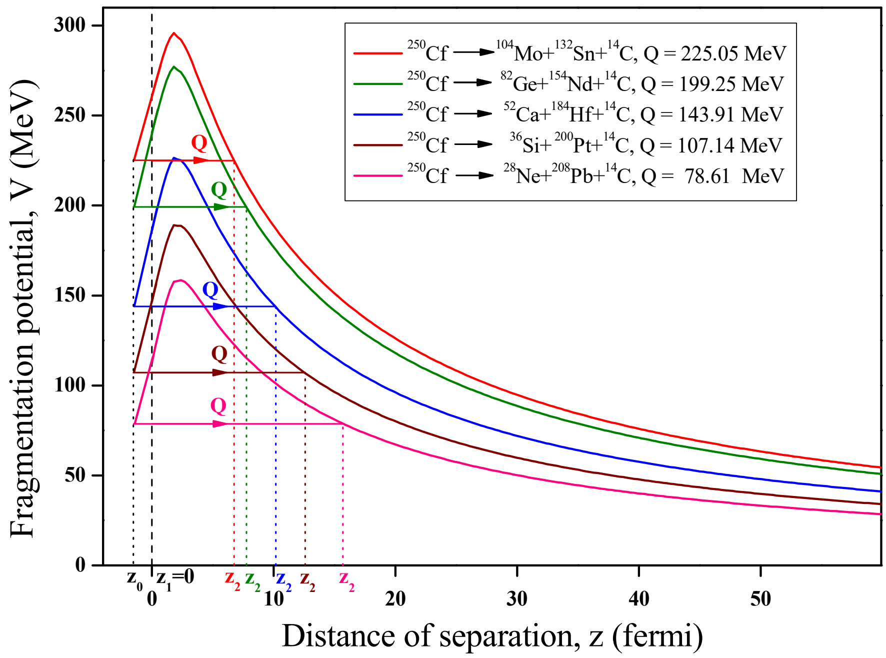

Figure 4.29. The calculated fragmentation potential for various ternary splitting in ^{250}Cf, plotted as a function of the separation distance. The corresponding Q value, inner turning point z_0 and outer turning point z_2 are labelled.

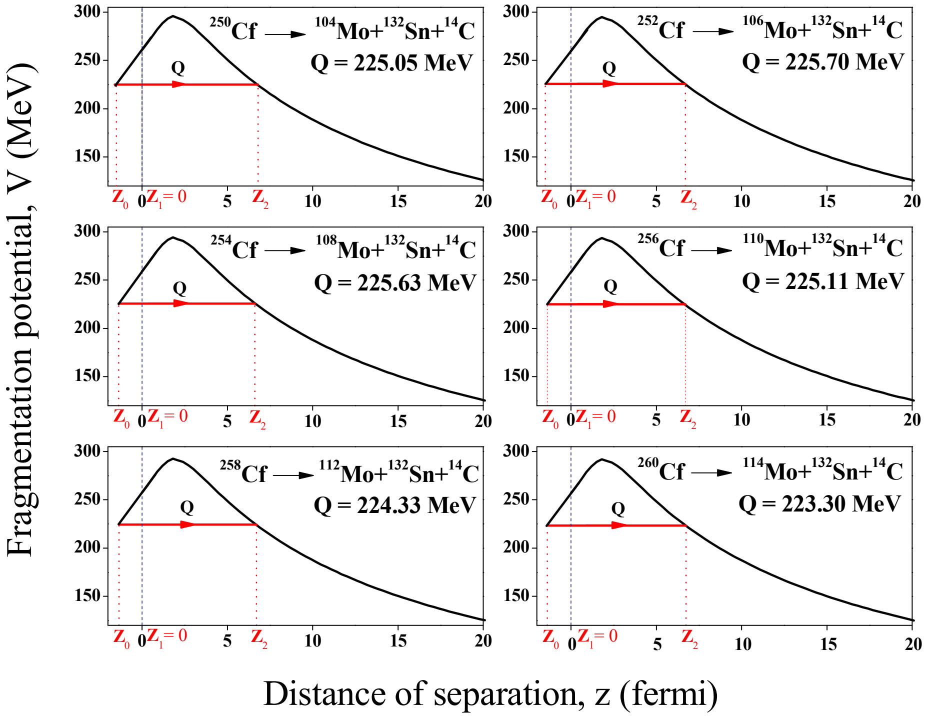

Figure 4.30. The calculated fragmentation potential in the ^{14}C accompanied ternary fission of even-even $^{250-260}Cf$ isotope is plotted as a function of separation distance. The corresponding Q value, inner turning point z_0 and outer turning point z_2 are labelled.

4.5.1 Summary

The cold ternary fission of even-even $^{250-260}Cf$ isotopes with ^{14}C as light charged particle have been studied using the recently proposed Unified ternary fission model (UTFM), in which the interacting barrier is taken as the sum of Coulomb and proximity potential. The highest yield obtained for the ^{14}C accompanied cold ternary fission of ^{250}Cf, ^{252}Cf, ^{254}Cf, ^{256}Cf, ^{258}Cf and ^{260}Cf isotopes are for $^{104}Mo+^{132}Sn+^{14}C$, $^{106}Mo+^{132}Sn+^{14}C$, $^{108}Mo+^{132}Sn+^{14}C$, $^{110}Mo+^{132}Sn+^{14}C$, $^{112}Mo+^{132}Sn+^{14}C$ and $^{114}Mo+^{132}Sn+^{14}C$ respectively. It should be noted that, the most favourable ternary splitting is obtained for the fragment combination with doubly magic nuclei ^{132}Sn (N=82, Z=50) as the heavier fragment. Hence we can conclude that, the presence of doubly magic nuclei ^{132}Sn plays a vital role for the most favourable splitting in the ternary fission process of even-even $^{250-260}Cf$ isotopes. The relative yield of the most favourable fragment combinations found in the ^{14}C

accompanied cold ternary fission of ^{252}Cf isotope are compared with the experimental data. It is to be noted that, the fragment combinations with higher relative yield obtained using our formalism are in agreement with that observed in the experiment using triple gamma coincidence technique at Gammasphere facility for the ^{14}C accompanied spontaneous cold ternary fission of ^{252}Cf isotope.

4.6 ^{10}Be accompanied ternary fission of even-even $^{250\text{-}260}Cf$ isotopes

The ternary fission of ^{250}Cf, ^{252}Cf, ^{254}Cf, ^{256}Cf, ^{258}Cf and ^{260}Cf isotopes have studied in detail with the Unified ternary fission model. The fragments are considered to be emitted in both equatorial and collinear configuration.

4.6.1 ^{10}Be accompanied ternary fission of ^{250}Cf with fragments in equatorial configuration.

In the ^{10}Be accompanied ternary fission of ^{250}Cf isotope with fragments in equatorial configuration, the driving potential is calculated for all fragment combinations. **Figure 4.31** represents the cold reaction valley; a plot connects the driving potential versus fragment mass number A_1 in the ternary fission process. Here the minima is found for the mass number A_1= ^{4}He, ^{10}Be, ^{14}C, ^{16}C, ^{18}C, ^{20}O, ^{22}O, ^{24}O, ^{26}Ne, ^{28}Mg, ^{30}Mg etc. The least driving potential is found for the fragment combination $^{4}He+^{10}Be+^{236}U$, which have the Q value of 13.6931 MeV. The minimum found for the splitting $^{32}Mg+^{10}Be+^{208}Pb$ is due to the presence of doubly magic nuclei ^{208}Pb (N=126, Z=82). The next minimum is found for the fragment combination $^{82}Ge+^{10}Be+^{158}Sm$, which is due to the presence of neutron shell closure N=50 of ^{82}Ge. The fragment combination $^{110}Ru+^{10}Be+^{130}Sn$ shows a deep minimum in the cold reaction valley and which is due to the presence of near doubly magic nucleus ^{130}Sn (N=82, Z=50). Also it should be noted that the same fragment combination possess high Q value. Hence the fragment combination around $^{110}Ru+^{10}Be+^{130}Sn$ may be the most favourable fragment splitting found in the ternary fission as it possess the presence of doubly magic nuclei and high Q value. This justification can be clarified only with the calculation of barrier penetrability and hence the relative yield obtained for a particular fragmentation found in the ternary fission of ^{250}Cf isotope with ^{10}Be as light charged particle.

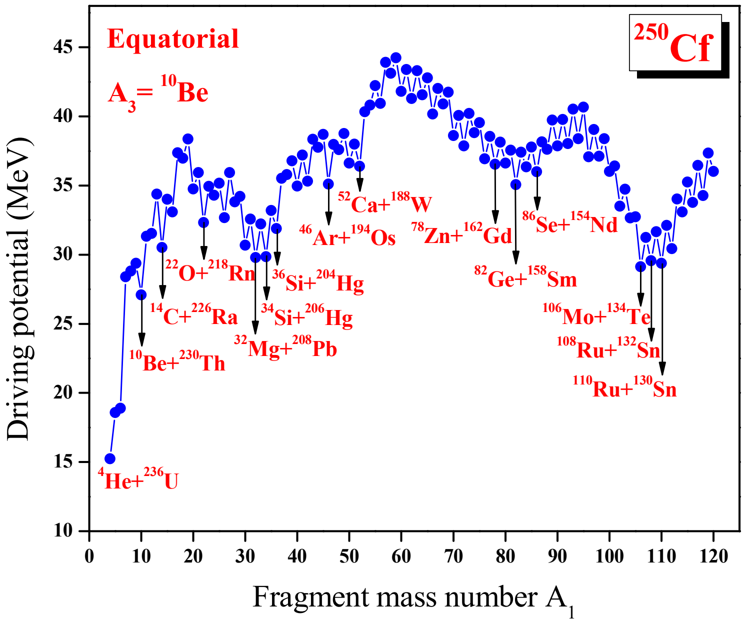

Figure 4.31. The plot connects the driving potential versus the fragment mass number A_1 in the ^{10}Be accompanied ternary fission of ^{250}Cf isotope with fragments in equatorial configuration.

The barrier penetrability is calculated for all possible fragmentations found in the cold reaction valley and hence the relative yield is calculated for each fragmentation. **Figure 4.32** represents the plot connects the relative yield versus the fragment mass number A_1 and A_2. From the figure it is clear that the highest relative yield is found for the fragment combination ^{110}Ru+^{10}Be+^{130}Sn, which posses near doubly magic nucleus ^{130}Sn (N=82, Z=50) and is the same fragment combination with minimum driving potential and high Q value in the cold reaction valley plot. The next highest relative yield is obtained for the fragment combination ^{108}Ru+^{10}Be+^{132}Sn which includes the presence of doubly magic nuclei ^{132}Sn (N=82, Z=50). The next favoured fragment combinations found in this ternary fission process are for ^{106}Mo+^{10}Be+^{134}Te, ^{112}Ru+^{10}Be+^{128}Sn and ^{114}Ru+^{10}Be+^{126}Sn which includes the presence of near doubly magic nuclei ^{134}Te (N=82, Z=52), proton shell closure Z=50 of ^{128}Sn and ^{126}Sn respectively.

Some other fragment combinations which possess probable relative yield are also labelled in the figure. In the figure the hatched bars represents the odd mass numbers and the black ones belongs the even mass number fragments.

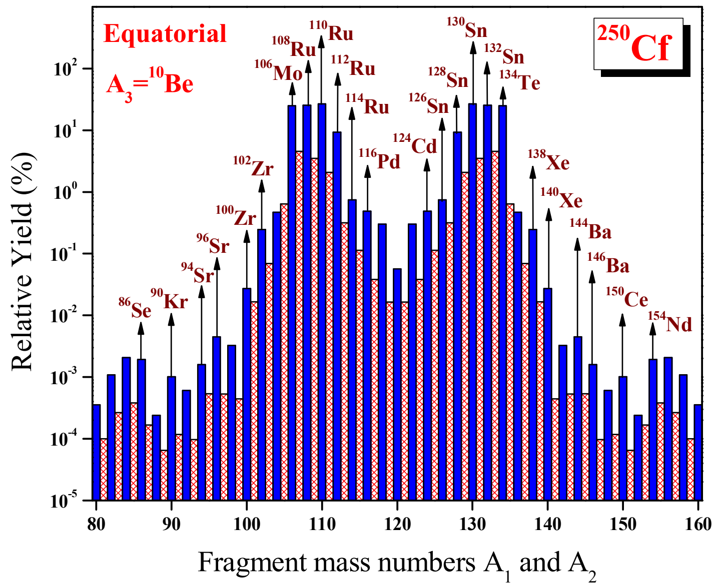

Figure 4.32. The plot connects the relative yield versus the fragment mass number A_1 and A_2 in ^{10}Be accompanied ternary fission of ^{250}Cf isotope with fragments in equatorial configuration.

4.6.2 ^{10}Be accompanied ternary fission of ^{252}Cf with fragments in equatorial configuration.

In the ^{10}Be accompanied ternary fission of ^{252}Cf isotope with fragments in equatorial configuration, the driving potential is calculated for all fragment combinations. Figure 4.33 represents the cold reaction valley; a plot connects the driving potential versus fragment mass number A_1 in the ternary fission process. Here the minima is found for the A_1 = ^4He, ^{10}Be, ^{14}C, ^{16}C, ^{18}C, ^{20}O, ^{22}O, ^{24}O, ^{26}Ne, ^{28}Mg, ^{30}Mg, ^{32}Mg, ^{34}Mg, ^{36}Si etc. The least driving potential is found for the fragment combination ^4He+^{10}Be+^{238}U, which have the Q value of 13.6935 MeV. The minimum found for the splitting ^{36}Si+^{10}Be+^{206}Hg is due to the presence of near doubly magic nuclei ^{206}Hg (N=126, Z=80). The next minimum is found for the fragment combination ^{82}Ge+^{10}Be+^{160}Sm, which is due to the presence of neutron shell closure N=50 of ^{82}Ge. The fragment combination ^{110}Ru+^{10}Be+^{132}Sn

shows a deep minimum is due to the presence of doubly magic nuclei ^{132}Sn (N=82, Z=50) and the same fragment combination possess high Q value. Hence the fragment combination around $^{110}Ru+^{10}Be+^{132}Sn$ may be the most favourable fragment splitting found in the ternary fission as it possess the presence of doubly magic nuclei and high Q value. This can be clarified only with the calculation of barrier penetrability and hence the relative yield obtained for every particular fragmentation found in the ternary fission of ^{252}Cf isotope with ^{10}Be as light charged particle.

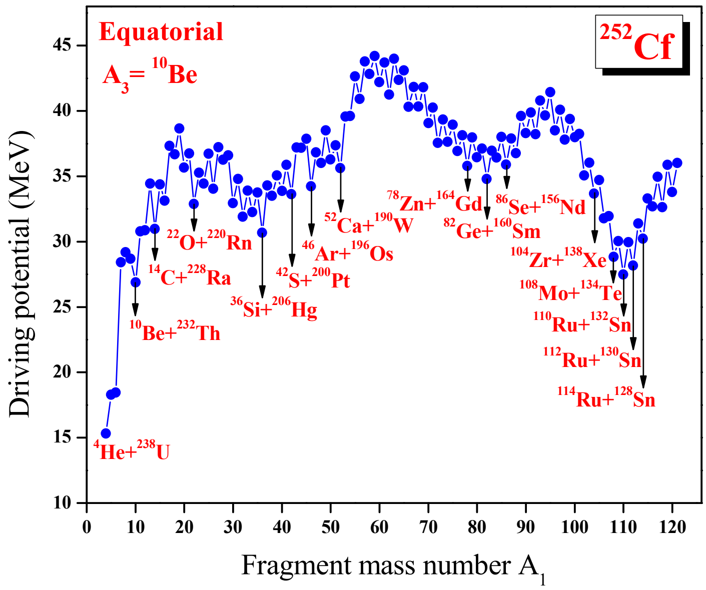

Figure 4.33. The plot connects the driving potential versus the fragment mass number A_1 in the ^{10}Be accompanied ternary fission of ^{252}Cf isotope with fragments in equatorial configuration.

The barrier penetrability is calculated for all possible fragmentation found in the cold reaction valley and hence the relative yield is calculated for each fragmentation. **Figure 4.34** represents the plot connects the relative yield versus the fragment mass number A_1 and A_2. From the figure it is clear that the highest relative yield is found for the fragment combination $^{110}Ru+^{10}Be+^{132}Sn$, which is the same fragment combination with a minimum driving potential, high Q value and possess the presence of doubly magic nucleus ^{132}Sn (N=82, Z=50) in the cold reaction valley plot. The next highest relative yield is obtained for the fragment combination $^{112}Ru+^{10}Be+^{130}Sn$ which includes the presence of doubly magic nuclei ^{130}Sn (N=80, Z=50). The next favoured fragment combinations found in this ternary fission process is for ^{108}Mo+^{10}Be+^{134}Te and ^{114}Ru+^{10}Be+^{128}Sn which includes the presence of near doubly magic nucleus ^{134}Te (N=82, Z=52) and the proton shell closure Z=50 of ^{128}Sn respectively. The next highest relative yield is found for the splitting ^{118}Pd+^{10}Be+^{124}Cd. Some other fragment combinations which possess probable relative yield are also labelled in the figure in which the hatched bars represents the odd mass number fragments and the black bars belongs to the even mass number fragments.

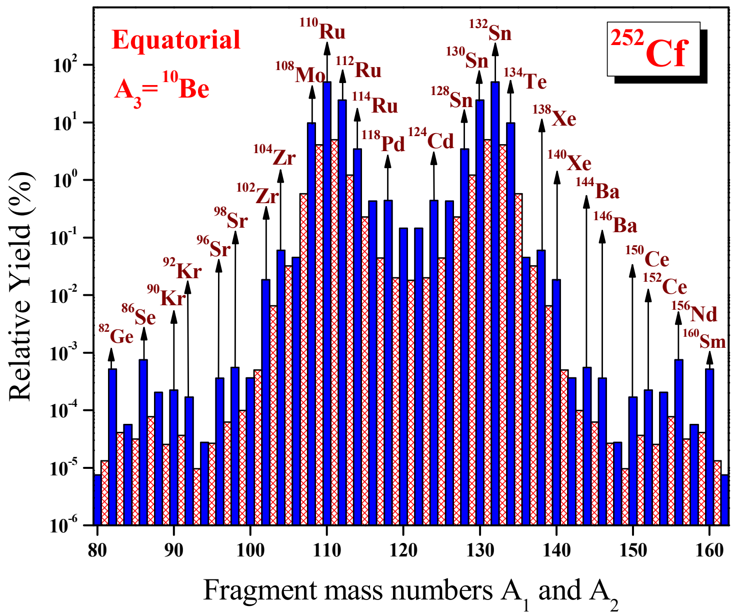

Figure 4.34. The plot connects the relative yield versus the fragment mass number A_1 and A_2 in ^{10}Be accompanied ternary fission of ^{252}Cf isotope with fragments in equatorial configuration.

4.6.3 ^{10}Be accompanied ternary fission of ^{254}Cf with fragments in equatorial configuration.

In the ^{10}Be accompanied ternary fission of ^{254}Cf isotope with fragments in equatorial configuration, the driving potential is calculated for all fragment combinations. Figure 4.35 represents the cold reaction valley; a plot connects the driving potential versus fragment mass number A_1 in the ternary fission process. Here the minima is found for the mass number A_1 = ^{4}He, ^{10}Be, ^{12}Be, ^{14}C, ^{16}C, ^{18}C, ^{20}O, ^{22}O, ^{24}O, ^{26}Ne, ^{28}Ne, ^{30}Mg, ^{32}Mg, ^{34}Mg, ^{36}Si etc. The least driving potential is found for the fragment combination $^{4}He+^{10}Be+^{240}U$, which have the Q value 13.5936 MeV. The minimum found for the splitting $^{38}Si+^{10}Be+^{206}Hg$ is due to the presence of near doubly magic nuclei ^{206}Hg (N=126, Z=80). The next minimum is found for the fragment combination $^{82}Ge+^{10}Be+^{162}Sm$, which is due to the presence of neutron shell closure N=50 of ^{82}Ge. The fragment combination $^{112}Ru+^{10}Be+^{132}Sn$ shows a deep minimum in cold reaction valley which includes the presence of doubly magic nuclei ^{132}Sn (N=82, Z=50). Also it should be noted that the same fragment combination possess high Q value. Hence the fragment combination around $^{112}Ru+^{10}Be+^{132}Sn$ may be the most favourable fragment splitting found in the ternary fission as it possess the presence of doubly magic nuclei and high Q value. The barrier penetrability and hence the relative yield obtained for all possible fragmentations are calculated, which found in the ternary fission of ^{254}Cf isotope with ^{10}Be as light charged particle in order to prove this justification.

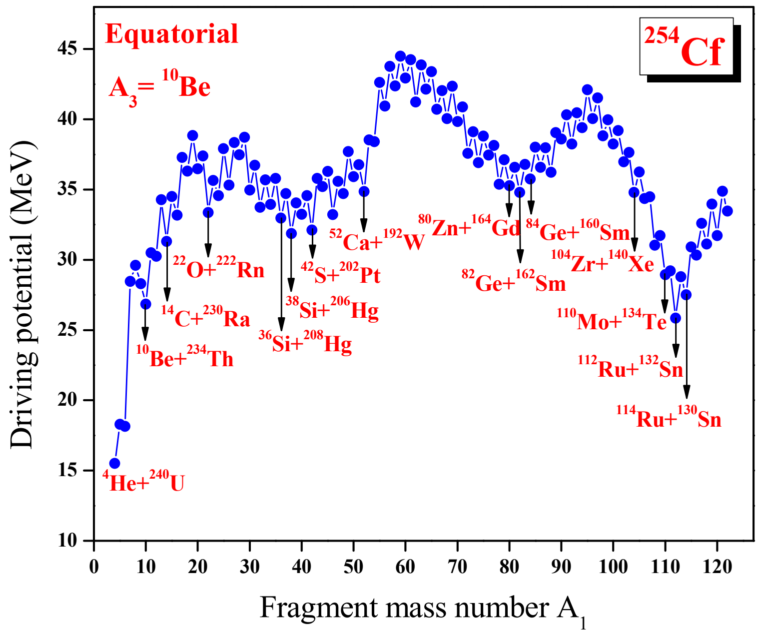

Figure 4.35. The plot connects the driving potential versus the fragment mass number A_1 in the ^{10}Be accompanied ternary fission of ^{254}Cf isotope with fragments in equatorial configuration.

The barrier penetrability is calculated for all possible fragmentation found in the cold reaction valley and hence the relative yield is calculated for each fragmentation. **Figure 4.36** represents the plot connects the relative yield versus the fragment mass number A_1 and A_2. From the figure it is clear that the highest relative yield is found for the fragment combination ^{112}Ru+^{10}Be+^{132}Sn, which is the same fragment combination with minimum driving potential and high Q value in the cold reaction valley plot. The next highest relative yield is obtained for the fragment combination ^{114}Ru+^{10}Be+^{130}Sn which includes the presence of doubly magic nuclei ^{130}Sn (N=80, Z=50). The next favoured fragment combinations found in this ternary fission process is for ^{110}Mo+^{10}Be+^{134}Te and ^{116}Ru+^{10}Be+^{128}Sn, which includes the presence of near doubly magic nuclei ^{134}Te (N=82, Z=52) and proton shell closure Z=50 of ^{128}Sn respectively. Some other fragment combinations which possess probable relative yield are also labelled in the figure. In the figure the hatched bars represents the odd mass numbers and the black ones belongs the even mass number fragments.

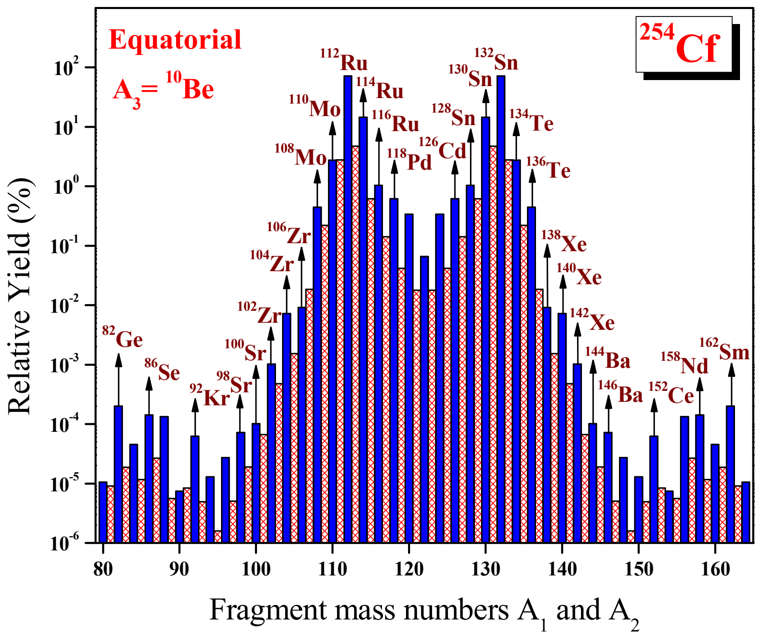

Figure 4.36. The plot connects the relative yield versus the fragment mass number A_1 and A_2 in ^{10}Be accompanied ternary fission of ^{254}Cf isotope with fragments in equatorial configuration.

4.6.4 ^{10}Be accompanied ternary fission of ^{256}Cf with fragments in equatorial configuration.

In the ^{10}Be accompanied ternary fission of ^{256}Cf isotope with fragments in equatorial configuration, the driving potential is calculated for all fragment combinations. **Figure 4.37** represents the cold reaction valley; a plot connects the driving potential versus fragment mass number A_1 in the ternary fission process. Here the minima is found for the A_1 = ^{4}He, ^{6}He, ^{10}Be, ^{12}Be, ^{14}C, ^{16}C, ^{18}C, ^{20}O, ^{22}O, ^{24}O, ^{26}Ne, ^{28}Ne, ^{30}Mg, ^{32}Mg etc. The least driving potential is found for the fragment combination ^{4}He+^{10}Be+^{242}U, which have the Q value of 13.3876 MeV. The minimum found for the splitting ^{42}S+^{10}Be+^{204}Pt is due to the presence of magic nuclei ^{204}Pt (N=126, Z=78). The next minimum is found for the fragment combination ^{80}Zn+^{10}Be+^{166}Gd, which is due to the presence of neutron shell closure N=50 of ^{80}Zn. The fragment combination ^{114}Ru+^{10}Be+^{132}Sn shows next deep minimum, which is due to the presence of doubly magic nuclei ^{132}Sn (N=82, Z=50). Also it should be noted that the same fragment combination possess high Q value.

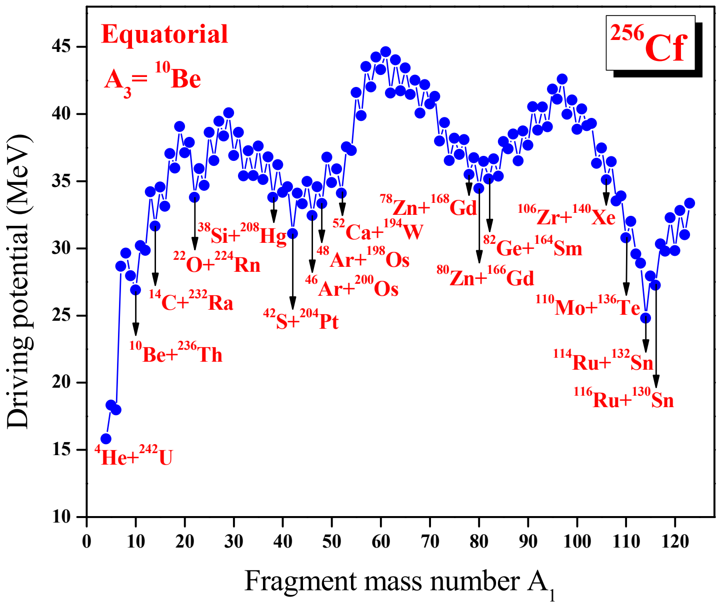

Figure 4.37. The plot connects the driving potential versus the fragment mass number A_1 in the ^{10}Be accompanied ternary fission of ^{256}Cf isotope with fragments in equatorial configuration.

The barrier penetrability is calculated for all possible fragmentation found in the cold reaction valley and hence the relative yield is calculated for every fragmentations. **Figure 4.38** represents the plot connects the relative yield versus the fragment mass number A_1 and A_2. From the figure it is clear that the highest relative yield is found for the fragment combination ^{114}Ru+^{10}Be+^{132}Sn, which is the same fragment combination with minimum driving potential and high Q value in the cold reaction valley plot. The next highest relative yield is obtained for the fragment combination ^{116}Ru+^{10}Be+^{130}Sn which includes the presence of near doubly magic nuclei ^{130}Sn (N=80, Z=50). The next favoured fragment combinations found in the ternary fission process is for ^{112}Mo+^{10}Be+^{134}Te and ^{118}Pd+^{10}Be+^{128}Cd which includes the presence near doubly magic nucleus ^{134}Te (N=82, Z=52) and neutron shell closure N=80 of ^{128}Cd respectively. The fragment combination ^{110}Mo+^{10}Be+^{136}Te possess a probable relative yield which is due to the presence of near doubly magic nucleus ^{136}Te (N=84, Z=52).

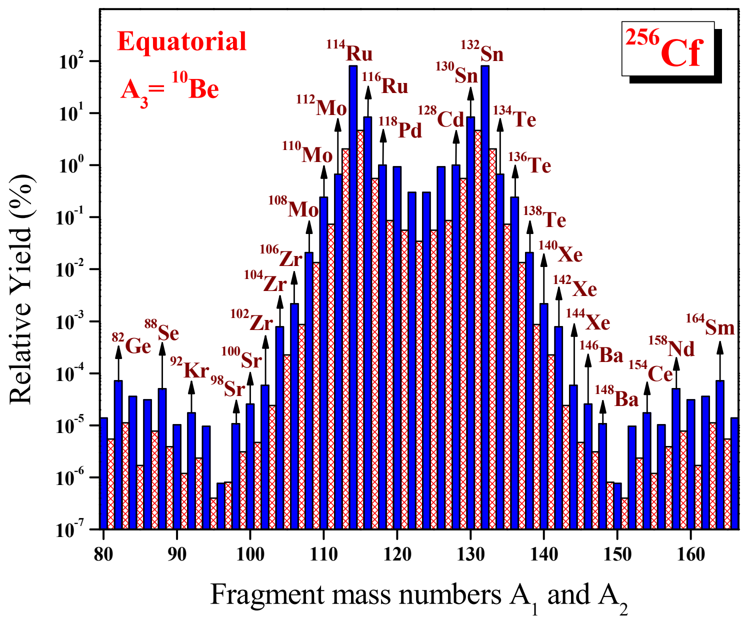

Figure 4.38. The plot connects the relative yield versus the fragment mass number A_1 and A_2 in ^{10}Be accompanied ternary fission of ^{256}Cf isotope with fragments in equatorial configuration.

4.6.5 ^{10}Be accompanied ternary fission of ^{258}Cf with fragments in equatorial configuration.

In the ^{10}Be accompanied ternary fission of ^{258}Cf isotope with fragments in equatorial configuration, the driving potential is calculated for all fragment combinations. **Figure 4.39** represents the cold reaction valley; a plot connects the driving potential versus fragment mass number A_1 in the ternary fission process. Here the minima is found for the mass number A_1 = ^{4}He, ^{6}He, ^{10}Be, ^{12}Be, ^{14}Be, ^{14}C, ^{16}C, ^{18}C, ^{20}O, ^{22}O, ^{24}O, ^{26}Ne, ^{28}Ne, ^{30}Mg, ^{32}Mg, ^{34}Mg, ^{36}Si etc. The least driving potential is found for the fragment combination ^{4}He+^{10}Be+^{244}U, which have the Q value of 13.9376 MeV. The minima found for the splitting ^{44}S+^{10}Be+^{204}Pt is due to the presence of magic nuclei ^{204}Pt (N=126, Z=78). The next minimum is found for the fragment combination ^{80}Zn+^{10}Be+^{168}Gd, which is due to the presence of neutron shell closure N=50 of ^{80}Zn. The fragment combination ^{116}Ru+^{10}Be+^{132}Sn shows another deep minimum in the cold reaction valley, which includes the presence of doubly magic nuclei ^{132}Sn (N=82, Z=50).

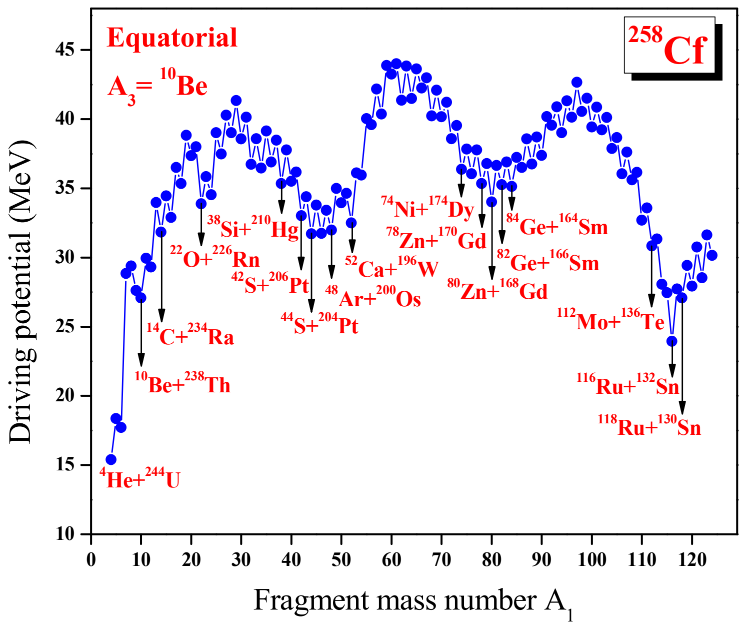

Figure 4.39. The plot connects the driving potential versus the fragment mass number A_1 in the ^{10}Be accompanied ternary fission of ^{258}Cf isotope with fragments in equatorial configuration.

The barrier penetrability is calculated for all possible fragmentation found in the cold reaction valley and hence the relative yield is calculated for each fragmentation. **Figure 4.40** represents the plot connects the relative yield versus the fragment mass number A_1 and A_2. From the figure it is clear that the highest relative yield is found for the fragment combination ^{116}Ru+^{10}Be+^{132}Sn, which is the same fragment combination with minimum driving potential and high Q value in the cold reaction valley plot. The next highest relative yield is obtained for the fragment combination ^{118}Ru+^{10}Be+^{130}Sn which includes the presence of near doubly magic nuclei ^{130}Sn (N=80, Z=50). The next favoured fragment combinations found in this ternary fission process is for ^{120}Pd+^{10}Be+^{128}Cd, ^{114}Ru+^{10}Be+^{134}Sn and ^{112}Mo+^{10}Be+^{136}Te which includes the presence of near doubly magic nuclei ^{128}Cd (N=80, Z=48), ^{134}Sn (N=84, Z=50) and ^{136}Te (N=84, Z=52) respectively. Some other fragment combinations which possess probable relative yield are also labelled in the figure. In the figure the hatched bars represents the odd mass numbers and the black ones belongs the even mass number fragments.

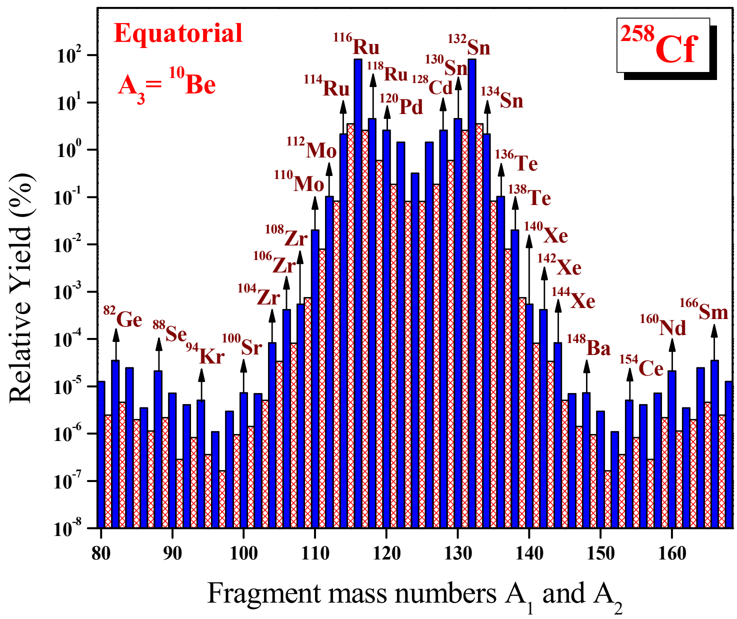

Figure 4.40. The plot connects the relative yield versus the fragment mass number A_1 and A_2 in ^{10}Be accompanied ternary fission of ^{258}Cf isotope with fragments in equatorial configuration.

4.6.6 ^{10}Be accompanied ternary fission of ^{260}Cf with fragments in equatorial configuration.

In the ^{10}Be accompanied ternary fission of ^{260}Cf isotope with fragments in equatorial configuration, the driving potential is calculated for all fragment combinations. Figure 4.41 represents the cold reaction valley; a plot connects the driving potential versus fragment mass number A_1 in the ternary fission process. Here the minima is found for the A_1 = ^{4}He, ^{6}He, ^{10}Be, ^{12}Be, ^{14}C, ^{16}C, ^{18}C, ^{20}O, ^{22}O, ^{24}O, ^{26}Ne, ^{28}Ne, ^{30}Mg, ^{32}Mg, ^{34}Mg, ^{36}Si etc. The least driving potential is found for the fragment combination ^{4}He+^{10}Be+^{246}U, which have the Q value of 13.6075 MeV. The minima found for the splitting ^{48}Ar+^{10}Be+^{202}Os is due to the presence of proton shell closure Z=18 of ^{48}Ar and neutron shell closure N=126 of ^{202}Os nuclei. The next minimum is found for the fragment combination ^{80}Zn+^{10}Be+^{170}Gd, which is due to the presence of neutron shell closure N=50 of ^{80}Zn. The fragment combination ^{118}Ru+^{10}Be+^{132}Sn shows a next deep minimum which includes the presence of doubly magic nuclei ^{132}Sn (N=82, Z=50).

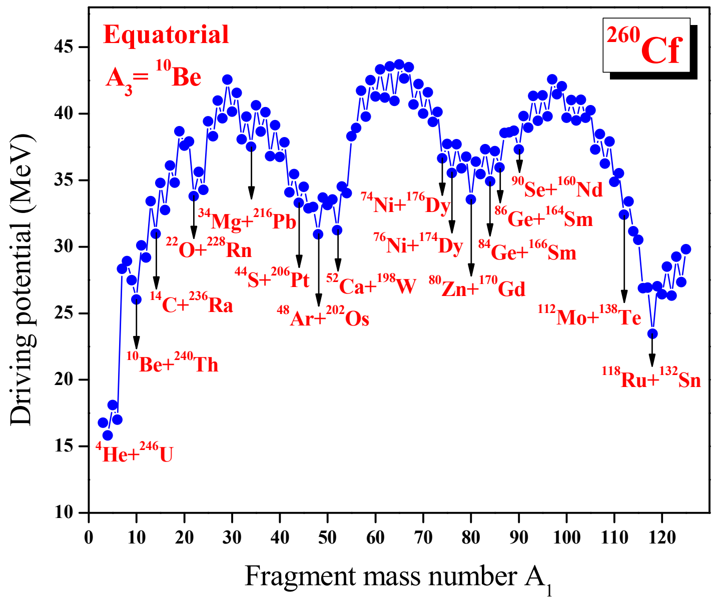

Figure 4.41. The plot connects the driving potential versus the fragment mass number A_1 in the ^{10}Be accompanied ternary fission of ^{260}Cf isotope with fragments in equatorial configuration.

The barrier penetrability is calculated for all possible fragmentation found in the cold reaction valley and hence the relative yield is calculated for each fragmentation. **Figure 4.42** represents the plot connects the relative yield versus the fragment mass number A_1 and A_2. From the figure it is clear that the highest relative yield is found for the fragment combination $^{118}Ru+^{10}Be+^{132}Sn$, which is the same fragment combination with minimum driving potential and high Q value in the cold reaction valley plot. The next highest relative yield is obtained for the fragment combination $^{122}Pd+^{10}Be+^{128}Cd$ which includes the presence of near doubly magic nuclei ^{128}Cd (N=80, Z=48). The next favoured fragment combinations found in the ternary fission process is for $^{120}Pd+^{10}Be+^{130}Cd$ and $^{116}Ru+^{10}Be+^{134}Sn$ which includes the presence of near doubly magic nuclei ^{130}Cd (N=82, Z=48) and ^{134}Sn (N=84, Z=50) respectively. Some other fragment combinations which possess probable relative yield are also labelled in the figure. In the figure the hatched bars represents the odd mass numbers and the black ones belongs the even mass number fragments.

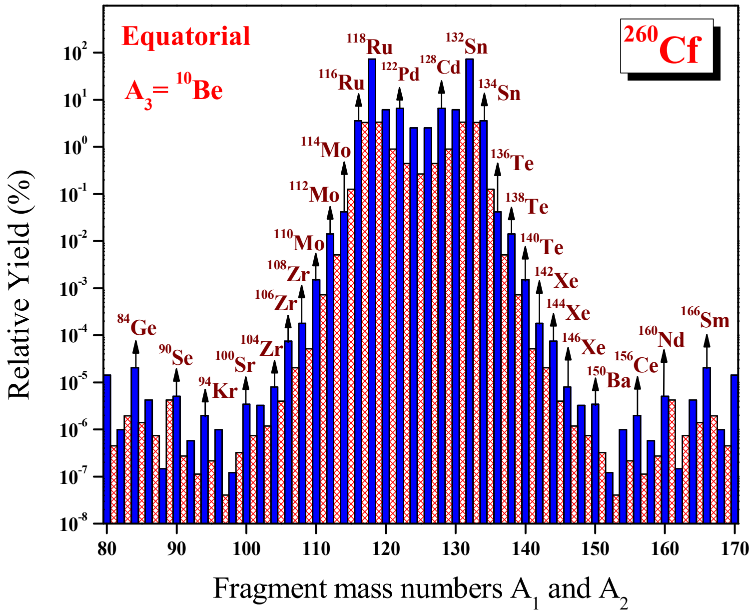

Figure 4.42. The plot connects the relative yield versus the fragment mass number A_1 and A_2 in ^{10}Be accompanied ternary fission of ^{260}Cf isotope with fragments in equatorial configuration.

4.6.7 ^{10}Be accompanied ternary fission of ^{250}Cf with fragments in collinear configuration.

In the ^{10}Be accompanied ternary fission of ^{250}Cf isotope with fragments in collinear configuration, the driving potential is calculated for all fragment combinations. Figure 4.43 represents the cold reaction valley; a plot connects the driving potential versus fragment mass number A_1 in the ternary fission process. The least driving potential is found for the fragment combination ^{110}Ru+^{10}Be+^{130}Sn, which possess a Q value of 218.768 MeV. Also it should be noted that the same fragment combination possess high Q value. The second minimum is found for the splitting ^{108}Ru+^{10}Be+^{132}Sn and is due to the presence of doubly magic nuclei ^{132}Sn (N=82, Z=50). The next minimum is found for the fragment combination ^{106}Mo+^{10}Be+^{134}Te, which is due to the presence of near doubly magic nuclei ^{134}Te (N=52, Z=82).

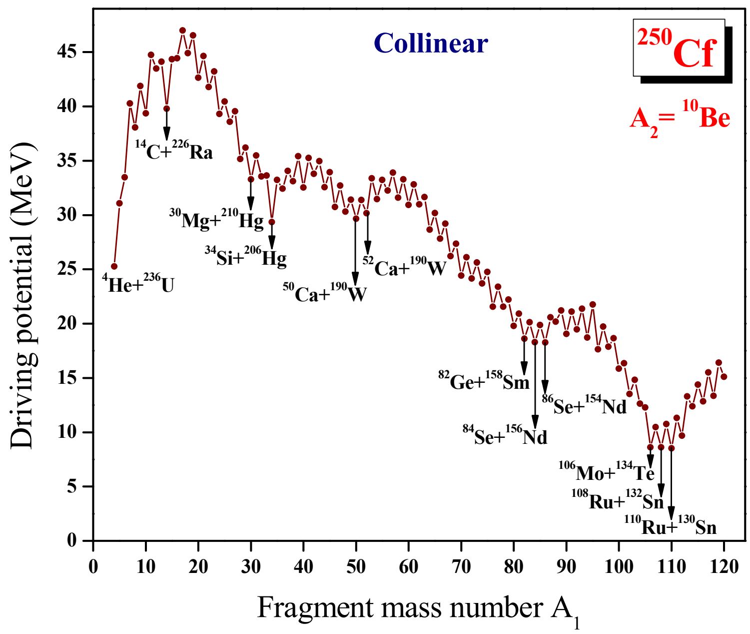

Figure 4.43. The plot connects the driving potential versus the fragment mass number A_1 in the ^{10}Be accompanied ternary fission of ^{250}Cf isotope with fragments in collinear configuration.

The barrier penetrability is calculated for all possible fragmentation found in the cold reaction valley and hence the relative yield is calculated for each fragmentation. **Figure 4.44** represents the plot connects the relative yield versus the fragment mass number A_1 and A_3. From the figure it is clear that the highest relative yield is found for the fragment combination ^{110}Ru+^{10}Be+^{130}Sn, which is the same fragment combination with the least driving potential and high Q value in the cold reaction valley plot. The second highest relative yield is obtained for the fragment combination ^{108}Ru+^{10}Be+^{132}Sn which includes the presence of doubly magic nuclei ^{132}Sn (N=82, Z=50). The next highest relative yield is obtained for ^{106}Mo+^{10}Be+^{134}Te which includes the presence of near doubly magic nuclei ^{134}Te (N=82, Z=52). The next favoured fragment combinations found in this ternary fission process is for ^{112}Ru+^{10}Be+^{128}Sn and ^{114}Ru+^{10}Be+^{126}Sn which includes the presence of proton shell closure Z=50 of ^{128}Sn and ^{126}Sn respectively.

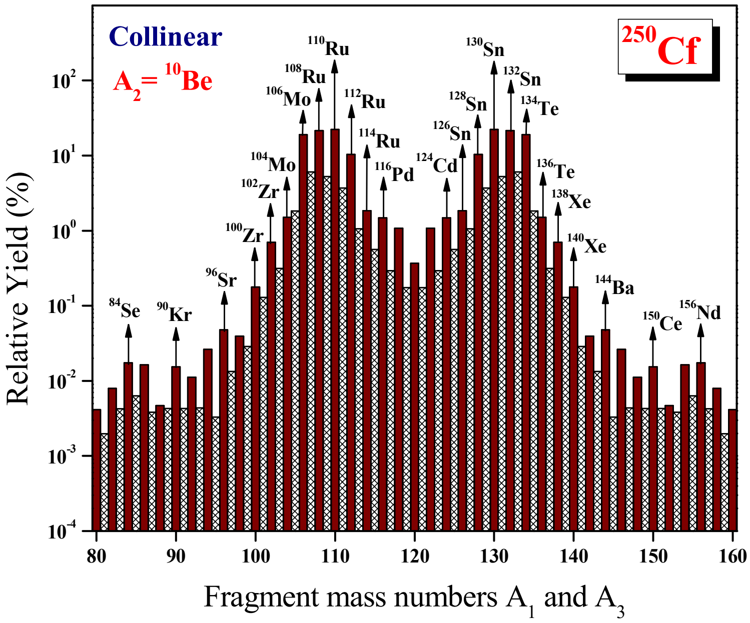

Figure 4.44. The plot connects the relative yield versus the fragment mass number A_1 and A_2 in ^{10}Be accompanied ternary fission of ^{250}Cf isotope with fragments in collinear configuration.

4.6.8 ^{10}Be accompanied ternary fission of ^{252}Cf with fragments in collinear configuration.

In the ^{10}Be accompanied ternary fission of ^{252}Cf isotope with fragments in collinear configuration, the driving potential is calculated for all fragment combinations. Figure 4.45 represents the cold reaction valley; a plot connects the driving potential versus fragment mass number A_1 in the ternary fission process. The least driving potential is found for the fragment combination $^{110}Ru+^{10}Be+^{132}Sn$, which have the Q value of 220.042 MeV. The next minimum is found for the splitting $^{112}Ru+^{10}Be+^{130}Sn$ and is due to the presence of near doubly magic nuclei ^{130}Sn (N=80, Z=50). The minimum found for the fragment splitting $^{108}Mo+^{10}Be+^{134}Te$ is due to the presence of near doubly magic nuclei ^{134}Te (N=82, Z=52). The fragment combination $^{82}Ge+^{10}Be+^{160}Sm$ shows a minimum which is due to the presence of neutron shell closure N=50 of ^{82}Ge.

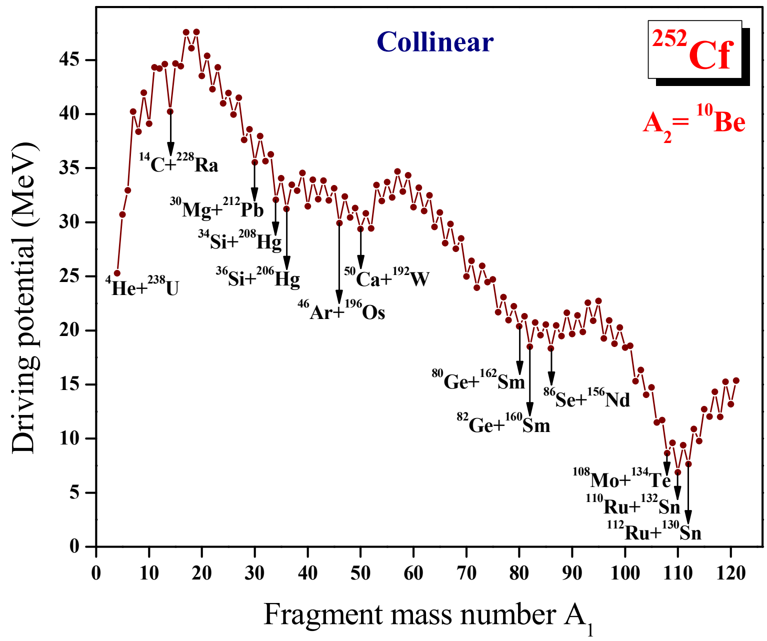

Figure 4.45. The plot connects the driving potential versus the fragment mass number A_1 in the ^{10}Be accompanied ternary fission of ^{252}Cf isotope with fragments in collinear configuration.

The barrier penetrability is calculated for all possible fragmentations found in the cold reaction valley and hence the relative yield is calculated for each fragmentation. **Figure 4.46** represents the plot connects the relative yield versus the fragment mass number A_1 and A_3.

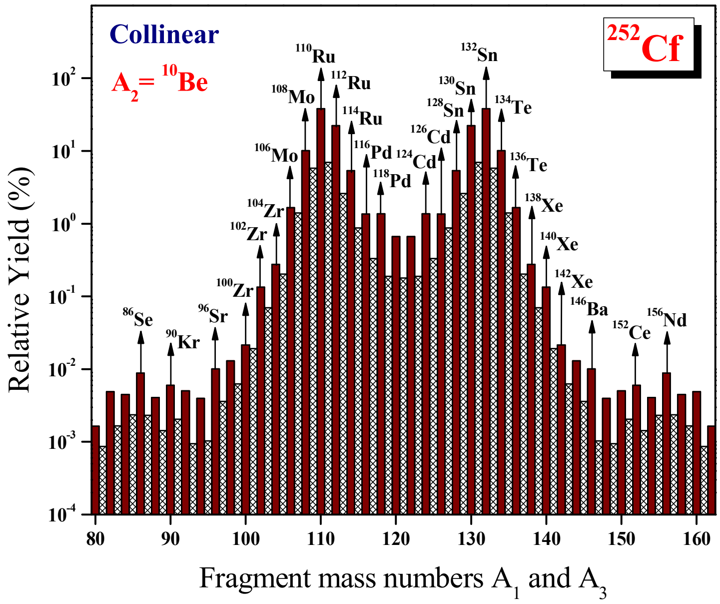

Figure 4.46. The plot connects the relative yield versus the fragment mass number A_1 and A_2 in ^{10}Be accompanied ternary fission of ^{252}Cf isotope with fragments in collinear configuration.

From the figure it is clear that the highest relative yield is found for the fragment combination $^{110}Ru+^{10}Be+^{132}Sn$, which is the same fragment combination with minimum driving potential and high Q value in the cold reaction valley plot. The next highest relative yield is obtained for the fragment combination $^{112}Ru+^{10}Be+^{130}Sn$ which includes the presence of near doubly magic nuclei ^{130}Sn (N=80, Z=50). The next favoured fragment combinations found in this ternary fission process is for $^{108}Mo+^{10}Be+^{134}Te$ which includes the presence of near doubly magic nuclei ^{134}Te (N=82, Z=52). The fragment combinations $^{114}Ru+^{10}Be+^{128}Sn$ and $^{106}Mo+^{10}Be+^{136}Te$ have higher relative yield which is due to the presence of proton shell closure Z=50 of ^{128}Sn and near doubly magic nucleus ^{136}Te (N=84, Z=52) respectively. Some other fragment combinations which possess probable relative yield are also labelled in the figure.

A comparative study has been made with the relative yield obtained in the equatorial and collinear configuration of the ^{10}Be accompanied ternary fission of ^{252}Cf isotope with the experimental data [39]. The ^{10}Be accompanied ternary fission has experimentally observed by Hamilton *et al.,* [39] and identified heavier correlated pairs using the triple gamma coincidence technique with 72 gamma ray detectors. The experimental ternary fission yields of ^{252}Cf with ^{10}Be as light charged particle are observed for the correlated pairs of $^{96}Sr/^{146}Ba$, $^{98}Sr/^{144}Ba$, $^{100}Sr/^{142}Ba$, $^{100}Zr/^{142}Xe$, $^{102}Zr/^{140}Xe$, $^{104}Zr/^{138}Xe$, $^{106}Mo/^{136}Te$, $^{108}Mo/^{134}Te$, $^{110}Ru/^{132}Sn$, $^{112}Ru/^{130}Sn$. **Figure 4.47** shows the comparison of the relative yield with the experimental data found in the ternary fission of ^{252}Cf isotope with ^{10}Be as light charged particle. Here the most probable fragment combinations which are observed in the experiment using Gammasphere facility and that obtained using the Unified ternary fission model are found to the same.

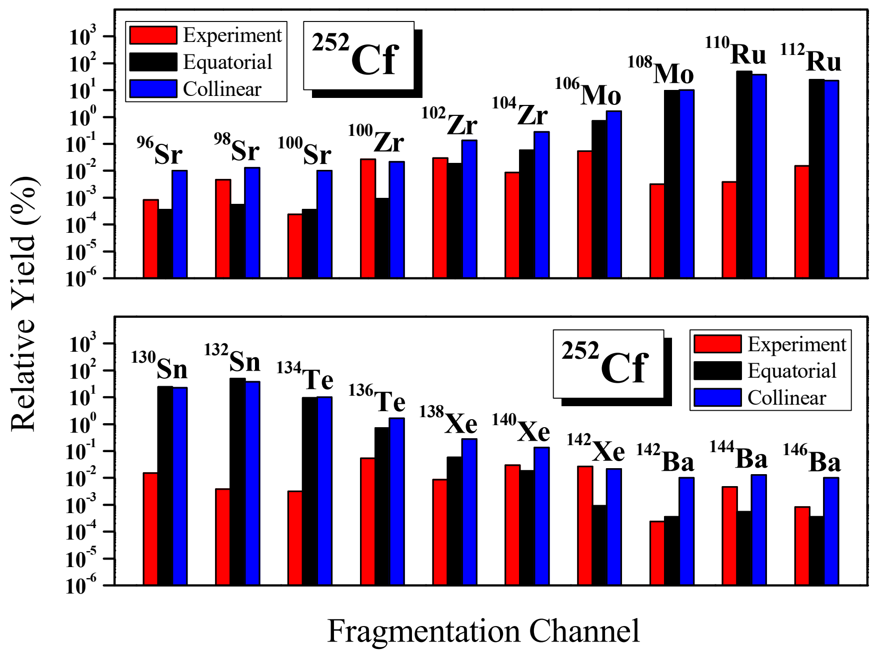

Figure 4.47. Comparison of the relative yield obtained in the equatorial and collinear configuration for the ^{10}Be accompanied ternary fission of ^{252}Cf isotope with the experimental data [39].

4.6.9 ^{10}Be accompanied ternary fission of ^{254}Cf with fragments in collinear configuration.

In the ^{10}Be accompanied ternary fission of ^{254}Cf isotope with fragments in collinear configuration, the driving potential is calculated for all fragment combinations. **Figure 4.48** represents the cold reaction valley. The least driving potential is found for the fragment combination ^{112}Ru+^{10}Be+^{132}Sn, which have the Q value of 220.907 MeV. The minimum found for the splitting ^{114}Ru+^{10}Be+^{130}Sn is due to the presence of near doubly magic nuclei ^{130}Sn (N=80, Z=50). The next minimum is found for the fragment combination ^{110}Mo+^{10}Be+^{134}Te, which is due to the presence of near doubly magic nuclei ^{134}Te (N=82, Z=52). The fragment combination ^{116}Ru+^{10}Be+^{128}Sn shows a minimum which includes the presence of proton shell closure Z=50 of ^{128}Sn. The fragmentation ^{108}Mo+^{10}Be+^{136}Te possess a minimum which is due to the near doubly magic nucleus ^{136}Te (N=84, Z=52).

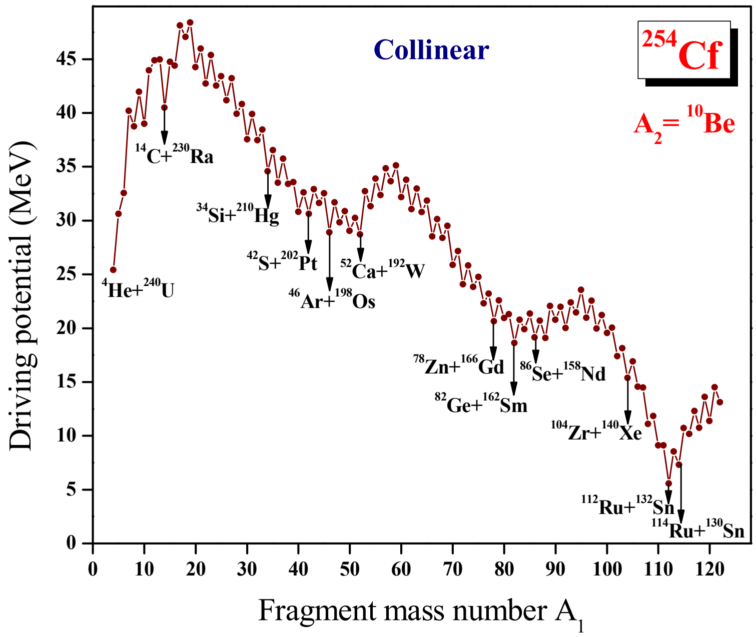

Figure 4.48. The plot connects the driving potential versus the fragment mass number A_1 in the ^{10}Be accompanied ternary fission of ^{254}Cf isotope with fragments in collinear configuration.

The barrier penetrability is calculated for all possible fragmentations found in the cold reaction valley and hence the relative yield is calculated for each fragmentation. **Figure 4.49** represents the plot connects the relative yield versus the fragment mass number A_1 and A_3. From the figure it is clear that the highest relative yield is found for the fragment combination $^{112}Ru+^{10}Be+^{132}Sn$, which is the same fragment combination with minimum driving potential and high Q value in the cold reaction valley plot. The next highest relative yield is obtained for the fragment combination $^{114}Ru+^{10}Be+^{130}Sn$ which includes the presence of near doubly magic nucleus ^{130}Sn (N=80, Z=50). The next favoured fragment combinations found in this ternary fission process is for $^{110}Mo+^{10}Be+^{134}Te$ which include the presence of near doubly magic nucleus ^{134}Te. The fragmentation $^{116}Ru+^{10}Be+^{128}Sn$ and $^{108}Mo+^{10}Be+^{136}Te$ possess a higher relative yield due to the presence of proton shell closure Z=50 of ^{128}Sn and near doubly magic nucleus ^{136}Te (N=84, Z=52) respectively.

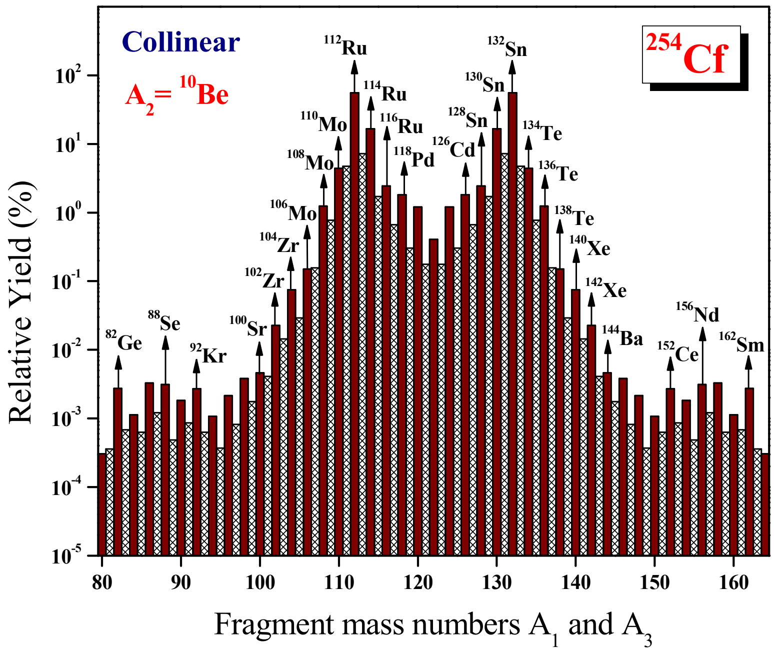

Figure 4.49. The plot connects the relative yield versus the fragment mass number A_1 and A_2 in ^{10}Be accompanied ternary fission of ^{254}Cf isotope with fragments in collinear configuration.

4.6.10 ^{10}Be accompanied ternary fission of ^{256}Cf with fragments in collinear configuration.

In the ^{10}Be accompanied ternary fission of ^{256}Cf isotope with fragments in collinear configuration, the driving potential is calculated for all fragment combinations. **Figure 4.50** represents the cold reaction valley; a plot connects the driving potential versus fragment mass number A_1 in the ternary fission process. The least driving potential is found for the fragment combination ^{114}Ru+^{10}Be+^{132}Sn, which have the Q value of 221.198 MeV. The minimum found for the splitting ^{116}Ru+^{10}Be+^{130}Sn is due to the presence of near doubly magic nuclei ^{130}Sn (N=80, Z=50). The next minima is found for the fragment combination ^{112}Ru+^{10}Be+^{134}Sn, which is due to the presence of near doubly magic nuclei ^{134}Sn (N=84, Z=50). The fragment combination ^{118}Pd+^{10}Be+^{128}Cd shows a minimum which includes the presence of near doubly magic nuclei ^{128}Cd (N=80, Z=48).

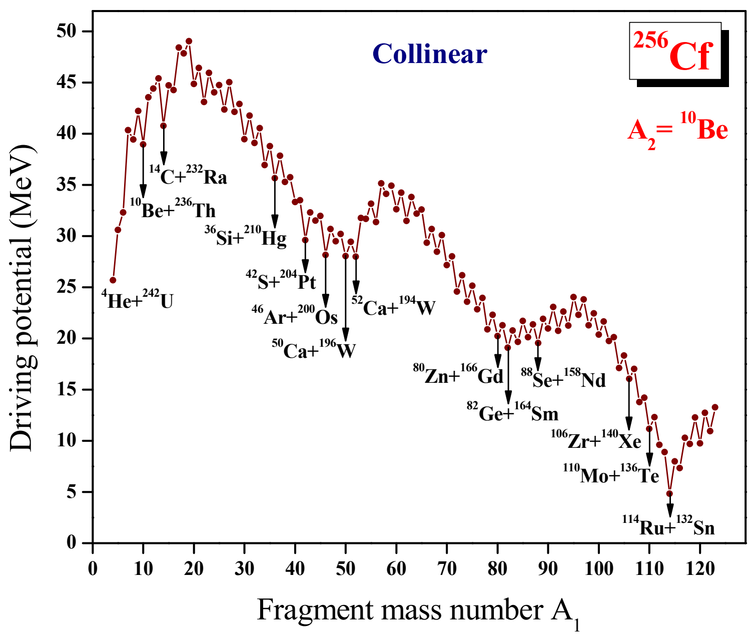

Figure 4.50. The plot connects the driving potential versus the fragment mass number A_1 in the ^{10}Be accompanied ternary fission of ^{256}Cf isotope with fragments in collinear configuration.

The barrier penetrability is calculated for all possible fragmentation found in the cold reaction valley and hence the relative yield is calculated for each fragmentation. **Figure 4.51** represents the plot connects the relative yield versus the fragment mass number A_1 and A_3.

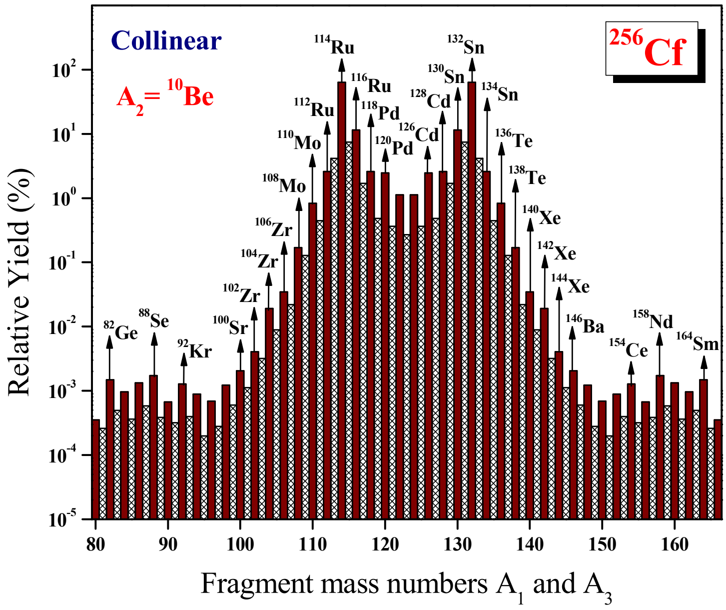

Figure 4.51. The plot connects the relative yield versus the fragment mass number A_1 and A_2 in ^{10}Be accompanied ternary fission of ^{256}Cf isotope with fragments in collinear configuration.

From the figure it is clear that the highest relative yield is found for the fragment combination ^{114}Ru+^{10}Be+^{132}Sn, which is the same fragment combination with minimum driving potential and high Q value in the cold reaction valley plot. The next highest relative yield is obtained for the fragment combination ^{116}Ru+^{10}Be+^{130}Sn which includes the presence of near doubly magic nuclei ^{130}Sn (N=80, Z=50). The next favoured fragment combinations found in this ternary fission process is for ^{112}Ru+^{10}Be+^{134}Sn which includes the presence of near doubly magic nucleus ^{134}Sn (N=84, Z=50). The fragment combinations ^{118}Pd+^{10}Be+^{128}Cd and ^{110}Mo+^{10}Be+^{136}Te have a higher relative yield which is due to the presence of near doubly magic nuclei ^{128}Cd (N=80, Z=48) and ^{136}Te (N=86, Z=52) respectively. Some other fragment combinations which possess probable relative yield are also labelled in the figure.

4.6.11 ^{10}Be accompanied ternary fission of ^{258}Cf with fragments in collinear configuration.

In the ^{10}Be accompanied ternary fission of ^{258}Cf isotope with fragments in collinear configuration, the driving potential is calculated for all fragment combinations and is plotted as shown in **Figure 4.52**. The least driving potential is found for the fragment combination ^{116}Ru+^{10}Be+^{132}Sn, which have the Q value of 221.355 MeV. The minimum found for the splitting ^{118}Ru+^{10}Be+^{130}Sn is due to the presence of near doubly magic nuclei ^{130}Sn (N=80, Z=50). The next minima is found for the fragment combination ^{120}Cd+^{10}Be+^{128}Cd, which is due to the presence of near doubly magic nuclei ^{128}Cd (N=80, Z=48). The fragment combination ^{114}Ru+^{10}Be+^{134}Sn shows a minimum which includes the presence of near doubly magic nuclei ^{134}Sn (N=84, Z=50).

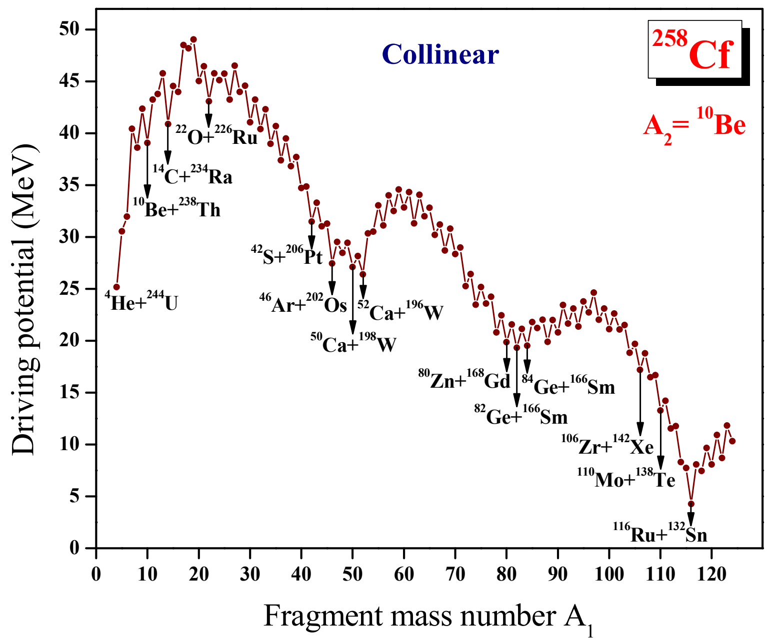

Figure 4.52. The plot connects the driving potential versus the fragment mass number A_1 in the ^{10}Be accompanied ternary fission of ^{258}Cf isotope with fragments in collinear configuration.

The barrier penetrability is calculated for all possible fragmentations found in the cold reaction valley and hence the relative yield is calculated for each fragmentation. **Figure 4.53** represents the plot connects the relative yield versus the fragment mass number A_1 and A_3.

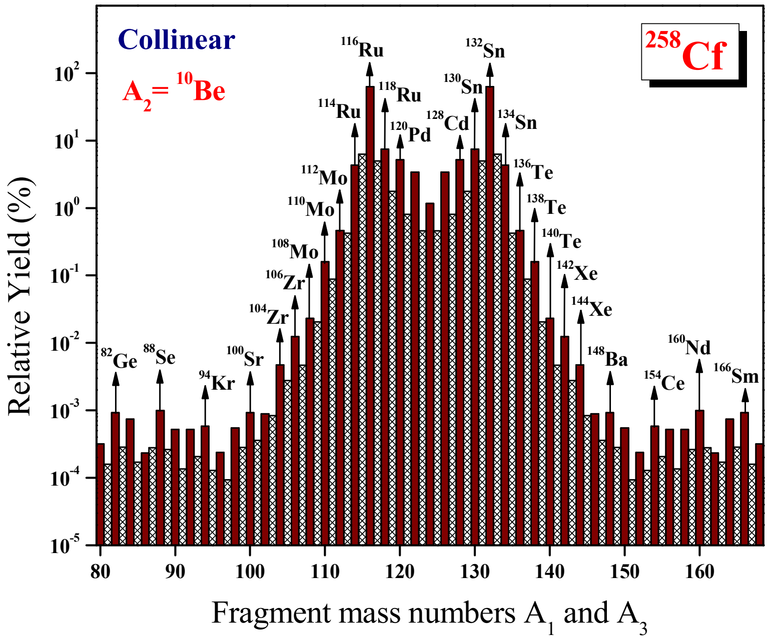

Figure 4.53. The plot connects the relative yield versus the fragment mass number A_1 and A_2 in ^{10}Be accompanied ternary fission of ^{258}Cf isotope with fragments in collinear configuration.

From the figure it is clear that the highest relative yield is found for the fragment combination $^{116}Ru+^{10}Be+^{132}Sn$, which is the same fragment combination with minimum driving potential and high Q value in the cold reaction valley plot. The next highest relative yield is obtained for the fragment combination $^{118}Ru+^{10}Be+^{130}Sn$ which includes the presence of doubly magic nuclei ^{130}Sn (N=80, Z=50). The next favoured fragment combinations found in the ternary fission process is for $^{120}Pd+^{10}Be+^{128}Cd$ and $^{114}Ru+^{10}Be+^{134}Sn$ which include the presence of near doubly magic nuclei ^{128}Cd and ^{134}Sn respectively. Some other fragment combinations which possess probable relative yield are also labelled in the figure. In the figure the hatched bars represents the odd mass numbers and the black ones belongs the even mass number fragments.

4.6.12 ^{10}Be accompanied ternary fission of ^{260}Cf with fragments in collinear configuration.

In the ^{10}Be accompanied ternary fission of ^{260}Cf isotope with fragments in collinear configuration, the driving potential is calculated for all fragment combinations. **Figure 4.54** represents the cold reaction valley; a plot connects the driving potential versus fragment mass number A_1 in the ternary fission process. The least driving potential is found for the fragment combination ^{118}Ru+^{10}Be+^{132}Sn, which have the Q value of 221.166 MeV. The minimum found for the splitting ^{120}Pd+^{10}Be+^{130}Cd is due to the presence of near doubly magic nuclei ^{130}Cd (N=82, Z=48). The next minima is found for the fragment combination ^{122}Pd+^{10}Be+^{128}Cd, which is due to the presence of near doubly magic nuclei ^{128}Cd (N=80, Z=48). The fragment combination ^{116}Ru+^{10}Be+^{134}Sn shows a minimum which includes the presence of near doubly magic nuclei ^{134}Sn (N=84, Z=50).

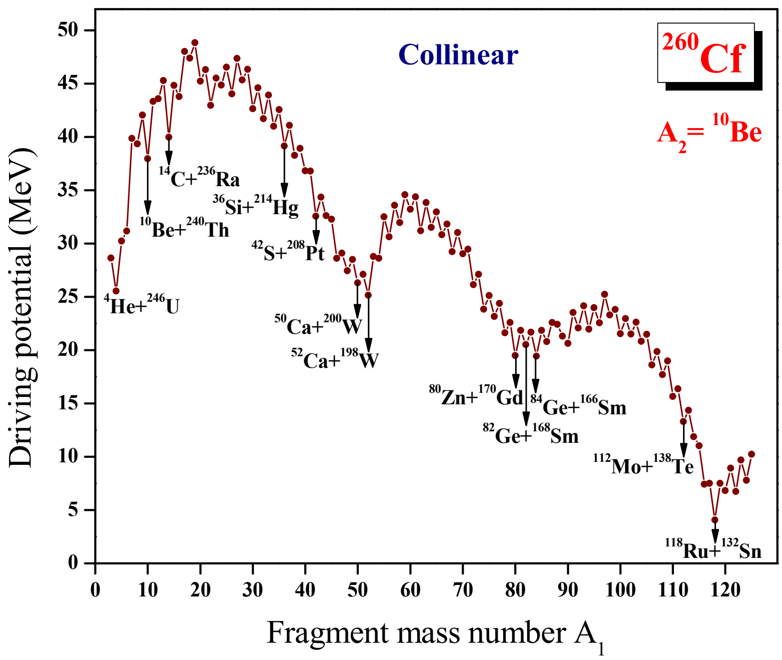

Figure 4.54. The plot connects the driving potential versus the fragment mass number A_1 in the ^{10}Be accompanied ternary fission of ^{260}Cf isotope with fragments in collinear configuration.

The barrier penetrability is calculated for all possible fragmentations found in the cold reaction valley and hence the relative yield is calculated for each fragmentation. **Figure 4.55** represents the plot connects the relative yield versus the fragment mass number A_1 and A_3. From the figure it is clear that the highest relative yield is found for the fragment combination ^{118}Pd+^{10}Be+^{132}Sn, which is the same fragment combination with minimum driving potential and high Q value in the cold reaction valley plot. The next highest relative yield is obtained for the fragment combinations ^{120}Pd+^{10}Be+^{130}Cd, ^{122}Pd+^{10}Be+^{128}Cd and ^{116}Ru+^{10}Be+^{134}Sn. Some other fragment combinations which possess probable relative yield are also labelled in the figure. In the figure the hatched bars represents the odd mass numbers and the black bars belongs to the even mass number fragments.

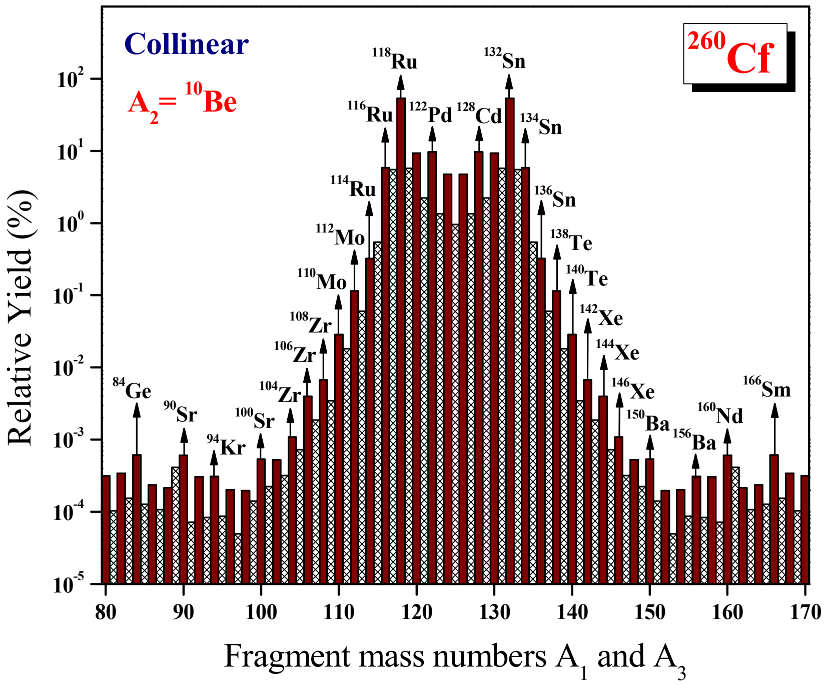

Figure 4.55. The plot connects the relative yield versus the fragment mass number A_1 and A_2 in ^{10}Be accompanied ternary fission of ^{260}Cf isotope with fragments in collinear configuration.

4.6.13 Summary

The cold ternary fission of even-even $^{250\text{-}260}$Cf isotope with ^{10}Be as light charged particle emitted in equatorial and collinear configuration has studied using the Unified ternary fission model (UTFM) in which the interacting potential barrier is taken as the sum of Coulomb and proximity potential. In both equatorial and collinear configuration of the fragments, the fragment combination with the highest yield is found to be the same. In the ^{10}Be accompanied ternary fission of ^{250}Cf isotope, the highest yield is found for the ternary splitting ^{110}Ru+^{10}Be+^{130}Sn, which possess the highest Q value and includes the presence of near doubly magic nucleus ^{130}Sn (N=80, Z=50). In the ternary fission of ^{252}Cf, ^{254}Cf, ^{256}Cf, ^{258}Cf and ^{260}Cf isotopes with ^{10}Be as light charged particle, the highest yield is obtained for the fragmentation ^{110}Ru+^{10}Be+^{132}Sn, ^{112}Ru+^{10}Be+^{132}Sn ^{114}Ru+^{10}Be+^{132}Sn, ^{116}Ru+^{10}Be+^{132}Sn and ^{118}Ru+^{10}Be+^{132}Sn respectively; all of which possess the presence of doubly magic nucleus ^{132}Sn. Hence the presence of high Q value and doubly or near doubly magic nucleus plays a significant role in the ternary fission of even-even $^{250\text{-}260}$Cf isotope with ^{10}Be as light charged particle. The yield obtained for both the equatorial and collinear configuration are compared with the experimental data and found that the most favourable fragment combinations obtained using our formalism and that observed in the experiment using the Gammasphere facility are to be the same.

4.7 The emission probabilities of long range alpha particles from even-even $^{244\text{-}252}$Cm isotopes.

The ternary fragmentation of ^{244}Cm, ^{246}Cm, ^{248}Cm, ^{250}Cm and ^{252}Cm with ^{4}He as light charged particle for the equatorial configuration is studied using the concept of cold reaction valley which was introduced in relation to the structure of minima in the so called driving potential. The emission probability and kinetic energy of long range alpha particle emitted from the ternary fission process of various isotopes of Cm are also studied in detail.

4.7.1 Alpha accompanied ternary fission of ^{244}Cm

The driving potential is calculated for the cold ternary fission of ^{244}Cm with ^{4}He as light charged particle and is plotted as a function of mass number A_1 as shown in **Figure 4.56**. In the cold valley, the minima is found for the fragment combinations with mass number A_1= ^{4}He, ^{10}Be, ^{14}C, ^{16}C, ^{20}O, ^{22}O, ^{24}O, ^{26}Ne, ^{30}Mg, ^{32}Mg, ^{34}Si, ^{36}Si, ^{40}S, ^{42}S, ^{44}Ar, ^{46}Ar, ^{48}Ar, ^{50}Ca, ^{52}Ca etc. The deepest minimum is found for the fragment combination ^{4}He+^{4}He+^{236}U. The other minima valleys are found around the fragment combinations ^{82}Ge+^{4}He+^{158}Sm and ^{106}Mo+^{4}He+^{134}Te. Of these, the fragment combinations ^{106}Mo+^{4}He+^{134}Te with higher *Q* values will be the most favourable fragments for the alpha accompanied ternary fission of ^{244}Cm and is due to the presence of near doubly magic nuclei ^{134}Te (N=82, Z=52). The barrier penetrability is calculated for each charge minimized fragments in the cold ternary fission of ^{244}Cm using the formalism described above. The relative yield is calculated and plotted as a function of mass numbers A_1 and A_2 as shown in **Figure 4.57(b)**. The highest yield is obtained for the fragment combination ^{110}Ru+^{4}He+^{130}Sn, which is due to the presence of near doubly magic nuclei ^{130}Sn (N=80, Z=50) and the Q value of 216.233MeV, which is very high. The next highest yield found for the fragment combinations ^{106}Mo+^{4}He+^{134}Te is due to the near doubly magic nuclei ^{134}Te (N=82, Z=52) and the yield obtained for the fragment combination ^{108}Ru+^{4}He+^{132}Sn is due to the presence of doubly magic nuclei ^{132}Sn (N=82, Z=50). The closed shell effect Z=50 of ^{128}Sn and ^{126}Sn makes the fragment combinations ^{112}Ru+^{4}He+^{128}Sn and ^{114}Ru+^{4}He+^{126}Sn with relative higher yield.

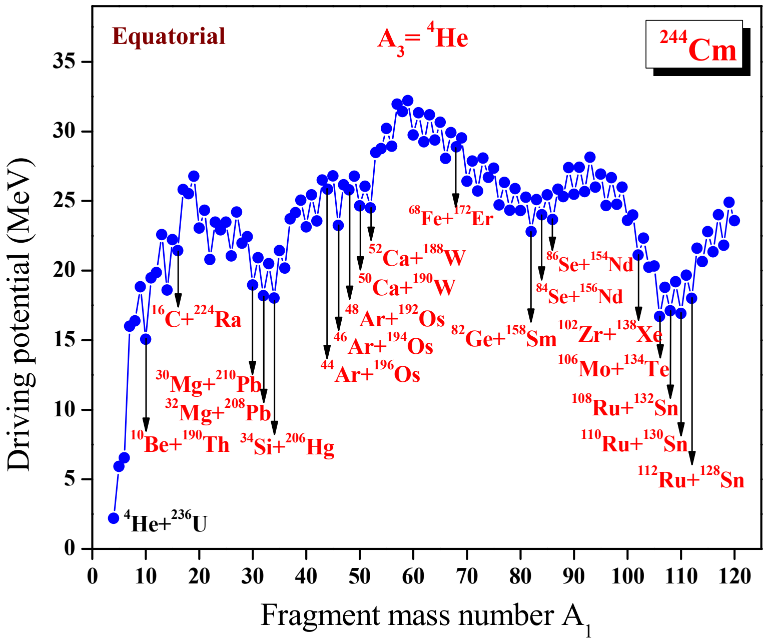

Figure 4.56. The driving potential for ^{244}Cm isotope with ^{4}He as light charged particle, with fragments in the equatorial configuration plotted as a function of fragment mass number A_1.

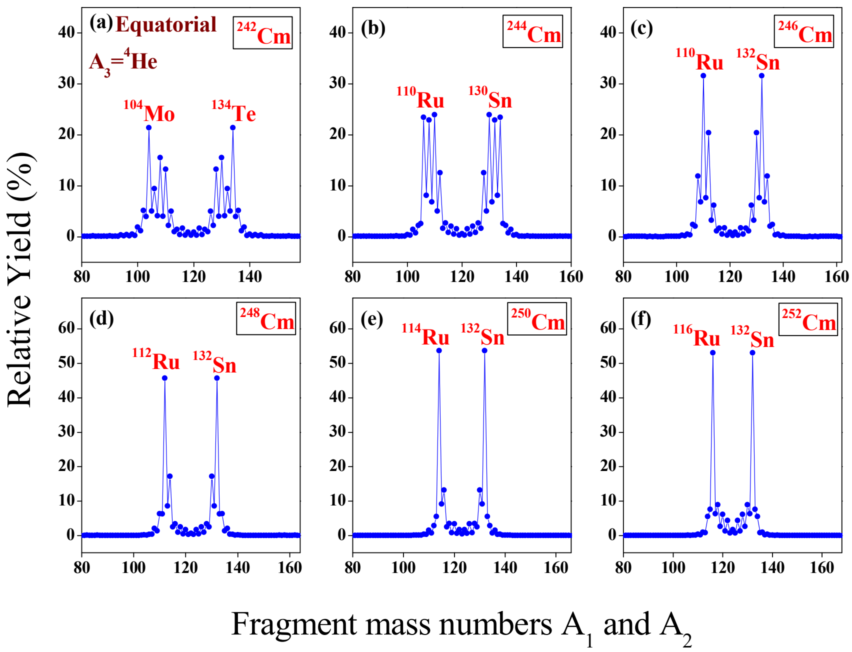

Figure 4.57. The calculated yields for the charge minimized third fragment ^{4}He in the case of equatorial configuration plotted as a function of mass numbers A_1 and A_2 for the isotopes $^{242-252}$Cm. The fragment combinations with highest yield are labelled.

For a better comparison of the yield, a histogram is plotted as a function of mass numbers A_1 and A_2 as shown in **Figure 4.58**. The hatched bars belong to odd mass numbers and the dark ones belong to even mass numbers.

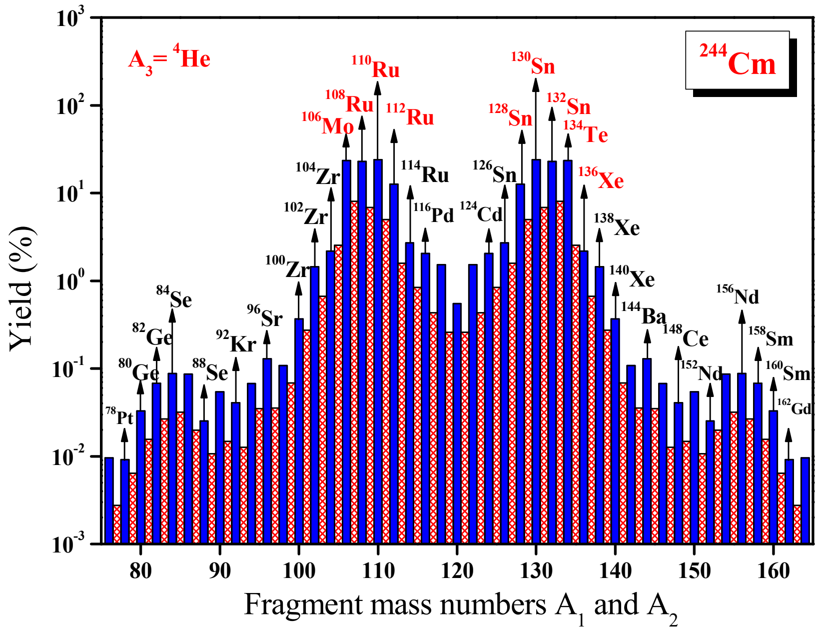

Figure 4.58. The calculated yields for the charge minimized third fragment ^{4}He in the case of equatorial configuration for ^{244}Cm plotted as a function of fragment mass numbers A_1 and A_2.

4.7.2 Alpha accompanied ternary fission of ^{246}Cm

For the alpha accompanied ternary fission of ^{246}Cm, the driving potential is calculated and plotted as a function of mass number A_1 as shown in **Figure 4.65**. The minima is found for the fragment combinations with mass number A_1= ^{4}He, ^{10}Be, ^{14}C, ^{16}C, ^{18}C, ^{20}O, ^{22}O etc. The deepest minimum is found for the fragment combination $^{4}He+^{4}He+^{238}U$. Moving on the fission region three deep valleys are found; one around $^{36}Si+^{4}He+^{206}Hg$ which possess near doubly magic nuclei ^{206}Hg, second one around $^{82}Ge+^{4}He+^{160}Sm$ possessing the neutron closed shell N=50 of ^{82}Ge and the third one around $^{110}Ru+^{4}He+^{132}Sn$ which possess near doubly magic nuclei ^{132}Sn (N=82, Z=50) and also higher Q value.

The relative yield is calculated and plotted as a function of mass numbers A_1 and A_2 as shown in **Figure 4.57(c)**. The highest yield is obtained for $^{110}Ru+^{4}He+^{132}Sn$ which possess doubly magic nuclei ^{132}Sn (N=82, Z=50) and highest Q value of 216.808MeV. The presence of near doubly magic nuclei ^{130}Sn (N=80, Z=50) and ^{134}Te (N=82, Z=52) respectively makes the fragment combinations $^{112}Ru+^{4}He+^{130}Sn$ and $^{108}Mo+^{4}He+^{134}Te$ with relatively higher yield. The high yield found for the splitting $^{114}Ru+^{4}He+^{128}Sn$ is due to the proton magic number Z=50 of ^{128}Sn and the presence of near doubly magic nuclei ^{136}Te (N=84, Z=52) is to be quoted as the reason for the high yield obtained for $^{106}Mo+^{4}He+^{136}Te$.

4.7.3 Alpha accompanied ternary fission of ^{248}Cm

The driving potential is calculated for the alpha accompanied ternary fission of ^{248}Cm and plotted it as a function of mass number A_1 as shown in **Figure 4.66**. In the cold valley the minima is found for the fragment combination with A_1= ^{4}He, ^{10}Be, ^{14}C, ^{16}C, ^{18}C, ^{20}O, ^{22}O etc. The deepest minimum is found for the fragment combination $^{4}He+^{4}He+^{240}U$, possesses Q value of 9.8271MeV. The other deep valleys are found around the fragment combinations $^{38}Si+^{4}He+^{206}Hg$ which possess near doubly magic nuclei ^{206}Hg (N=126, Z=80) and $^{82}Ge+^{4}He+^{162}Sm$ which possess closed shell effect Z=50 of ^{82}Ge. The fragment combination occur around $^{112}Ru+^{4}He+^{132}Sn$ with high Q value 217.141MeV may be the most favourable fragments occur in the ^{4}He accompanied ternary fission of ^{248}Cm which is due to the presence of and doubly magic nuclei ^{132}Sn.

The relative yield is calculated and plotted it as a function of mass number A_1 as shown in **Figure 4.57(d)**. The highest yield is obtained for the fragment combination $^{112}Ru+^{4}He+^{132}Sn$ which possess doubly magic nuclei ^{132}Sn (N=82, Z=50) and highest Q value of 217.141MeV. The next highest yield obtained for the splitting $^{114}Ru+^{4}He+^{130}Sn$ and $^{110}Mo+^{4}He+^{134}Te$ is due to the presence of near doubly magic nuclei ^{130}Sn (N=80, Z=50) and ^{134}Te (N=82, Z=52) respectively and the yield obtained for $^{116}Ru+^{4}He+^{128}Sn$ is due to the closed shell effect of ^{128}Sn (Z=50). The presence of near doubly magic nuclei ^{136}Te makes the fragment combination $^{108}Mo+^{4}He+^{136}Te$ with relative higher yield.

4.7.4 Alpha accompanied ternary fission of ^{250}Cm

The driving potential is calculated for the alpha accompanied ternary fission of ^{250}Cm and plotted it as a function of mass number A_1 as shown in **Figure 4.67**. The minima obtained in the cold valley for the fragment combinations with mass number A_1= ^{4}He, ^{10}Be, ^{14}C, ^{16}C, ^{18}C, ^{20}O, ^{22}O etc. The deepest minimum valley is obtained for the fragment combination ^{4}He+^{4}He+^{242}U which possess a low Q value 9.520MeV. Moving on the fission region three deep valleys are found one around the fragment combination ^{42}S+^{4}He+^{204}Pt which possess neutron closed shell of ^{204}Pt (N=126), second one around the fragment combination ^{80}Zn+^{4}He+^{166}Gd possessing the neutron closed shell of ^{80}Zn (N=50) and the third one around ^{114}Ru+^{4}He+^{132}Sn. The fragment combination ^{114}Ru+^{4}He+^{132}Sn possess the presence of doubly magic nuclei ^{132}Sn (N=82, Z=50). The relative yield is calculated and plotted it as a function of mass numbers A_1 and A_2 as shown in **Figure 4.57(e)**. The highest yield obtained for the fragment combinations ^{110}Mo+^{4}He+^{136}Te and ^{112}Mo+^{4}He+^{134}Te are due to the nearly doubly magic nuclei ^{136}Te (N=84, Z=52) and ^{134}Te (N=82, Z=52) respectively. The highest yield is obtained for the fragment combination ^{114}Ru+^{4}He+^{132}Sn which possess doubly magic nuclei ^{132}Sn (N=82, Z=50) and highest Q value 217.331MeV. The next highest yield obtained for the fragment combination ^{116}Ru+^{4}He+^{130}Sn is due to the presence of near doubly magic nuclei ^{130}Sn (N=80, Z=50) and the yield obtained for the fragment combination ^{118}Pd+^{4}He+^{128}Cd is due to the presence of neutron closed shell N=80 of ^{128}Cd.

4.7.5 Alpha accompanied ternary fission of ^{252}Cm

The driving potential is calculated for the alpha accompanied ternary fission of ^{252}Cm and plotted it as a function of mass number A_1 as shown in **Figure 4.68**. In the cold valley the minima is found for the fragment combination with A_1= ^{4}He, ^{6}He, ^{10}Be, ^{12}Be, ^{14}C, ^{16}C, ^{18}C, ^{20}O, ^{22}O etc. The deepest minimum is found for the fragment combination with ^{4}He+^{4}He+^{244}U. The other minimum valleys are found around the fragment combination ^{50}Ca+^{4}He+^{198}W (possess proton shell closure Z=20 of ^{50}Ca and near neutron shell closure N=124 of ^{198}W) and ^{80}Zn+^{4}He+^{168}Gd (possess neutron shell closure N=50 of ^{80}Zn). The deep minimum valley occur at the fragment combination $^{116}Ru+^{4}He+^{132}Sn$ possess doubly magic nuclei ^{132}Sn and highest Q value 217.248MeV may be the probable fragment combination with highest yield.

The relative yield is calculated for each charge minimized third fragment and plotted as a function of mass number A_1 and A_2 as shown in **Figure 4.57(f)**. The highest yield is found for the fragment combination $^{116}Pd+^{4}He+^{132}Sn$ is due to the doubly magic nuclei ^{132}Sn and highest Q value of 217.248MeV. The next highest yield is found for the fragment combination $^{118}Ru+^{4}He+^{130}Sn$ which possess near doubly magic nuclei ^{130}Sn (N=80, Z=50) and the yield obtained for the fragment combinations $^{112}Mo+^{4}He+^{136}Te$ and $^{114}Ru+^{4}He+^{134}Sn$ are due to the near doubly magic nuclei ^{136}Te (N=84, Z=52) and ^{134}Sn (N=84, Z=50) respectively.

In **Figure 4.57**, the relative yield is plotted for all the considered isotopes of curium as a function of mass numbers A_1 and A_2. The most probable fragment combinations occur with the alpha accompanied ternary fission is labelled. The relative yield obtained for the isotope ^{242}Cm is also included from our recent work on light charged particle accompanied ternary fission of ^{242}Cm with ^{4}He, ^{10}Be and ^{14}C as light charged particles. The mass numbers are labelled in the X-axis with A_1>80 and A_2<168 as the fragment combination possess higher Q values between the corresponding range of mass numbers. In all the cases, the plot of relative yield with mass number shows a two humped structure. From the figure, it is clear that the relative yield obtained in each isotope of curium increases with the increasing mass number.

4.7.6 Emission probability of long range alpha particle

The emission probability of long range alpha particle LRA is determined with the number of fission events B, and the usual notation for the emission probability is LRA/B. Carjan [41] suggests that LRA emission is possible only if the α cluster is formed inside the fissioning nucleus and should gain enough energy to overcome the Coulomb barrier of the scission nucleus. Serot and Wagemans [19] demonstrated that the emission probability of long range alpha particle is strongly dependent on the spectroscopic factor or α cluster preformation factor S_α which can be calculated in a semi-empirical way proposed by Blendowske *et al.,* [42] as,

$S_\alpha = b\lambda_e / \lambda_{WKB}$, where b is the branching ratio for the ground state to ground state transition, λ_e is the experimental α decay constant and λ_{WKB} is the α decay constant calculated from the WKB approximation. Vermote *et al.,* [21] proved that ^{4}He emission probability in spontaneous fission is about 20% higher than for neutron induced fission. The absolute emission probability is given by,

$$\frac{LRA}{B} = S_\alpha P_{LRA} \qquad (4.7.6.1)$$

With P_{LRA} as the probability of the alpha particle when it is already present in fissioning nucleus given as,

$$\mathrm{P}_{LRA} = \exp\left\{ -\frac{2}{\hbar}\int_{z_0}^{z_1}\sqrt{2\mu(V-Q)}dz \right\} \qquad (4.7.6.2)$$

Here the first turning point is determined from the equation $V(z_0) = Q$, where Q is the decay energy, and the second turning point z_1=0 represent the touching configuration. For the internal (overlap) region, the potential is taken as a simple power law interpolation. Here we have computed the emission probabilities of long range alpha particle in the case of ^{242}Cm, ^{244}Cm, ^{246}Cm and ^{248}Cm. The obtained results are found to be in good agreement with the experimental data [19, 21]. The spectroscopic factors and corresponding emission probabilities of $^{242\text{-}252}$Cm isotopes are listed in **Table 4.7**.

Table 4.7. The calculated and experimental emission probability [19, 21] for the ternary α's of different curium isotopes. The computed spectroscopic factor S_α and P_{LRA} are also listed.

Isotope	S_α	P_{LRA}	$\frac{LRA}{B}[10^{-3}]$	$\left(\frac{LRA}{B}\right)_{EXP.}[10^{-3}]$
^{242}Cm	0.0249	0.1141	2.84	3.34 ± 0.26
^{244}Cm	0.0243	0.1128	2.74	2.73 ± 0.20
^{246}Cm	0.0247	0.1614	3.98	2.49 ± 0.12
^{248}Cm	0.0271	0.1713	4.64	2.30 ± 0.30

4.7.7 Kinetic energy of long range alpha particle

The kinetic energy of long range alpha particle (LRA) emitted in the ternary fission of $^{242\text{-}252}$Cm isotopes are computed using the formalism reported by Fraenkel [44]. The conservation of total momentum in the direction of light particle and in a direction perpendicular to light particle leads to the relations,

$$(m_L E_L)^{1/2} = (m_H E_H)^{1/2} \cos\theta_R - (m_\alpha E_\alpha)^{1/2} \cos\theta_L \quad (4.7.7.1)$$

$$(m_H E_H)^{1/2} \sin\theta_R = (m_\alpha E_\alpha)^{1/2} \sin\theta_L \quad (4.7.7.2)$$

Here m_L, m_H, and m_α are the masses of the light, heavy and the α particle respectively. E_L, E_H and E_α represent the final energies of the light, heavy and the α particle respectively. The kinetic energy of the long range alpha particle can be derived from eqn. (4.7.7.1) and eqn. (4.7.7.2) and is given as,

$$E_\alpha = E_L\left(\frac{m_L}{m_\alpha}\right)(\sin\theta_L \cot\theta_R - \cos\theta_L)^{-2} \quad (4.7.7.3)$$

Here θ_L is the angle between the alpha particle and the light particle and θ_R is the recoil angle. The kinetic energy of light fragment E_L is related to the total kinetic energies of fission fragments TKE as,

$$E_L = \frac{A_H}{A_L + A_H} TKE \quad (4.7.7.4)$$

The total kinetic energies of fission fragments TKE can be computed using the expressions reported by Viola *et al.,* [45] or can be taken from Herbach *et al.,* [46]. In the present work we have used the expression taken from Herbach *et al.,* [46] given as,

$$TKE = \frac{0.2904\,(Z_L + Z_H)^2}{A_L^{1/3} + A_H^{1/3} - (A_L + A_H)^{1/3}} \frac{A_L A_H}{(A_L + A_H)^2} \quad (4.7.7.5)$$

Here A_L and A_H are the mass numbers of light and heavy fragments respectively.

Using the formalism described above we have computed the energy of long range alpha particle emitted from $^{242\text{-}252}$Cm isotopes for various fragmentation channels and is tabulated in **Table 4.8**, where we have given the fragmentation channel and kinetic energy of the long range alpha particle E_α.

Table 4.8. Comparison of the calculated kinetic energy of alpha particle E_α emitted in the ternary fission of even-even $^{242\text{-}252}$Cm isotopes with the experimental data [21, 4].

Fragmentation channel	E_α (MeV) Calc.	E_α (MeV) Expt.	Fragmentation channel	E_α (MeV) Calc.	E_α (MeV) Expt.
$^{242}Cm \rightarrow {}^{96}Sr + {}^{4}He + {}^{142}Ba$	15.14		$^{248}Cm \rightarrow {}^{100}Sr + {}^{4}He + {}^{144}Ba$	15.53	
$^{242}Cm \rightarrow {}^{98}Zr + {}^{4}He + {}^{140}Xe$	15.31		$^{248}Cm \rightarrow {}^{102}Sr + {}^{4}He + {}^{142}Ba$	15.68	
$^{242}Cm \rightarrow {}^{100}Zr + {}^{4}He + {}^{138}Xe$	15.46		$^{248}Cm \rightarrow {}^{104}Zr + {}^{4}He + {}^{140}Xe$	15.82	
$^{242}Cm \rightarrow {}^{102}Zr + {}^{4}He + {}^{136}Xe$	15.60		$^{248}Cm \rightarrow {}^{106}Zr + {}^{4}He + {}^{138}Xe$	15.95	
$^{242}Cm \rightarrow {}^{104}Mo + {}^{4}He + {}^{134}Te$	15.72		$^{248}Cm \rightarrow {}^{108}Mo + {}^{4}He + {}^{136}Te$	16.06	
$^{242}Cm \rightarrow {}^{106}Mo + {}^{4}He + {}^{132}Te$	15.83	15.50 ± 1.00	$^{248}Cm \rightarrow {}^{110}Mo + {}^{4}He + {}^{134}Te$	16.16	15.97 ± 0.12
$^{242}Cm \rightarrow {}^{108}Ru + {}^{4}He + {}^{130}Sn$	15.92		$^{248}Cm \rightarrow {}^{112}Ru + {}^{4}He + {}^{132}Sn$	16.24	
$^{242}Cm \rightarrow {}^{110}Ru + {}^{4}He + {}^{128}Sn$	16.00		$^{248}Cm \rightarrow {}^{114}Ru + {}^{4}He + {}^{130}Sn$	16.31	
$^{242}Cm \rightarrow {}^{112}Ru + {}^{4}He + {}^{126}Sn$	16.06		$^{248}Cm \rightarrow {}^{116}Ru + {}^{4}He + {}^{128}Sn$	16.36	
$^{242}Cm \rightarrow {}^{114}Pd + {}^{4}He + {}^{124}Cd$	16.11		$^{248}Cm \rightarrow {}^{118}Pd + {}^{4}He + {}^{126}Cd$	16.40	
$^{242}Cm \rightarrow {}^{116}Pd + {}^{4}He + {}^{122}Cd$	16.14		$^{248}Cm \rightarrow {}^{120}Pd + {}^{4}He + {}^{124}Cd$	16.42	
$^{242}Cm \rightarrow {}^{118}Pd + {}^{4}He + {}^{120}Cd$	16.16		$^{248}Cm \rightarrow {}^{122}Pd + {}^{4}He + {}^{122}Cd$	16.43	
$^{244}Cm \rightarrow {}^{96}Sr + {}^{4}He + {}^{144}Ba$	15.16		$^{250}Cm \rightarrow {}^{98}Sr + {}^{4}He + {}^{148}Ba$	15.38	
$^{244}Cm \rightarrow {}^{98}Sr + {}^{4}He + {}^{142}Ba$	15.33		$^{250}Cm \rightarrow {}^{100}Sr + {}^{4}He + {}^{146}Ba$	15.55	
$^{244}Cm \rightarrow {}^{100}Zr + {}^{4}He + {}^{140}Xe$	15.49		$^{250}Cm \rightarrow {}^{102}Zr + {}^{4}He + {}^{144}Xe$	15.71	
$^{244}Cm \rightarrow {}^{102}Zr + {}^{4}He + {}^{138}Xe$	15.63		$^{250}Cm \rightarrow {}^{104}Zr + {}^{4}He + {}^{142}Xe$	15.85	
$^{244}Cm \rightarrow {}^{104}Zr + {}^{4}He + {}^{136}Xe$	15.76		$^{250}Cm \rightarrow {}^{106}Zr + {}^{4}He + {}^{140}Xe$	15.98	
$^{244}Cm \rightarrow {}^{106}Mo + {}^{4}He + {}^{134}Te$	15.88	15.99 ± 0.08	$^{250}Cm \rightarrow {}^{108}Mo + {}^{4}He + {}^{138}Te$	16.10	
$^{244}Cm \rightarrow {}^{108}Ru + {}^{4}He + {}^{132}Sn$	15.97		$^{250}Cm \rightarrow {}^{110}Mo + {}^{4}He + {}^{136}Te$	16.21	
$^{244}Cm \rightarrow {}^{110}Ru + {}^{4}He + {}^{130}Sn$	16.06		$^{250}Cm \rightarrow {}^{112}Mo + {}^{4}He + {}^{134}Te$	16.29	
$^{244}Cm \rightarrow {}^{112}Ru + {}^{4}He + {}^{128}Sn$	16.12		$^{250}Cm \rightarrow {}^{114}Ru + {}^{4}He + {}^{132}Sn$	16.37	
$^{244}Cm \rightarrow {}^{114}Ru + {}^{4}He + {}^{126}Sn$	16.18		$^{250}Cm \rightarrow {}^{116}Ru + {}^{4}He + {}^{130}Sn$	16.43	
$^{244}Cm \rightarrow {}^{116}Pd + {}^{4}He + {}^{124}Cd$	16.22		$^{250}Cm \rightarrow {}^{118}Pd + {}^{4}He + {}^{128}Cd$	16.47	
$^{244}Cm \rightarrow {}^{118}Pd + {}^{4}He + {}^{122}Cd$	16.24		$^{250}Cm \rightarrow {}^{120}Pd + {}^{4}He + {}^{126}Cd$	16.50	
$^{244}Cm \rightarrow {}^{120}Pd + {}^{4}He + {}^{120}Cd$	16.25		$^{250}Cm \rightarrow {}^{122}Pd + {}^{4}He + {}^{124}Cd$	16.52	
$^{246}Cm \rightarrow {}^{96}Sr + {}^{4}He + {}^{146}Ba$	15.17		$^{252}Cm \rightarrow {}^{100}Sr + {}^{4}He + {}^{148}Ba$	15.56	
$^{246}Cm \rightarrow {}^{98}Sr + {}^{4}He + {}^{144}Ba$	15.35		$^{252}Cm \rightarrow {}^{102}Sr + {}^{4}He + {}^{146}Ba$	15.73	
$^{246}Cm \rightarrow {}^{100}Sr + {}^{4}He + {}^{142}Ba$	15.51		$^{252}Cm \rightarrow {}^{104}Zr + {}^{4}He + {}^{144}Xe$	15.88	
$^{246}Cm \rightarrow {}^{102}Zr + {}^{4}He + {}^{140}Xe$	15.66		$^{252}Cm \rightarrow {}^{106}Zr + {}^{4}He + {}^{142}Xe$	16.02	
$^{246}Cm \rightarrow {}^{104}Zr + {}^{4}He + {}^{138}Xe$	15.79		$^{252}Cm \rightarrow {}^{108}Zr + {}^{4}He + {}^{140}Xe$	16.14	
$^{246}Cm \rightarrow {}^{106}Mo + {}^{4}He + {}^{136}Te$	15.92	16.41 ± 0.20	$^{252}Cm \rightarrow {}^{110}Mo + {}^{4}He + {}^{138}Te$	16.25	
$^{246}Cm \rightarrow {}^{108}Mo + {}^{4}He + {}^{134}Te$	16.02		$^{252}Cm \rightarrow {}^{112}Mo + {}^{4}He + {}^{136}Te$	16.34	
$^{246}Cm \rightarrow {}^{110}Ru + {}^{4}He + {}^{132}Sn$	16.11		$^{252}Cm \rightarrow {}^{114}Ru + {}^{4}He + {}^{134}Sn$	16.42	
$^{246}Cm \rightarrow {}^{112}Ru + {}^{4}He + {}^{130}Sn$	16.18		$^{252}Cm \rightarrow {}^{116}Ru + {}^{4}He + {}^{132}Sn$	16.49	
$^{246}Cm \rightarrow {}^{114}Ru + {}^{4}He + {}^{128}Sn$	16.24		$^{252}Cm \rightarrow {}^{118}Ru + {}^{4}He + {}^{130}Sn$	16.54	
$^{246}Cm \rightarrow {}^{116}Pd + {}^{4}He + {}^{126}Cd$	16.29		$^{252}Cm \rightarrow {}^{120}Pd + {}^{4}He + {}^{128}Cd$	16.58	
$^{246}Cm \rightarrow {}^{118}Pd + {}^{4}He + {}^{124}Cd$	16.32		$^{252}Cm \rightarrow {}^{122}Pd + {}^{4}He + {}^{126}Cd$	16.60	
$^{246}Cm \rightarrow {}^{120}Pd + {}^{4}He + {}^{122}Cd$	16.34		$^{252}Cm \rightarrow {}^{124}Pd + {}^{4}He + {}^{124}Cd$	16.61	

The computed *TKE* values are found to be around 170MeV and according to Fraenkel [44], for the mean total energies of fission fragments (≈ 168 MeV), the maximum value of the recoil angle $\theta_R = 4.5^0$, and this maximum value is obtained for $\theta_L = 92.25^0$. For this reason, in the present manuscript we have taken $\theta_R = 4.5^0$ and $\theta_L = 92.25^0$. The experimental kinetic energy [21, 4] of the long range alpha particle in the ternary fission of $^{242,244,246,248}Cm$ is also given in the table and has been compared with our calculated values. It is to be noted that, our predicted values are in good agreement with the experimental kinetic energies.

4.7.8. Alpha accompanied ternary fission of $^{242\text{-}252}Cm$ in collinear configuration

The ternary fission of $^{242\text{-}252}Cm$ isotopes with fragments in the collinear configuration are studied using the concept of cold reaction valley. In the collinear configuration, the light charged particle ^{4}He (A_2) is considered in between the other two fragments. The driving potential (*V-Q*) for each parent nuclei $^{242\text{-}252}Cm$ is calculated and plotted as a function of mass number A_1 and is shown in **Figure 4.59**. The fragment combinations with minimum driving potential (with high Q value) usually possess high relative yield. In the ternary fission of $^{242,\,244}Cm$ isotopes, the fragment combinations $^{104}Mo+^{4}He+^{134}Te$ and $^{110}Ru+^{4}He+^{130}Sn$ which possess near doubly magic nuclei ^{134}Te (N=82, Z=52) and ^{132}Sn (N=80, Z=50) respectively, may have higher yields which can be verified through the calculation of penetrability. For the parent nuclei $^{246,\,248,\,250,\,252}Cm$, the minimum occurs for the fragment combination with the isotopes of $^{110,\,112,\,114,\,116}Ru$ and doubly magic ^{132}Sn (N=82, Z=50) respectively.

The barrier penetrability is calculated for all fragment combinations in the ternary fission of the parent nuclei ^{242}Cm using and hence the yield is calculated and plotted as a function of mass numbers A_1 and A_3 as shown in **Figure 4.60(a)**. The highest yield is obtained for the fragment combination $^{104}Mo+^{4}He+^{134}Te$, which possesses near doubly magic nuclei ^{134}Te (N=82, Z=52). The next higher relative yield is obtained for the fragment combinations $^{106}Mo+^{4}He+^{132}Te$, $^{108}Ru+^{4}He+^{130}Sn$ and $^{110}Ru+^{4}He+^{128}Sn$, due to the presence of near doubly magic nuclei ^{132}Te (N=80, Z=52), near doubly magic nuclei ^{130}Sn (N=80, Z=50) and the proton magicity of ^{128}Sn (Z = 50) respectively.

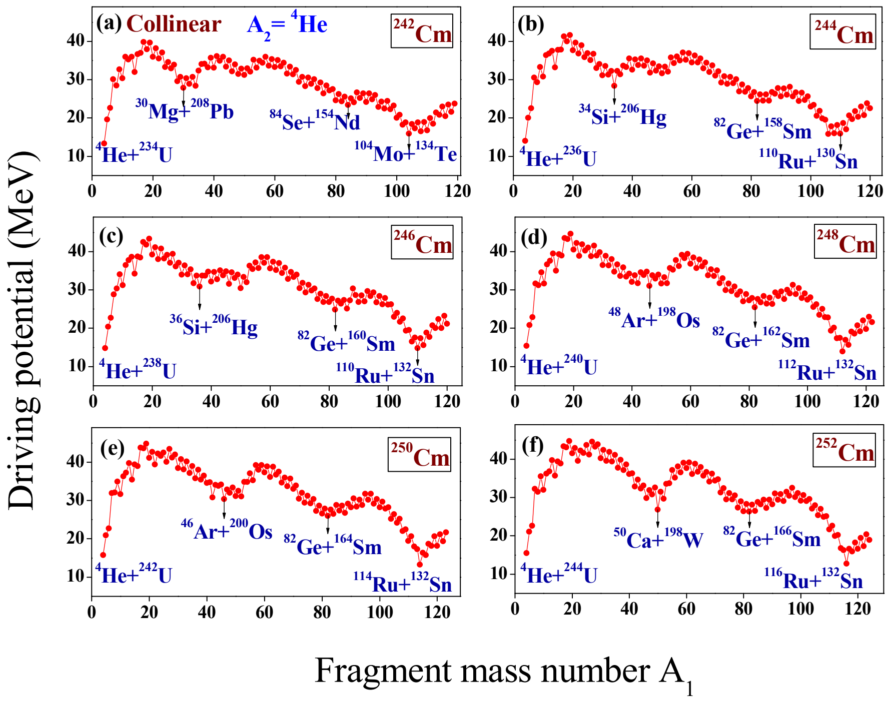

Figure 4.59. The driving potential for $^{242-252}Cm$ isotope with ^{4}He as light charged particle in the case of collinear configuration plotted as a function of fragment mass number A_1.

For the ternary fission of ^{244}Cm, the relative yield is plotted as a function of mass numbers A_1 and A_3 as shown in **Figure 4.60(b)**. The highest yield is obtained for the fragment combination $^{110}Ru+^{4}He+^{130}Sn$ which possesses near doubly magic nuclei ^{130}Sn (N=80, Z=50). The next higher relative yield found for the fragment combinations $^{106}Mo+^{4}He+^{134}Te$, $^{108}Ru+^{4}He+^{132}Sn$ and $^{112}Ru+^{4}He+^{128}Sn$ is due to the presence of near double magicity of ^{134}Te (N=82, Z=52), doubly magic nuclei ^{132}Sn (N=82, Z=50) and the proton magicity of ^{128}Sn (Z = 50) respectively.

In **Figure 4.60(c)**, the relative yield obtained in the ternary fission of ^{246}Cm is plotted as a function of mass numbers A_1 and A_3, in which the highest yield found for the fragment combination $^{110}Ru+^{4}He+^{132}Sn$ which is due to the presence of doubly magic nuclei ^{132}Sn (N=82, Z=50). The next higher yield obtained for the fragment combination $^{108}Mo+^{4}He+^{134}Te$, $^{112}Ru+^{4}He+^{130}Sn$ and $^{114}Ru+^{4}He+^{128}Sn$ is due to the presence of near doubly magic nuclei ^{134}Te (N=82, Z=52), near double magicity of ^{130}Sn (N=80, Z=50) and the presence of proton magic number Z=50 of ^{128}Sn respectively.

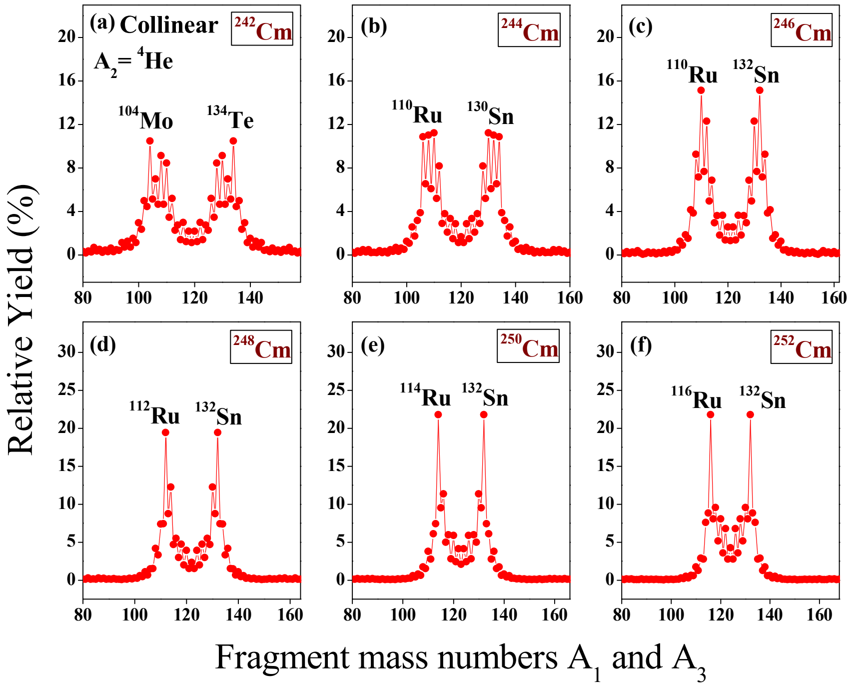

Figure 4.60. The calculated yields for the ternary fission of $^{242\text{-}252}$Cm isotopes with charge minimized third fragment ^{4}He in the case of collinear configuration plotted as a function of mass numbers A_1 and A_3. The fragment combinations with highest yield are labelled.

Figures 4.60(d) - 4.60(f) represent the relative yield versus mass numbers A_1 and A_3 for the ternary fission of ^{248}Cm - ^{252}Cm respectively. In **Figure 4.60(d)**, the highest yield obtained for the fragment combination ^{112}Ru+^{4}He+^{132}Sn is due to the doubly magic nuclei ^{132}Sn (N=82, Z=50). The relative yield obtained for the fragment combinations ^{110}Mo+^{4}He+^{134}Te and ^{114}Ru+^{4}He+^{130}Sn are due to the near double magicity of ^{134}Te (N=82, Z=52) and ^{130}Sn (N=80, Z=50) respectively. From the **Figure 4.60(e)** it is clear that, the highest yield is obtained for the fragment combination ^{114}Ru+^{4}He+^{132}Sn which is due to the presence of doubly magic nuclei ^{132}Sn (N=82, Z=50). The yield found for the fragment combination ^{116}Ru+^{4}He+^{130}Sn is due to the presence of near doubly magic nuclei ^{130}Sn (N=80, Z=50). In the case of

^{252}Cm as shown in **Figure 4.60(f)**, the highest yield is obtained for the fragment combination $^{116}Ru+^{4}He+^{132}Sn$ which possesses doubly magic nuclei ^{132}Sn (N=82, Z=50). The next higher yield found for the fragment combination $^{118}Ru+^{4}He+^{130}Sn$ is due to the near double magicity of ^{130}Sn (N=80, Z=50).

Our study on ternary fragmentation of $^{242-252}Cm$ with fragments in collinear configuration reveals the role of doubly magic nuclei ^{132}Sn (N=82, Z=50), near double magicity of ^{130}Sn (N=80, Z=50) and ^{134}Te (N=82, Z=52). From the comparison of **Figure 4.57** and **Figure 4.60** for respective parent nuclei, it can be seen that the fragment combinations with highest yield obtained in the equatorial and collinear configurations are found to be the same. Also it should be noted that yield for equatorial configuration is twice as that of the collinear configuration and this reveals that equatorial configuration is the preferred configuration than collinear configuration in light charged particle accompanied ternary fission.

4.7.9 Binary fission of $^{242-252}Cm$ isotopes

The driving potential for the binary fission of $^{242-252}Cm$ is calculated using the concept of cold reaction valley and plotted as a function of mass number A_1 as shown in **Figure 4.61**. In the binary fission of ^{242}Cm and ^{244}Cm, the fragment combinations occurring around $^{108}Ru+^{134}Te$ and $^{110}Ru+^{134}Te$ respectively have the minimum value of (V-Q) due to the presence of the near doubly magic ^{134}Te (N=82, Z=52). For the binary fission of $^{246-252}Cm$ isotopes, the fragment combinations found around the doubly magic nuclei ^{132}Sn (N=82, Z=50) have higher relative yield which can be verified through the calculation of penetrability.

The barrier penetrability is calculated for all the possible binary fragmentations of ^{242}Cm and hence the yield is calculated and plotted as a function of mass numbers A_1 and A_2 as shown in **Figure 4.62(a)**. The highest yield is obtained for the fragment combination $^{108}Ru+^{134}Te$ which possesses the near doubly magic nuclei ^{134}Te (N=82, Z=52). The yield found for the splitting $^{110}Ru+^{132}Te$, $^{112}Pd+^{130}Sn$ and $^{114}Pd+^{128}Sn$ is due to the presence of near double magicity of ^{132}Te (N=80, Z=52), near doubly magic nuclei ^{130}Sn (N=82, Z=50) and the closed shell effect Z=50 of ^{128}Sn respectively.

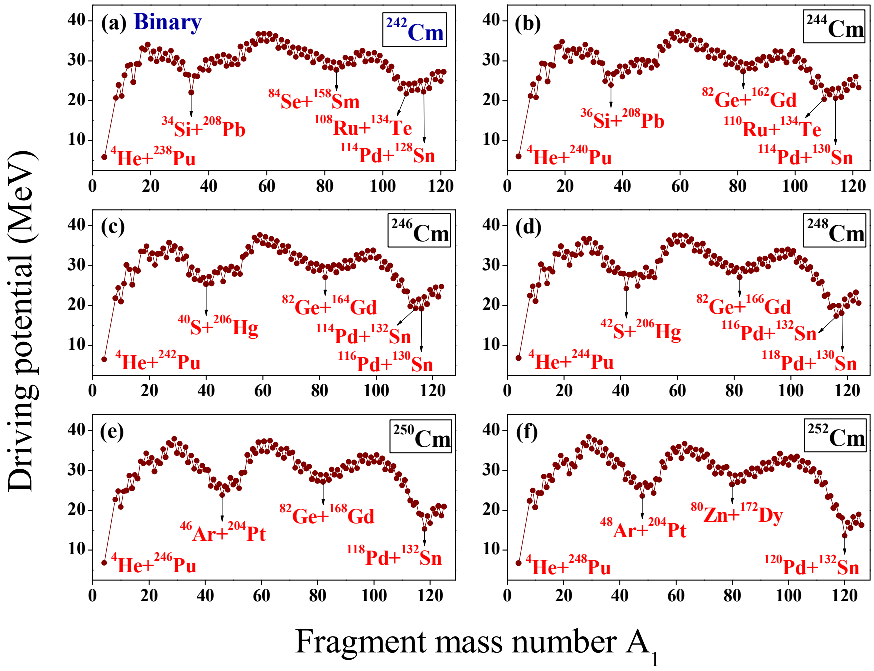

Figure 4.61. The driving potential for the binary fission of $^{242-252}Cm$ isotope plotted as a function of mass number A_1.

In the ^{244}Cm binary fragmentation, the yield is calculated and plotted as a function of mass numbers A_1 and A_2 as shown in **Figure 4.62(b)**. The highest yield is obtained for the fragment combination $^{110}Ru+^{134}Te$ which possesses near doubly magic nuclei ^{134}Te (N=82, Z=52). The yield found for the fragment combination $^{112}Pd+^{132}Sn$, $^{114}Pd+^{130}Sn$ and $^{116}Pd+^{128}Sn$ is due to the presence of doubly magic nuclei ^{132}Sn (N=82, Z=50), near doubly magic nuclei ^{130}Sn (N=80, Z=50) and the proton magicity of ^{128}Sn (Z = 50) respectively. For the binary fission of ^{246}Cm as shown in **Figure 4.62(c)**, the highest relative yield is found for the fragment combination $^{114}Pd+^{132}Sn$ which possesses the presence of doubly magic nuclei ^{132}Sn (N=82, Z=50). The yield found for the fragment combination $^{112}Ru+^{134}Te$, $^{116}Pd+^{130}Sn$ and $^{118}Pd+^{128}Sn$ is due to the presence of near double magicity of ^{134}Te (N=82, Z=52), ^{130}Sn (N=80, Z=50) and proton shell effect Z=50 of ^{128}Sn respectively. **Figures 4.62(d) – 4.62(f)** represent the relative yield versus mass numbers A_1 and A_2 for the binary fission of ^{248}Cm - ^{252}Cm respectively. In **Figure 4.62(d)**, the highest yield is found for the fragment combination $^{116}Pd+^{132}Sn$

which possesses doubly magic nuclei ^{132}Sn (N=82, Z=50). The next higher yield is found for the fragment combination ^{118}Pd+^{130}Sn, which also possesses near double magicity of ^{130}Sn (N=80, Z=50). In the binary fission of ^{250}Cm as shown in **Figure 4.62(e)** the highest yield is found for the fragment combination ^{118}Pd+^{132}Sn, which is due to the presence of doubly magic nuclei ^{132}Sn. The next higher yield is found for the fragment combination ^{120}Pd+^{130}Sn, which possesses near double magicity of ^{130}Sn (N=80, Z=50). In the case of ^{252}Cm, the highest relative yield is obtained for the fragment combination ^{120}Pd+^{132}Sn which possesses doubly magic nuclei ^{132}Sn (N=82, Z=50).

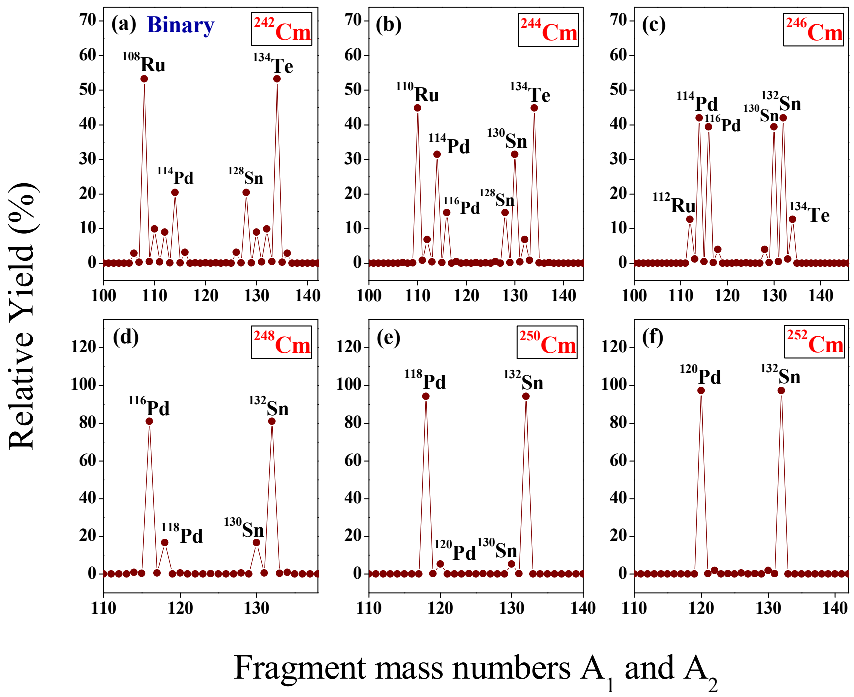

Figure 4.62. The calculated relative yields for the binary fission of $^{242\text{-}252}$Cm isotopes plotted as a function of mass numbers A_1 and A_2. The fragment combinations with highest yield are labelled.

The relative yields obtained for the binary fission of $^{242\text{-}252}$Cm isotopes are compared with that of ternary fission (both the equatorial and collinear configuration) and plotted in **Figure 4.63** as a bar graph. It can be seen that the yield obtained for the equatorial configuration is higher than that of the collinear configuration. From the figure it can also be seen that the yield for binary fission is higher than that of ternary fission (both equatorial and collinear configuration). This indicates to the fact that the probability for the occurrence of binary fragmentation is higher than that of ternary fragmentation and ternary fragmentation is observed 1 in 500 binary fissions.

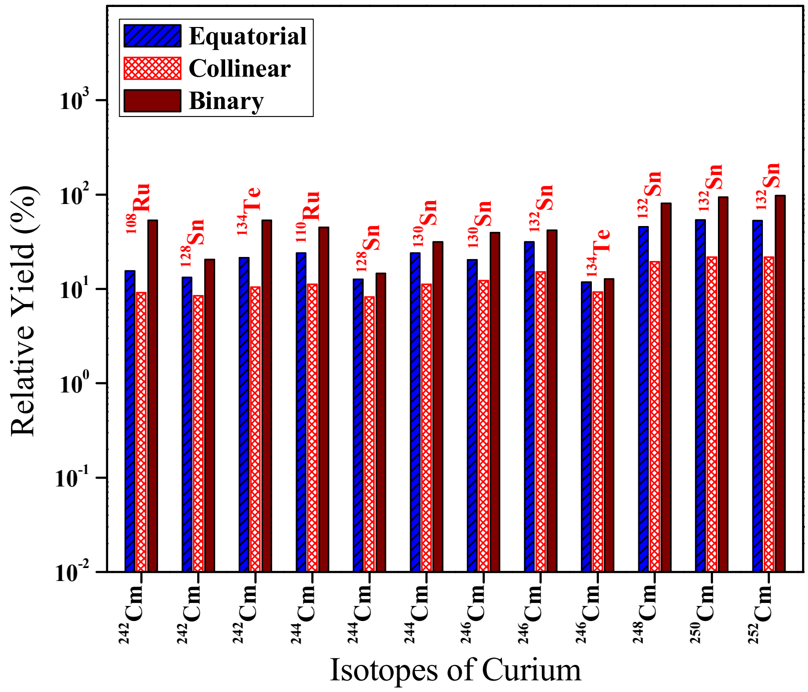

Figure 4.63. Comparison of relative yields for the ^{4}He accompanied ternary fission (both equatorial and collinear configurations) of $^{242\text{-}252}$Cm with the yield for binary fission.

4.7.10 Effect of deformation and orientation of fragments

The effect of deformation and orientation of fragments in ^{4}He accompanied ternary fission of $^{244\text{-}252}$Cm isotopes have been analyzed taking the Coulomb and proximity potential as the interacting barrier. The Coulomb interaction between the two deformed and oriented nuclei, which is taken from [47] and which includes higher multipole deformation [48, 49], is given as,

$$V_C = \frac{Z_1 Z_2 e^2}{r} + 3 Z_1 Z_2 e^2 \sum_{\lambda, i=1,2} \frac{1}{2\lambda+1} \frac{R_{0i}^{\lambda}}{r^{\lambda+1}} Y_{\lambda}^{(0)}(\alpha_i) \left[\beta_{\lambda i} + \frac{4}{7} \beta_{\lambda i}^{2} Y_{\lambda}^{(0)}(\alpha_i) \delta_{\lambda,2} \right] \qquad (4.7.10.1)$$

with $R_i(\alpha_i) = R_{0i}\left[1+\sum_{\lambda}\beta_{\lambda i}Y_{\lambda}^{(0)}(\alpha_i)\right]$ (4.7.10.2)

where $R_{0i} = 1.28A_i^{1/3} - 0.76 + 0.8A_i^{-1/3}$. Here α_i is the angle between the radius vector and symmetry axis of the i^{th} nuclei (see Fig.1 of Ref [48]) and it is to be noted that the quadrupole interaction term proportional to $\beta_{21}\beta_{22}$, is neglected because of its short range character. In proximity potential, $V_P(z) = 4\pi\gamma b\bar{R}\Phi(\varepsilon)$, the deformation comes only in the mean curvature radius. For spherical nuclei, mean curvature radius is defined as $\bar{R} = \frac{C_1C_2}{C_1+C_2}$, where C_1 and C_2 are Süssmann central radii of fragments. The mean curvature radius, $\bar{R}$ for two deformed nuclei lying in the same plane can be obtained by the relation,

$$\frac{1}{\bar{R}^2} = \frac{1}{R_{11}R_{12}} + \frac{1}{R_{21}R_{22}} + \frac{1}{R_{11}R_{22}} + \frac{1}{R_{21}R_{12}} \qquad (4.7.10.3)$$

The four principal radii of curvature R_{11}, R_{12}, R_{21} and R_{22} are given by Baltz and Bayman [50].

Figures 4.64 – 4.68 represent the cold valley plots, the plot connecting the driving potential $(V-Q)$ and the mass number A_1 for ^{244}Cm to ^{252}Cm isotopes. In these plots three cases are considered (1) three fragments taken as spherical (2) two fragments (A_1 and A_2) as deformed with $0^0 - 0^0$ orientation and (3) two fragments (A_1 and A_2) as deformed with $90^0 - 90^0$ orientation. For computing driving potential we have used experimental quadrupole deformation (β_2) values taken from Ref. [51] and for the cases for which there are no experimental values, we have taken them from Moller *et al.,* [52].

It can be seen from these plots that in most of the cases, $0^0 - 0^0$ orientation have a low value for driving potential, but in few cases, $90^0 - 90^0$ orientation has the low value. In the former case, either both the fragments are prolate or one fragment is prolate and the other one is spherical; and in latter case both fragments are either oblate or one fragment is oblate and the other one is spherical. It can be seen that when deformation are included, the optimum fragment combination are also found to be changed.

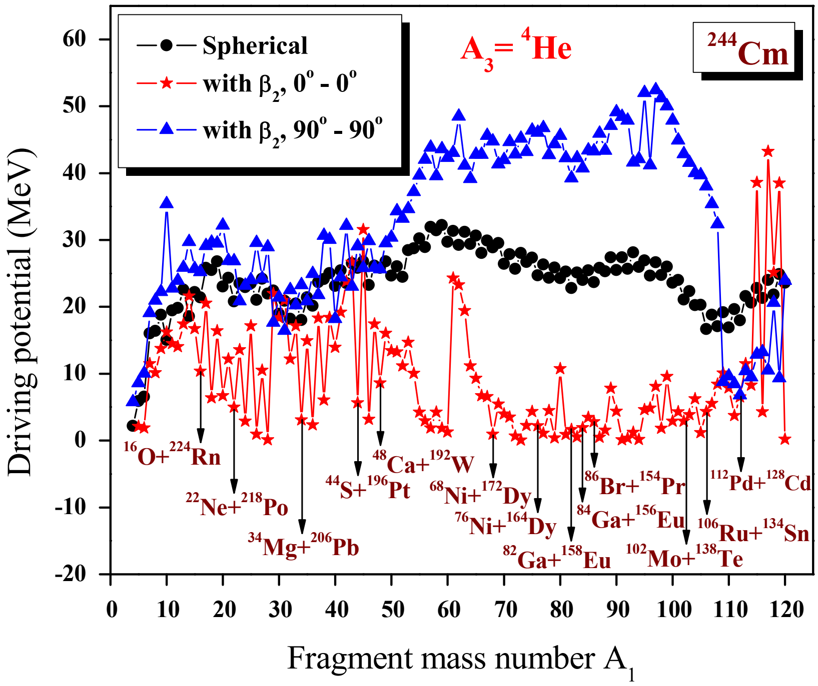

Figure 4.64. The driving potential for ^{244}Cm isotope with ^{4}He as light charged particle with the inclusion of quadrupole deformation β_2 and for different orientation plotted as a function of mass number A_1.

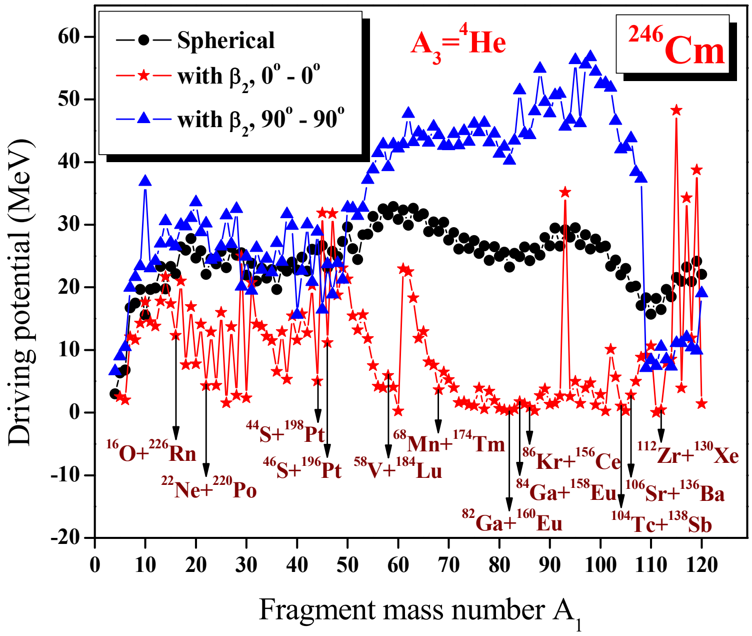

Figure 4.65. The driving potential for ^{246}Cm isotope with ^{4}He as light charged particle with the inclusion of quadrupole deformation β_2 and for different orientation plotted as a function of mass number A_1.

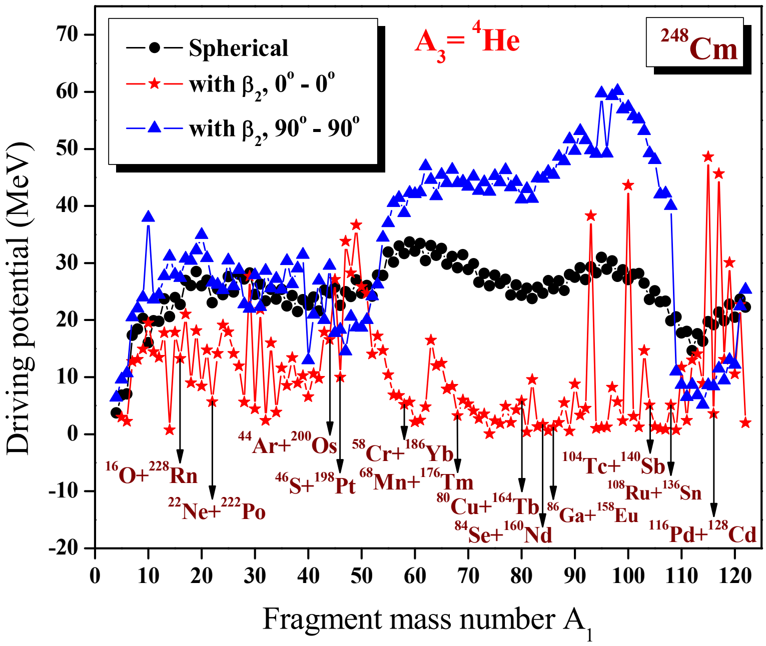

Figure 4.66. The driving potential for ^{248}Cm isotope with ^{4}He as light charged particle with the inclusion of quadrupole deformation β_2 and for different orientation plotted as a function of mass number A_1.

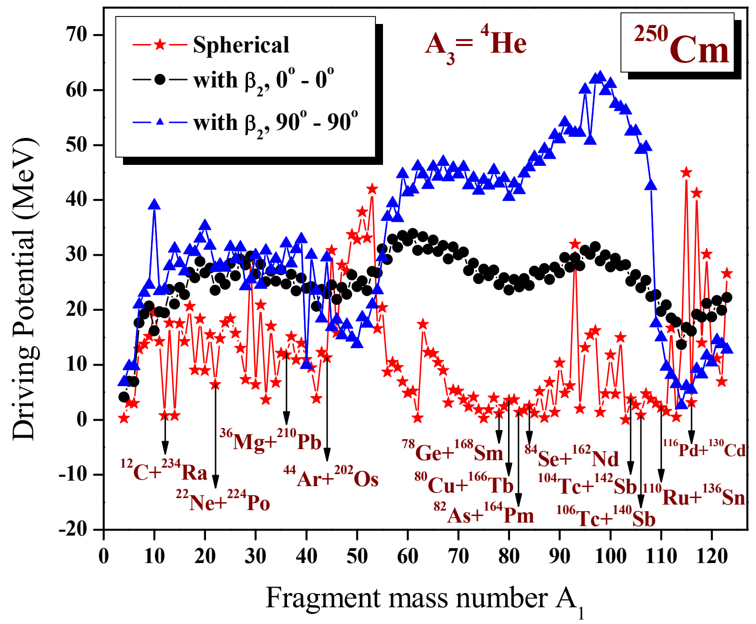

Figure 4.67. The driving potential for ^{250}Cm isotope with ^{4}He as light charged particle with the inclusion of quadrupole deformation β_2 and for different orientation plotted as a function of mass number A_1.

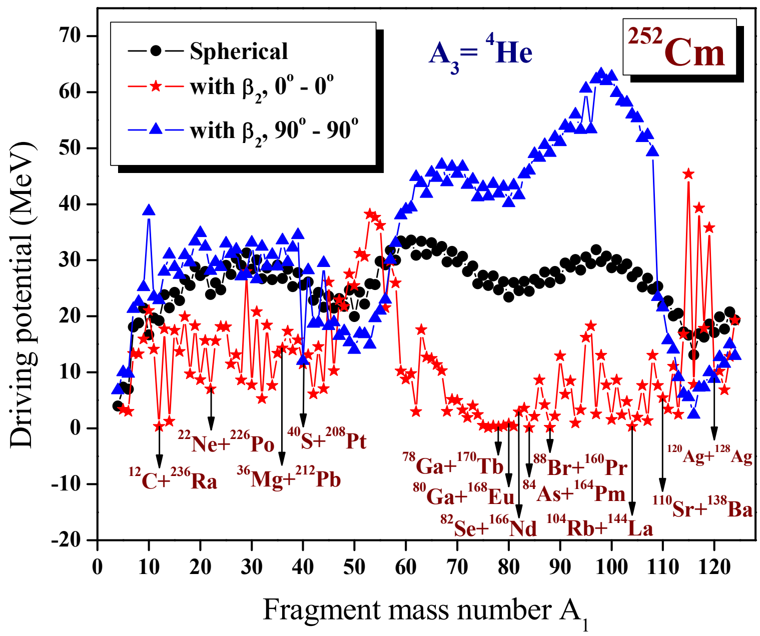

Figure 4.68. The driving potential for ^{252}Cm isotope with ^{4}He as light charged particle with the inclusion of quadrupole deformation β_2 and for different orientation plotted as a function of mass number A_1.

For example, in the case of ^{244}Cm the fragment combination ^{112}Ru+^{4}He+^{128}Sn are changed to ^{112}Pd+^{4}He+^{128}Cd when deformation is included; and in the case of ^{248}Cm the fragment combination ^{116}Ru+^{4}He +^{128}Sn changed to ^{116}Pd+^{4}He +^{128}Cd with the inclusion of deformation. We have computed barrier penetrability for all fragment combinations in the cold valley plot (**Figures 4.64 – 4.68**) which have the minimum $(V-Q)$ value, with including the quadrupole deformation. The computations are done using the deformed Coulomb potential and deformed nuclear proximity potential. Inclusion of quadrupole deformation (β_2) reduces the height and width of the barrier and as a result, the barrier penetrability is found to increase. For e.g. in the case of ^{244}Cm, the fragment combination ^{86}Br+^{4}He+^{154}Pr have barrier penetrability $P^{spherical} = 4.04\times10^{-14}$ when treated as spherical and $P^{deformed} = 4.96\times10^{-12}$ when deformation of fragments are included; and in the case of ^{246}Cm the fragment combination ^{110}Tc+^{4}He+^{132}Sb have barrier penetrability $P^{spherical} = 2.28\times10^{-11}$ when treated as spherical and $P^{deformed} = 3.09\times10^{-10}$ when deformation of fragments are included. It is to be noted that both the fragments are prolate deformed {^{86}Br ($\beta_2 = 0.071$), ^{154}Pr ($\beta_2 = 0.27$)} in the former case and oblate deformed {^{110}Tc ($\beta_2 = -0.258$), ^{132}Sb ($\beta_2 = -0.026$)} in the latter case.

The relative yield is calculated and **Figure 4.69 – 4.70** represent the plot connecting relative yield versus fragment mass number A_1 and A_2 for ^{244}Cm to ^{252}Cm. By comparing the **Figure 4.69 – 4.70** with corresponding plots for the spherical case, equatorial configuration (**Figure 4.57**) and collinear configuration (**Figure 4.60**), it can be seen that fragments with highest yield are also found to be changed. For e.g. in the case of ^{244}Cm the fragments with highest yield are ^{110}Ru and ^{130}Sn when fragments are treated as spheres, but when deformation are included, the highest yield is found for the fragments ^{116}Pd and ^{124}Cd. For a better comparison of the result, a histogram is plotted with yield as a function of mass numbers A_1 and A_2 for the ternary fragmentation of $^{244-252}$Cm isotopes with the inclusion of quadrupole deformation β_2 as shown in **Figure 4.71 – Figure 4.75**. The studies on the influence of deformation in the alpha accompanied ternary fission of $^{244-252}$Cm isotopes reveal that the ground state deformation has an important role in ternary fission as that of shell effect. Vermote *et al.*, [21] experimentally studied the emission probability and the energy distribution of alpha particles in the ternary fission of $^{244-248}$Cm isotopes, but its mass distribution has not been studied so far. We have computed the emission probability of long range alpha particle emitted in the ternary fission of $^{242-248}$Cm isotopes and are in good agreement with the experimental data [19, 21]. Using our formalism we have calculated the mass distribution of heavy fragments in the ternary fission of $^{244-252}$Cm isotopes and have predicted the fragments with highest yield. Our study shows that the fragments ^{109}Tc, ^{131}Sb, ^{116}Pd and ^{124}Cd from ^{244}Cm; ^{109}Tc, ^{114}Ru, ^{116}Pd, ^{126}Cd, ^{128}Sn and ^{133}Sb from ^{246}Cm; ^{114}Ru, ^{116}Pd, ^{128}Cd and ^{130}Sn from ^{248}Cm; ^{114}Ru and ^{132}Sn from ^{250}Cm; and ^{115}Ru, ^{116}Ru, ^{132}Sn and ^{133}Sn from ^{252}Cm have relative yield greater than 10%. We hope that our prediction on the yield of heavy fragments in ternary fission of $^{244-252}$Cm isotopes will guide the future experiments and hope these fragments can be detected using triple gamma coincidence method with the help of Gammasphere as done in the case of alpha accompanied ternary fission of ^{252}Cf isotope [8].

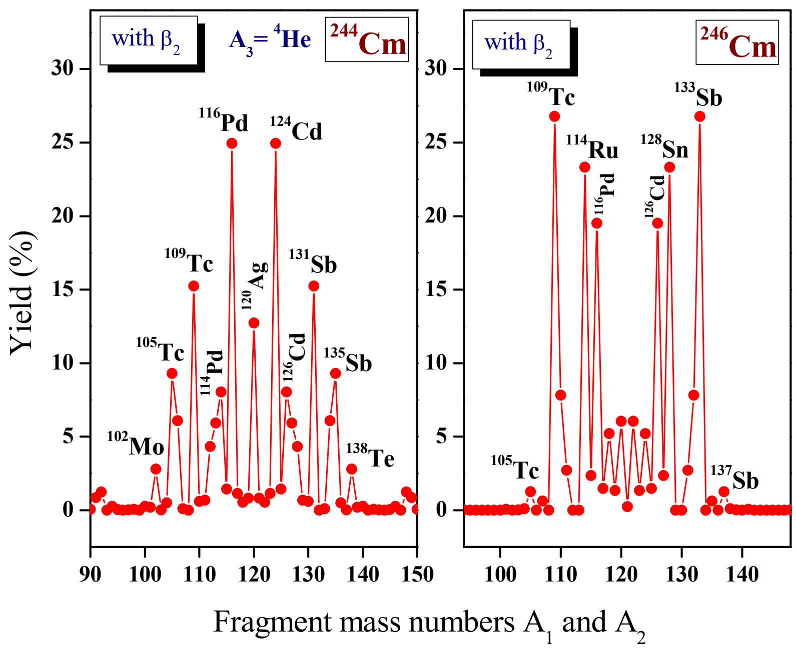

Figure 4.69. The calculated yields for the charge minimized third fragment ^{4}He with the inclusion of quadrupole deformation β_2 plotted as a function of mass numbers A_1 and A_2 for ^{244,246}Cm isotopes. The fragment combinations with higher yields are labelled.

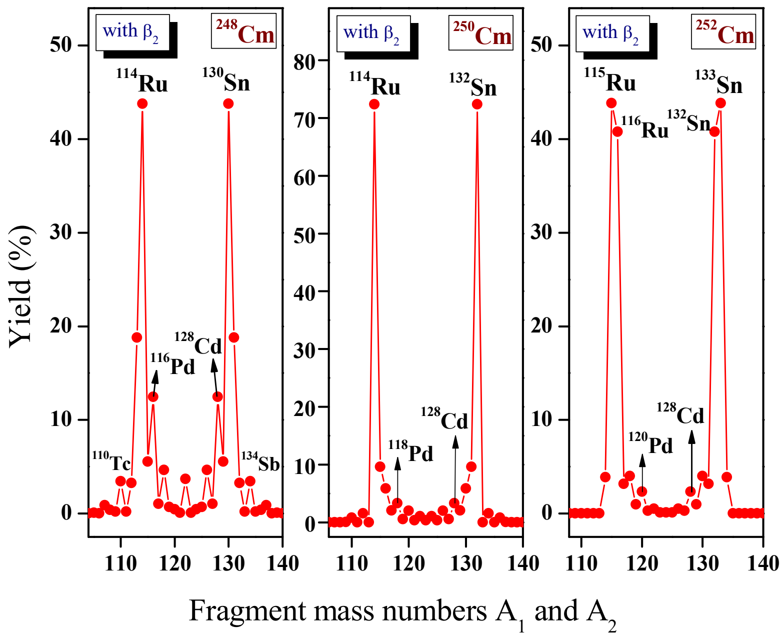

Figure 4.70. The calculated yields for the charge minimized third fragment ^4He with the inclusion of quadrupole deformation β_2 plotted as a function of mass numbers A_1 and A_2 for $^{248,250,252}Cm$ isotopes. The fragment combinations with higher yields are labelled.

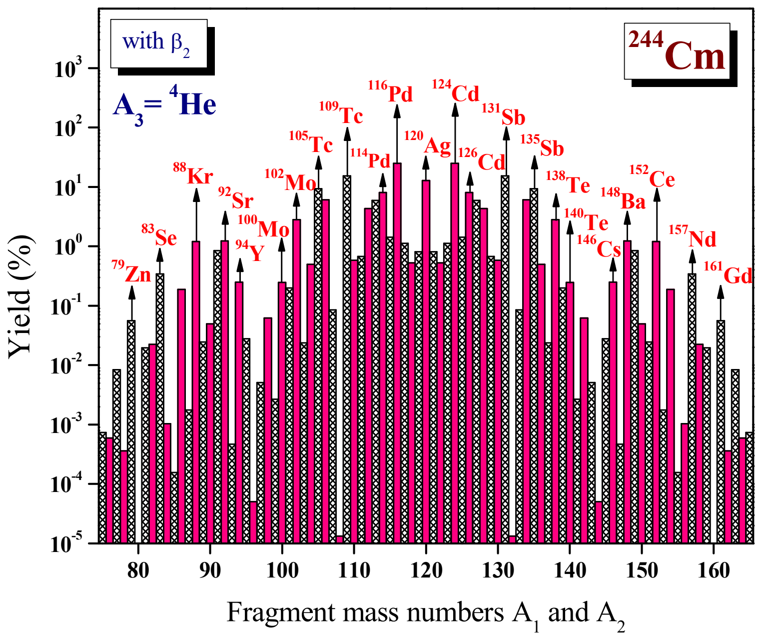

Figure 4.71. The calculated yields for the charge minimized third fragment ^4He with the inclusion of quadrupole deformation β_2 plotted as a function of mass numbers A_1 and A_2 for ^{244}Cm isotope.

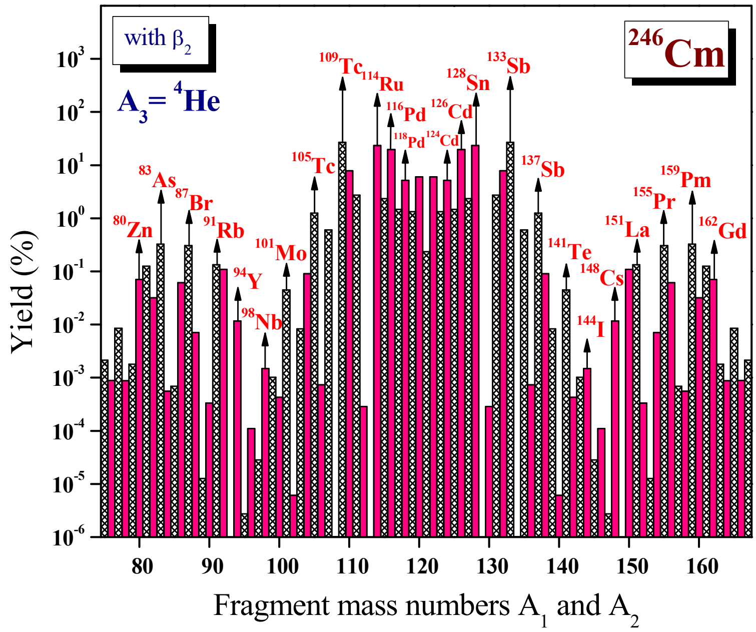

Figure 4.72. The calculated yields for the charge minimized third fragment ^{4}He with the inclusion of quadrupole deformation β_2 is plotted as a function of mass numbers A_1 and A_2 for ^{246}Cm isotope.

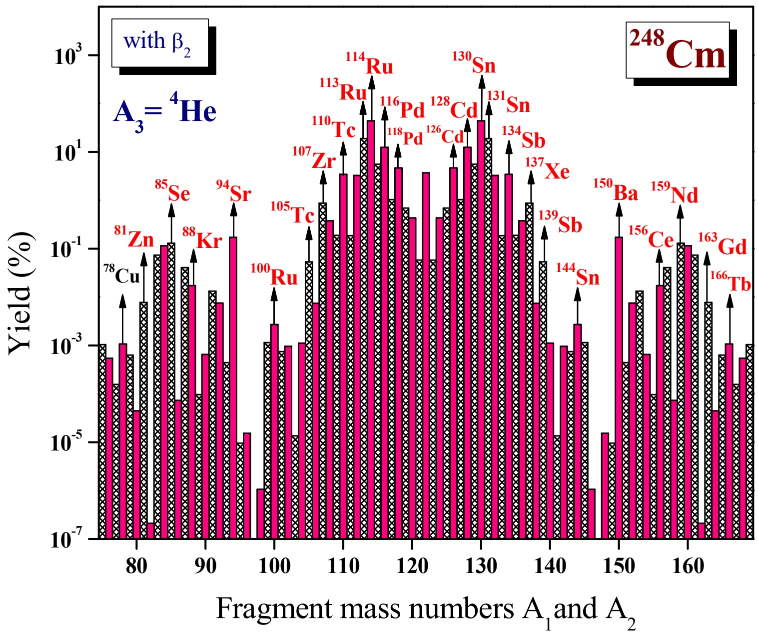

Figure 4.73. The calculated yields for the charge minimized third fragment ^{4}He with the inclusion of quadrupole deformation β_2 plotted as a function of mass numbers A_1 and A_2 for ^{248}Cm isotope.

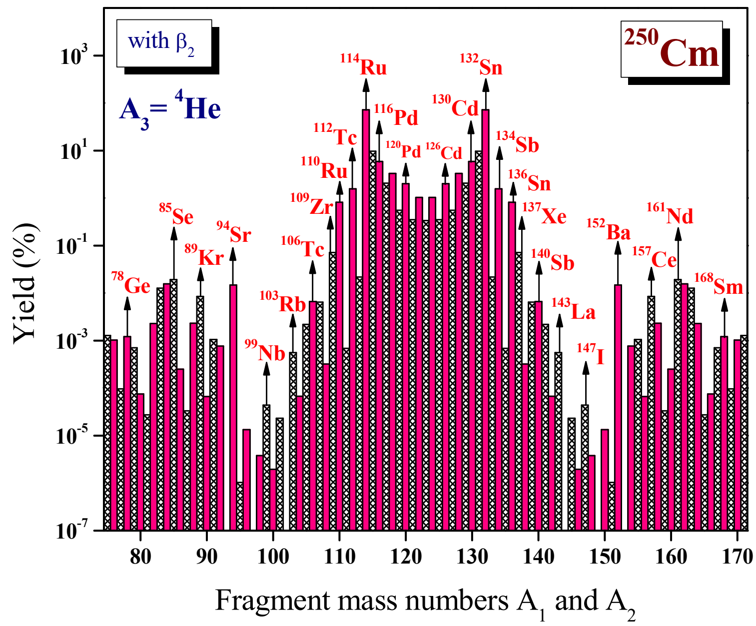

Figure 4.74. The calculated yields for the charge minimized third fragment ^{4}He with the inclusion of quadrupole deformation β_2 plotted as a function of mass numbers A_1 and A_2 for ^{250}Cm isotope.

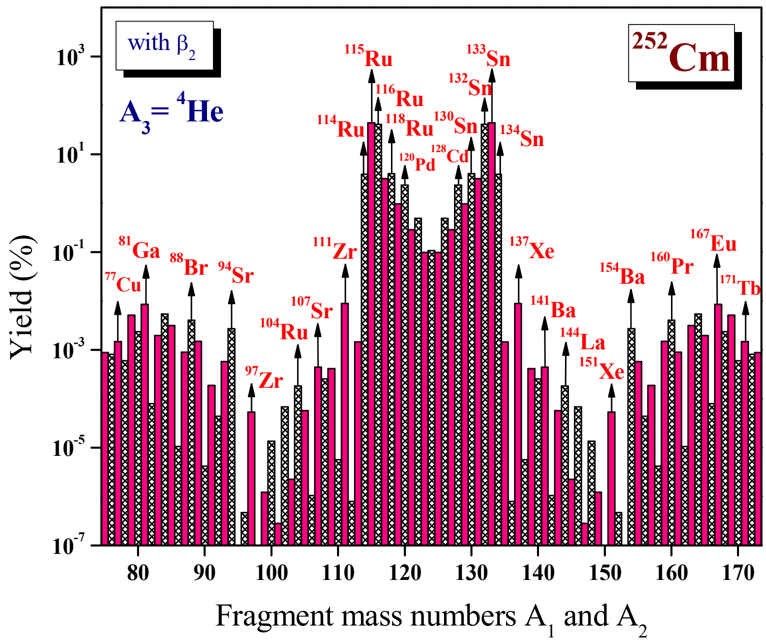

Figure 4.75. The calculated yields for the charge minimized third fragment ^{4}He with the inclusion of quadrupole deformation β_2 plotted as a function of mass numbers A_1 and A_2 for ^{252}Cm isotope.

4.7.11 Summary

With ^{4}He as light charged particle, the relative yield is calculated by taking the interacting barrier as the sum of Coulomb and proximity potential with fragments in equatorial configuration for the ternary fission of ^{244}Cm, ^{246}Cm, ^{248}Cm, ^{250}Cm and ^{252}Cm. In the ternary fission of ^{244}Cm, the highest yield is found for the splitting $^{110}Ru+^{4}He+^{130}Sn$ which possess nearly doubly magic nuclei ^{130}Sn. The highest yield found for alpha accompanied the ternary fragmentation of ^{246}Cm, ^{248}Cm, ^{250}Cm and ^{252}Cm is with $^{110}Ru+^{4}He+^{132}Sn$, $^{112}Ru+^{4}He+^{132}Sn$, $^{114}Ru+^{4}He+^{132}Sn$ and $^{116}Ru+^{4}He+^{132}Sn$ respectively, all of which possesses a higher Q value and doubly magic nuclei ^{132}Sn. Hence for the most favourable fragment combination to occur in ternary fission, the presence of doubly magic nuclei and high Q values play a crucial role. The emission probabilities and kinetic energies of long range alpha particle are computed for the isotopes ^{242}Cm, ^{244}Cm, ^{246}Cm, ^{248}Cm and are found to be in good agreement with the experimental data. The yield obtained for the equatorial configuration is higher than that of the collinear configuration. It is also found that the relative yield for binary exit channel is found to be higher than that of ternary fragmentation (both equatorial and collinear configuration). The studies on the influence of deformation in the alpha accompanied ternary fission of $^{244\text{-}252}Cm$ isotopes reveal that the ground state deformation has an important role in ternary fission as that of shell effect.

4.8 Alpha accompanied cold ternary fission of $^{238\text{-}244}Pu$ isotopes in equatorial and collinear configuration

The ternary fragmentation of ^{238}Pu, ^{240}Pu, ^{242}Pu and ^{244}Pu with ^{4}He as light charged particle for the equatorial and collinear configurations have studied using the Unified Ternary Fission Model.

4.8.1 Alpha accompanied ternary fission of ^{238}Pu

The driving potential is calculated for the ternary fragmentation of ^{238}Pu, treating ^{4}He as the light charged particle (LCP) and is plotted as function of fragment mass number A_1 as shown in **Figure 4.76**. The minima occur in the cold valley is for

A_1 = ^{4}He, ^{10}Be, ^{14}C, ^{22}O, ^{26}Ne, ^{30}Mg, ^{34}Si, ^{40}S, ^{46}Ar, ^{50}Ca, ^{52}Ca, ^{56}Ti, ^{60}Cr, ^{64}Fe, ^{68}Ni, ^{76}Zn, ^{82}Ge etc. The minimum is found for the fragment configuration ^{26}Ne+^{208}Pb+^{4}He, and is due to the doubly magic ^{208}Pb (N=126, Z=82). The second minimum valley is found around ^{82}Ge for the fragment combinations ^{76}Zn+^{158}Sm+^{4}He, ^{80}Ge+^{154}Nd+^{4}He, ^{82}Ge+^{152}Nd+^{4}He, ^{84}Se+^{150}Ce+^{4}He and is likely to be the possible fission fragments. Another deep valley occurs around ^{130}Sn for the fragment combinations ^{98}Sr+^{136}Xe+^{4}He, ^{100}Zr+^{134}Te+^{4}He, ^{102}Mo+^{132}Sn+^{4}He, ^{104}Mo+^{130}Sn+^{4}He, ^{106}Mo+^{128}Sn+^{4}He. The barrier penetrability is calculated for each charge minimized fragment combinations found in the alpha accompanied cold ternary fission of ^{238}Pu. The relative yield is calculated and is plotted as a function of mass numbers A_1 and A_2 as shown in **Figure 4.77(a)**. The fragment combination ^{100}Zr+^{134}Te+^{4}He with ^{4}He as LCP possess highest yield due to the presence of near doubly magic nucleus ^{134}Te (Z=52, N=82). The second highest yield is observed for the fragment combination ^{104}Mo+^{130}Sn+^{4}He due to the presence of near doubly magic nucleus ^{130}Sn (Z=50, N=80).

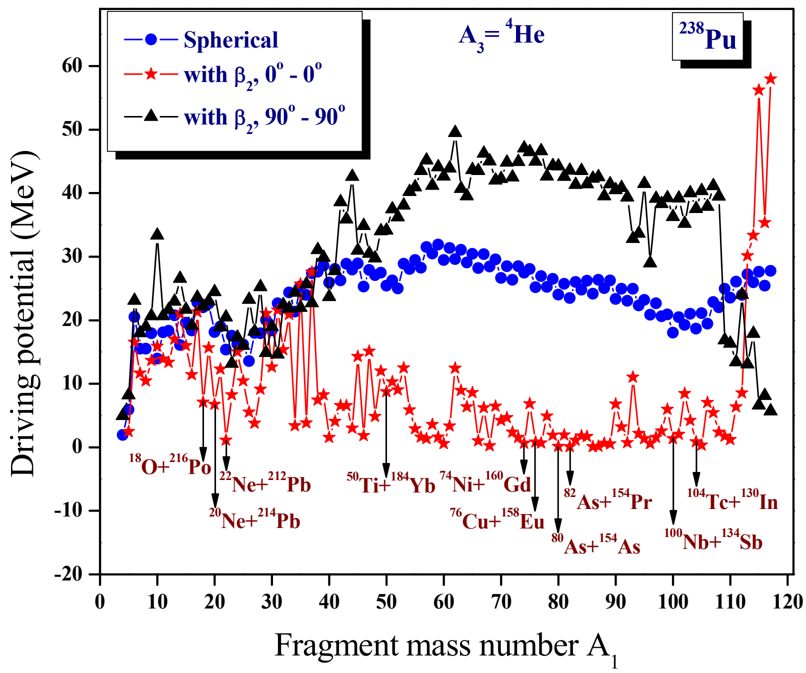

Figure 4.76. The driving potential for ^{238}Pu isotope with ^{4}He as light charged particle with the inclusion of quadrupole deformation β_2 and for different orientation plotted as a function of mass number A_1.

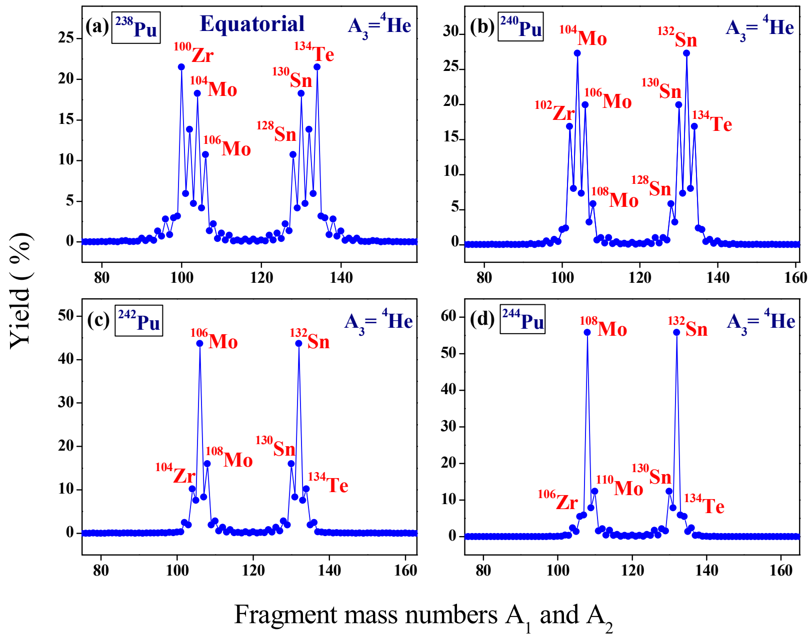

Figure 4.77. The calculated yield for the charge minimized third fragment ^{4}He is plotted as a function of fragment mass numbers A_1 and A_2 for the ternary fission of $^{238\text{-}244}$Pu isotopes.

The other fragment combinations observed in the alpha accompanied ternary fission of ^{238}Pu nucleus are ^{108}Mo+^{126}Sn+^{4}He, ^{106}Mo+^{128}Sn+^{4}He, ^{102}Mo+^{132}Sn+^{4}He, ^{96}Sr+^{138}Xe+^{4}He. Among these, the first two reactions can be attributed to the proton shell closure at Z=50 for ^{126}Sn and ^{128}Sn, respectively. The fragment combination ^{102}Mo+^{132}Sn+^{4}He is due to the presence of doubly magic nucleus ^{132}Sn (Z=50, N=82). Also, the fragment combination ^{96}Sr+^{138}Xe+^{4}He is observed due to the presence of near neutron closure of ^{138}Xe at N=84.

4.8.2 Alpha accompanied ternary fission of ^{240}Pu

The driving potential is calculated for each charge minimized fragment combinations found in the ternary fission of ^{240}Pu with ^{4}He as light charged particle (LCP) and is plotted as a function of fragment mass number A_1 as shown in **Figure 4.78**. In the cold valley plot the minima is found for the fragment combination with A_1 = ^{4}He, ^{8}Be, ^{10}Be, ^{14}C, ^{22}O, ^{26}Ne, ^{28}Ne, ^{30}Mg, ^{34}Si, ^{36}Si, ^{40}S, ^{42}S, ^{46}Ar, ^{50}Ca, ^{52}Ca, ^{56}Ti, ^{60}Cr etc. The deep valley occurs around ^{134}Te, for the fragment combinations ^{102}Zr+^{134}Te+^{4}He, ^{104}Mo+^{132}Sn+^{4}He, ^{106}Mo+^{130}Sn+^{4}He, ^{108}Mo+^{128}Sn+^{4}He may be the most favourable fragment combinations. Here the minima found for $^{102}Zr+^{134}Te+^{4}He$ is due to the near double magicity (Z=52, N=82) of ^{134}Te. The fragment combination with $^{104}Mo+^{132}Sn+^{4}He$ and $^{106}Mo+^{130}Sn+^{4}He$ is due to the presence of the doubly magic ^{132}Sn (Z=50, N=82) and nearly doubly magic ^{130}Sn (Z=50, N=80) respectively.

The relative yield is calculated and plotted as a function of fragment mass number A_1 and A_2, as in the **Figure 4.77(b)**. From the figure, it is clear that the fragment combination $^{104}Mo+^{132}Sn+^{4}He$ with ^{4}He as LCP possess highest yield due to the presence of doubly magic ^{132}Sn (Z=50, N=82). The next higher yield can be observed for the $^{106}Mo+^{130}Sn+^{4}He$ combination and is due to the nearly doubly magic ^{130}Sn (Z=50, N=80). The various other fragment combination observed in this α-accompanied ternary fission of parent nuclei ^{240}Pu are $^{108}Mo+^{128}Sn+^{4}He$ and $^{102}Zr+^{134}Te+^{4}He$. Of these the first one is attributed to the magic shell Z=50 of ^{128}Sn, while the second fragment combination is due to the nearly doubly closed shell Z=52 and N=82 of ^{134}Te.

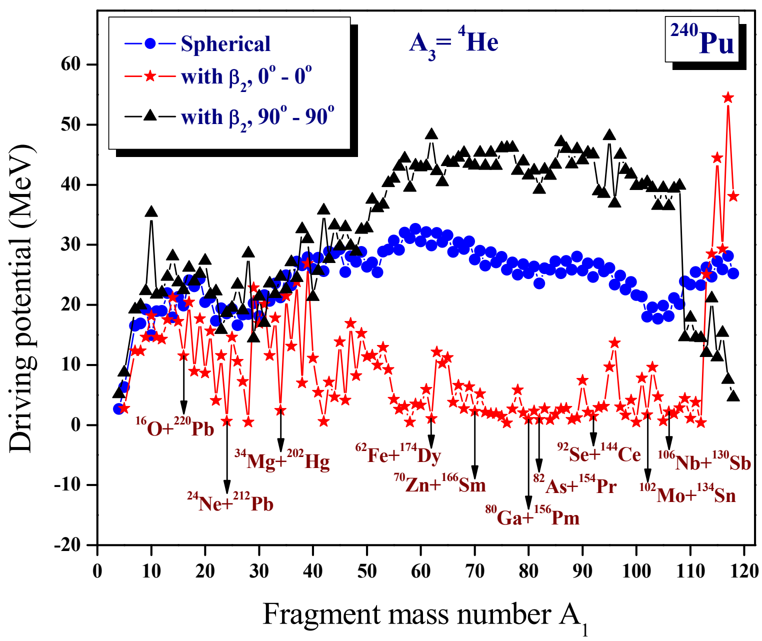

Figure 4.78. The driving potential for ^{240}Pu isotope with ^{4}He as light charged particle with the inclusion of quadrupole deformation β_2 and for different orientation plotted as a function of mass number A_1.

4.8.3 Alpha accompanied ternary fission of ^{242}Pu

The driving potential for the possible fragment combinations are calculated for the alpha accompanied ternary fragmentation of ^{242}Pu isotope and plotted as a function of fragment mass number A_1, as shown in **Figure 4.79**. Keeping ^{4}He as light charged particle, the minima found in the cold valley is for A_1 = ^{4}He, ^{10}Be, ^{14}C, ^{22}O, ^{26}Ne, ^{32}Mg, ^{42}S, ^{46}Ar, ^{52}Ca, ^{62}Cr, ^{78}Zn, ^{80}Zn, ^{82}Ge, ^{92}Kr, ^{104}Zr etc. The deep valley occurs around ^{132}Sn for the fragment combinations $^{104}Zr+^{134}Te+^{4}He$, $^{106}Mo+^{132}Sn+^{4}He$, $^{108}Mo+^{130}Sn+^{4}He$. In this the minimum found for the combination $^{106}Mo+^{132}Sn+^{4}He$ is due to the presence of doubly magic nucleus ^{132}Sn (N=82, Z=50). Also, the minima for the combinations $^{104}Zr+^{134}Te+^{4}He$ and $^{108}Mo+^{130}Sn+^{4}He$ due to the presence of near doubly magic nucleus ^{134}Te (N=82,Z=52) and ^{130}Sn (N=80, Z=50).

The barrier penetrability is calculated for each charge minimized fragment combinations found in the cold ternary fission of ^{242}Pu with ^{4}He as LCP. The relative yield is calculated and plotted as a function of mass numbers A_1 and A_2 as shown in **Figure 4.77(c)**. From the plot it is seen that, the fragment combination $^{106}Mo+^{132}Sn+^{4}He$ possess highest yield which is due to the presence of doubly magic ^{132}Sn (N=82, Z=50). The second highest yield is found for the splitting $^{108}Mo+^{130}Sn+^{4}He$ and is due to the near doubly magic nuclei ^{130}Sn (N=80, Z=82). The various other fragment combinations observed in this alpha accompanied ternary fission of ^{242}Pu are $^{102}Zr+^{136}Te+^{4}He$, $^{104}Zr+^{134}Te+^{4}He$ and $^{110}Mo+^{128}Sn+^{4}He$. The combination $^{104}Zr+^{134}Te+^{4}He$ is due to the presence of near doubly magic ^{134}Te (N=82, Z=52). The splitting $^{110}Mo+^{128}Sn+^{4}He$ is due to the proton shell closure of ^{128}Sn at Z=50.

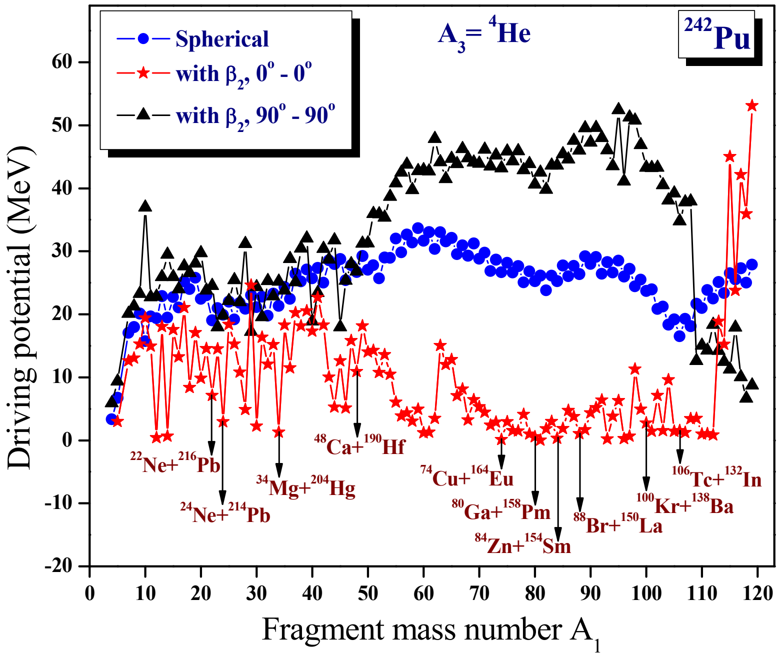

Figure 4.79. The driving potential for ^{242}Pu isotope with ^{4}He as light charged particle with the inclusion of quadrupole deformation β_2 and for different orientation plotted as a function of mass number A_1.

4.8.4 Alpha accompanied ternary fission of ^{244}Pu

The driving potential for ^{244}Pu as a representative parent nucleus with ^{4}He as light charged particle (LCP) is calculated and is plotted as a function of fragment mass number A_1 as shown in **Figure 4.80**. The minima is found for the splitting with A_1 = ^{4}He, ^{10}Be, ^{14}C, ^{16}C, ^{22}O, ^{24}O, ^{26}Ne, ^{32}Mg, ^{34}Mg, ^{36}Si,^{42}S, ^{46}Ar, ^{52}Ca, ^{62}Cr, ^{74}Ni, ^{78}Zn etc. The deepest minima for the fragment combination with ^{108}Mo+^{132}Sn+^{4}He and ^{110}Mo+^{130}Sn+^{4}He is due to the presence of the doubly magic ^{132}Sn (Z=50, N=82) and near doubly magic ^{130}Sn (Z=50, N=80).

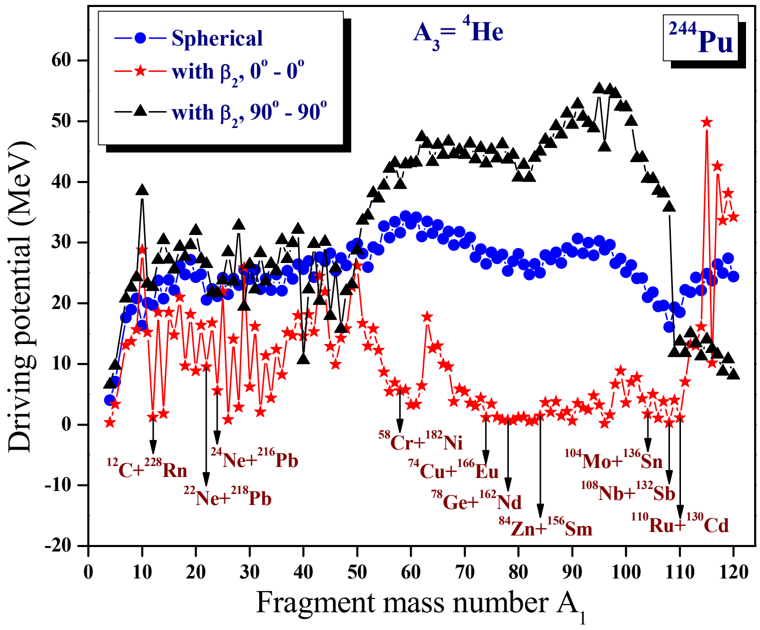

Figure 4.80. The driving potential for ^{244}Pu isotope with ^{4}He as light charged particle with the inclusion of quadrupole deformation β_2 and for different orientation plotted as a function of mass number A_1.

The barrier penetrability is calculated for each charge minimized fragment combination found in the cold ternary fission of ^{244}Pu. The relative yield is calculated and plotted as a function of fragment mass number A_1 and A_2 as shown in **Figure 4.77(d)**. The fragment combination with ^{108}Mo+^{132}Sn+^{4}He possess highest yield due to the presence of doubly magic nuclei ^{132}Sn (Z=50, N=82). The other fragment combination observed in this α-accompanied ternary fission of parent nuclei ^{244}Pu is ^{110}Mo+^{130}Sn+^{4}He which is due to the nearly doubly closed shell effect of ^{130}Sn (Z=50, N=80). The next highest yield can be observed for ^{106}Mo+^{134}Te+^{4}He combination and is due to near double magicity (Z=52, N=82) of ^{134}Te.The next higher yield can be observed for ^{104}Zr+^{136}Te+^{4}He.

4.8.5 Alpha accompanied ternary fission of $^{238\text{-}244}$Pu isotopes in collinear configuration

The alpha accompanied ternary fission of $^{238\text{-}244}$Pu isotopes has been studied with fragments in collinear configuration, in which the light charged particle ^{4}He lies in between the other two fission fragments. The driving potential is calculated for all possible fragment combinations of $^{238\text{-}244}$Pu isotopes and has been plotted as a function of mass numbers A_1 and is shown in **Figure 4.81**. From the plot it is clear that, in all cases, the least driving potential is obtained for the fragment combination with ^{4}He as A_1. But the fragment combinations with higher Q values and those with doubly or near doubly magic nuclei will be the most favourable fragment combinations, and this could be clarified through the calculation of barrier penetrability. In the ternary fission of ^{238}Pu isotope, the fragment combinations ^{100}Zr+^{4}He+^{134}Te may be the most favourable as it possess near doubly magic nuclei ^{134}Te (Z=52, N=82) and for ^{240,242,244}Pu isotopes, the fragment combinations with the doubly magic nuclei ^{132}Sn (Z=50, N=82) may be the most favourable.

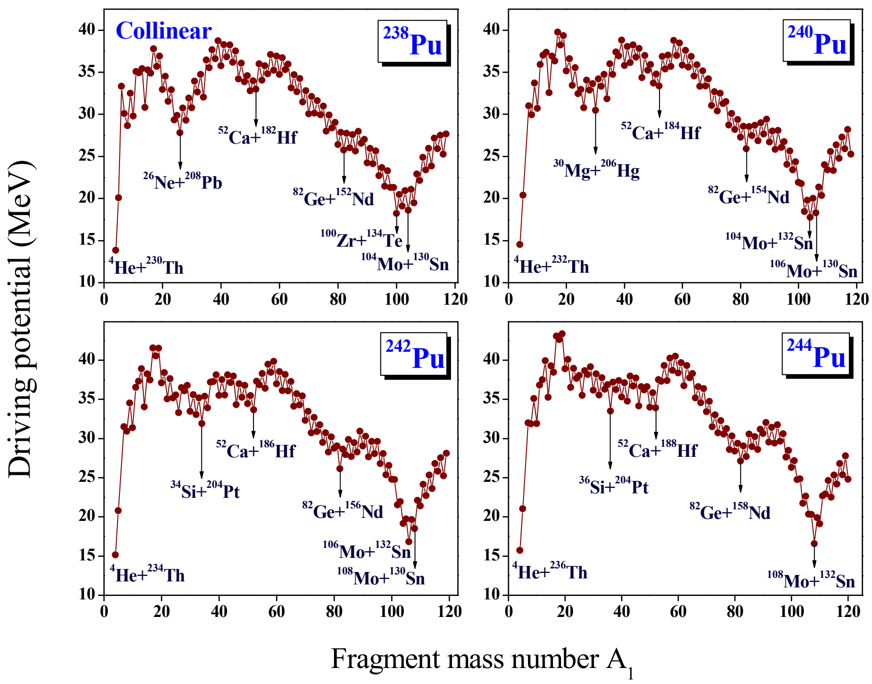

Figure 4.81. The driving potential for $^{238\text{-}244}$Pu isotope with ^{4}He as light charged particle in the case of collinear configuration plotted as a function of fragment mass number A_1.

The barrier penetrability is calculated for the alpha accompanied ternary fission of $^{238,240,242,244}Pu$ isotope and hence the relative yield is calculated. In **Figure 4.82**, the relative yield is plotted as a function of mass numbers A_1 and A_3 and also the fragments with higher relative yield are labelled. For ^{238}Pu isotope, the highest yield is obtained for the fragment combination $^{100}Zr+^{4}He+^{134}Te$ which possess near doubly magic nuclei ^{134}Te (Z=52, N=82). The next highest yield is obtained for the fragment combination $^{104}Mo+^{4}He+^{130}Sn$, which also possess near doubly magic nuclei ^{130}Sn (Z=50, N=80).

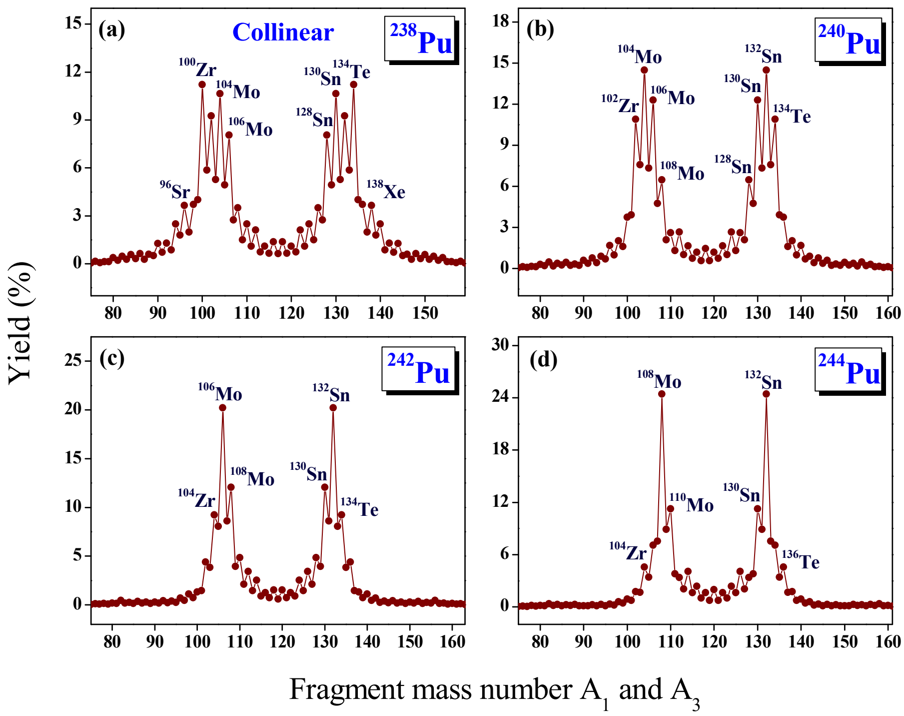

Figure 4.82. The calculated yields for the ternary fission of $^{238\text{-}244}Pu$ isotopes with charge minimized second fragment ^{4}He in the case of collinear configuration plotted as a function of mass numbers A_1 and A_3. The fragment combinations with highest yield are labelled.

For the alpha accompanied ternary fission of ^{240}Pu isotope, the highest yield is obtained for the fragment combination $^{104}Mo+^{4}He+^{132}Sn$ which possess doubly magic nuclei ^{132}Sn (Z=50, N=82). The next highest yield is obtained for the fragment combination $^{106}Mo+^{4}He+^{130}Sn$, in which ^{130}Sn (Z=50, N=80) is a near doubly magic nuclei. In the case of ^{242}Pu isotope, the highest yield is obtained for $^{106}Mo+^{4}He+^{132}Sn$ and the next highest yield is obtained for the fragment combination

^{108}Mo+^{4}He+^{130}Sn, which possess near doubly magic nuclei ^{130}Sn (Z=50, N=80). For the ^{244}Pu isotope, the highest yield is obtained for the fragment combination ^{108}Mo+^{4}He+^{132}Sn and the next highest yield is obtained for the splitting ^{110}Mo+^{4}He+^{130}Sn, which posses doubly magic nuclei ^{132}Sn (Z=50, N=82) and near doubly magic nuclei ^{130}Sn (Z=50, N=80) respectively.

With the fragments in collinear configuration, the ternary fission of $^{238-244}$Pu isotope has been studied with ^{4}He as light charged particle and it was found that the fragments splitting with higher Q value and doubly or near doubly magic nuclei plays an important role for the most favorable fragment combinations. From a comparative study with the relative yield obtained from the equatorial and collinear configuration of fragments, it could be seen that, in both equatorial and collinear configuration the highest yield is obtained for the same fragment combination. Also from **Figure 4.77** and **Figure 4.82**, it is clear that the relative yield found for the equatorial configuration is twice as that of the collinear one. Hence we can conclude that the equatorial configuration is the most preferred configuration than the collinear configuration in the alpha accompanied ternary fission of $^{238-244}$Pu isotope. We would like to mention that, if the absolute values of yields are ignored, **Figure 4.77** and **Figure 4.82** are almost the same, this is because the alpha particle is so small compared with the main fission fragments and therefore the initial configuration of equatorial and collinear configurations are almost the same.

4.8.6 Role of deformation and orientation of fragments

The effect of deformation and orientation of fragments in ^{4}He accompanied ternary fission of $^{238-244}$Pu isotopes have been analyzed taking the Coulomb and proximity potential as the interacting barrier. **Figures 4.76**, **4.78**, **4.79**, **4.80** represent the cold valley plots, the plot connecting the driving potential (*V-Q*) and the mass number A_1 for even-even ^{238}Pu to ^{244}Pu isotopes. In the case of ^{238}Pu isotope, the fragment combinations ^{104}Mo+^{4}He+^{130}Sn and ^{100}Zr+^{4}He+^{134}Te changed to ^{104}Tc+^{4}He+^{130}In and ^{100}Nb+^{4}He+^{134}Sb respectively. In the case of ^{240}Pu isotope, the fragment combinations ^{106}Mo+^{4}He+^{130}Sn and ^{102}Zr+^{4}He+^{134}Te changed to ^{106}Nb+^{4}He+^{130}Sb and ^{102}Mo+^{4}He+^{134}Sn respectively. In the case of ^{242}Pu isotope, the fragment combinations ^{100}Sr+^{4}He+^{138}Xe and ^{106}Mo+^{4}He+^{132}Sn changed to

$^{102}Kr+^{4}He+^{138}Ba$ and $^{106}Tc+^{4}He+^{132}In$ respectively. In the case of ^{244}Pu isotope, the fragment combinations $^{108}Mo+^{4}He+^{132}Sn$ and $^{110}Mo+^{4}He+^{130}Sn$ changed to $^{108}Nb+^{4}He+^{132}Sb$ and $^{110}Ru+^{4}He+^{130}Cd$ respectively. By including the quadrupole deformation, the barrier penetrability is calculated for all possible fragment combinations that occur in the cold valley plot which have the minimum (*V*-*Q*) value. By comparing the **Figure 4.83(a)** – **Figure 4.83(d)** with corresponding plots for the spherical case figures 3(a)-3(d), it can be seen that fragments with highest yield are also found to be changed. For the alpha accompanied ternary fission of ^{238}Pu and ^{240}Pu isotope, the highest yield is found for the fragment combination $^{94}Sr+^{4}He+^{140}Xe$ and $^{112}Ru+^{4}He+^{124}Cd$ respectively, with the inclusion of deformation. In the case of ^{242}Pu and ^{244}Pu isotopes, the highest yield is found for the fragment combination $^{110}Ru+^{4}He+^{128}Cd$ and $^{110}Ru+^{4}He+^{130}Cd$ respectively. For a better comparison of the result, a histogram is plotted with yield as a function of mass numbers A_1 and A_2 for the ternary fragmentation of $^{238\text{-}244}Pu$ isotopes with the inclusion of quadrupole deformation β_2 as shown in **Figure 4.84** - **Figure 4.87**.

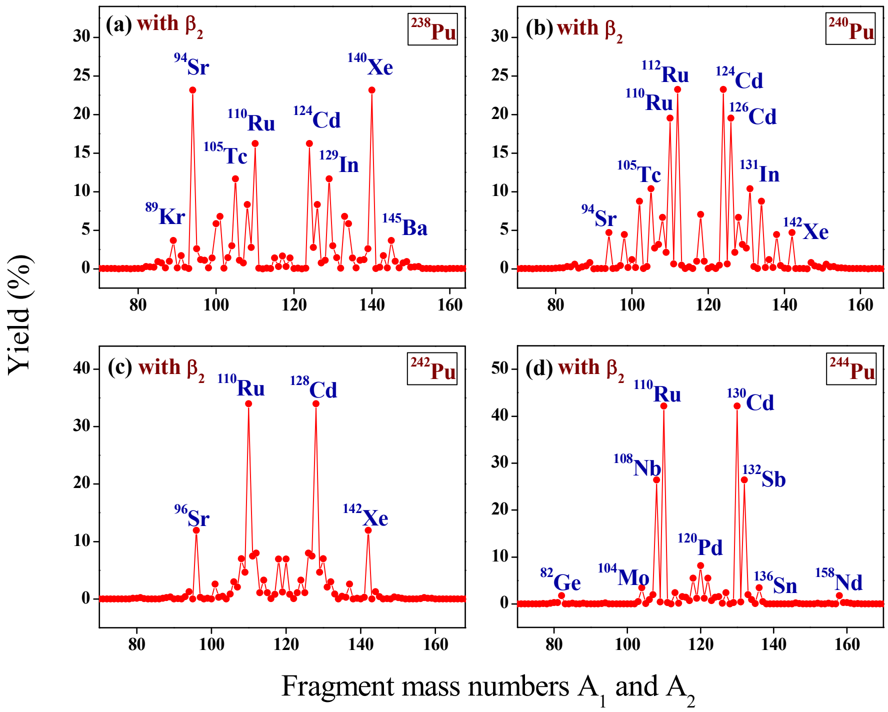

Figure 4.83. The calculated yields for the charge minimized third fragment ^{4}He with the inclusion of quadrupole deformation β_2 plotted as a function of mass numbers A_1 and A_2 for $^{238\text{-}244}Pu$ isotopes.

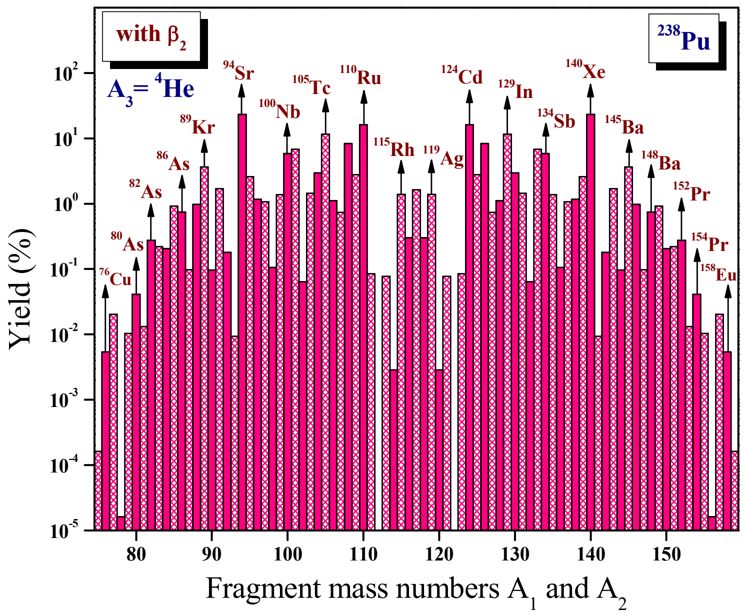

Figure 4.84. The calculated yields for the charge minimized third fragment ^{4}He with the inclusion of quadrupole deformation β_2 plotted as a function of mass numbers A_1 and A_2 for ^{238}Pu isotopes. The fragment combinations with higher yields are labelled.

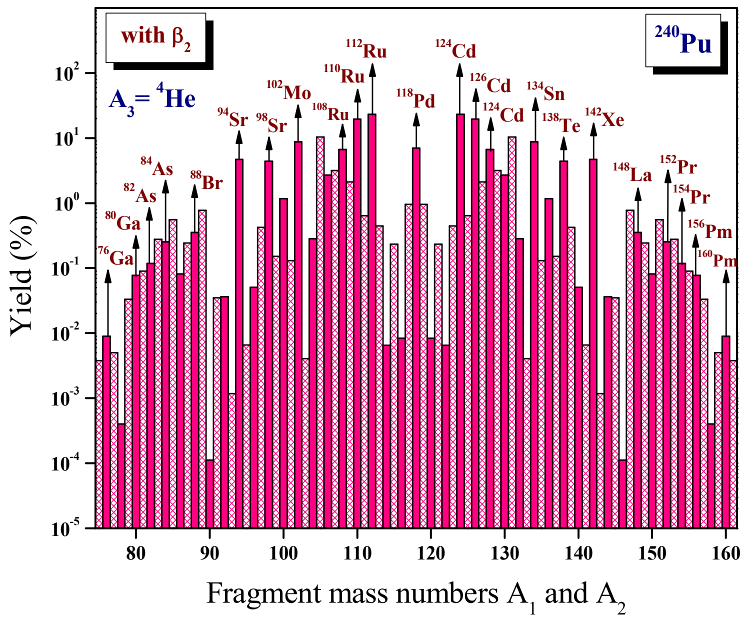

Figure 4.85. The calculated yields for the charge minimized third fragment ^{4}He with the inclusion of quadrupole deformation β_2 plotted as a function of mass numbers A_1 and A_2 for ^{240}Pu isotopes. The fragment combinations with higher yields are labelled.

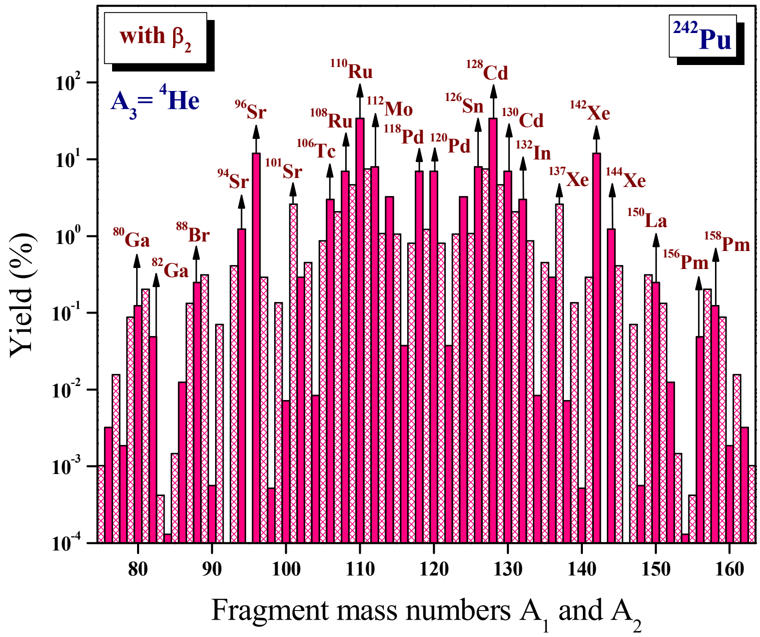

Figure 4.86. The calculated yields for the charge minimized third fragment ^{4}He with the inclusion of quadrupole deformation β_2 plotted as a function of mass numbers A_1 and A_2 for ^{242}Pu isotopes. The fragment combinations with higher yields are labelled.

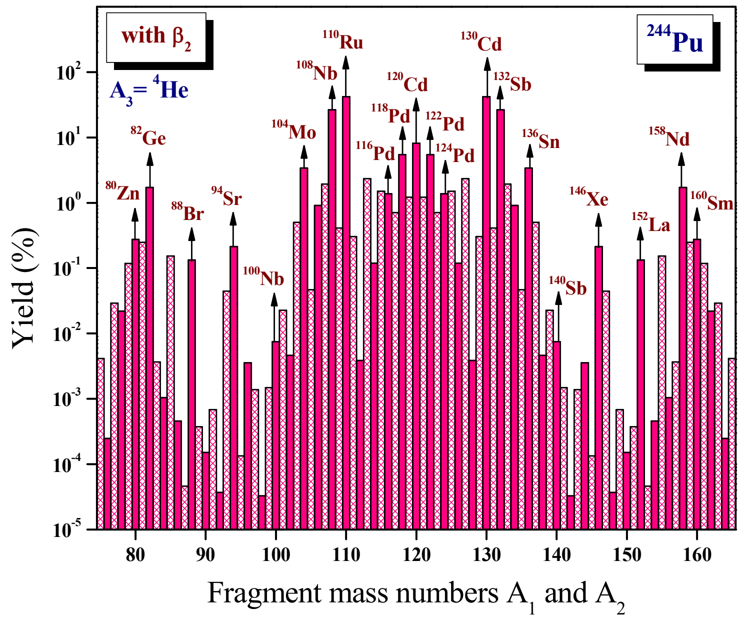

Figure 4.87. The calculated yields for the charge minimized third fragment ^{4}He with the inclusion of quadrupole deformation β_2 plotted as a function of mass numbers A_1 and A_2 for ^{244}Pu isotopes. The fragment combinations with higher yields are labelled.

The studies on the influence of deformation in the alpha accompanied ternary fission of $^{238-244}Pu$ isotopes reveal that the ground state deformation has an important role in determining the isotopic yield in the ternary fission as that of shell effect.

4.8.7 Emission probability of long range alpha particle

Using the formalism described in section **4.7.6**, we have computed the emission probabilities of long range alpha particle in the case of ^{238}Pu, ^{240}Pu, ^{242}Pu and ^{244}Pu isotopes and the obtained results are found to be in good agreement with the experimental data [19]. The spectroscopic factors and corresponding emission probabilities of $^{238-244}Pu$ isotopes are listed in **Table 4.9**.

Table 4.9. The calculated emission probability of alpha particle in the ternary fission of different Pu isotopes and the corresponding experimental data [19] are listed. The computed spectroscopic factor S_α and P_{LRA} are also listed.

Isotope	S_α	P_{LRA}	$\frac{LRA}{B}$	$\left(\frac{LRA}{B}\right)_{EXP.}$
^{238}Pu	0.0317	0.1080	3.42×10^{-3}	$(2.76 \pm 0.13) \times 10^{-3}$
^{240}Pu	0.0421	0.1067	4.49×10^{-3}	$(2.50 \pm 0.14) \times 10^{-3}$
^{242}Pu	0.0426	0.1335	5.69×10^{-3}	$(2.17 \pm 0.07) \times 10^{-3}$
^{244}Pu	0.0378	0.1507	5.70×10^{-3}	$(1.17 \pm 0.09) \times 10^{-3}$

4.8.8 Kinetic energy of long range alpha particle

Using the formalism described in section **4.7.7**, we have calculated the kinetic energy of the long range alpha particle in the ternary fission of $^{238-244}Pu$ and is given in **Table 4.10**. It is to be noted that the obtained results are found to be in good agreement with the experimental data [19].

Table 4.10. The calculated kinetic energy of alpha particle E_α emitted in the ternary fragmentation of even-even $^{238\text{-}244}$Pu isotopes and the corresponding experimental data [19].

Fragmentation channel	E_α (MeV) Calc.	E_α (MeV) Expt.	Fragmentation channel	E_α (MeV) Calc.	E_α (MeV) Expt.
$^{238}Pu \to {}^{98}Sr + {}^{4}He + {}^{136}Xe$	14.62	15.91 ± 0.22	$^{242}Pu \to {}^{100}Sr + {}^{4}He + {}^{138}Xe$	14.81	15.79 ± 0.21
$^{238}Pu \to {}^{100}Zr + {}^{4}He + {}^{134}Te$	14.76		$^{242}Pu \to {}^{102}Zr + {}^{4}He + {}^{136}Te$	14.94	
$^{238}Pu \to {}^{102}Mo + {}^{4}He + {}^{132}Sn$	14.88		$^{242}Pu \to {}^{104}Zr + {}^{4}He + {}^{134}Te$	15.06	
$^{238}Pu \to {}^{104}Mo + {}^{4}He + {}^{130}Sn$	14.98		$^{242}Pu \to {}^{106}Mo + {}^{4}He + {}^{132}Sn$	15.16	
$^{238}Pu \to {}^{106}Mo + {}^{4}He + {}^{128}Sn$	15.08		$^{242}Pu \to {}^{108}Mo + {}^{4}He + {}^{130}Sn$	15.25	
$^{238}Pu \to {}^{108}Mo + {}^{4}He + {}^{126}Sn$	15.15		$^{242}Pu \to {}^{110}Mo + {}^{4}He + {}^{128}Sn$	15.33	
$^{238}Pu \to {}^{110}Ru + {}^{4}He + {}^{124}Cd$	15.21		$^{242}Pu \to {}^{112}Ru + {}^{4}He + {}^{126}Cd$	15.39	
$^{238}Pu \to {}^{112}Ru + {}^{4}He + {}^{122}Cd$	15.25		$^{242}Pu \to {}^{114}Ru + {}^{4}He + {}^{124}Cd$	15.43	
$^{238}Pu \to {}^{114}Ru + {}^{4}He + {}^{120}Cd$	15.29		$^{242}Pu \to {}^{116}Ru + {}^{4}He + {}^{122}Cd$	15.46	
$^{238}Pu \to {}^{116}Pd + {}^{4}He + {}^{118}Pd$	15.30		$^{242}Pu \to {}^{118}Pd + {}^{4}He + {}^{120}Pd$	15.48	
$^{240}Pu \to {}^{100}Zr + {}^{4}He + {}^{136}Te$	14.79	16.55 ± 0.27	$^{244}Pu \to {}^{102}Zr + {}^{4}He + {}^{138}Te$	14.98	16.04 ± 0.25
$^{240}Pu \to {}^{102}Zr + {}^{4}He + {}^{134}Te$	14.91		$^{244}Pu \to {}^{104}Zr + {}^{4}He + {}^{136}Te$	15.10	
$^{240}Pu \to {}^{104}Mo + {}^{4}He + {}^{132}Sn$	15.02		$^{244}Pu \to {}^{106}Zr + {}^{4}He + {}^{134}Te$	15.21	
$^{240}Pu \to {}^{106}Mo + {}^{4}He + {}^{130}Sn$	15.12		$^{244}Pu \to {}^{108}Mo + {}^{4}He + {}^{132}Sn$	15.30	
$^{240}Pu \to {}^{108}Mo + {}^{4}He + {}^{128}Sn$	15.20		$^{244}Pu \to {}^{110}Mo + {}^{4}He + {}^{130}Sn$	15.38	
$^{240}Pu \to {}^{110}Ru + {}^{4}He + {}^{126}Cd$	15.27		$^{244}Pu \to {}^{112}Ru + {}^{4}He + {}^{128}Cd$	15.45	
$^{240}Pu \to {}^{112}Ru + {}^{4}He + {}^{124}Cd$	15.32		$^{244}Pu \to {}^{114}Ru + {}^{4}He + {}^{126}Cd$	15.50	
$^{240}Pu \to {}^{114}Ru + {}^{4}He + {}^{122}Cd$	15.36		$^{244}Pu \to {}^{116}Ru + {}^{4}He + {}^{124}Cd$	15.54	
$^{240}Pu \to {}^{116}Pd + {}^{4}He + {}^{120}Pd$	15.38		$^{244}Pu \to {}^{118}Pd + {}^{4}He + {}^{122}Pd$	15.56	
$^{240}Pu \to {}^{118}Pd + {}^{4}He + {}^{118}Pd$	15.39		$^{244}Pu \to {}^{120}Pd + {}^{4}He + {}^{120}Pd$	15.56	

4.8.9 Summary

For alpha accompanied ternary fission of even-even $^{238\text{-}244}$Pu isotopes, the relative yield is calculated by taking the interacting barrier as the sum of Coulomb and proximity potential, with fragments in equatorial and collinear configuration, within the Unified ternary fission model (UTFM). In the ternary fission of ^{238}Pu isotopes with ^{4}He as light charged particle, the highest yield is obtained for the fragment combination $^{100}Zr+{}^{4}He+{}^{134}Te$, which possess near doubly magic nuclei ^{134}Te (N=82, Z=52). For the alpha accompanied ternary fission of ^{240}Pu, ^{242}Pu and ^{244}Pu isotopes, the highest yield is obtained for the fragment combination

$^{104}Mo+^{4}He+^{132}Sn$, $^{106}Mo+^{4}He+^{132}Sn$ and $^{108}Mo+^{4}He+^{132}Sn$ respectively, of which ^{132}Sn (N=82, Z=50) is a doubly magic nuclei. The effect of deformation and orientation is also studied in detail and found that ground state deformation also plays an important role as that of shell effect in determining the isotopic yield in the alpha accompanied ternary fission of $^{238\text{-}244}Pu$ isotopes. The kinetic energy and emission probability of alpha particle is calculated and are found to be in good agreement with the experimental data.

4.9 Deformation effects in the alpha accompanied cold ternary fission of even-even $^{244\text{-}260}Cf$ isotopes

Using the concept of cold reaction valley, which was introduced in relation to the structure of minima in the so called driving potential, the alpha accompanied cold ternary fission of even-even $^{244\text{-}260}Cf$ isotopes are studied in equatorial configuration.

4.9.1 Alpha accompanied cold ternary fission of $^{244\text{-}260}Cf$ isotopes

The driving potential is calculated for the alpha accompanied cold ternary fission of ^{244}Cf isotope and is plotted as a function of fragment mass number A_1 as shown in **Figure 4.88**. The minima found in the cold valley are at ^{4}He, ^{6}He, ^{10}Be, ^{14}C, ^{32}Si, ^{34}Si, ^{46}Ar, ^{50}Ca, ^{52}Ca, ^{80}Ge, ^{84}Se etc. In the cold reaction valley plot, the fragment combination $^{4}He+^{4}He+^{236}Pu$ possesses the least driving potential. The fragment combination around $^{108}Ru+^{4}He+^{132}Te$ may possess the highest yield due to the presence of doubly or near doubly magic Te isotopes and also due to high Q value. Next the barrier penetrability is calculated for the alpha accompanied cold ternary fission of ^{244}Cf isotope using the formalism described above.

The relative yield is calculated and plotted as a function of fragment mass number A_1 and A_2 as shown in **Figure 4.89(a)**. From the figure it is clear that the combination $^{108}Ru+^{132}Te+^{4}He$ has the highest yield due to the presence of near doubly magic nuclei ^{132}Te (Z=52, N=80). The next highest yield can be observed for the fragment combinations $^{106}Ru+^{134}Te+^{4}He$ and $^{104}Mo+^{136}Xe+^{4}He$ which is due to the presence of near doubly magic nuclei ^{134}Te (Z=52, N=82) and neutron shell closure N=82 of ^{136}Xe respectively.

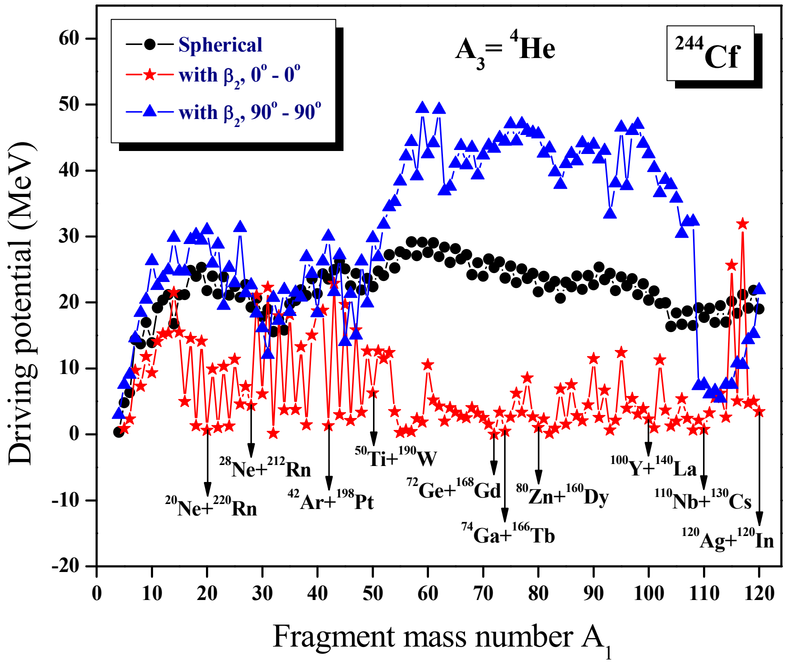

Figure 4.88. The driving potential is plotted as a function of fragment mass number A_1 for the alpha accompanied ternary fission of ^{244}Cf isotope with the inclusion of quadrupole deformation β_2 and for different orientation.

In the alpha accompanied ternary fission of $^{246-260}$Cf isotopes, the driving potential were calculated and studied as a function of fragment mass number A_1. In the cold reaction valley plots, the minima occur at ^{4}He, ^{6}He,^{10}Be, ^{14}C, ^{16}C, ^{22}O, ^{24}Ne, ^{28}Mg, ^{32}Si, ^{38}S, ^{40}S, ^{46}Ar, ^{50}Ca, ^{52}Ca etc.

The barrier penetrability and relative yield is calculated for the alpha accompanied ternary fission of ^{246}Cf isotope and is plotted as a function of fragment mass number A_1 and A_2 as shown in **Figure 4.89(b)**. From the figure it is clear that the fragment combination ^{108}Ru+^{4}He+^{134}Te has the highest yield which is due to the presence of nearly doubly magic nuclei ^{134}Te (Z=52, N=82). The next highest yield can be observed for the fragment combination ^{114}Pd+^{4}He+^{128}Sn which possess proton shell closure Z=50 of ^{128}Sn. The other fragment combinations which possess highest yield are ^{112}Pd+^{4}He+^{130}Sn and ^{110}Ru+^{4}He+^{132}Te which is due to the presence of near doubly magic nuclei ^{130}Sn (N=80, Z=50) and ^{132}Te (N=80, Z=52) respectively.

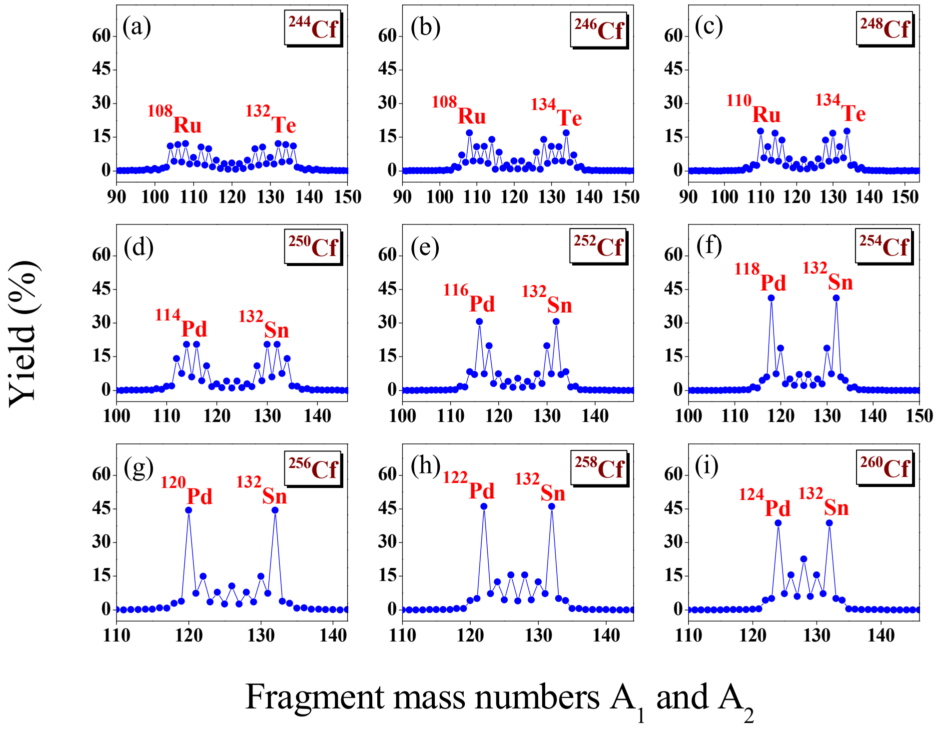

Figure 4.89. The calculated yield is plotted as a function of fragment mass numbers A_1 and A_2 for the alpha accompanied cold ternary fission of even-even $^{244-260}$Cf isotopes with fragments treated as spherical.

The most possible fragment combination occur in the ternary fission of ^{248}Cf is found by calculating the relative yield and plotted as a function of mass numbers A_1 and A_2 as shown in **Figure 4.89(c)**. The fragment combination ^{110}Ru+^{4}He+^{134}Te has highest yield because of the near doubly magic nuclei ^{134}Te (N=82, Z=52). The next highest yields are obtained for the fragment combinations ^{114}Pd+^{4}He+^{130}Sn and ^{116}Pd+^{4}He+^{128}Sn which possess near doubly magic nuclei ^{130}Sn (N=80, Z=50) and proton shell closure Z=50 of ^{128}Sn respectively.

In the case of ^{250}Cf isotope, the barrier penetrability is calculated for each charge minimized fragments found in the cold valley plot and thereafter the relative yield is calculated and plotted as a function of fragment mass numbers A_1 and A_2 as shown in **Figure 4.89(d)**. The highest yield is found for the fragment combination ^{114}Pd+^{4}He+^{132}Sn which is due to the doubly magic nuclei ^{132}Sn (N=82, Z=50). The next highest yield is found for the fragment combination ^{116}Pd+^{4}He+^{130}Sn which is due to nearly doubly magic nuclei ^{130}Sn (N=80, Z=50). The yield obtained for the fragment combination $^{112}Ru+^{4}He+^{134}Te$ is due to the presence of nearly doubly magic ^{134}Te (N=82, Z=52).

In the case of ^{252}Cf isotope, the relative yield is calculated for each charge minimized fragment combinations found in the cold valley plot and plotted as a function of fragment mass numbers A_1 and A_2 as shown in **Figure 4.89(e)**. The highest yield is found for the fragment combination $^{116}Pd+^{4}He+^{132}Sn$, in which ^{132}Sn is a doubly magic nuclei (N=82, Z=50). The next highest yield is obtained for the fragment combinations $^{118}Pd+^{4}He+^{130}Sn$ and $^{114}Ru+^{4}He+^{134}Te$ which possess the presence of near doubly magic nuclei ^{130}Sn (N=80, Z=50) and ^{134}Te (N=82, Z=52) respectively.

Keeping ^{4}He as the light charged particle, the relative yield is calculated for each charge minimized fragments found in the cold reaction valley of ^{254}Cf isotope and plotted as a function of fragment mass numbers A_1 and A_2 as shown in **Figure 4.89(f)**. The highest yield is obtained for the fragment combination $^{118}Pd+^{4}He+^{132}Sn$, which possess high Q value and doubly magic nuclei ^{132}Sn (N=82, Z=50). The next highest yield is obtained for the fragment combination $^{120}Pd+^{4}He+^{130}Sn$, which possess near doubly magic nuclei ^{130}Sn (N=80, Z=50).

In the case of ^{256}Cf isotope as the parent nucleus with ^{4}He as the light charged particle (LCP), the relative yield is calculated and plotted as a function of fragment mass numbers A_1 and A_2 as shown in **Figure 4.89(g)**. The highest yield is obtained for the fragment combination $^{120}Pd+^{4}He+^{132}Sn$, which is due to the presence of doubly magic nuclei ^{132}Sn (N=82, Z=50). The next highest yield is obtained for the fragment combination $^{122}Pd+^{4}He+^{130}Sn$, which possess near doubly magic nuclei ^{130}Sn (N=80, Z=50). The relative yield is calculated for alpha accompanied ternary fission of ^{258}Cf isotope and plotted as a function of fragment mass numbers A_1 and A_2 as shown in **Figure 4.89(h)**. The highest yield is found for the fragment combination $^{122}Pd+^{4}He+^{132}Sn$, which possess doubly magic nuclei ^{132}Sn (N=82, Z=50) and the next highest yield is obtained for the fragment combination $^{126}Cd + ^{128}Cd + ^{4}He$.

For ^{260}Cf isotope the relative yield is calculated and plotted as a function of fragment mass numbers A_1 and A_2 as shown in **Figure 4.89(i)**. The highest yield is found for the fragment combination $^{124}Pd+^{4}He+^{132}Sn$, which possess doubly magic nuclei ^{132}Sn (N=82, Z=50). The next highest yields are obtained for the fragment combinations $^{126}Cd+^{4}He+^{130}Cd$ and $^{128}Cd+^{4}He+^{128}Cd$.

From the study of alpha accompanied ternary fission of even-even $^{244\text{-}260}Cf$ isotopes, we have concluded that, the fragment combinations with the higher Q value and having doubly or near doubly magic nuclei as the heavier fragment possess the highest yield.

4.9.2 Effect of deformation and orientation of fragments

With the inclusion of deformation and orientation of fragments, the driving potential is calculated for all fragment combinations found in the alpha accompanied ternary fission of even-even $^{244\text{-}260}Cf$ isotopes. In the case of ^{244}Cf isotope with ^{4}He as light charged particle, the driving potential is plotted as a function of fragment mass number A_1 as shown in **Figure 4.88**. In the cold reaction valley plot, three different cases are considered, (1) three fragments taken as spherical (2) two fragments (A_1 and A_2) as deformed with orientation 0^0-0^0 and (3) two fragments (A_1 and A_2) as deformed with orientation 90^0-90^0. It is clear from the plot that, in most of the cases, the fragment combinations with 0^0-0^0 orientation have a low value for driving potential compared to the fragment combinations with 90^0-90^0, but in few cases 90^0-90^0 orientation has the low value. In 0^0-0^0 orientation of fragments, both fragments are either prolate or one fragment is prolate and the other fragment is spherical, whereas in the case of 90^0-90^0 orientation, both fragments are either oblate or one fragment is oblate and the other one is spherical. It is also noted that, the optimum fragment combinations change with the inclusion of deformation and orientation of fragments.

In fission process, the fragments are strongly polarized due to nuclear force and the fragments take either 0^0-0^0 orientation or 90^0-90^0 orientation. In the present manuscript we have considered only two orientations 0^0-0^0 and 90^0-90^0, because it is well established by Gupta and co-workers [49] that optimum orientation for prolate-prolate/spherical fragments is $0^0 - 0^0$, and for oblate-oblate/spherical fragments optimum orientation is $90^0 - 90^0$. It should be noted that Manimaran *et al.,* [25] also considered only $0^0 - 0^0$ and $90^0 - 90^0$ orientations in their study on the effect of deformation and orientation in the ^{4}He and ^{10}Be accompanied ternary fission of ^{252}Cf.

For example in the case of ^{244}Cf isotope, the fragment combinations obtained with the spherical case ^{110}Ru+^{4}He+^{130}Te and ^{120}Cd+^{4}He+^{120}Cd changed to ^{110}Nb+^{4}He+^{130}Cs and ^{120}Ag+^{4}He+^{120}In respectively with the inclusion of deformation of fragments. In the case of ^{246}Cf isotope, the fragment combinations ^{110}Ru+^{4}He+^{132}Te and ^{120}Cd+^{4}He+^{122}Cd changed to ^{110}Zr+^{4}He+^{132}Ba and ^{120}In+^{4}He+^{122}Ag respectively with the inclusion of deformation of fragments. For ^{248}Cf isotope, the fragment combinations ^{104}Mo+^{4}He+^{140}Xe and ^{120}Cd+^{4}He+^{124}Cd obtained in spherical case changed to ^{104}Ru+^{4}He+^{140}Te and ^{120}Ag+^{4}He+^{124}In respectively with the inclusion of deformation. In the case of ^{250}Cf isotope, the fragment combinations obtained in spherical case ^{108}Mo+^{4}He+^{138}Xe and ^{112}Ru+^{4}He+^{134}Te changed to ^{108}Ru+^{4}He+^{138}Te and ^{112}Zr+^{4}He+^{134}Ba respectively with the inclusion of deformation of fragments. For ^{252}Cf isotope, the fragment combination ^{110}Mo+^{4}He+^{138}Xe and ^{120}Pd+^{4}He+^{128}Sn obtained in spherical case changed to ^{110}Nb+^{4}He+^{138}Cs and ^{120}Cd+^{4}He+^{128}Cd respectively with the inclusion of deformation. In the case of ^{254}Cf isotope, ^{106}Zr+^{4}He+^{144}Ba and ^{120}Pd+^{4}He+^{130}Sn obtained in spherical case changed to ^{106}Ru+^{4}He+^{144}Te and ^{120}Ag+^{4}He+^{130}In respectively with the inclusion of deformation. For ^{256}Cf isotope, the fragment combinations ^{104}Zr+^{4}He+^{148}Ba and ^{116}Ru+^{4}He+^{136}Te obtained with the spherical fragments changed to ^{104}Tc+^{4}He+^{148}I and ^{116}Pd+^{4}He+^{136}Sn respectively with the inclusion of deformation. In the case of ^{258}Cf isotope, the fragment combination obtained with the spherical fragments ^{80}Zn+^{4}He+^{174}Dy and ^{104}Zr+^{4}He+^{150}Ba changed to ^{80}Ga+^{4}He+^{174}Tb and ^{104}Tc+^{4}He+^{150}I respectively with the inclusion of deformation of fragments. For ^{260}Cf isotope, the fragment combination obtained with the spherical fragments ^{108}Zr+^{4}He+^{148}Ba and ^{102}Sr+^{4}He+^{154}Ce changed to ^{108}Ru+^{4}He+^{148}Te and ^{102}Mo+^{4}He+^{154}Xe respectively with the inclusion of deformation. For this reason we came to the conclusion that, the inclusion of deformation and orientation effects of the nuclei play a significant role in the alpha accompanied ternary fission of even-even $^{244-260}$Cf isotopes as that of closed shell effect. The quadrupole deformation is included for all possible fragment combinations occurring in the alpha accompanied ternary fission of even-even $^{244-260}$Cf isotopes and hence the corresponding relative yield is calculated and plotted as a function of fragment mass number A_1 and A_2 as shown in **Figure 4.90(a)** – **Figure 4.90(i)**. Here the calculations are done by taking the deformed Coulomb potential and deformed nuclear proximity potential. With the inclusion of quadrupole deformation (β_2), the width and height of the barrier are found to be reduced which in turn increases the barrier penetrability.

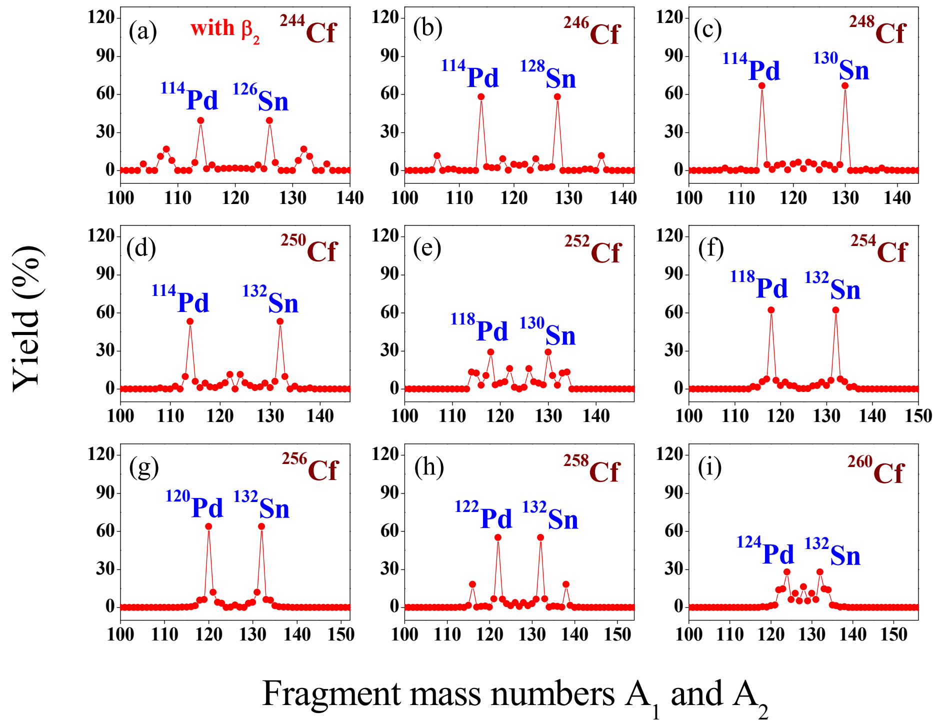

Figure 4.90. The calculated yields for the alpha accompanied cold ternary fission of $^{244-260}$Cf isotopes plotted as a function of fragment mass numbers A_1 and A_2 with the inclusion of quadrupole deformation β_2.

For the alpha accompanied ternary fission of ^{244}Cf and ^{246}Cf isotopes, the highest yield is found for the fragment combination ^{114}Pd+^{4}He+^{126}Sn and

^{114}Pd+^{4}He+^{128}Sn respectively, both of these fragment combinations possess proton shell closure Z=50 of Sn nuclei. In the case of ^{248}Cf and ^{252}Cf isotopes, the highest yield is obtained for the fragment combinations ^{114}Pd+^{4}He+^{130}Sn and ^{118}Pd+^{4}He+^{130}Sn, in which ^{130}Sn (N=80, Z=50) is a near doubly magic nuclei. For ^{250}Cf, ^{254}Cf, ^{256}Cf, ^{258}Cf and ^{260}Cf isotopes, the highest yield is obtained for the fragment combination ^{114}Pd+^{4}He+^{132}Sn, ^{118}Pd+^{4}He+^{132}Sn, ^{120}Pd+^{4}He+^{132}Sn, ^{122}Pd+^{4}He+^{132}Sn and ^{124}Pd+^{4}He+^{132}Sn respectively, all of which possess the presence of doubly magic nuclei ^{132}Sn (N=82, Z=50). In **Figure 4.91**, the calculated yields obtained in the alpha accompanied ternary fission of ^{252}Cf isotope are compared with the experimental data [8]. The calculations are made for the fragments considered as spherical and also for the fragments with the inclusion of quadrupole deformation β_2. From the graph it is clear that, the theoretical calculations we have made in the case of alpha accompanied ternary fission of ^{252}Cf isotope are found to be agreement with the experimental data.

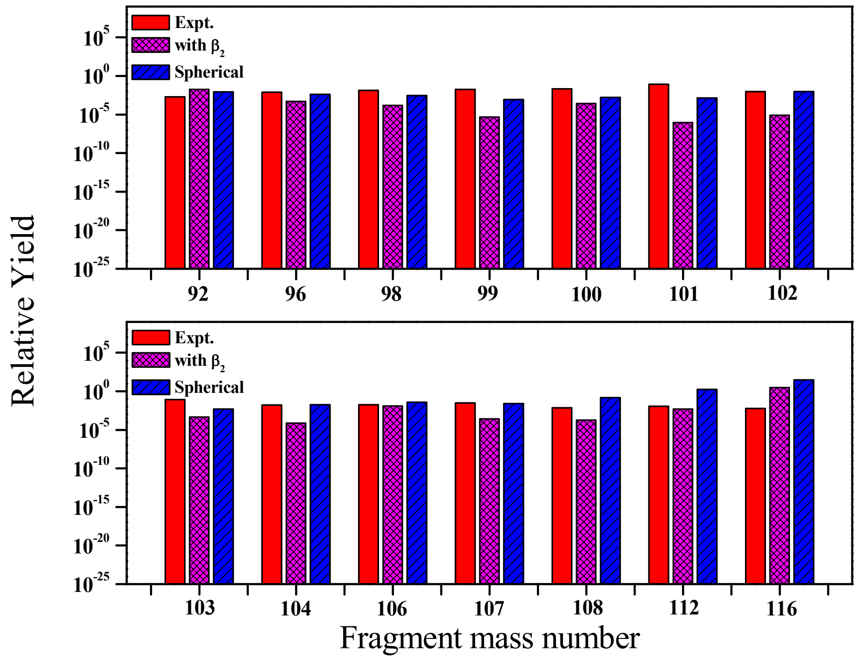

Figure 4.91. The calculated yields obtained with the inclusion of quadrupole deformation of fragments and for the fragments considered as spherical are compared with the experimental data [8].

4.9.3 Emission probability of long range alpha particle

The emission probabilities of long range alpha particle in the ternary fission of even-even $^{244-260}Cf$ isotopes are computed using the formalism discussed in section **4.7.6** and are given in **Table 4.11**. The alpha cluster preformation factor S_α and corresponding probability for the alpha particle preformed in the fissioning nucleus P_{LRA} are also listed in the table. The calculated emission probabilities of long range alpha particle are found to agree well with the experimental data [22].

Table 4.11. The calculated emission probability of long range alpha particle in the ternary fission of $^{244-260}Cf$ isotopes and the corresponding experimental data [22] are listed. The corresponding spectroscopic factor S_α and P_{LRA} are also listed.

Isotope	S_α	P_{LRA}	$\frac{LRA}{B}$	$\left(\frac{LRA}{B}\right)_{EXP.}$
^{244}Cf	0.0195	0.1178	2.29 x 10^{-3}	-
^{246}Cf	0.0201	0.1365	2.74 x 10^{-3}	-
^{248}Cf	0.0165	0.1400	2.31 x 10^{-3}	-
^{250}Cf	0.0161	0.1631	2.63 x 10^{-3}	(2.93 ± 0.10) x 10^{-3}
^{252}Cf	0.0252	0.2364	5.96 x 10^{-3}	(2.56 ± 0.07) x 10^{-3}
^{254}Cf	0.0138	0.3109	4.29 x 10^{-3}	-
^{256}Cf	0.0128	0.3775	4.83 x 10^{-3}	-
^{258}Cf	0.0120	0.4591	5.51 x 10^{-3}	-
^{260}Cf	0.0112	0.5417	6.06 10^{-3}	-

4.9.4 Kinetic energy of long range alpha particle

We have calculated the kinetic energy of long range alpha particle emitted in the ternary fission of $^{244-260}Cf$ isotopes using the formalism reported by Fraenkel [44]. In the present manuscript, for the potential energy calculation, yield calculation and for the kinetic energy calculation we have assumed a triangular configuration. The kinetic energy of long range alpha particle emitted in the ternary fission of $^{244-260}Cf$ isotopes is calculated using the formalism described above and the corresponding experimental values are listed in **Table 4.12**. The calculated results for which experimental data is available are in good agreement with each other [22].

Table 4.12. The calculated kinetic energy of alpha particle E_α emitted in the ternary fission of $^{244\text{-}260}$Cf isotopes and the corresponding experimental data [22] are listed.

Fragmentation channel	E_α (MeV) Calc.	E_α (MeV) Expt.	Fragmentation channel	E_α (MeV) Calc.	E_α (MeV) Expt.
$^{244}Cf \rightarrow ^{104}Mo + ^{4}He + ^{136}Xe$	16.442		$^{252}Cf \rightarrow ^{120}Pd + ^{4}He + ^{128}Sn$	17.295	
$^{244}Cf \rightarrow ^{106}Ru + ^{4}He + ^{134}Te$	16.560		$^{252}Cf \rightarrow ^{122}Cd + ^{4}He + ^{126}Cd$	17.318	15.96
$^{244}Cf \rightarrow ^{108}Ru + ^{4}He + ^{132}Te$	16.663		$^{252}Cf \rightarrow ^{124}Cd + ^{4}He + ^{124}Cd$	17.325	±
$^{244}Cf \rightarrow ^{110}Ru + ^{4}He + ^{130}Te$	16.751		$^{252}Cf \rightarrow ^{126}Cd + ^{4}He + ^{122}Cd$	17.318	0.09
$^{244}Cf \rightarrow ^{112}Pd + ^{4}He + ^{128}Sn$	16.823		$^{252}Cf \rightarrow ^{128}Cd + ^{4}He + ^{120}Cd$	17.295	
$^{246}Cf \rightarrow ^{108}Ru + ^{4}He + ^{134}Te$	16.712		$^{254}Cf \rightarrow ^{116}Ru + ^{4}He + ^{134}Te$	17.265	
$^{246}Cf \rightarrow ^{110}Ru + ^{4}He + ^{132}Te$	16.806		$^{254}Cf \rightarrow ^{118}Pd + ^{4}He + ^{132}Sn$	17.325	
$^{246}Cf \rightarrow ^{112}Pd + ^{4}He + ^{130}Sn$	16.885		$^{254}Cf \rightarrow ^{120}Pd + ^{4}He + ^{130}Sn$	17.371	
$^{246}Cf \rightarrow ^{114}Pd + ^{4}He + ^{128}Sn$	16.948		$^{254}Cf \rightarrow ^{122}Pd + ^{4}He + ^{128}Sn$	17.401	
$^{246}Cf \rightarrow ^{116}Pd + ^{4}He + ^{126}Sn$	16.995		$^{254}Cf \rightarrow ^{124}Cd + ^{4}He + ^{126}Cd$	17.416	
$^{248}Cf \rightarrow ^{110}Ru + ^{4}He + ^{134}Te$	16.858		$^{256}Cf \rightarrow ^{118}Pd + ^{4}He + ^{134}Sn$	17.391	
$^{248}Cf \rightarrow ^{112}Pd + ^{4}He + ^{132}Sn$	16.943		$^{256}Cf \rightarrow ^{120}Pd + ^{4}He + ^{132}Sn$	17.444	
$^{248}Cf \rightarrow ^{114}Pd + ^{4}He + ^{130}Sn$	17.013		$^{256}Cf \rightarrow ^{122}Pd + ^{4}He + ^{130}Sn$	17.481	
$^{248}Cf \rightarrow ^{116}Pd + ^{4}He + ^{128}Sn$	17.068		$^{256}Cf \rightarrow ^{124}Cd + ^{4}He + ^{128}Cd$	17.504	
$^{248}Cf \rightarrow ^{118}Pd + ^{4}He + ^{126}Sn$	17.107		$^{256}Cf \rightarrow ^{126}Cd + ^{4}He + ^{126}Cd$	17.511	
$^{250}Cf \rightarrow ^{112}Ru + ^{4}He + ^{134}Te$	16.998		$^{258}Cf \rightarrow ^{118}Ru + ^{4}He + ^{136}Te$	17.454	
$^{250}Cf \rightarrow ^{114}Pd + ^{4}He + ^{132}Sn$	17.075	15.95	$^{258}Cf \rightarrow ^{120}Pd + ^{4}He + ^{134}Sn$	17.513	
$^{250}Cf \rightarrow ^{116}Pd + ^{4}He + ^{130}Sn$	17.137	±	$^{258}Cf \rightarrow ^{122}Pd + ^{4}He + ^{132}Sn$	17.557	
$^{250}Cf \rightarrow ^{118}Pd + ^{4}He + ^{128}Sn$	17.184	0.13	$^{258}Cf \rightarrow ^{124}Pd + ^{4}He + ^{130}Sn$	17.587	
$^{250}Cf \rightarrow ^{120}Pd + ^{4}He + ^{126}Sn$	17.215		$^{258}Cf \rightarrow ^{126}Cd + ^{4}He + ^{128}Cd$	17.602	
$^{252}Cf \rightarrow ^{110}Mo + ^{4}He + ^{138}Xe$	16.952		$^{260}Cf \rightarrow ^{120}Pd + ^{4}He + ^{136}Sn$	17.578	
$^{252}Cf \rightarrow ^{112}Ru + ^{4}He + ^{136}Te$	17.050	15.96	$^{260}Cf \rightarrow ^{122}Pd + ^{4}He + ^{134}Sn$	17.629	
$^{252}Cf \rightarrow ^{114}Ru + ^{4}He + ^{134}Te$	17.134	±	$^{260}Cf \rightarrow ^{124}Pd + ^{4}He + ^{132}Sn$	17.667	
$^{252}Cf \rightarrow ^{116}Pd + ^{4}He + ^{132}Sn$	17.203	0.09	$^{260}Cf \rightarrow ^{126}Cd + ^{4}He + ^{130}Cd$	17.688	
$^{252}Cf \rightarrow ^{118}Pd + ^{4}He + ^{130}Sn$	17.256		$^{260}Cf \rightarrow ^{128}Cd + ^{4}He + ^{128}Cd$	17.696	

4.9.5 Summary

In the alpha accompanied cold ternary fission of ^{244}Cf isotope, the highest yield is found for the fragment combination ^{108}Ru+^{4}He+^{132}Te, in which ^{132}Te (N=82, Z=52) is a near doubly magic nuclei. In the case of ^{246}Cf and ^{248}Cf isotopes, the highest yield is found for the fragment combination ^{108}Ru+^{4}He+^{134}Te and ^{110}Ru+^{4}He+^{134}Te, both of which possess near doubly magic nuclei ^{134}Te (N=82, Z=52). For alpha accompanied ternary fission of ^{250}Cf, ^{252}Cf, ^{254}Cf, ^{256}Cf, ^{258}Cf and ^{260}Cf isotopes, the highest yield is obtained for the fragment combinations ^{114}Pd+^{4}He+^{132}Sn, ^{116}Pd+^{4}He+^{132}Sn, ^{118}Pd+^{4}He+^{132}Sn, ^{120}Pd+^{4}He+^{132}Sn, ^{122}Pd+^{4}He+^{132}Sn and ^{124}Pd+^{4}He+^{132}Sn respectively, all of which possess doubly magic nuclei ^{132}Sn (N=82, Z=50). With the inclusion of deformation and orientation of fragments, the driving potential and relative yield of all possible fragment combinations are studied in detail and found that, in addition to closed shell effect, ground state deformation also plays an important role in the alpha accompanied ternary fission of $^{244\text{-}260}$Cf isotopes. The computed isotopic yields for alpha accompanied ternary fission of ^{252}Cf isotope are found to be in agreement with the experimental data. The emission probability and kinetic energy of long range alpha particle is calculated for the various isotopes of Cf and the values obtained agree well with the experimental data.

4.10 All possible tri-partition of ^{236}U isotope in collinear configuration

We have studied the ternary fission of ^{236}U isotope taking scattering potential as the sum of Coulomb and proximity potential, with fragments in collinear configuration. Here we have considered all possible ternary fragmentation of ^{236}U isotope, in order to find the fragment combination with higher yields. We have studied the tri-partition of ^{236}U isotope keeping the mass of the middle fragment as fixed which ranges from A_2 = 1 to 78. When A_2=1, one possible combination is that in which the other two fragments have mass number either 117 or 118. For the case A_2=78, other two fission fragments have mass numbers 79 each, which is the case of true ternary fission. For a given value of A_2, there are various Z_2 values and hence we have considered all possible Z_2 values for a particular value of A_2. Also for a given middle fragment (A_2, Z_2) we have considered all possible mass splitting and we would like to mention that in the tri-partition of ^{236}U isotope, there are about 7.786×10^5 possible ways of splitting and this value is according to the recent mass tables of Wang *et al.,* [36]. In the present work, we have studied all these possible fragmentations, in order to find the most probable ternary splitting of ^{236}U isotope and the repetition of the fragment combinations are avoided.

For a given mass of middle fragment, say A_2=34, there are 11 possible Z_2 values ranges from 10 (^{34}Ne) to 20 (^{34}Ca). We have studied the fragmentation of ^{236}U isotope, keeping the middle fragment as ^{34}Ne, ^{34}Na, ^{34}Mg, ^{34}Al, ^{34}Si, ^{34}P, ^{34}S, ^{34}Cl, ^{34}Ar, ^{34}K and ^{34}Ca using the concept of cold reaction valley. Keeping middle fragment as ^{34}Ca, the driving potential is calculated and plotted as a function of fragment mass number A_1 as shown in **Figure 4.92**. It can be seen that with ^{34}Ca as the middle fragment, the combination ^{76}Ni+^{34}Ca+^{126}Ru have the least driving potential and high Q value. In the case of ^{34}Ne, ^{34}Na, ^{34}Mg and ^{34}Al as the middle fragment, the fragment combination with least driving potential and high Q value is found for the splitting ^{84}Se+^{34}Ne+^{118}Cd, ^{76}Ga+^{34}Na+^{126}Sn, ^{68}Ni+^{34}Mg+^{134}Te and ^{69}Ni+^{34}Al+^{133}Sb respectively. With ^{34}Si and ^{34}P as the middle fragment formed in the tri-partition, the fragment combination with least driving potential and high Q value is found for ^{70}Ni+^{34}Si+^{132}Sn and ^{70}Co+^{34}P+^{132}Sn respectively. For A_2=34, the other favourable fragment combination are found for ^{70}Fe+^{34}S+^{132}Sn, ^{74}Ni+^{34}Cl+^{128}Ag, ^{76}Ni+^{34}Ar+^{126}Pd and ^{75}Ni+^{34}K+^{127}Rh respectively in the case of middle fragment as ^{34}S, ^{34}Cl, ^{34}Ar and ^{34}K. Among the all possible Z_2 values for A_2=34, the lowest driving potential is found for the fragment combination with ^{34}Si as the middle fragment. Thus, we can mention that among the all possible charges for a particular mass number of the middle fragment A_2=34, the most favourable fragment combination is obtained for ^{70}Ni+^{34}Si+^{132}Sn, in the ternary fission of ^{236}U isotope in collinear configuration. In order to prove our justification about the most favourable fragment combination, the barrier penetrability and hence the relative yield is calculated for the mass number of the middle fragment A_2=34 with charge ranges from Z_2 = 10 to 20.

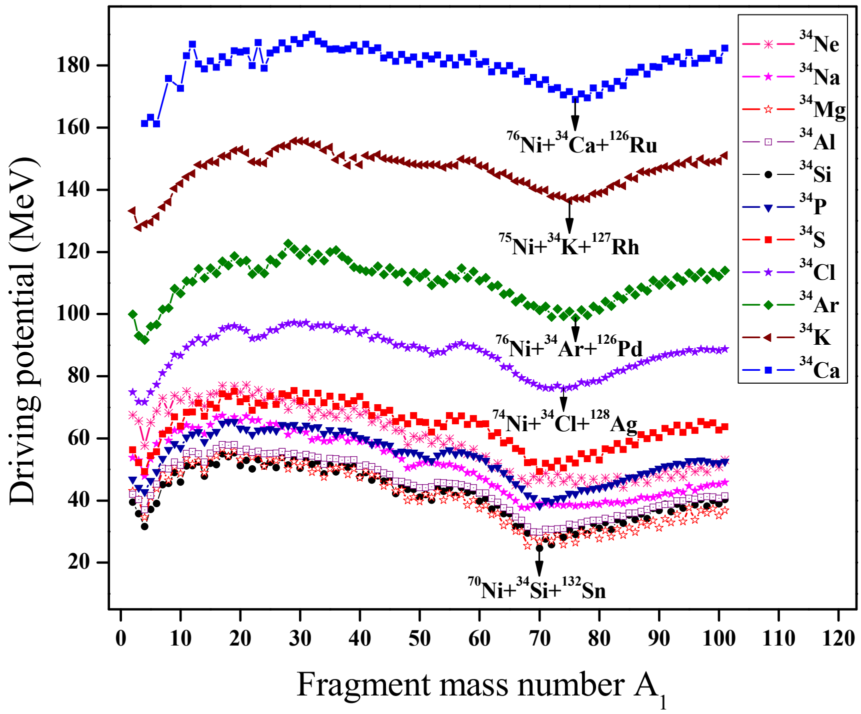

Figure 4.92 The driving potential is plotted as a function of fragment mass number A_1 for all possible middle fragment with mass number $A_2 = 34$.

In the case of middle fragment as ^{34}Ne, the barrier penetrability is calculated for all possible fragmentations found in the cold reaction valley and hence the relative yield is calculated and plotted as a function of fragment mass numbers A_1 and A_3 as shown in **Figure 4.93(a)**. From the **Figure 4.93(a)**, it is clear that the highest relative yield is found for the fragment splitting ^{84}Se+^{34}Ne+^{118}Cd, which is the same fragment combination obtained with the least driving potential and high Q value from the cold reaction valley plot. For ^{34}Na and ^{34}Mg as the middle fragment, the highest relative yield is obtained for the fragment combination ^{76}Ga+^{34}Na+^{126}Sn and ^{68}Ni+^{34}Mg+^{134}Te respectively, whereas in the case of ^{34}Al and ^{34}Si, the highest relative yield is found for ^{69}Ni+^{34}Al+^{133}Sb and ^{70}Ni+^{34}Si+^{132}Sn respectively. In the case of middle fragment ^{34}P, ^{34}S, ^{34}Cl and ^{34}Ar the highest relative yield is found for the splitting ^{70}Co+^{34}P+^{132}Sn, ^{70}Fe+^{34}S+^{132}Sn, ^{74}Ni+^{34}Cl+^{128}Ag and ^{76}Ni+^{34}Ar+^{126}Pd respectively. In a similar manner, the barrier penetrability and hence the relative yield is calculated for other possible fragmentations found for the particular mass number of the middle fragment A_2=34.

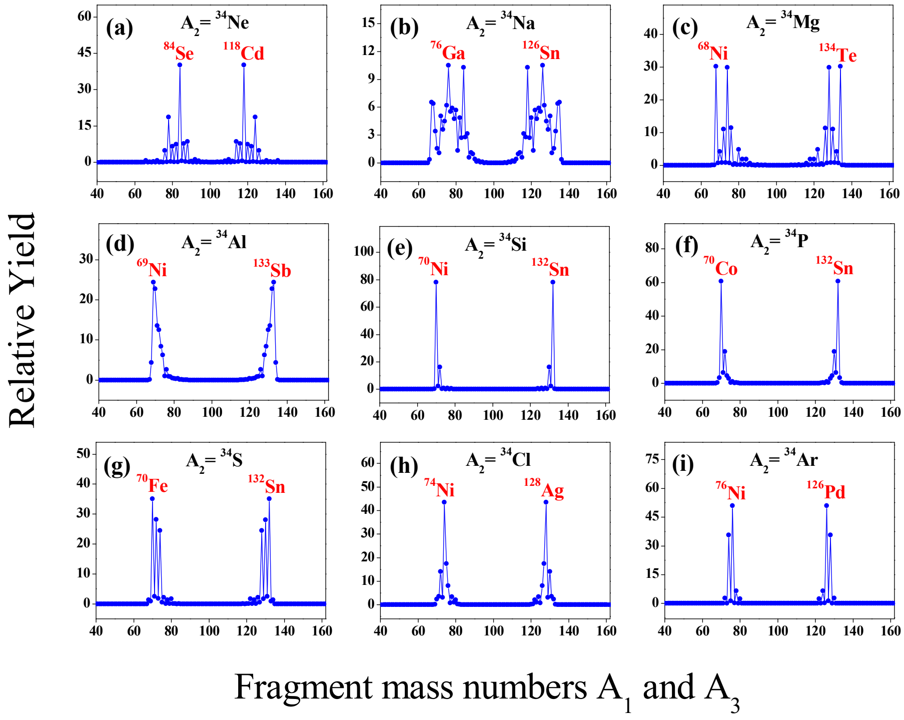

Figure 4.93 The relative yield is plotted as a function of fragment mass numbers A_1 and A_3 for all possible middle fragment with mass number $A_2 = 34$.

Figure 4.93 represents the relative yield plotted as a function of fragment mass numbers A_1 and A_3, keeping the mass of the middle fragment as $A_2 = 34$. From the **Figure 4.93**, it can be seen that the highest magnitude of relative yield is found for the fragment combination ^{70}Ni+^{34}Si+^{132}Sn which includes the presence of doubly magic nuclei ^{132}Sn (Z=50, N=82) nuclei and the proton shell closure Z=28 of ^{70}Ni. Here we would like to mention that, the fragment combination obtained with highest relative yield for a particular mass A_2=34, is the same as that obtained with least driving potential and high Q value from the cold reaction valley plot. The fragment combination with highest yield (minimum driving potential and maximum yield) for the tri-partition of ^{236}U with A_2 = 40, 46, 54, 56, 58 are for ^{64}Fe+^{40}S+^{132}Sn, ^{58}Cr+^{46}Ar+^{132}Sn, ^{48}Ca+^{54}Ca+^{134}Te, ^{48}Ca+^{56}Ti+^{132}Sn, ^{48}Ca+^{58}Ti+^{130}Sn respectively.

In a similar manner, the driving potential and the relative yield is calculated for all possible fragment combinations found in the tri-partition of ^{236}U isotope. It should be noted that, about seven hundred thousand fragment splitting is possible in the tri-partition of ^{236}U isotope, out of which the most favourable fragment combination for a particular mass number of the middle fragment ranges from A_2= 1 to 78 is shortlisted. In **Figure 4.94**, the driving potential of the most favourable fragment combination for a particular mass number of the middle fragment ranges from A_2= 1 to 78 is plotted as a function of fragment mass number A_2 obtained in the tri-partition of ^{236}U isotope.

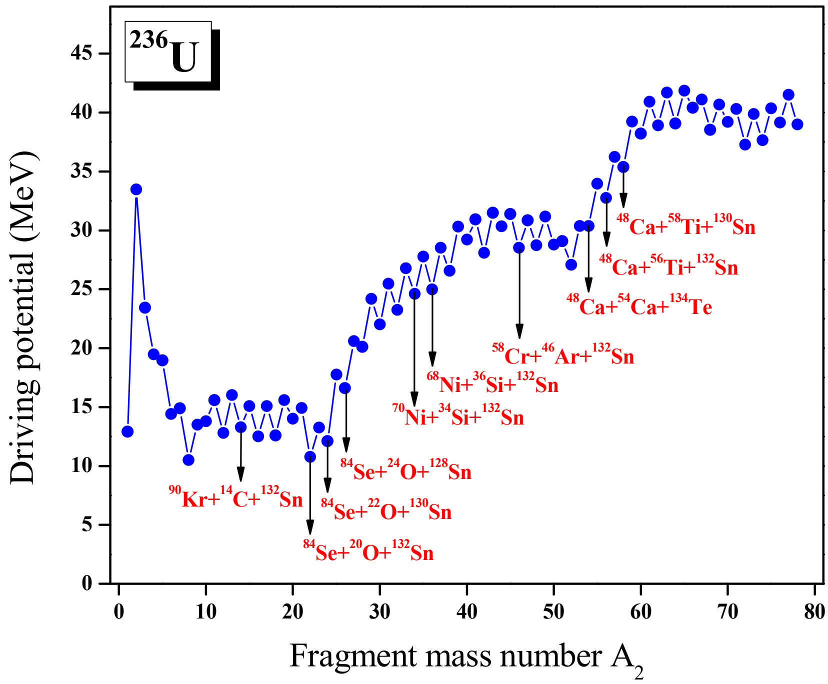

Figure 4.94 The driving potential of the most favourable fragment combination for a particular mass number of the middle fragment ranges from A_2= 1 to 78 plotted as a function of fragment mass number A_2, in the tri-partition of ^{236}U isotope.

Figure 4.95 represents the comparison of individual yield of the most favourable fragment combination for a particular mass number of the middle fragment ranges from A_2= 1 to 78 plotted as a function of fragment mass number A_2. The fragment combinations with the yield greater than 60 obtained in the tri-partition of ^{236}U are listed in **Table 4.13**. The highest yield is obtained for the fragment combination $^{48}Ca+^{58}Ti+^{130}Sn$, where ^{130}Sn (Z=50, N=80) is a near doubly magic nucleus and ^{48}Ca (Z=20, N=28) is a doubly magic nucleus.

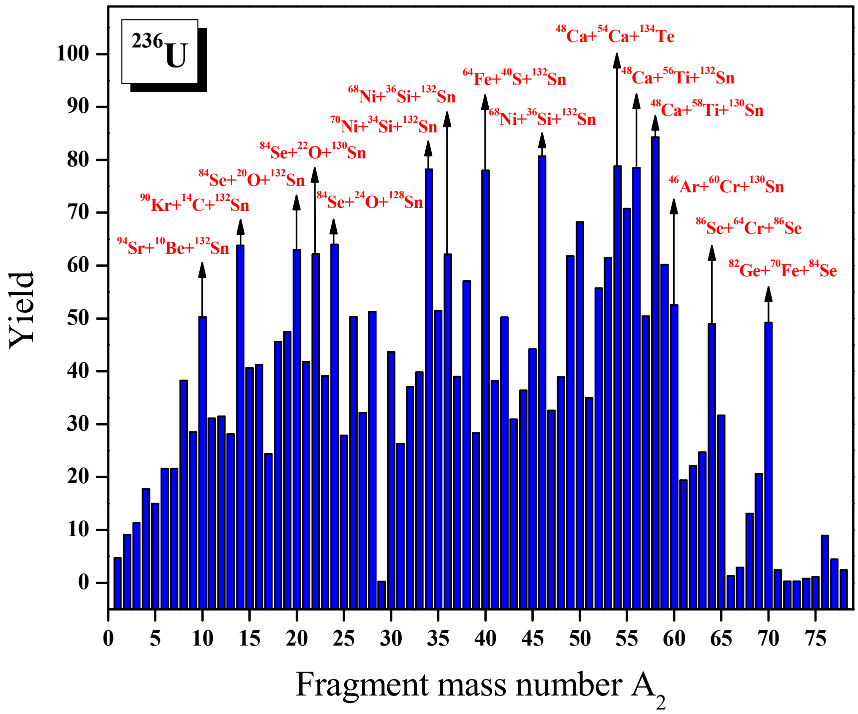

Figure 4.95 The yield of the most favourable fragment combination for a particular mass number of the middle fragment ranges from $A_2 = 1$ to 78, plotted as a function of fragment mass number A_2 in the tri-partition of ^{236}U isotope.

The next highest yield is obtained for the fragment combination ^{58}Cr+^{46}Ar+^{132}Sn, where ^{132}Sn (Z=50, N=82) is a doubly magic nucleus. The highest yield found for the fragment combination ^{48}Ca+^{54}Ca+^{134}Te and ^{48}Ca+^{56}Ti+^{132}Sn is due to the presence of near doubly magic nucleus ^{134}Te (Z=52, N=82) and doubly magic nucleus ^{132}Sn (Z=50, N=82) respectively. It should be noted that, in both cases the lighter fragment ^{48}Ca (Z=20, N=28) is a doubly magic nucleus. In the case of ^{34}Si as the middle fragment, the highest yield is found for the fragment combination with ^{70}Ni (Z=28) and doubly magic nucleus ^{132}Sn (Z=50, N=82) as the edge fragments. In the case of ^{36}Si as the middle fragment, the highest yield is found for the fragment combination with ^{68}Ni (Z=28) and doubly magic nucleus ^{132}Sn (Z=50, N=82) as the edge fragments. Thus the possibility for the formation of ^{68}Ni and ^{70}Ni as the edge fragment connecting the Sn isotope by Si, which has proved in the tri-partition of ^{236}U isotope using the Unified ternary fission model. This observation is in good agreement with the result obtained from the theoretical analysis done by Oertzen *et al.,* [30] and Nasirov *et al.,* [53].

Table 4.13. The fragment combinations obtained in the collinear tri-partition of ^{236}U isotope with a magnitude of yield greater than 60 are listed.

First fragment A_1	Middle fragment A_2	Third fragment A_3	Q value (MeV)	Yield Y (%)
^{90}Kr	^{14}C	^{132}Sn	190.93	63.81
^{84}Se	^{20}O	^{132}Sn	191.14	62.98
^{84}Se	^{22}O	^{130}Sn	189.25	62.21
^{84}Se	^{24}O	^{128}Sn	183.26	63.97
^{70}Ni	^{34}Si	^{132}Sn	198.16	78.24
^{68}Ni	^{36}Si	^{132}Sn	194.84	62.18
^{64}Fe	^{40}S	^{132}Sn	196.80	78.07
^{58}Cr	^{46}Ar	^{132}Sn	200.55	80.72
^{54}Ti	^{49}K	^{133}Sb	196.58	61.83
^{52}Ca	^{50}Ca	^{134}Te	198.83	68.29
^{49}Ca	^{53}Ca	^{134}Te	194.74	61.50
^{48}Ca	^{54}Ca	^{134}Te	193.99	78.86
^{49}Ca	^{55}Ti	^{132}Sn	201.96	70.82
^{48}Ca	^{56}Ti	^{132}Sn	202.43	78.51
^{48}Ca	^{58}Ti	^{130}Sn	197.91	84.35
^{47}K	^{59}V	^{130}Sn	196.12	60.28

The formation of ^{68}Ni and ^{70}Ni as the edge fragment connecting the ^{132}Sn isotope by Si, in the tri-partition of ^{236}U observed in FOBOS experimental setup by Pyatkov *et al.,* [54] proves the reliability of our present work using Unified ternary fission model. An overall relative yield is calculated which is defined as the ratio of the penetration probability of a particular fragment to the all possible fragmentations with the various fragment mass number A_2. **Figure 4.96** represents the overall relative yield of the most favourable fragment combination for a particular mass number of the middle fragment ranges from A_2 = 1 to 78 plotted as a function of fragment mass number A_2 in the tri-partition of ^{236}U. In **Figure 4.97**, the yield of favourable fragments obtained in the tri-partition of ^{236}U isotope is compared with the binary fission of ^{236}U. It is clear from the graph that, yield obtained for the binary fission of ^{236}U isotope is found to be higher than the tri-partition of ^{236}U isotope.

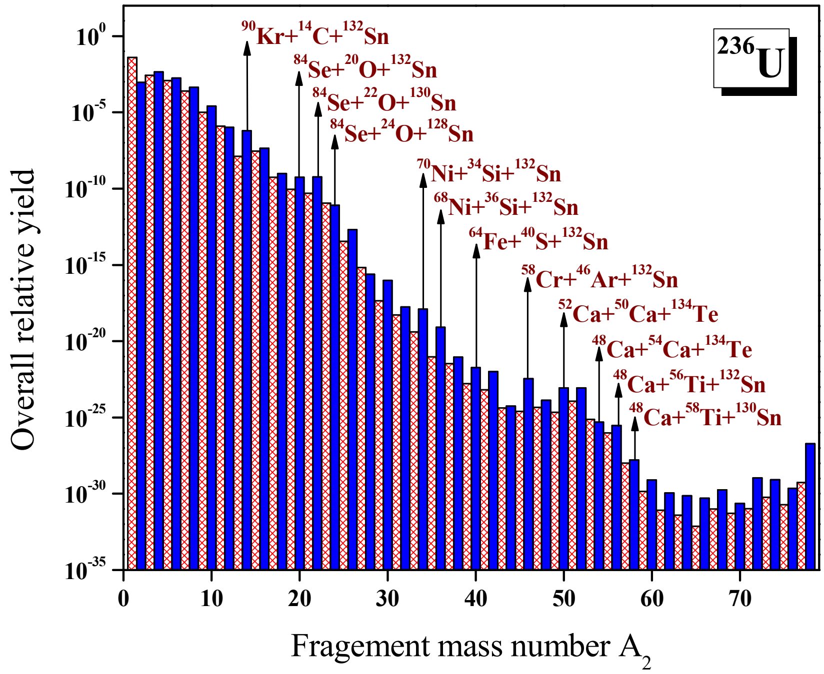

Figure 4.96 The overall relative yield of the most favourable fragment combination for a particular mass number of the middle fragment ranges from A_2= 1 to 78, plotted as a function of fragment mass number A_2.

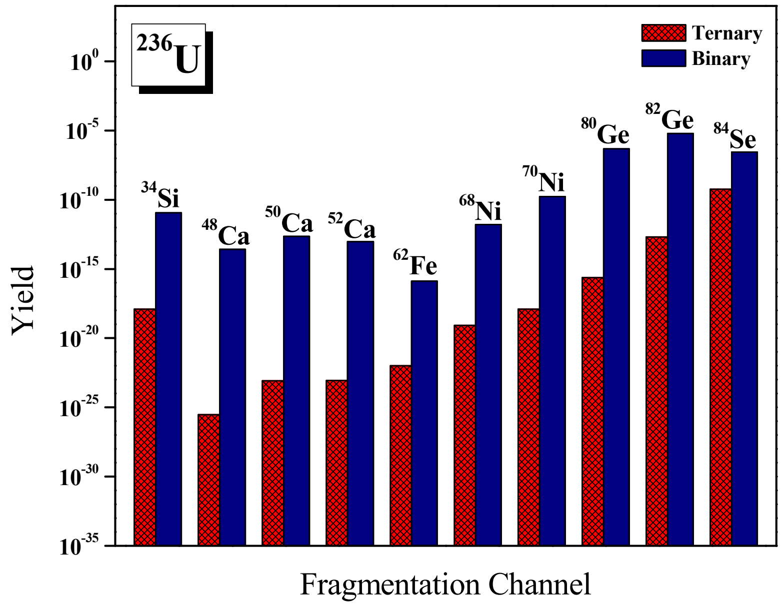

Figure 4.97 Comparison of yield of the favourable fragments obtained in the tri-partition of ^{236}U with the binary fission of ^{236}U.

4.10.1 Summary

The tri-partition of ^{236}U isotope has been studied for all possible fragmentation using the recently proposed Unified ternary fission model (UTFM). The highest yield is found for the fragmentation $^{48}Ca+^{58}Ti+^{130}Sn$, which possess the presence of doubly magic nucleus ^{48}Ca (Z=20, N=28) and near doubly magic nucleus ^{130}Sn (Z=50, N=80). The next highest yield is found for the fragmentation $^{58}Cr+^{46}Ar+^{132}Sn$, which also possess the presence of doubly magic nucleus ^{132}Sn (Z=50, N=82). The presence of closed shell or doubly closed shell effect plays an important role in the tri-partition of ^{236}U isotope. The formation of experimentally observed Ni isotope as the edge fragment connecting to Sn isotope by Si has been theoretically proved in the tri-partition of ^{236}U isotope using the Unified ternary fission model (UTFM). The formation of ^{68}Ni and ^{70}Ni as the edge fragment linking the doubly magic nucleus ^{132}Sn by the isotope of Si is in good agreement with experimental [56] and theoretical studies [53, 57], in the collinear cluster tri-partition of ^{236}U isotope which reveals the reliability of our model UTFM in ternary fission.

4.11 ^{34}Si accompanied ternary fission of ^{242}Cm in equatorial and collinear configuration

Taking the interacting potential as the sum of Coulomb and proximity potential we have studied all possible fragment combinations formed in the ^{34}Si accompanied ternary fission of ^{242}Cm with equatorial and collinear configuration. We have studied all the possible binary fragmentation of ^{242}Cm and compared the relative yield for binary exit channel with that of ternary fission. Here we have used a different method for the calculation of barrier penetrability and the method is briefly described as follows.

In the case of equatorial configuration there are three different barriers (due to three necks connecting the fragments), and in the case of collinear configuration there are two different barriers (due to two necks). So the barrier penetration probability P for equatorial configuration can be written as,

$$P = \exp\left\{-\frac{2}{\hbar}\int_{z_1'}^{z_2'}\sqrt{2\mu_{12}(V_{12}-Q_{12})}dz'\right\}\times\exp\left\{-\frac{2}{\hbar}\int_{z_1''}^{z_2''}\sqrt{2\mu_{23}(V_{23}-Q_{23})}dz''\right\}$$

$$\times\exp\left\{-\frac{2}{\hbar}\int_{z_1'''}^{z_2'''}\sqrt{2\mu_{31}(V_{31}-Q_{31})}dz'''\right\} \quad (4.11.1)$$

and for collinear configuration barrier penetrability is given as

$$P = \exp\left\{-\frac{2}{\hbar}\int_{z_1'}^{z_2'}\sqrt{2\mu_{12}(V_{12}-Q_{12})}dz'\right\}\times\exp\left\{-\frac{2}{\hbar}\int_{z_1''}^{z_2''}\sqrt{2\mu_{23}(V_{23}-Q_{23})}dz''\right\} \quad (4.11.2)$$

Here V_{12}, V_{23}, V_{31} be the interacting potential between the fragments A_1 and A_2, fragments A_2 and A_3, fragments A_3 and A_1 respectively. Q_{12}, Q_{23}, Q_{31} are the energy released when the respective nuclei breaks into fragments A_1 and A_2, A_2 and A_3, A_3 and A_1 respectively. It is to be noted that the sum $Q_{12}+Q_{23}+Q_{31}\neq Q$, the energy released in ternary fission. We would like to mention that the difference in Q value is being utilized for the deformation of the ternary fission fragments. The mass parameter in the above equations are replaced by reduced mass, $\mu_{12}=m\frac{A_1A_2}{A_1+A_2}$, $\mu_{23}=m\frac{A_2A_3}{A_2+A_3}$ and $\mu_{31}=m\frac{A_3A_1}{A_3+A_1}$, where m is the nucleon mass. The turning point $z_1'=z_2''=z_3'''=0$ represent the touching configuration and the outer turning points z_2', z_2'', z_2''' are given by the equations $V_{12}(z_2')=Q_{12}$, $V_{23}(z_2'')=Q_{23}$, $V_{31}(z_2''')=Q_{31}$ respectively.

4.11.1 Ternary fission of ^{242}Cm with ^{34}Si as light charged particle.

In this work, keeping ^{34}Si as the third charged particle emitted in equatorial configuration, the fragmentation potential is calculated and the driving potential is plotted as a function of A_1 in **Figure 4.98**. The Q values and (V-Q) values of the probable ternary fragmentation in equatorial configuration are listed in **Table 4.14**. The minima is found in the cold valley are at A_1 = ^{1}n, ^{4}He, ^{20}O, ^{22}O, ^{40}S, ^{42}S, ^{46}Ar, ^{50}Ca, ^{52}Ca, etc. The deepest minima found for the combination ^{1}n+ ^{207}Pb + ^{34}Si, and the next minima found for the fragment combination ^{4}He + ^{204}Hg + ^{34}Si, arises due to near doubly magic ^{207}Pb (Z = 82, N = 125) and the near doubly magic nuclei ^{204}Hg (Z = 80, N = 124) respectively. Of the two other valleys of minima observed around ^{50}Ca and ^{128}Sn, the first valley of minima around ^{50}Ca is due to the presence of the proton shell closure at Z = 20 and the second valley of minima around ^{128}Sn is due to the proton shell closure at Z = 50. The barrier penetrability is calculated for each charge minimized fragment combinations found in the cold ternary fission of ^{242}Cm using the formalism described above. The relative yield is calculated and is plotted as a function of fragment mass number A_1 in **Figure 4.99**.

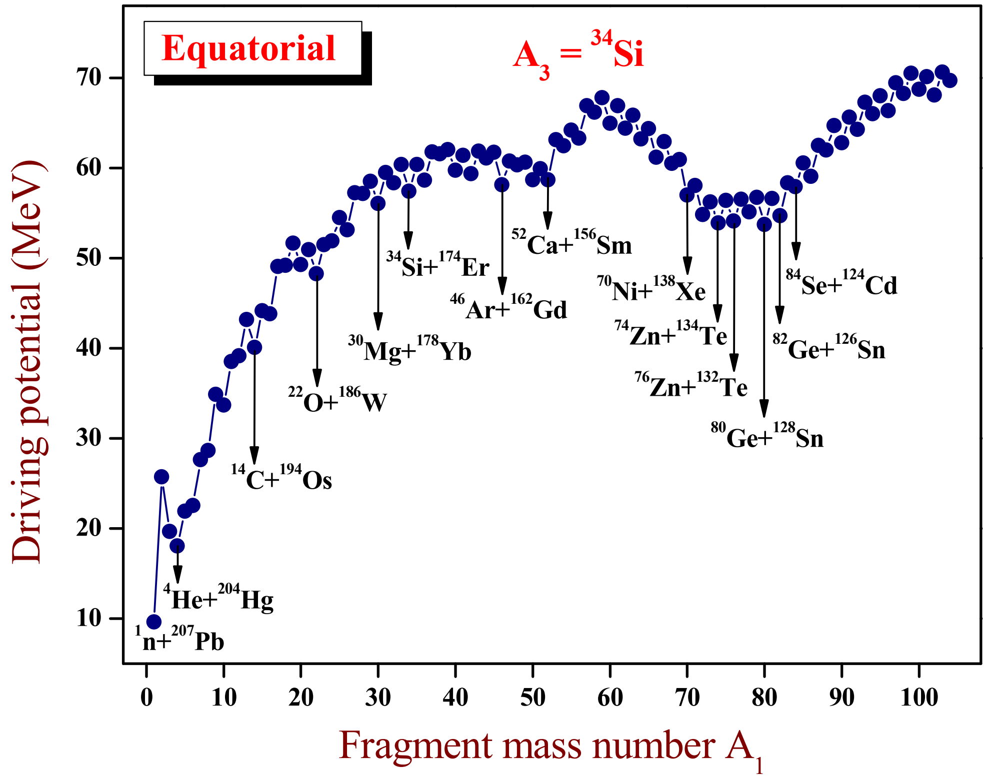

Figure 4.98. The driving potential for the ternary fission of ^{242}Cm with ^{34}Si as light charged particle, with fragments in equatorial configuration is plotted as a function of mass number A_1.

Table 4.14. The fragments occur in the cold valley for the equatorial emission of fragments in the case of ^{34}Si accompanied ternary fission of ^{242}Cm. The corresponding Q-values and (V-Q) for the touching configuration of fragments are listed.

First Fragment (A_1)	LCP (A_3)	Second Fragment (A_2)	Q-value (MeV)	V-Q (MeV)	First Fragment (A_1)	LCP (A_3)	Second Fragment (A_2)	Q-value (MeV)	V-Q (MeV)
^{4}He	^{34}Si	^{204}Hg	97.027	18.032	^{56}Ti	^{34}Si	^{152}Nd	184.12	63.284
^{6}He	^{34}Si	^{202}Hg	84.515	22.556	^{58}Cr	^{34}Si	^{150}Ce	191.43	66.173
^{8}He	^{34}Si	^{200}Hg	72.656	28.636	^{60}Cr	^{34}Si	^{148}Ce	191.66	64.944
^{10}Be	^{34}Si	^{198}Pt	92.060	33.692	^{62}Cr	^{34}Si	^{146}Ce	191.28	64.391
^{12}Be	^{34}Si	^{196}Pt	82.331	39.136	^{64}Fe	^{34}Si	^{144}Ba	201.49	63.198
^{14}C	^{34}Si	^{194}Os	104.18	40.088	^{66}Fe	^{34}Si	^{142}Ba	202.67	61.182
^{16}C	^{34}Si	^{192}Os	96.952	43.807	^{68}Ni	^{34}Si	^{140}Xe	211.21	60.489
^{18}C	^{34}Si	^{190}Os	88.551	49.181	^{70}Ni	^{34}Si	^{138}Xe	213.94	56.994
^{20}O	^{34}Si	^{188}W	109.63	49.267	^{72}Ni	^{34}Si	^{136}Xe	215.41	54.836
^{22}O	^{34}Si	^{186}W	107.99	48.251	^{74}Zn	^{34}Si	^{134}Te	223.05	53.897
^{24}O	^{34}Si	^{184}W	101.97	51.910	^{76}Zn	^{34}Si	^{132}Te	222.25	54.088
^{26}Ne	^{34}Si	^{182}Hf	120.33	53.113	^{78}Ge	^{34}Si	^{130}Sn	226.75	55.138
^{28}Mg	^{34}Si	^{180}Hf	134.38	57.153	^{80}Ge	^{34}Si	^{128}Sn	227.65	53.702
^{30}Mg	^{34}Si	^{178}Yb	133.34	56.036	^{82}Ge	^{34}Si	^{126}Sn	226.19	54.699
^{32}Mg	^{34}Si	^{176}Yb	129.081	58.337	^{84}Se	^{34}Si	^{124}Cd	227.41	57.913
^{34}Si	^{34}Si	^{174}Er	146.66	57.393	^{86}Se	^{34}Si	^{122}Cd	225.87	59.050
^{36}Si	^{34}Si	^{172}Er	143.63	58.627	^{88}Se	^{34}Si	^{120}Cd	222.60	61.989
^{38}Si	^{34}Si	^{170}Er	139.04	61.576	^{90}Kr	^{34}Si	^{118}Pd	225.11	62.804
^{40}S	^{34}Si	^{168}Dy	156.16	59.732	^{92}Kr	^{34}Si	^{116}Pd	223.36	64.286
^{42}S	^{34}Si	^{166}Dy	154.98	59.378	^{94}Sr	^{34}Si	^{114}Ru	223.83	66.025
^{44}Ar	^{34}Si	^{164}Gd	167.20	61.104	^{96}Sr	^{34}Si	^{112}Ru	223.32	66.341
^{46}Ar	^{34}Si	^{162}Gd	168.772	58.132	^{98}Zr	^{34}Si	^{110}Ru	221.25	68.268
^{48}Ca	^{34}Si	^{160}Sm	179.222	60.351	^{100}Zr	^{34}Si	^{108}Mo	221.90	68.726
^{50}Ca	^{34}Si	^{158}Sm	179.601	58.675	^{102}Zr	^{34}Si	^{106}Mo	222.49	68.071
^{52}Ca	^{34}Si	^{156}Sm	178.385	58.696	^{104}Zr	^{34}Si	^{104}Mo	220.84	69.713
^{54}Ti	^{34}Si	^{154}Nd	186.042	62.463					

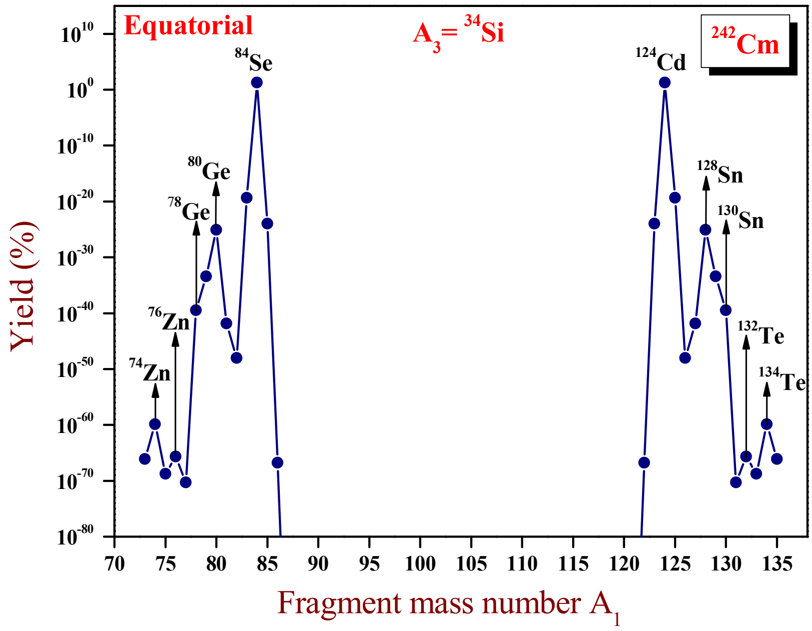

Figure 4.99. The calculated yields for the ternary fission of ^{242}Cm isotope with charge minimized third fragment ^{34}Si, with fragments in equatorial configuration is plotted as a function of mass number A_1.

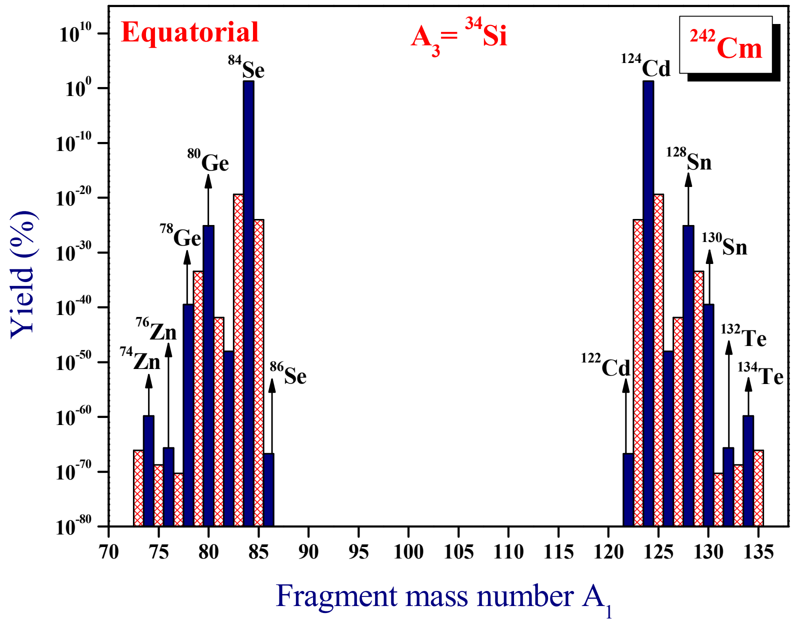

Figure 4.100. The histogram of the calculated yields for the ternary fission of ^{242}Cm isotope with charge minimized third fragment ^{34}Si, with fragments in equatorial configuration is plotted as a function of mass number A_1.

Our calculations reveal that, the asymmetric mass splitting (mass $A_1 < 70$) is not favourable in ternary fission with equatorial configuration. The highest yield is obtained for the fragment combination ^{84}Se + ^{124}Cd + ^{34}Si and is due to the neutron shell closure of ^{84}Se (N = 50) and near neutron shell closure of ^{124}Cd (N ≈ 50). Corresponding to the valley of minima around ^{128}Sn (Z = 50) in **Figure 4.99**, the presence of near doubly magic nuclei ^{130}Sn (Z = 50, N = 80), ^{134}Te (Z = 52, N = 82) and ^{132}Te (Z = 52, N = 80) can be attributed to the high yields observed for the fragment combinations ^{78}Ge+^{130}Sn+^{34}Si, ^{74}Zn+^{134}Te+^{34}Si and ^{76}Zn+^{132}Te+^{34}Si, respectively. The proton shell closure at Z = 50 of ^{128}Sn, can be attributed to the high yields observed for the fragment combination ^{80}Ge + ^{128}Sn + ^{34}Si. For a better view of the result, a histogram is plotted with yield as a function of mass number A_1 as shown in **Figure 4.100**.

In the collinear configuration, the light charged particle ^{34}Si (A_2) is considered in between the other two fragments. The driving potential (V-Q) is plotted as a function of fragment mass number A_1 and is as shown in **Figure 4.101**. The Q values and (V-Q) values of the probable ternary fragmentation in collinear configuration are listed in **Table 4.15**. The deepest minimum is found for the fragment combination with ^{1}n. The other minima is observed for the fragment combination with A_1 = ^{4}He, ^{12}C, ^{14}C, ^{32}Si, ^{34}Si, etc. The two deep valleys seen around ^{48}Ca and ^{128}Sn, is due to the presence of the doubly magic ^{48}Ca (Z = 20, N = 28) and the neutron shell closure at Z = 50 of ^{128}Sn respectively. It is to be noted that the minimum around ^{128}Sn is found to be close to that of the driving potential obtained for neutron and has a lower driving potential compared to the ternary fragmentation in the case of equatorial emission shown in **Figure 4.98**.

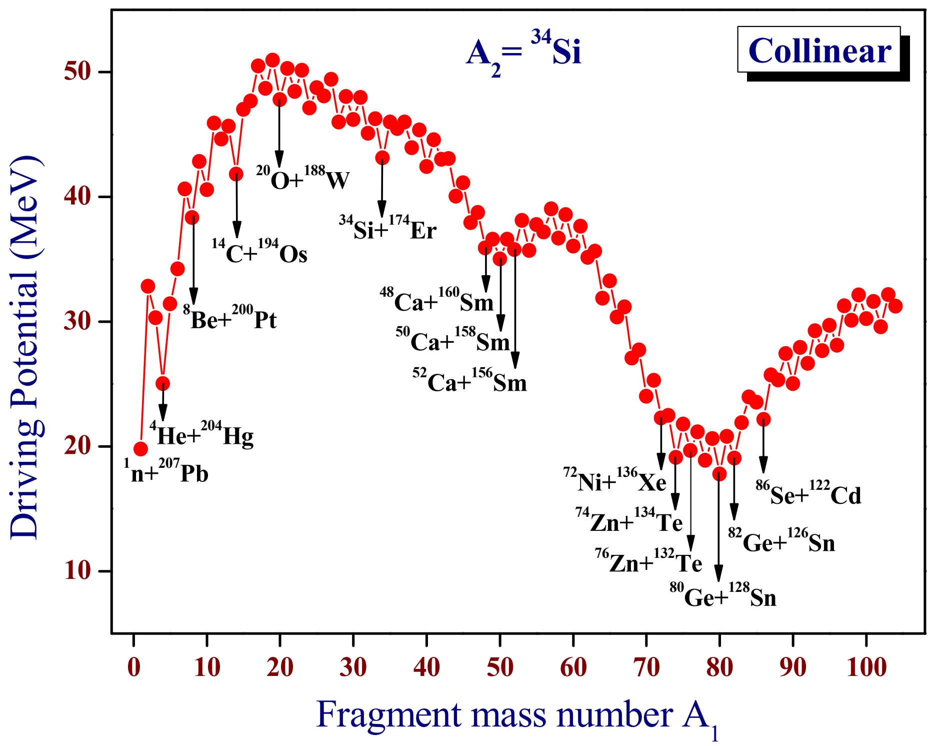

Figure 4.101. The driving potential for the ternary fission of ^{242}Cm isotope with ^{34}Si as light charged particle with fragments in the collinear configuration is plotted as a function of mass number A_1.

The relative yield as a function of fragment mass numbers A_1 is plotted as shown in **Figure 4.102**. In collinear configuration also, the asymmetric mass splitting (with mass $A_1 < 70$) is not found to be favourable. The highest yield is obtained for the fragment combination ^{84}Se + ^{34}Si + ^{124}Cd and is due to the neutron shell closure of ^{84}Se (N = 50) and near neutron shell closure of ^{124}Cd (N ≈ 50). The presence of the near doubly magic nuclei ^{134}Te (Z = 52, N = 82), the near doubly magic nuclei ^{132}Te (Z = 52, N = 80) and the proton shell closure at Z = 50 of ^{128}Sn, can be attributed to the high yields observed for the fragment combinations ^{74}Zn + ^{34}Si + ^{134}Te, ^{76}Zn + ^{34}Si + ^{132}Te and ^{80}Ge + ^{34}Si + ^{128}Sn, respectively. For a better view of the result, a histogram is plotted with yield as a function of mass number A_1 as shown in **Figure 4.103**.

Table 4.15. The fragments occur in the cold valley for the collinear emission of fragments in the ternary fission of ^{242}Cm isotope with ^{34}Si as the light charged particle. The corresponding Q-values and (V-Q) for the touching configuration of fragments are listed.

First Fragment (A_1)	LCP (A_2)	Third Fragment (A_3)	Q-value (MeV)	V-Q (MeV)	First Fragment (A_1)	LCP (A_2)	Third Fragment (A_3)	Q-value (MeV)	V-Q (MeV)
^{4}He	^{34}Si	^{204}Hg	97.0277	25.036	^{56}Ti	^{34}Si	^{152}Nd	184.121	37.203
^{6}He	^{34}Si	^{202}Hg	84.5158	34.229	^{58}Cr	^{34}Si	^{150}Ce	191.439	36.687
^{8}Be	^{34}Si	^{200}Pt	96.4217	38.363	^{60}Cr	^{34}Si	^{148}Ce	191.660	36.064
^{10}Be	^{34}Si	^{198}Pt	92.0606	40.578	^{62}Fe	^{34}Si	^{146}Ba	198.580	35.168
^{12}C	^{34}Si	^{196}Os	103.042	44.634	^{64}Fe	^{34}Si	^{144}Ba	201.499	31.875
^{14}C	^{34}Si	^{194}Os	104.180	41.836	^{66}Fe	^{34}Si	^{142}Ba	202.673	30.369
^{16}C	^{34}Si	^{192}Os	96.9523	47.697	^{68}Ni	^{34}Si	^{140}Xe	211.212	27.071
^{18}O	^{34}Si	^{190}W	109.925	48.696	^{70}Ni	^{34}Si	^{138}Xe	213.948	24.029
^{20}O	^{34}Si	^{188}W	109.636	47.804	^{72}Ni	^{34}Si	^{136}Xe	215.418	22.293
^{22}O	^{34}Si	^{186}W	107.993	48.434	^{74}Zn	^{34}Si	^{134}Te	223.055	19.125
^{24}Ne	^{34}Si	^{184}Hf	122.214	47.132	^{76}Zn	^{34}Si	^{132}Te	222.253	19.684
^{26}Ne	^{34}Si	^{182}Hf	120.335	48.093	^{78}Ge	^{34}Si	^{130}Sn	226.757	18.900
^{28}Mg	^{34}Si	^{180}Yb	134.381	46.005	^{80}Ge	^{34}Si	^{128}Sn	227.659	17.778
^{30}Mg	^{34}Si	^{178}Yb	133.340	46.204	^{82}Ge	^{34}Si	^{126}Sn	226.192	19.061
^{32}Si	^{34}Si	^{176}Er	145.470	45.115	^{84}Ge	^{34}Si	^{124}Sn	221.145	23.959
^{34}Si	^{34}Si	^{174}Er	146.669	43.136	^{86}Se	^{34}Si	^{122}Cd	225.878	22.180
^{36}Si	^{34}Si	^{172}Er	143.636	45.474	^{88}Se	^{34}Si	^{120}Cd	222.603	25.327
^{38}S	^{34}Si	^{170}Dy	155.283	43.955	^{90}Kr	^{34}Si	^{118}Pd	225.110	25.035
^{40}S	^{34}Si	^{168}Dy	156.160	42.428	^{92}Kr	^{34}Si	^{116}Pd	223.364	26.678
^{42}S	^{34}Si	^{166}Dy	154.984	43.024	^{94}Sr	^{34}Si	^{114}Ru	223.830	27.691
^{44}Ar	^{34}Si	^{164}Gd	167.205	40.050	^{96}Sr	^{34}Si	^{112}Ru	223.321	28.118
^{46}Ar	^{34}Si	^{162}Gd	168.772	37.938	^{98}Sr	^{34}Si	^{110}Ru	221.259	30.130
^{48}Ca	^{34}Si	^{160}Sm	179.222	35.910	^{100}Zr	^{34}Si	^{108}Mo	221.906	30.220
^{50}Ca	^{34}Si	^{158}Sm	179.602	35.018	^{102}Zr	^{34}Si	^{106}Mo	222.497	29.602
^{52}Ca	^{34}Si	^{156}Sm	178.385	35.776	^{104}Zr	^{34}Si	^{104}Mo	220.848	31.256
^{54}Ti	^{34}Si	^{154}Nd	186.042	35.712					

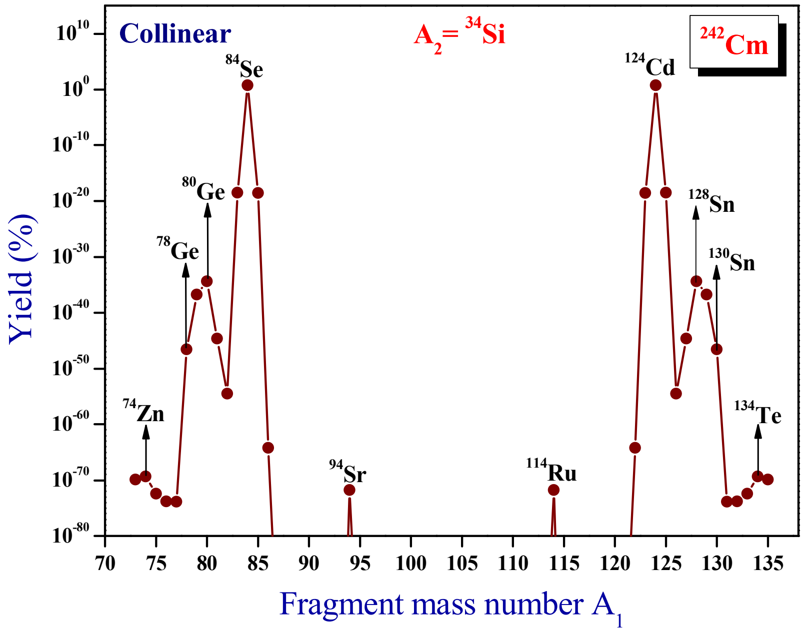

Figure 4.102. The calculated yields for the ternary fission of ^{242}Cm isotope with charge minimized third fragment ^{34}Si, with fragments in the collinear configuration is plotted as a function of mass number A_1.

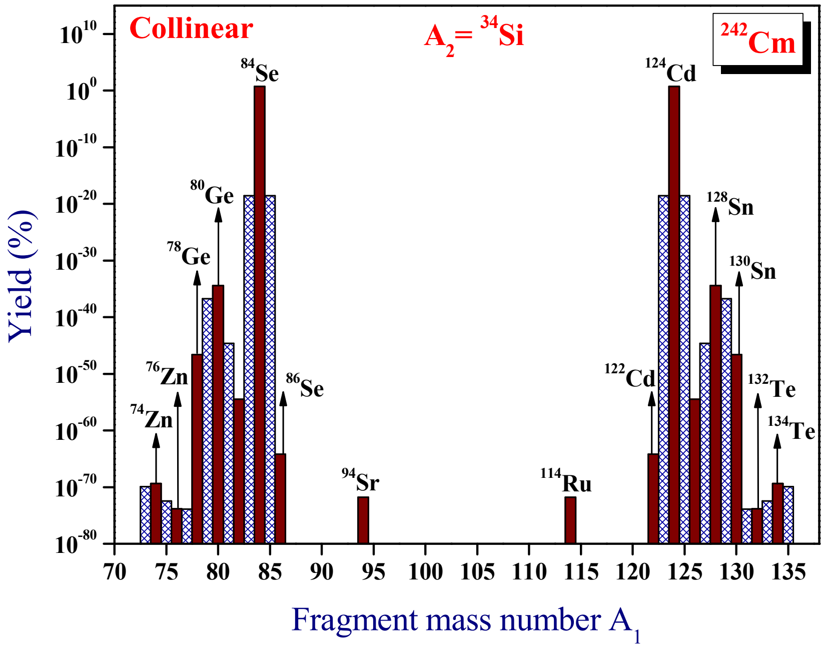

Figure 4.103. The histogram of the calculated yields for the ternary fission of ^{242}Cm isotope with charge minimized third fragment ^{34}Si, with fragments in the collinear configuration is plotted as function of mass number A_1.

4.11.2 Binary fission of ^{242}Cm

The driving potential (V-Q) for the binary fragmentation of ^{242}Cm is plotted as a function of fragment mass number A_2 and is shown in **Figure 4.104**. The Q values and (V-Q) values of the probable binary fragmentation are listed in the **Table 4.16**. From the cold valley plot it is clear that the deepest minimum is found for the fragment combination ^{4}He + ^{238}Pu. The other minima in the plot is for the fragment combination with A_2 = ^{14}C, ^{34}Si, ^{44}Ar, ^{46}Ar, ^{48}Ca, ^{50}Ca, ^{52}Ca, etc. The deep minima observed for ^{34}Si + ^{208}Pb can be attributed to the presence of the doubly magic ^{208}Pb (Z = 82, N = 126). Another valley of minimum can be observed around ^{84}Se + ^{158}Sm, with three comparable minima ^{80}Ge + ^{162}Gd, ^{82}Ge + ^{160}Gd and ^{86}Se + ^{156}Sm. The fragment combination with A_1 = ^{136}Xe, ^{134}Xe, ^{132}Te, ^{130}Sn and ^{128}Sn forms the next deep minimum in the cold valley.

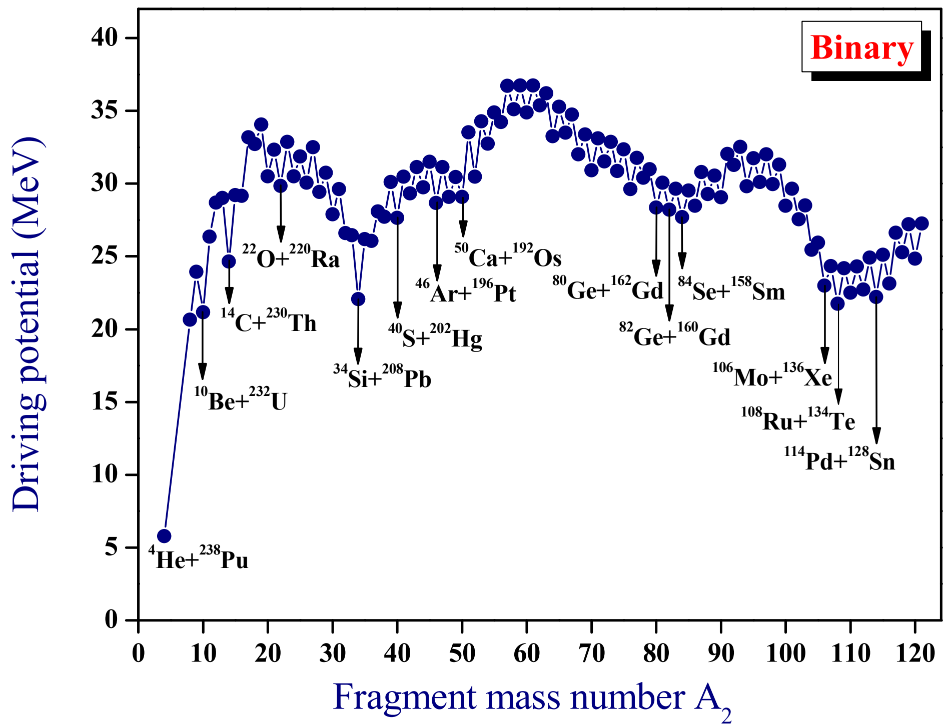

Figure 4.104. The driving potential for the binary fission of ^{242}Cm isotope is plotted as a function of mass number A_2.

Table 4.16. The fragments occur in the cold valley for the binary fission of ^{242}Cm isotope. The corresponding Q-values and (V-Q) for the touching configuration of fragments are listed.

First Fragment (A_1)	Second Fragment (A_2)	Q-value (MeV)	V-Q (MeV)	First Fragment (A_1)	Second Fragment (A_2)	Q-value (MeV)	V-Q (MeV)
^{238}Pu	^{4}He	6.216	5.789	^{178}Yb	^{64}Fe	159.469	33.259
^{234}U	^{8}Be	11.717	20.654	^{176}Yb	^{66}Fe	158.363	33.500
^{232}U	^{10}Be	7.587	21.157	^{174}Er	^{68}Ni	170.219	31.998
^{230}Th	^{12}C	23.941	28.697	^{172}Er	^{70}Ni	170.503	30.915
^{228}Th	^{14}C	25.013	24.654	^{170}Er	^{72}Ni	169.141	31.521
^{226}Th	^{16}C	17.914	29.164	^{168}Dy	^{74}Zn	179.122	30.871
^{224}Ra	^{18}O	36.761	32.715	^{166}Dy	^{76}Zn	179.692	29.608
^{222}Ra	^{20}O	36.687	30.486	^{164}Dy	^{78}Zn	178.255	30.389
^{220}Ra	^{22}O	35.254	29.839	^{162}Gd	^{80}Ge	188.621	28.350
^{218}At	^{24}Na	55.539	30.497	^{160}Gd	^{82}Ge	188.161	28.215
^{216}Rn	^{26}Ne	54.073	30.051	^{158}Sm	^{84}Se	196.003	27.682
^{214}Po	^{28}Mg	74.294	29.410	^{156}Sm	^{86}Se	194.672	28.480
^{212}Po	^{30}Mg	74.058	27.875	^{154}Nd	^{88}Kr	200.177	29.276
^{210}Pb	^{32}Si	93.611	26.604	^{152}Nd	^{90}Kr	199.914	29.066
^{208}Pb	^{34}Si	96.511	22.059	^{150}Nd	^{92}Kr	197.254	31.285
^{206}Pb	^{36}Si	90.981	26.052	^{148}Ce	^{94}Sr	204.049	29.818
^{204}Hg	^{38}S	106.357	27.715	^{146}Ce	^{96}Sr	203.376	30.116
^{202}Hg	^{40}S	104.989	27.643	^{144}Ba	^{98}Zr	207.865	29.955
^{200}Hg	^{42}S	101.947	29.333	^{142}Ba	^{100}Zr	209.030	28.468
^{198}Pt	^{44}Ar	117.384	29.742	^{140}Ba	^{102}Zr	209.669	27.539
^{196}Pt	^{46}Ar	117.182	28.675	^{138}Xe	^{104}Mo	215.134	25.449
^{194}Os	^{48}Ca	131.467	29.081	^{136}Xe	^{106}Mo	217.376	22.975
^{192}Os	^{50}Ca	130.279	29.080	^{134}Te	^{108}Rn	221.000	21.741
^{190}Os	^{52}Ca	127.775	30.458	^{132}Te	^{110}Ru	220.064	22.503
^{188}W	^{54}Ti	139.075	32.732	^{130}Sn	^{112}Pd	221.260	22.718
^{186}W	^{56}Ti	136.526	34.228	^{128}Sn	^{114}Pd	221.658	22.204
^{184}Hf	^{58}Cr	148.135	35.094	^{126}Sn	^{116}Pd	220.652	23.123
^{182}Hf	^{60}Cr	147.357	34.889	^{124}Sn	^{118}Pd	218.429	25.289
^{180}Yb	^{62}Fe	158.283	35.358	^{122}Cd	^{120}Cd	219.375	24.832

The relative yield for various fragment combination in the binary fission of ^{242}Cm is plotted for mass number ranging from $A_1 = 25$ to $A_2 = 217$ is shown in **Figure 4.105**.

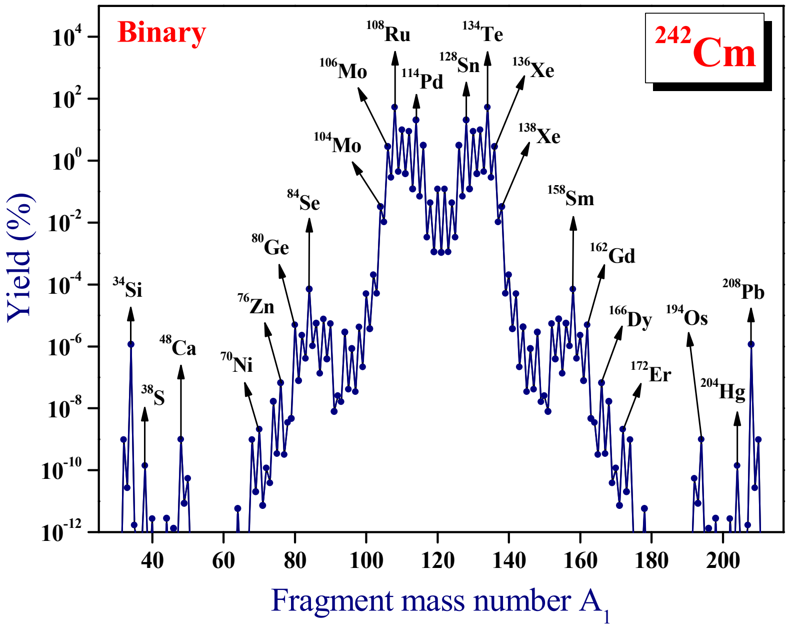

Figure 4.105. The calculated yields for the binary fission of ^{242}Cm isotope is plotted as a function of mass number A_1.

In the case of binary fragmentation, we have computed the yields of all fragments including the very asymmetric fragments. But we have not shown these (fragments with $A_2 < 28$) in **Figure 4.105** and **Figure 4.106** because, an appreciable yield (1.059 x 10^{-4} %) was found only for the alpha particle ($A_2 = 4$) and the yield for other fragments with $A_2 < 28$ is very low (below 10-22%). The high value of yield observed for ^{34}Si + ^{208}Pb, ^{48}Ca + ^{194}Os, ^{114}Pd + ^{128}Sn, ^{110}Ru + ^{132}Te and ^{108}Ru + ^{134}Te, is to be attributed to the presence of doubly magic nuclei ^{208}Pb (N = 126, Z = 82), doubly magic ^{48}Ca (Z = 20, N = 28), the magic shell closure at Z = 50 of ^{128}Sn, the near doubly magic ^{132}Te (Z = 50, N = 82) and the near double magic ^{134}Te (Z = 52, N = 82) respectively. For a better view of the result, a histogram is plotted with yield as a function of mass number A_1 as shown in **Figure 4.106**.

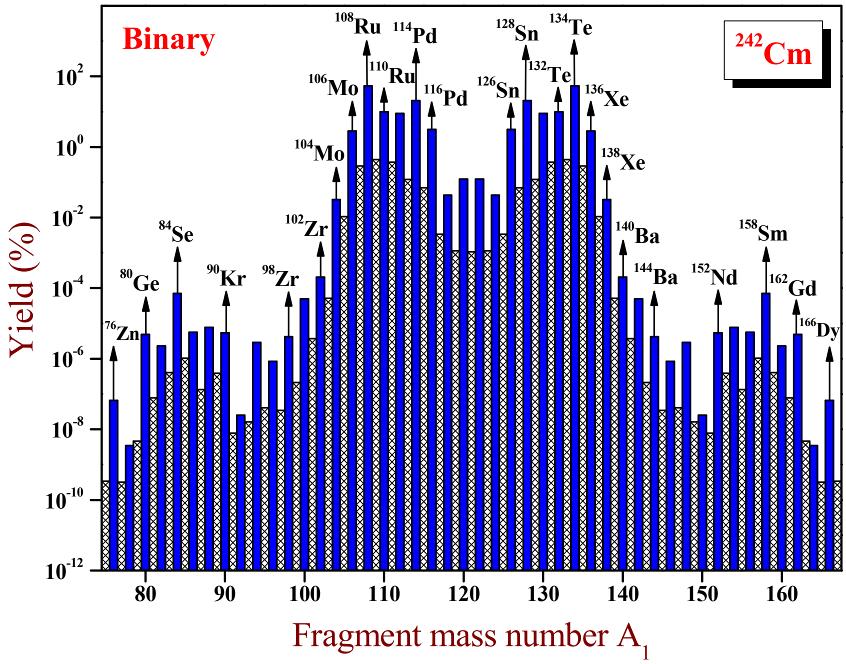

Figure 4.106. The histogram of the calculated yields for the binary fission of ^{242}Cm isotope is plotted as a function of mass number A_1.

Using our formalism, we have computed the penetrability, decay constant and half lives, for the binary fragmentation of ^{242}Cm, emitting ^{4}He and ^{34}Si. The computed half life values are in agreement with the experimental data. In the case of ^{4}He emission, $T_{1/2}^{present} = 6.606 \times 10^{7}s$ and $T_{1/2}^{expt.} = 1.407 \times 10^{7}s$ [55] and in the case of ^{34}Si emission, $T_{1/2}^{present} = 1.425 \times 10^{23}s$ and $T_{1/2}^{expt.} = 1.412 \times 10^{23}s$. We have also compared the predicted yields for the fragmentation of ^{4}He and ^{34}Si from ^{242}Cm, with that of the yields extracted from the corresponding experimental data. In the case of ^{4}He emission, $P_{\alpha}(extracted\ from\ experiment) = 1.72 \times 10^{-28}$ and $P_{\alpha}(present) = 6.17 \times 10^{-29}$ and the corresponding yields are $Y_{expt.} = 2.96 \times 10^{-4}\%$ and $Y_{the} = 1.06 \times 10^{-4}\%$. Here P_{α} is the penetrability of the alpha particle. It can be seen that both the predicted penetrability and yields are in agreement with the experimental values.

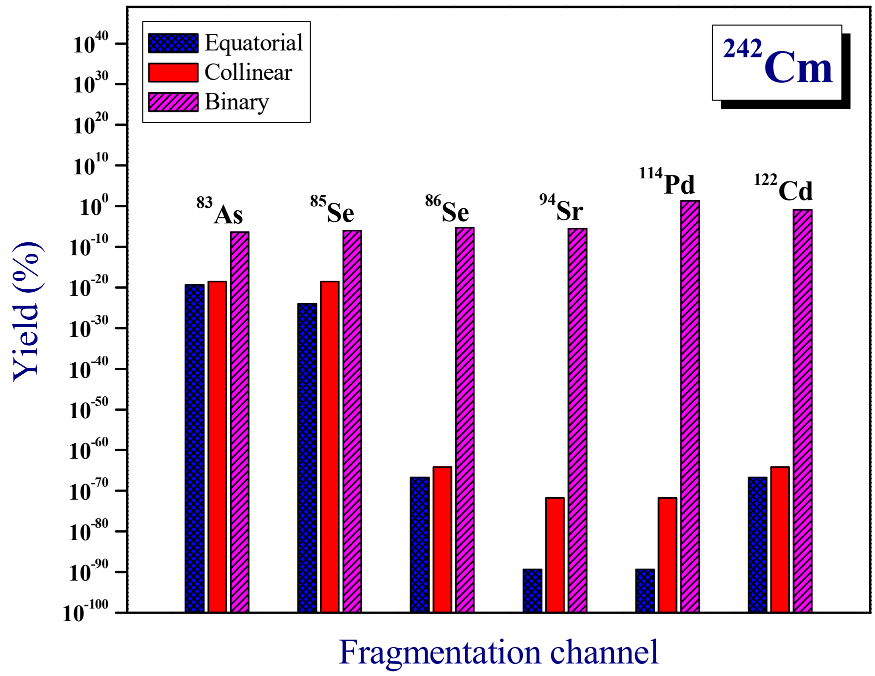

Figure 4.107. Comparison of calculated yield for ^{34}Si accompanied ternary fission (equatorial and collinear configuration) of ^{242}Cm with the yield for binary fission of ^{242}Cm.

We have compared the relative yield for binary exit channel of ^{242}Cm with that of ternary decay (both equatorial and collinear configuration) and are displayed in **Figure 4.107**. From the figure it can be seen that relative yield for collinear configuration is very large compared to equatorial configuration. It is also to be noted that, these theoretical predictions using the proximity potential on the relative yield of ternary fragmentation, is in agreement with those theoretical predictions reported by Manimaran *et al.,* [26] using the Three cluster model with Yukawa + Exponential potential. We would also like to mention that, Oertzen *et al.,* [29] have experimentally observed that, the ternary fragmentation of heavy nuclei with heavy third particle (heavier than ^{4}He, ^{10}Be, etc.), is only possible in a collinear configuration. This experimental observation supports our theoretical prediction on the preference of collinear geometry over equatorial configuration in the case of ^{34}Si accompanying ternary fission of ^{242}Cm. It is also clear from **Figure 4.107** that the relative yield for binary fragmentation is found to be higher than that of ternary fragmentation (both equatorial and collinear configuration).

4.11.3 Summary

Taking Coulomb and proximity potential as interacting potential the ternary fragmentation of ^{242}Cm with third charged particle as ^{34}Si, with equatorial and collinear configuration have been studied. The calculation of the fragmentation potential and Q-value for all possible fission components reveals that the even mass number fragments is more favoured than odd mass number fragments. The relative yield has been evaluated so as to obtain the favourable fragment combination. The role of near doubly magic shell closures (of ^{130}Sn, ^{132}Te and ^{134}Te, etc.) in the ^{34}Si accompanied ternary fission is revealed through the study. The comparison of relative yield reveals that in ^{34}Si accompanied ternary fission collinear configuration is preferred than the equatorial configuration. It is also found that the relative yield for binary exit channel is found to be higher than that of ternary fragmentation (both equatorial and collinear configuration).

References

[1] L. W. Alvarez, as reported by G. Farwell, E. Segre and C. Wiegand, Phys. Rev. **71**, 327 (1947).

[2] N. A. Perfilov, Z. I. Soloveva and R. A. Filov, Atomnaya energiya (Atomic Energy) **14,** 575 (1963).

[3] N. A. Perfilov, Z. I. Soloveva, R. A. Filov and G. I. Khlebnikov, Sov. Phys. JETP **17**, 1232 (1963).

[4] N. A. Perfilov, Z. I. Soloveva and R. A. Filov, Sov. Phys. JETP **19**, 1515 (1964).

[5] L. Z. Malkin, I. D. Alkhazov, A. S. Krisvokhatskii, K. A. Petrzhak and L. M. Belov, Translated from Atomnaya Energiya **16**, 148 (1964).

[6] P. B. Vitta, Nucl. Phys. A **170**, 417 (1971).

[7] J. P. Theobald, P. Heeg, M. Mutterer, Nucl. Phys. A **502**, 343c (1989).

[8] A. V. Ramayya, J. H. Hamilton, J. K. Hwang, L. K. Peker, J. Kormicki, B. R. S. Babu, T. N. Ginter, A. Sandulescu, A. Florescu, F. Carstoiu, W. Greiner, G. M. Ter-Akopian, Yu. Ts. Oganessian, A. V. Daniel, W. C. Ma, P. G. Varmette, J. O. Rasmussen, S. J. Asztalos, S. Y. Chu, K. E. Gregorich, A. O. Macchiavelli, R. W. Macleod, J. D. Cole, R. Aryaeinejad, K. Butler-Moore, M. W. Drigert, M. A. Stoyer, L. A. Bernstein, R. W. Lougheed, K. J. Moody, S. G. Prussin, S. J. Zhu, H. C. Griffin and R. Donangelo, Phys. Rev. C **57**, 2370 (1998).

[9] A. V. Ramayya, J. H. Hamilton, J. K. Hwang, Rom. Rep. Phys. **59**, 595 (2007).

[10] A. Sandulescu, F. Carstoiu, S. Misicu, A. Florescu, A. V. Ramayya, J. H. Hamilton and W. Greiner, J. Phys. G: Nucl. Part. Phys. **24**, 181 (1998).

[11] Y. Ronen, Ann. of Nucl. En. **29**, 1013 (2002).

[12] D. N. Poenaru, R. A. Gherghescu, W. Greiner, Y. Nagame, J. H. Hamilton and A. V. Ramayya, Rom. Rep. Phys. **55**, 549 (2003).

[13] Yu. V. Pyatkov, D. V. Kamanin, W. H. Trzaska, W. von Oertzen, S. R. Yamaletdinov, A. N. Tjukavkin, V. G. Tishchenko, V. G. Lyapin, Yu. E. Peinionzhkevich, A. A. Alexandrov, S. V. Khlebnikov, Rom. Rep. Phys. **59**, 569 (2007).

[14] K. R. Vijayaraghavan, M. Balasubramaniam and W. von Oertzen, Phys. Rev. C **90**, 024601 (2014).

[15] A. Sandulescu, F. Carstiou, I. Bulboaca and W. Greiner, Phys. Rev C **60**, 044613 (1999).

[16] A. Florescu, A. Sandulescu, D. S. Delion, J. H. Hamilton, A. V. Ramayya and W. Greiner, Phys. Rev. C **61**, 051602 (2000).

[17] D. S. Delion, A. Florescu and A. Sandulescu, Phys. Rev. C **63**, 044312 (2001).

[18] Yu. N. Kopatch, M. Mutterer, D. Schwalm, P. Thirolf and F. Gonnenwein, Phys. Rev. C **62**, 044614 (2002).
[19] O. Serot, C. Wagemans, Nucl. Phys. A **641**, 34 (1998).
[20] O. Serot, N. Carjan and C. Wagemans, Eur. Phys. J. A **8**, 187 (2000).
[21] S. Vermote, C. Wagemans, O. Serot, J. Heyse, J. Van Gils, T. Soldner and P. Geltenbort, Nucl. Phys. A **806**, 1 (2008).
[22] S. Vermote, C. Wagemans, O. Serot, J. Heyse, J. Van Gils, T. Soldner, P. Geltenbort, I. AlMahamid, G. Tian, L. Rao, Nucl. Phys. A **837**, 176 (2010).
[23] K. Manimaran and M. Balasubramaniam, Phys. Rev. C **79**, 024610 (2009).
[24] K. Manimaran and M. Balasubramaniam, Eur. Phys. J. A **45**, 293 (2010).
[25] K. Manimaran and M. Balasubramaniam, J. Phys. G: Nucl. Part. Phys. **37**, 045104 (2010).
[26] K. Manimaran and M. Balasubramaniam, Phys. Rev. C **83**, 034609 (2011).
[27] K. R. Vijayaraghavan, W. von Oertzen and M. Balasubramaniam, Eur. Phys. J. A **48**, 27 (2012).
[28] Yu. V. Pyatkov, D. V. Kamanin, W. von Oertzen, A. A. Alexandrov, I. A. Alexandrova, O. V. Falomkina, N. A. Kondratjev, Yu. N. Kopatch, E. A. Kuznetsova, Yu. E. Lavrova, A. N. Tyukavkin, W. Trzaska and V. E. Zhuhcko, Eur. Phys. J. A **45**, 29 (2010).
[29] W. von Oertzen, Y. V. Pyatkov, D. Kamanin, Acta. Phys. Pol. B **44**, 447 (2013).
[30] W. von Oertzen and A. K. Nasirov, Phys. Lett B **734**, 234 (2014).
[31] J. Blocki, J. Randrup, W. J. Swiatecki, C. F. Tsang, Ann. Phys. (N.Y) **105**, 427 (1977).
[32] J. Blocki, W. J. Swiatecki, Ann. Phys. (N.Y) **132**, 53 (1983).
[33] Y. J. Shi and W. J. Swiatecki, Nucl. Phys. A **438**, 450 (1985).
[34] S. S. Malik and R. K. Gupta, Phys.Rev.C **39**, 1992 (1989).
[35] W. D. Myers and W. J. Swiatecki, Ark. Fys. **36**, 343 (1967).
[36] M. Wang, G. Audi, A. H. Wapstra, F. G. Kondev, M. MacCormick, X. Xu and B. Pfeiffer, Chin. Phys. C **36**, 1603 (2012).
[37] H. Koura, T. Tachibana, M. Uno and M. Yamada, Prog. Theor. Phys. **113**, 305 (2005).
[38] A. V. Ramayya, J. K. Hwang, J. H. Hamilton, A. Sandulescu, A. Florescu, G. M. Ter-Akopian, A. V. Daniel, Yu. Tu. Oganessiamn, G. S. Popeko, W. Greiner, J. D. Cole and GANDS95 Collaboration, Phys. Rev. Lett. **81**, 947 (1998).
[39] J. H. Hamilton, A. V. Ramayya, J. K. Hwang, J. Kormicki, B. R. S. Babu, A. Sandulescu, A. Florescu, W. Greiner, G. M. Ter-Akopian, Yu. Ts. Oganessian, A. V. Daniel, S. J. Zhu, M. G. Wang, T. Ginter, J. K. Deng, W. C. Ma, G. S. Popeko, Q. H. Lu, E. Jones, R. Dodder, P. Gore, W. Nazarewicz, J. O. Rasmussen, S. Asztalos, I. Y. Lee, S. Y. Chu, K. E. Gregorich, A. O. Macchiavelli, M. F. Mohar, S. Prussin, M. A. Stoyer, R. W.

Lougheed, K. J. Moody, J. F. Wild, L. A. Bernstein, J. A. Becker, J. D. Cole, R. Aryaeinejad, Y. X. Dardenne, M. W. Drigert, K. Butler-Moore, R. Donangelo, H. C. Griffin, Prog. Part. Nucl. Phys. **38**, 273 (1997).

[40] A. Sandulescu, F. Carstoiu, S. Misicu, A. Florescu, A. V. Ramayya, J. H. Hamilton and W. Greiner, J. Phys. G: Nucl. Part. Phys. **24**, 181 (1998).

[41] N. Carjan, J. de Phys. **37**, 1279 (1976).

[42] R. Blendowske, T. Fliessbach and H. Walliser, Z. Phys. A **339**, 121 (1991).

[43] J. F. Wild, P. A. Baisden, R. J. Dougan, E. K. Hulet, R. W. Lougheed and J. H. Landrum, Phys. Rev. C **32**, 488 (1985).

[44] Z. Fraenkel, Phys. Rev. **156**, 1283 (1967).

[45] V. E. Viola, K. Kwiatkowski and M. Walker, Phys. Rev. C **31**, 1550 (1985).

[46] C. M. Herbach, D. Hilscher, V. G. Tishchenko, P. Gippner, D. V. Kamanin, W. von Oertzen, H. G. Ortlepp, Yu. E. Penionzhkevich, Yu. V. Pyatkov, G. Renz, K. D. Schilling, O. V. Strekalovsky, W. Wagner, V. E. Zhuchko, Nucl. Phys. A **712**, 207 (2002).

[47] C. Y. Wong, Phys. Rev. Lett. **31**, 766 (1973).

[48] N. Malhotra and R. K. Gupta, Phys. Rev. **C 31**, 1179 (1985).

[49] R. K. Gupta, M. Balasubramaniam, R. Kumar, N. Singh, M. Manhas and W. Greiner, J. Phys. G: Nucl. Part. Phys. **31**, 631 (2005).

[50] A. J. Baltz and B. F. Bayman, Phys. Rev. **C 26**, 1969 (1982).

[51] http://w.w.w.nds.iaea.org/RIPL-2

[52] P. Moller, J. R. Nix and K. L. Kratz, At. Data Nucl. Data Tables **66**, 131 (1997).

[53] A. K. Nasirov, W. von Oertzen, A. I. Muminov and R. B. Tashkhodjaev, Phys. Scr. **89**, 054022 (2014).

[54] Yu. V. Pyatkov, D. V. Kamanin, Yu. N. Kopach, A. A. Alexandrov, I. A. Alexandrova, S. B. Borzakov, Yu. N. Voronov, V. E. Zhuchko,E. A. Kuznetsova, Ts. Panteleev and A. N. Tyukavkin, Phys. Atomic Nucl. **73**, 1309 (2010).

[55] NuDat2.5, http://www.nndc.bnl.gov.

[56] R. B. Tashkhodjaev, A. I. Muminov, A. K. Nasirov, W. von Oertzen and Yongseok Oh, Phys. Rev. C **91**, 054612 (2015).

[57] Yu. V. Pyatkov, D. V. Kamanin, W. von Oertzen, A. A. Alexandrov, I. A. Alexandrova, O. V. Falomkina, N. Jacobs, N. A. Kondratjev, E. A. Kuznetsova, Yu. E. Lavrova, V. Malaza, Yu. V. Ryabov, O. V. Strekalovsky, A. N. Tyukavkin, and V. E. Zhuchko, Eur. Phys. J. A **48**, 94 (2012).

CHAPTER 5

Conclusion

Coulomb and proximity potential model (CPPM) has been used to study the heavy particle radioactivity from superheavy nuclei leading to $^{298}114$ daughter nuclei. Most of the predicted half lives are well within the present upper limit for measurements ($T_{1/2} < 10^{30}$ s) and the computed alpha half lives for $^{290,292}Lv$ agree well with the experimental data. Alpha decay chains from Z=118 superheavy nuclei in the range $271 \leq A \leq 310$ has been studied using CPPM. The α decay half-lives of $^{294}118$ and its decay products, evaluated using our formalisms, are in good agreement with the experimental results and we hope that the theoretical prediction of 5α decay chains consistently from $^{289\text{-}293}118$ isotopes provides a new perspective to experimentalists. Probable cluster decays from $^{270-318}118$ superheavy nuclei has been studied extensively within the CPPM. Most of the predicted half-lives are well within the present experimental upper limit (10^{30}s) and lower limit (10^{-6}s) for measurements and hence these predictions may be of great use for further experimental investigation on cluster decay in the superheavy region.

The cold binary fission of even-even $^{244\text{-}258}Cf$ isotopes has been studied by taking the interacting barrier as the sum of Coulomb and proximity potential. The fragment combinations with maximum yield reveal the role of doubly magic and near doubly magic nuclei in binary fission. It is found that asymmetric splitting is favoured for Cf isotopes with mass number $A \leq 250$ and symmetric splitting is favoured for Cf isotopes with $A > 252$. In the case of Cf isotope with A=252, there is an equal probability for asymmetric and symmetric splitting. For the binary fission of ^{238}Pu isotope, the highest yield is predicted for the fragments with isotope of Pb (Z=82) as one fragment, whereas for ^{240,242}Pu isotopes, fragments with isotope of Hg (Z=80) as one fragment possesses the highest yield. In the case of ^{244,246,248}Pu isotopes, the highest yield is for the fragments with Sn (Z=50) as one fragment. It is found that asymmetric splitting is superior for Pu isotopes with A $\leq$ 242 and symmetric splitting is superior for Pu isotopes with A $\geq$ 244. The binary fragmentations of even-even $^{230\text{-}250}$U isotopes are studied with Coulomb and proximity potential is taken as the interacting potential barrier. The role of the nuclear shell structure in the formation of fission products is revealed through our study and also the presence of doubly magic or near doubly magic nuclei plays an important role in the fission process of even-even $^{230\text{-}250}$U isotopes.

The alpha accompanied cold ternary fission of ^{252}Cf and the cold ternary fission of ^{242}Cm with ^{4}He, ^{10}Be, ^{14}C and ^{34}Si as light charged particle has been studied using Unified ternary fission model (UTFM), in which the interacting barrier is taken as the sum of Coulomb and proximity potential. The comparison of relative yield reveals that in ^{34}Si accompanied ternary fission of ^{242}Cm, collinear configuration is preferred than the equatorial configuration. The spontaneous cold ternary fission of ^{250,252}Cf isotope with ^{3}H and ^{6}He as light charged particle and even-even $^{250\text{-}260}$Cf isotope with ^{10}Be as light charged particle with the fragments in equatorial and collinear configuration has been studied using UTFM. The fragment combinations with maximum yields reveal the role of doubly magic and near doubly magic nuclei in cold ternary fission. In the ^{14}C accompanied ternary fission of even–even $^{250\text{–}260}$Cf isotopes, the highest yield is obtained for the fragment combination using our formalism, is found to be in agreement with that observed in the experiment using the triple gamma coincidence technique at the Gammasphere facility.

The emission probabilities and kinetic energies of long range alpha particles have been computed for the ternary fission of even-even $^{242\text{-}252}$Cm, $^{238\text{-}244}$Pu and $^{244\text{-}260}$Cf isotopes and are found to be in good agreement with the experimental data. The effect of deformation and orientation of fragments in the ^{4}He accompanied ternary fission of even-even $^{242\text{-}248}Cm$, $^{238\text{-}244}Pu$ and $^{244\text{-}260}Cf$ isotopes are studied. Our study reveals that the ground state deformation has as an important role in the alpha accompanied ternary fission as that of the shell effect. In the collinear cluster tri-partition of ^{236}U isotope, the formation of ^{68}Ni and ^{70}Ni as the edge fragment linking the doubly magic nucleus ^{132}Sn by the isotope of Si is in good agreement with experimental and theoretical studies, which reveals the reliability of our model (UTFM) in the ternary fission.